# Bioenabled Synthesis of Anisotropic Gold and Silver Nanoparticles

**Xi Geng**

A dissertation submitted to the faculty of Virginia Polytechnic Institute and State University in partial fulfillment of the requirements for the degree of

Doctor of Philosophy

in

Chemistry

Tijana Z. Grove, Chair

Alan R. Esker

Robert B. Moore

John R. Morris

May 3, 2017

Blacksburg, Virginia

Keywords: plasmonic, localized surface plasmon resonance (LSPR), anisotropic nanoparticles, bioenabled synthesis, nanoprisms, nanostars, SERS, repeat protein, lignin.

# Bioenabled Synthesis of Anisotropic Gold and Silver Nanoparticles

Xi Geng

## Abstract

Anisotropic plasmonic noble metallic nanoparticles (APMNs) have received enormous attention due to their distinct geometric features and fascinating physicochemical properties. Owing in large part to their tailored localized surface plasmon resonance (LSPR) and the intensive electromagnetic field at the sharp corners and edges, APMNs are exceptionally well suited for biomedical applications such as biosensing, bioimaging, diagnostics and therapeutics. Although a rich variety of surfactant-assisted colloidal routes have been developed to prepare well-defined APMNs, biomedical applications necessitate tedious and rigorous purification processes for the complete removal of toxic surfactants. In this dissertation, we aim to develop generic bioenabled green synthetic methodologies towards APMNs. By applying a series of thermodynamic, kinetic and seed quality control, a series of APMNs with varied morphologies such as branched nanostars and triangular nanoprisms have been successfully prepared.

We first presented the preparation of gold nanostars (Au NSTs) through a two-step approach utilizing a common Good's buffer, HEPES, as a weak reducing agent. Single crystalline Au NSTs with tunable branches up to 30 nm in length were produced and the halide ions rather than the ionic strength played a significant roles on the length of the branches of Au NSTs. Then consensus sequence tetratricopetide repeat (CTPR) proteins with increasing number of repeats were used as model proteins to probe the effects of concentration as well as the protein shape on the morphology and resulting physicochemical properties of plasmonic gold nanoparticles.

Since the underlying growth mechanism for the biomimetic synthesis of APMNs remains elusive and controversial, the other objective is to elucidate the molecular interactions between inorganic species and biopolymers during the course of NP evolution. Fluorescent quenching and 2D NMR experiments have confirmed the moderate binding affinity of CTPR to the Au(0) and Au(III). We observed that the initial complexation step between gold ions and CTPR3 is ionic strength dependent. Furthermore, we also found that NPs preferentially interact with the negatively charged face of CTPR3 as observed in 2D NMR. Knowledge of binding behavior between biospecies and metal ions/NPs will facilitate rational deign of proteins for biomimetic synthesis of metallic NPs.

A modified seed-mediated synthetic strategy was also developed for the growth of silver nanoprisms with low shape polydispersity, narrow size distribution and tailored plasmonic absorbance. During the seed nucleation step, CTPR proteins are utilized as potent stabilizers to facilitate the formation of planar-twinned Ag seeds. Ag nanoprisms were produced in high yield in a growth solution containing ascorbic acid and CTPR-stabilized Ag seeds. From the time-course UV-Vis and transmission electron microscopy (TEM) studies, we postulate that the growth mechanism is the combination of facet selective lateral growth and thermodynamically driven Ostwald ripening.

By incorporation of seeded growth and biomimetic synthesis, gold nanotriangles (Au NTs) with tunable edge length were synthesized *via* a green chemical route in the presence of the designed CTPR protein, halide anions ($Br^-$) and CTPR-stabilized Ag seeds. The well-defined morphologies, tailored plasmonic absorbance from visible-light to the near infrared (NIR) region, colloidal stability and biocompatibility are attributed to the synergistic action of CTPR, halide ions, and CTPR-stabilized Ag seeds.

We also ascertained that a vast array of biosustainable materials including negatively charged lignin and cellulose derivatives can serve as both a potent stabilizers and an efficient nanocrystal modifiers to regulate the growth of well-defined Ag nanoprisms using a one-pot or seeded growth strategy. The influential effects of reactants and additives including the concentration of sodium lignosulfonate, $H_2O_2$ and $NaBH_4$ were studied in great detail. It implies that appropriate physicochemical properties rather than the specific binding sequence of biomaterials are critical for the shaped-controlled growth of Ag NTs and new synthetic paradigms could be proposed based on these findings.

Last but not the least, we have demonstrated the resulting APMNs, particularly, Au NSTs and Ag NTs exhibit remarkable colloidal stability, enhanced SERS performance, making them promising materials for biosensing and photothermal therapy. Since the Ag nanoprisms are susceptible to morphological deformation in the presence of strong oxidant, they also hold great potential for the colorimetric sensing of oxidative metal cation species such as $Fe^{3+,}$ $Cr^{3+,}$ etc.

# Bioenabled Synthesis of Anisotropic Gold and Silver Nanoparticles

Xi Geng

## General Audience Abstract

When a beam of light impinges on the surface of noble metallic nanoparticle (NP), particularly gold (Au) and silver (Ag), the conduction electrons are excited which induces a collective oscillatory motion, resulting in an intense localized surface plasmon resonance (LSPR) absorbance as well as the amplified localized electromagnetic filed. Owing in large part to the tailored LSPR and the intensive electromagnetic field at the sharp corners and edges, anisotropic plasmonic noble metallic nanoparticles (APMNs) can be utilized to span an array of applications such as biosensing, bioimaging, diagnostics and therapeutics. Although great advancement has been made to prepare well-defined APMNs through versatile surfactant-assisted colloidal methodologies, biomedical applications necessitate tedious and rigorous purification processes for the complete removal of toxic surfactants. To address this ubiquitous challenge, biomimetic and bioinspired green synthesis have been extensively explored to fabricate APMNs under mild and ambient conditions.

In this dissertation, we aim to develop generic bioenabled synthetic strategies towards APMNs, particularly, Au nanostars and Au/Ag nanoprisms. Herein, protein mediated shape-selective synthesis of APMNs were presented, in which consensus sequence tetratricopetide repeat (CTPR) proteins and biological Good's buffers were employed as nanocrystal growth modifiers and mild reducing agents, respectively. The dramatic implications of repeat proteins on the morphological and optical properties of the Au NPs were explicitly discussed. The other objective of this dissertation is to elucidate the molecular interactions between inorganic species and biopolymers to further unravel the underlying growth mechanism during the course of

APMNs evolution. By incorporation of seeded growth and biomimetic synthesis, Ag/Au nanotriangles (Au NTs) with tunable edge length were synthesized in the presence of the designed CTPR protein, halide anions ($Br^-$) and CTPR-stabilized Ag seeds. The well-defined morphologies, tailored plasmonic absorbance from visible-light to the near infrared (NIR) region, colloidal stability and biocompatibility are attributed to the synergistic action of each components in the synthetic system. Last but not the least, we have demonstrated the resulting NPs exhibit remarkable colloidal stability, mitigated cytotoxicity and surface enhanced Raman spectroscopy (SERS) performance, making them good candidates for biosensing and photothermal therapy. This work might shed light on the roles biomolecules play in green synthesis of APMNs, along with rationalizing the design of biomimetic systems to bridge the gap between the bioenabled technique and traditional colloidal synthesis.

# Acknowledgements

First and foremost, I would like to express my sincere gratitude and acknowledgement to my advisor, Prof. Tijana Z. Grove. Through her enthusiasm, wisdom and openness to science, I have learned how to become a competent scientist. More important, I have gained the confidence to handle scientific projects independently under her mentorship. She does not only play the role of research advisor but act as a venerable mentor of life who has encouraged me to overcome difficulties and taught me to become a responsible person.

I am cordially thankful to my committee members, Prof. John R. Morris, Prof. Alan R. Esker, Prof. Robert B. Moore and Prof. Guoliang Liu for sharing insightful views and making inspirational advice on my research projects during all the milestone exams. Their passion for science and teaching, brilliant ideas of research and scrupulous attitude always prompt me to delve into the fundamental solutions to any scientific problem.

My sincerest thanks also go to my bright and talented colleagues in the Grove Lab. I want to thank Nathan Carter for his continuous support and exchanging of brilliant opinions throughout the past five years. I am also grateful for Anna Mercedes-Camacho's tutoring and guidance during my first year in the lab. I am really delightful to collaborate with Kristina Roth and Rachael Parker who demonstrate a strong work ethic that is so vital for accomplishing research goals. Christina Kim, Jennifer McCord and Yunhua Li, it has been a great pleasure to work with you and I sincerely wish you all the best moving forward. I would like to give my special thanks to all my friends at the Department of Chemistry of Virginia Tech, who made my graduate life at VT a joyful journey.

I also would like to acknowledge the NCFL staff, particularly, Dr. Chris Winkler for his assistance on the sample preparation and data interpretation. It is also a great privilege to work

with experienced scientist such as Weinan Leng, who has imparted the knowledge and skills pertinent to SERS.

Finally, I would like to extend my deepest gratitude to my parents, Shenghuai Geng and Ping Luo, and my wife Wei Wang for their continuous encouragement and support. I am dedicating this work to my beloved son Lucas Geng. I wish for him to grow up and be a great scientist in the future.

# Table of Contents

# List of Figures

**Chapter 1**

**Chapter 2**

# List of Schemes

# List of Tables

**Chapter 8**

# List of Abbreviations

| | |
|---|---|
| 4-MBA: | 4-mercaptobenzoic acid |
| AFM: | atomic force microscopy |
| APMNs: | anisotropic plasmonic noble metallic nanoparticles |
| AR: | aspect ratio |
| BSA: | bovine serum albumin |
| CD: | circular dichroism |
| CTAB: | cetyltrimethylammonium bromide |
| CTPR: | consensus sequence tetratricopeptide repeat protein |
| DDA: | discrete dipole approximation |
| DLS: | dynamic light scattering |
| EDS: | energy-dispersive X-ray spectroscopy |
| EELS: | electron energy-loss spectroscopy |
| EF: | enhancement factor of SERS |
| FBS: | fetal bovine serum |
| FCC(fcc): | face centered cubic |
| FESEM: | field emission scanning electron microscopy |
| FFT: | fast Fourier transform |
| FTO: | fluorine-doped tin oxide |
| FWHM: | full width at the half maximum |
| HEPES: | 4-(2-hydroxyethyl)-1-piperazineethanesulfonic acid |
| HRTEM: | high resolution transmission electron microscopy |
| HSQC: | heteronuclear single quantum coherence ($^{1}H$-$^{15}N$ 2D NMR) |
| LSPR: | localized surface plasmon resonance |
| MDS: | molecular dynamic simulation |
| MOPS: | 3-(N-morpholino)propanesulfonic acid |
| NIR: | near infrared |

NMR: nuclear magnetic resonance

NP: nanoparticle

NPL: nanoplate

NR: nanorod

NSP: nanosphere

NST: nanostar

PBS: phosphate-buffered saline

PSSS: sodium polystyrene sulfonate

PVP: polyvinylpyrrolidone

ROS: reactive oxygen species

SAED: selected area electron diffraction

SEM: scanning electron microscopy

SERS: surface enhanced Raman scattering

SLigS: sodium lignosulfonate

SWV: square-wave voltammetry

TEM: transmission electron microscopy

UPD: underpotential deposition

UV: ultraviolet

# Chapter 1. Introduction

## 1.1 Overview

Anisotropic plasmonic noble metallic nanoparticles (APMNs) have received enormous attention due to their distinct geometric features and fascinating physicochemical properties. Owing in large part to their tailored localized surface plasmon resonance (LSPR) and the intensive electromagnetic field at the sharp corners and edges, APMNs are exceptionally well suited for biomedical applications such as biosensing, bioimaging, diagnostics and therapeutics. To date, a rich variety of surfactant-assisted colloidal routes have been developed to prepare well-defined APMNs. Given that biomedical applications necessitate tedious and rigorous purification processes for the complete removal of toxic surfactants, extensive research has been conducted on the green synthesis of APMNs. In this dissertation, we aim to develop generic bioenabled synthetic methodologies towards APMNs, particularly, nanostars and nanoprisms. The other objective is to elucidate the molecular interactions between inorganic species and biopolymers to further unravel the underlying growth mechanism during the course of APMNs evolution. Last but not the least, we have demonstrated the resulting NPs exhibit remarkable colloidal stability, mitigated cytotoxicity and enhanced SERS performance, making them promising materials for biosensing and photothermal therapy.

Recent advances in the synthesis and the variety of applications of APMNs are briefly reviewed in the first chapter, focusing on the bioenabled colloidal synthesis of two dimensional (2D) nanoplates. In Chapter 2, a two-step approach is presented for the preparation of gold nanostars (Au NSTs), in which Good's buffer plays the dual roles of a mild reducing agent and a shape directing agent. In Chapter 3, we explicitly discuss the implications of repeat proteins on the morphology and plasmon absorbance of the Au NPs synthesized through a protein-mediated

procedure. It is followed by the meticulous investigation on the molecular interactions between protein and Au ions/Au NPs in Chapter 4. This research provided a foundation for the successful incorporation of seed-mediated synthetic strategies into biomimetic approaches, by which well-defined triangular Ag/Au nanoprisms are produced in high yield. The details about the synthetic protocols along with the growth mechanism of Ag and Au nanoprisms are presented in Chapter 5 - Chapter 7. In Chapter 8, additional biopolymer, lignin derivatives, were found to facilitate the formation of Ag nanoprisms through either seeded growth or $H_2O_2$ induced one pot synthesis indicating that a broad spectrum of sustainable biomaterials can be employed for governing the shape-controlled synthesis of APMNs. This work aims to lay the groundwork in better understanding the roles biomolecules play in green synthesis, along with demonstrating the need for rational design of biomimetic systems to bridge the gap between the bioenabled technique and traditional colloidal synthesis.

## 1.2 Plasmonic nanoparticles

Colloidal noble metallic nanoparticle (NP) solutions, particularly gold (Au) and silver (Ag), have been found to display spectacular colors, dating back to the Roman times.[1] The underlying mechanism of this intensive light absorbance remains elusive until the dawn of the 20th century. Mie and Gan provided seminal work to quantitatively describe the size and shape-dependent localized surface plasmon resonance (LSPR) and predict the optical properties for noble metal NPs.[1] When a beam of light impinges on a NP surface, the conduction electrons are excited which induces a collective oscillatory motion, resulting in an intense LSPR absorbance as well as the amplified localized electromagnetic filed (***Figure 1.1A***).[2] Indeed, SPR also takes place on the bulk metal and metal thin film. The LSPR bands of metallic NPs are narrow, well-defined and remarkably sensitive to the local dielectric environment, which holds great promises

for their use in molecular sensing, bioimaging and therapeutic applications.[3,4] Additionally, the coupling of electromagnetic fields between adjacent NPs brings about the further amplification of the spectroscopic signals allowing for the implementation of plasmon-enhanced spectroscopic tools and other advanced optoelectronic devices.[5-7]

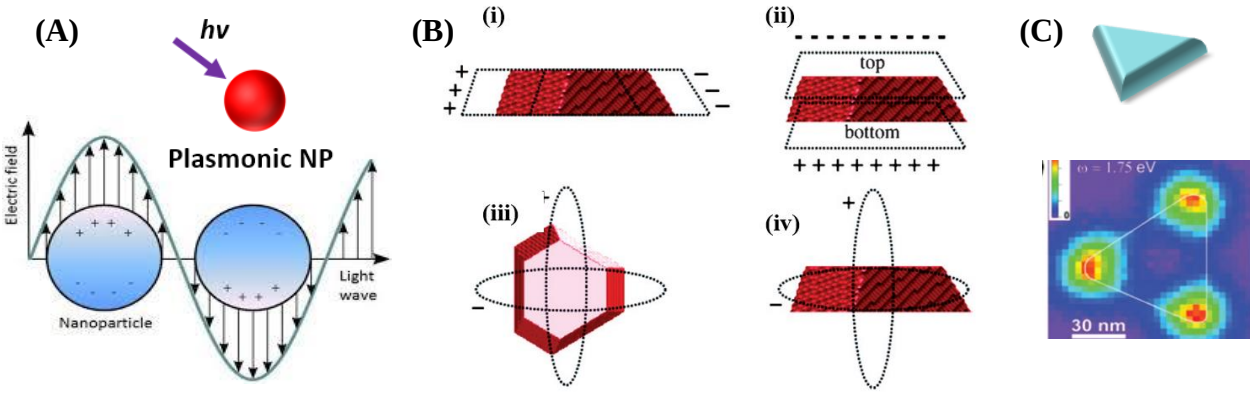


**Figure 1.1** Schematic representation of the LSPR involved in metallic (A) nanospheres (NSPs)[13] (Reprinted with permission from ref13, copyright (2014) Multidisciplinary Digital Publishing Institute) (B) the dipolar in-plane and out-of-plane modes of nanoprisms are represented in (i) and (ii), respectively. The corresponding in-plane and out-of-plane quadrupolar modes are represented in (iii) and (iv), respectively.[8] (Reprinted with permission from ref8, Copyright [2008] the Royal Society of Chemistry) (C) EELS mapping of Ag nanoprisms.[12] (Reprinted with permission from ref 12, Copyright [2007] Nature Publishing Group)

Generally, the LSPR of NPs is determined by their composition, geometric features, and their ensemble assembly patterns.[8,9] For instance, the representative LSPR band of spherical or quasi-globular Au and Ag NPs typically absorbs at 520 and 400 nm, respectively, which undergoes a slight red shift as the size increases. In sharp contrast, the LSPR band of anisotropic plasmonic noble metallic nanoparticles (APMNs) is more sensitive to the variation of shapes, and can be readily tailored from ultraviolet (UV) to near infrared (NIR) regions.[2,8] Despite the fact that other metals including Cu, Pt, Pd, Al also possess LSPR bands, they have attracted less attention owing to the relatively low intensity absorbance in the UV region. Theoretical approaches like discrete dipole approximation (DDA) simulation can serve as a powerful tool to predict the plasmonic behavior of the noble metallic NPs. For instance both DDA simulations

and UV-Vis spectral investigations have unambiguously confirmed the dual LSPR modes corresponding to a dipole and a quadrupole (***Figure 1.1B***),[10,11] while the electron energy-loss spectroscopy (EELS) mapping identified the plasmonic hot spots at the sharp tips of the nanoprisms (***Figure 1.1C***).[12]

## 1.3 General properties and applications of anisotropic plasmonic noble metallic nanoparticles (APMNs)

### 1.3.1 Geometric features and crystal structures

Anisotropy at the nanoscale results in the unprecedented physical and chemical properties of NPs. Over the past two decades, NPs with a wide array of shapes have been fabricated including polyhedral, one dimensional nanowires,[14,15] nanorods (NRs),[16] 2D nanoplates (also termed as nanodisks and nanoprisms),[10,17] 3D branched NPs,[18-20] and a diverse set of high-index concave and convex polyhedral nanocrystals.[21,22]

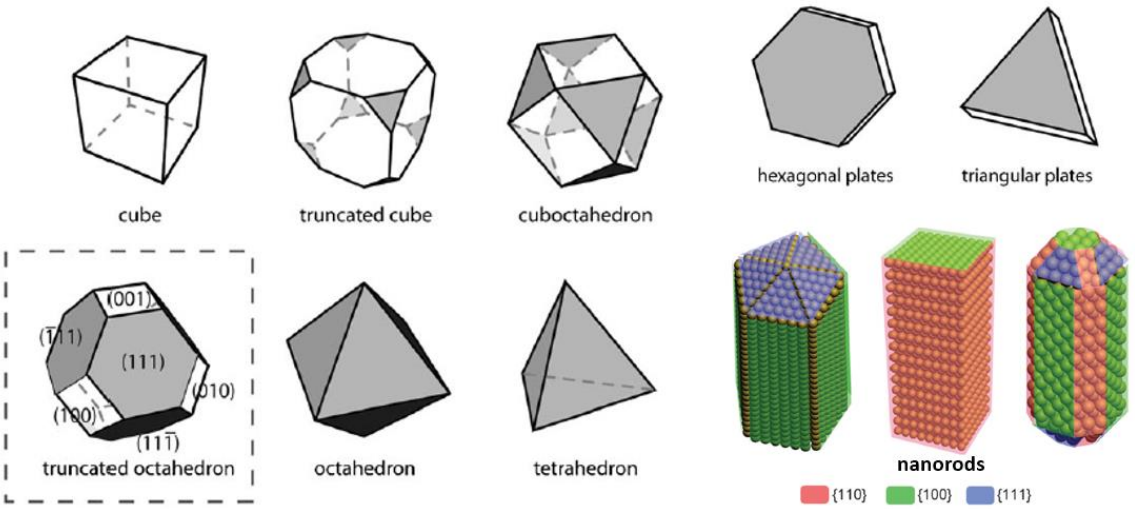


**Figure 1.2** Schematic representation of the single-crystalline polyhedrons (nanocube, truncated nanocubes, octahedron, truncated octahedron, tetrahedron), hexagonal and triangular nanoplates, [24] and nanorods with different ends (five-fold twinned, rectangular and octagonal cross-section).[25] (Reprinted with permission from ref 24, Copyright [2008] Wiley and from ref 25, Copyright [2011] the Royal Society of Chemistry)

The shape of APMNs are primarily determined by two structural factors, including crystallinity and surface facets. In terms of crystallinity, Ag and Au NPs typically exist in the form of face centered cubic (fcc) single-crystalline or polycrystalline structures. Aside from that, planar-twinned (possessing one or more parallel twin defects), penta-twinned (possessing five twins radiating from a center), multiply twinned (possessing 20 intersecting twin planes) and stacking faults are conventionally found for fcc Ag and Au NPs due to the low energy barrier.[23]

The facets stand for the exposed surface of polyhedral nanocrystals, consisting of a specific ordered arrangement of atoms. By convention, facets can be represented by a set of index, called Miller indices (h, l, k). For instance, single crystalline polyhedrons, 1D nanorods and 2D nanoplates are, respectively, enclosed by a set of facets as shown in the ***Figure 1.2***.

### 1.3.2 Catalytic performance

Large surface area and abundant surface defects (edges, corners, steps, kinks) result in the superior catalytic performance of APMNs as compared with their isotropic counterparts. The catalytic activity and selectivity is largely dependent upon the size, shape and surface facets of APMNs. For example, shape-dependent electrocatalytic behavior has been uncovered through cyclic voltammetry and chronoamperometry studies.[26] Ag nanoprisms rich in hcp lamellar defects outperformed Ag nanospheres and Ag nanocubes toward hydrazine and formaldehyde oxidation and hydrogen peroxide reduction.[26] By and large, APMNs with high-index facets, particularly concave and convex polyhedrons, showcase remarkably high catalytic activity[22] but suffer the major drawback of the structural instability originated from their high surface energy.[24]

### 1.3.3 Tunable spectral properties

One striking advantage of APMNs is that the in-plane dipole LSPR can be regulated by their aspect ratio. For instance, the LSPR of Ag nanoprisms could be conveniently tuned to span

a broad spectral range, from visible to the NIR region, through the variation of the quantities of Ag seeds used during the growth step (***Figure 1.3A-B***).[27] An linear relationship has also been identified between $\lambda_{max}$ and the aspect ratio, expressed by the empirical equation (1),

$$\lambda_{max} = 33.8\left[\frac{L}{T}\right] + 418.8 \quad (1)$$

where L and T refers to edge length and thickness, respectively. For the gold nanorods (NRs), the aspect ratio could be adjusted by the size of the seeds as well as the concentration of Ag ions additives (***Figure 1.3C***).[28,29] Regardless of the shape of the NPs, the larger aspect ratio produces a longer $\lambda_{max}$. The generic trend also holds for the branched gold nanostars (NSTs), the $\lambda_{max}$ of which is primarily determined by the length of the tips.[20]

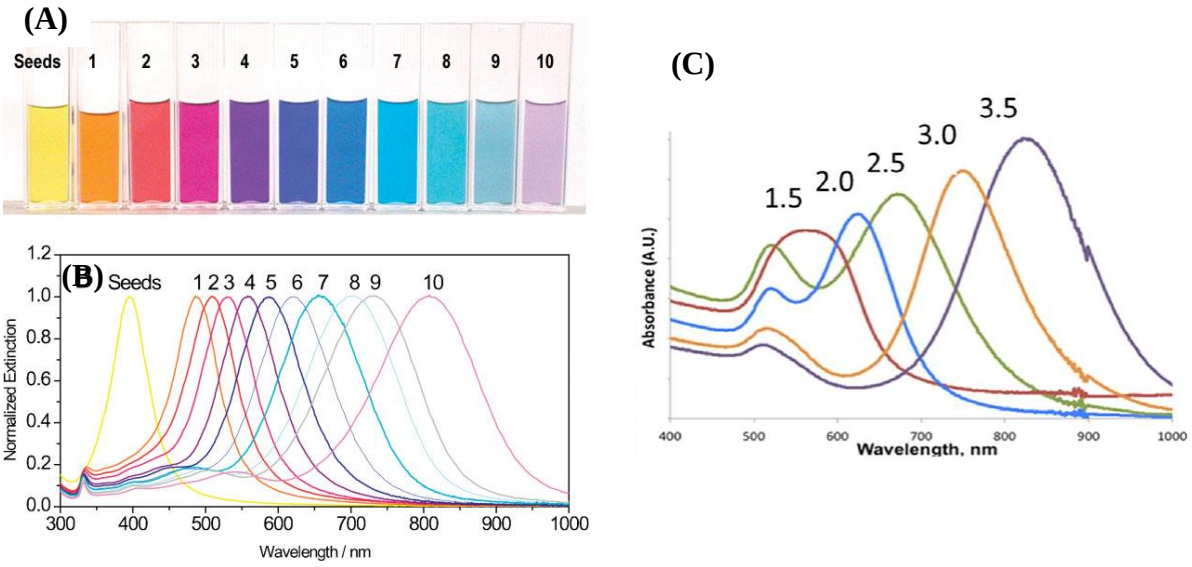


**Figure 1.3** (A) Photograph of a series of Ag nanoprisms colloidal solutions illustrating range of colors obtained. (B) Normalized UV-Vis spectra of a series of as-prepared samples obtained using different volumes of seed solution.[27] (Reprinted with permission from ref 27, Copyright [2008] Wiley) (C) UV−vis−NIR extinction spectra of Au NRs with aspect ratio (AR) of 1.5−3.5, AR are indicated above the absorbance spectrum of each sample.[29] (Reprinted with permission from ref29, Copyright [2013] American Chemical Society)

### 1.3.4 Plasmonic sensing

Owing to the high extinction coefficient in the visible-light region, functionalized APMNs have been widely used as colorimetric sensors. Their LSPR bands undergo dramatic variation in response to the environmental change.[30-33] The design principle can be illustrated by the following example.[30] Au NRs capped with MC-LR antibody could conjugate with their analogues anchored by MC-LR-OVA antigen either in a side-by-side or an end-to-end fashion (***Figure 1.4A***). Once the MC-LR toxin is added, the ordered self-assembly of Au NRs is disrupted due to the competitive interaction between the toxin and MC-LR-OVA antigen. The net effect can be envisioned as the shortening of a supramolecular assembled Au nanowire. The dramatic intensity and wavelength changes caused by the decrease in the aspect ratio (***Figure 1.4A***) can be used as a plasmonic probe to identify the MC-LR concentration and the detection limit was estimated to be 0.3 ng·ml$^{-1}$ and 0.06 ng·ml$^{-1}$, respectively (***Figure 1.4B***).

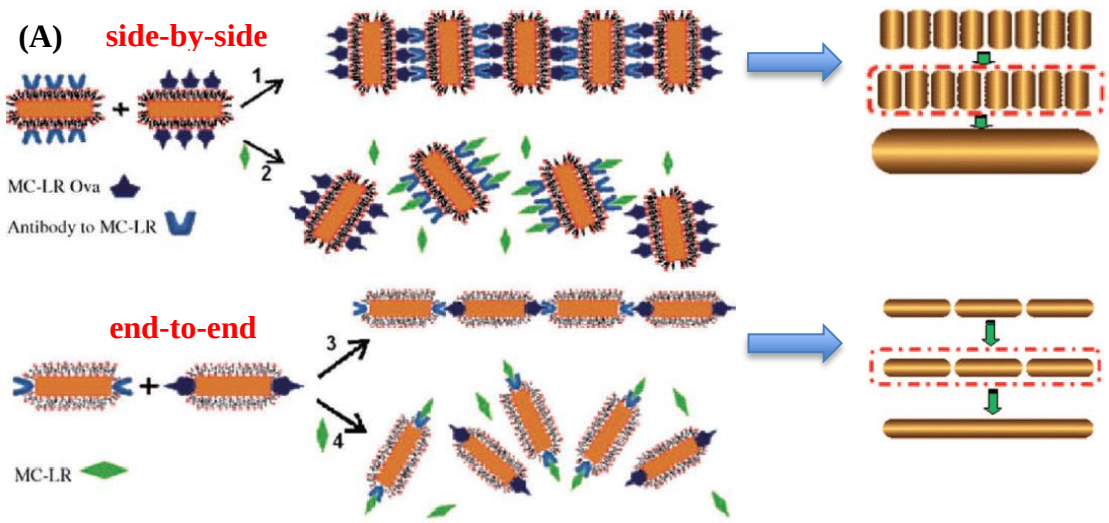


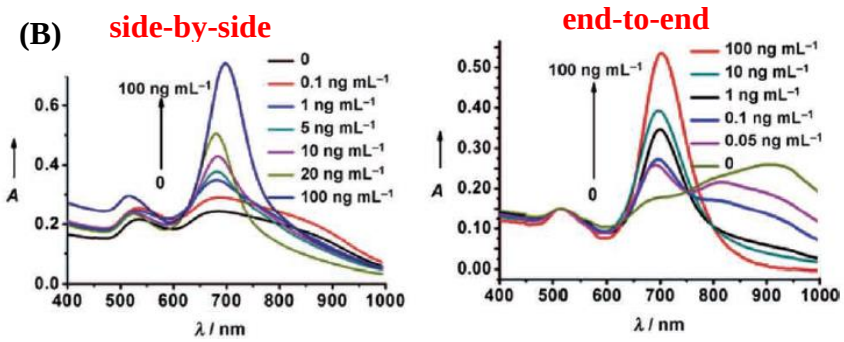

**Figure 1.4** (A) schematic illustration of toxin detection method with side-by-side and end-to-end Au NR assemblies (B) Evolution of LSPR of the Au NRs upon increasing concentrations of microcystin-LR (MC-LR).[30](Reprinted with permission from ref30, Copyright [2010] Wiley)

Triangular Ag nanoprisms (or nanotriangles, NTs) are featured by their sharp vertices and intense NIR absorbance located at approximately 800 nm. The dipole LSPR of Ag NTs is subject to a noticeable blue shift as the corner tips are rounded in the presence of strong oxidant.[32] This sharp plasmonic response confers the ultra-high chemical sensitivity upon Ag nanoprisms towards chemical and biological sensing of glucose, $Hg^{+}$, and DNA.[31-33]

### 1.3.5 Surface enhanced Raman scattering (SERS)

SERS has been demonstrated as a powerful spectroscopic technique for the detection of trace amount of biomolecules and hazardous substance.[34] APMNs, especially Ag and Au-based NSTs and nanoprisms exhibit remarkable SERS activities, which is mainly attributed to the sharp tips, corners and edges.[20,35] In a recent study by Qin et al., Ag nanoplates with either straight or wavy edges were prepared through a PVP mediated hydrothermal method followed by the solvothermal treatment in ethanol.[36] At the fixed concentration of Ag nanoplates, the SERS enhancement factors were found in the following order: wavy edge > straight edge > curvy edge. On the basis of massive field enhancement (e.g. plasmonic hot spots) originated from the plasmonic coupling of neighboring APMNs, bow-tie Ag NTs pairs and Au NSTs heterodimers have been fabricated as highly active SERS substrate and SERS probe.[5 37]

### 1.3.6 Other biomedical applications

Due to the long circulation time, enhanced permeability and retention (EPR) effect and strong LSPR absorbance in the NIR region, APMNs have also been applied in the development of targeted drug-delivery systems for controlled cargo release and photothermal therapy.[38-40] By covalent immobilization of Cys-Leu-Pro-Phe-Phe-Asp (CLPFFD) peptide onto the Au NRs,

improved cell viability and specific biorecognition capabilities toward β-amyloid are imparted to the Au NRs-peptide conjugates, which have great potential in therapeutics for Alzheimer's disease.[38] Additionally, a diverse set of APMNs such as Au NRs, nanoshells and branched nanohexapods have been demonstrated as high-performance photothermal transducers for the ablation of breast cancer tumors.[40]

## 1.4 Colloidal synthesis of APMNs

It is well known that well-defined nanostructures can be fabricated through top-down and bottom-up method. For noble-metal systems, bottom up techniques, especially colloidal synthesis is advantageous due to the following reasons: (i) cost-efficient: no specialized and extravagant instruments are necessary (ii) high throughput: solution-based processing can be readily implemented for scale up synthesis (iii) versatile: diverse shaped nanostructures can be realized through the rational design of synthetic procedures. In a general sense, solution-phase synthesis of colloidal nanocrystals with a specific shape is carried out by reducing metal precursors in the presence of stabilizers and shape-directing agents. The key to the exquisite size and shape control lies in the precise tuning of nucleation and the subsequent growth step aiming for the specific crystallographic structure.

Owing to the enormous efforts and pioneering work done by numerous scientists all over the world, shape-controlled synthesis of APMNs is no longer regarded as a fortuitous discovery. Instead, a set of guidelines have been developed in this respect, which can be briefly summarized as below:

(i) Appropriate thermodynamic and kinetic control over the nucleation and growth

(ii) Seed-mediated growth as a versatile toolbox

(iii) Seeds with desirable crystal structure

(iv) Diverse ligands as facet-selective adsorbate

(v) Self-assembled scaffolds as potent templates

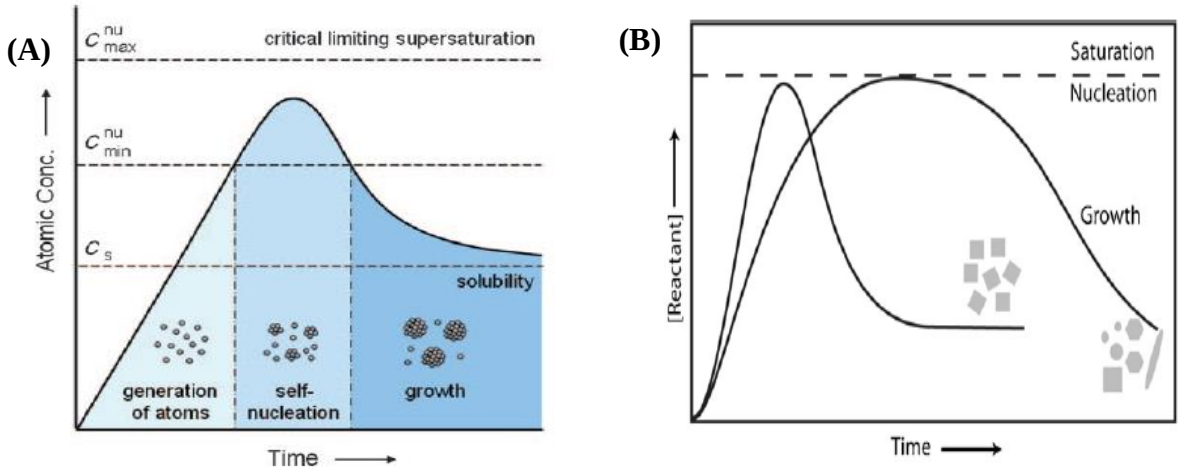


**Figure 1.5** (A) Plot of atomic concentration against time, illustrating the generation of atoms, nucleation, and subsequent growth.[41] (Reprinted with permission from ref41, Copyright [2015] American Chemical Society) (B) LaMer model of rapid nucleation vs slow nucleation.[24] (Reprinted with permission from ref24, Copyright [2008] Wiley)

The synthesis reactions are essentially governed by the combination of multiple thermodynamic (e.g. reduction potential, interfacial energy) and kinetic (e.g. concentration of reactants, diffusion rate, temperature, pH) factors. The total Gibbs free energy can be described in the following equation:

$$dG_{total} = dG_{bulk} + \gamma dA \quad (1)$$

where $G_{bulk}$ is the bulk Gibbs free energy, γ is the specific surface energy and A is the surface area. Nanocrystal take equilibrium shape under the condition that the total surface energy is minimized. Due to the intrinsic anisotropic atomic arrangement on the different crystallographic planes, the equilibrium shape of nanocrystal is typically polyhedron that can be predicted using Wulff Construction. For fcc metal, the order of surface energy for different faces is as follows: γ (111) < γ(100) < γ(110). Additionally, the surface energy can be finely tailored with the aid of capping agent so that a wide diversity of shapes deviated from the Wullf thereom can be

synthesized. As for kinetics control, the most efficient tools include the variation of concentrations, adjustment of temperature and addition of ligands. Note that in many cases, these thermodynamic and kinetic influential parameters are intertwined which make the situation even complicated. Controversial conclusions are often made by different research groups using similar synthetic protocols, even with consistent experimental observations.[9] Hence a profound understanding and application of these principles is so vital for the rational design and development of APMNs with controlled morphologies.

Since the crystal's free Gibbs energy is negative whereas the surface energy is positive, there is a critical size when $d\Delta G_{total}/dr=0$ (r = radius of size of nucleus). The critical size r corresponds to the minimum size at which the particle can survive without being redissolved into the solution. The LaMer model is conventionally adopted to describe the homogenous nucleation of seed as well as the growth of nanocrystals. At the initial stage, a rapid increases in the concentration of M(0) (M stands for metal) happens and reaches the critical value. Then burst-nucleation process will consume a large quantity of M(0) so that new nuclei can hardly be formed beyond this point. The follow-up growth step is generally described by the slow deposition of monomers(metal atoms) onto the pre-existing nuclei (***Figure 1.5A***).[41] As shown in the ***Figure 1.5B***, if there are abundant free M(0) atoms that are not depleted rapidly, a mixture of varied-shaped NPs with broad size distribution are formed due to the concurrent homogenous nucleation and growth.[24]

Seed-mediated growth, proposed by Murphy et al. in their pioneering work on the gold nanorods and nanospheres with tunable size,[16,42] has been successfully extended to prepare a rich variety of different shaped APMNs with low shape and size polydispersity. [17,27,43-46] Although multi-step protocols sacrifice the convenience of the traditional one-pot synthesis, the exquisite

control over the growth kinetics, and thus shape and size, is achieved by isolating the growth step from the initial nucleation of seeds. [41,47] The underlying reasons for the growth to proceed along one favourable orientation over another have not been indisputably addressed. Seeded growth is believed to boost the symmetry breaking event during the course of the shape evolution.[47]

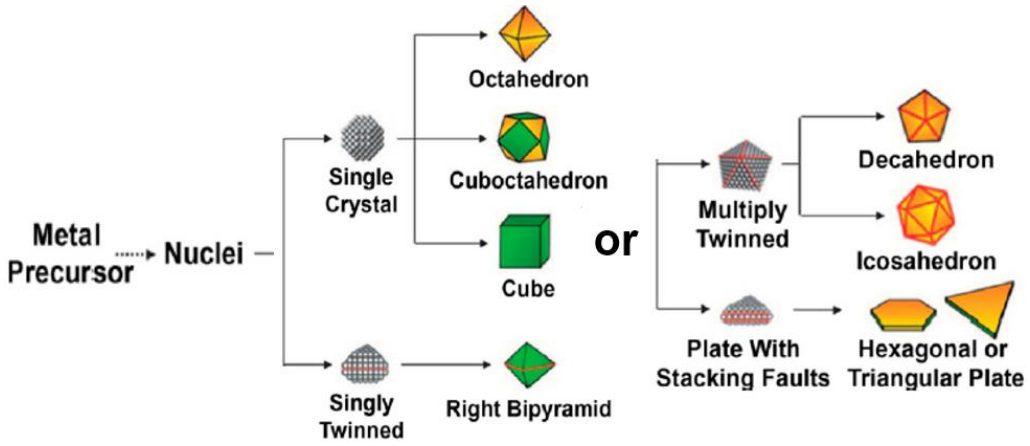


**Figure 1.6** Growth of APMNs using seeds with varied crystal structure. Yellow indicates (111) facets and green represents (100) facets. [48,49] (Reprinted with permission from ref48, ref49, Copyright [2013] American Chemical Society)

In the presence of seed nanocrystals, the deposition of metal atoms onto the pre-existing seeds is more favorable than homogenous nucleation due to the lower activation energy.[24] More important, the crystal structure including its twining defects plays a leading role in determining the shape evolution during the growth stage. For instance, single crystalline seed is the prerequisite for the synthesis of platonic NPs, such as octahedrons and cubes. Decahedrons and icosahedrons are favorable products when multiply twinned seeds are utilized (***Figure 1.6***). As for the 2D hexagonal nanoplates and nanoprisms, planar twining and inherent stacking faults are considered as one of the key driving forces.[49] Note that the crystallinity of seeds is significantly affected by the choice of surfactant or stabilizer. Multiply twinned and planar-twinned seeds are typically produced in the presence of citrate whereas single-crystalline seeds are generated by

using cetyltrimethylammonium bromide (CTAB), which is attributed to oxidative etching of less stable twin defects.[48,49]

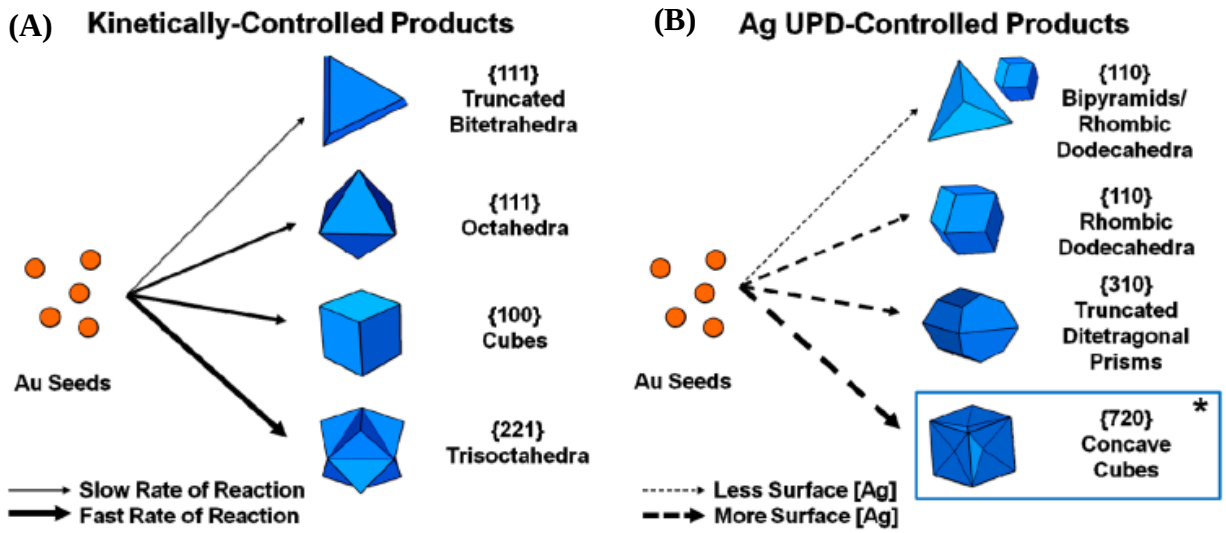


**Figure 1.7** Schematic representation of the two primary growth pathways of Au NPs: (A) kinetic control and (B) selective surface passivation (in this case, by Ag(0)).[50] (Reprinted with permission from ref50, Copyright [2012] American Chemical Society)

A high degree of shape control and tailorability is realized through a kinetic control and selective surface passivation during the growth stage. As shown in the ***Figure 1.7A***, more thermodynamically favored octahedrons bounded with (111) facets are produced at slower reduction rate, whereas fast reduction rates are in favor of high-index trisooctahedra with (221) facets. Additionally, a rich variety of adsorbates including the atomic adsorbate, Ag(0), small-molecule surfactant, CTAB, and polymeric stabilizer, PVP, can be used for the selective suppression of specific facet on the nanocrystal to maneuver the overgrowth process.[24] Taking into account the Ag underpotential deposition (UPD), the higher density of Ag deposition on Au NPs results in the formation of high-index products with more open facets, as shown in the ***Figure 1.7B***.[50]

Other thermodynamic driven processes, particularly, Ostwald ripening also get involved during the course of the nanocrystal formation. Ostwald ripening is a spontaneous

thermaldynamically-driven phenomenon which can be attributed to the reason that large particles are energetically favorable than the smaller counterparts. As demonstrated in the Chapter 6, both small nanoclusters and anisotropic nanoplates are generated at the initial seeded-growth stage. In order to minimize the total energy of the system, the small nanoclusters with high surface energy are dissolved and condensed onto the large Ag nanoplates over time.

## 1.5 Bioenabled synthesis of APMNs

Despite high-precision control over the morphology of NPs, harsh experimental conditions and energy-consuming processes, including the elevated temperatures and hazardous chemicals, are often involved. Furthermore, biomedical applications require tedious and stringent purification processes for the complete removal of toxic cationic surfactants.[51,52] An area of growing interest is the harnessing of biomolecules for the synthesis and assembly of NPs under mild ambient conditions for biosensing and catalysis (***Figure 1.8***).[53,54] Bioenabled strategies draw inspiration from nature where materials with unique structures, compositions, and functions are achieved through the process of biomineralization, where bio-scaffolds such as peptides, [55-61] proteins[62-68] and nucleic acids[69-75] interact strongly with inorganic materials. In particular, extensive research has focused on the biomimetic synthesis of Au/Ag NPs as the fundamental building blocks for the construction of catalytic, optoelectronic and biosensing devices.[63,76,77] In the following section, the state of the art in bioenabled synthesis of APMNs, especially Ag and Au nanoprisms, will be briefly reviewed.

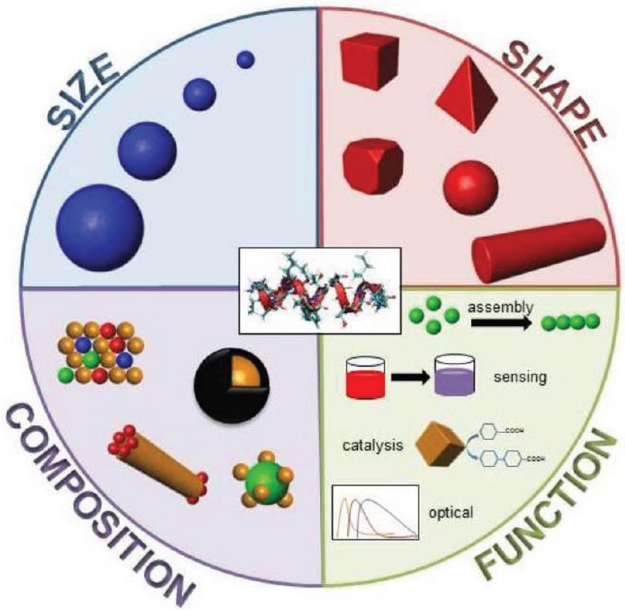


**Figure 1.8** Potential capabilities of proteins and peptides to control different characteristics of inorganic nanomaterials, including the size, shape, composition, and function.[78] (Reprinted with permission from ref78, Copyright [2012] American Chemical Society)

### 1.5.1 Bio-mediated in-situ synthesis

Bio-assisted approaches have recently opened up the potential of the green-synthesis of APMNs at ambient conditions. [55,79,80] For instance, biological Good's buffers have been reported to generate branched gold nanocrystals at room temperature and neutral pH.[18,20] The tip length along with the LSPR band of the Au NSTs could be readily tailored by adding varied amount of halide ions and repeat proteins.[20,81] In previous studies, plant extracts,[82,83] amino acids,[84] bovine serum albumin (BSA)[85,86] amyloid fibril[87] and other shape directing proteins[80] have demonstrated dual functions as stabilizers and reducing agents to produce anisotropic Au nanoplates with distinctive triangular or hexagonal shapes.

Since one-pot biomimetic strategies typically generate APMNs with broad morphological distribution. Bio-assisted seeded-growth along with the addition of halides has been invoked as the potent tools for the production of the Au and Ag nanoplates with improved morphological yield.[35,88-90] Aside from serving as efficient stabilizer, the presence of sustainable biopolymers

such as repeat protein and cellulose derivatives facilitate the formation of planar-twinned Ag seeds at the initial stage and control the growth kinetics of Ag/Au nanoprisms during the subsequent process. As demonstrated in our recent work, the incorporation of seed-mediated techniques into conventional biomineralizaton has the potential to provide unprecedented control over NP size and shape while maintaining biocompatibility requirements.[90]

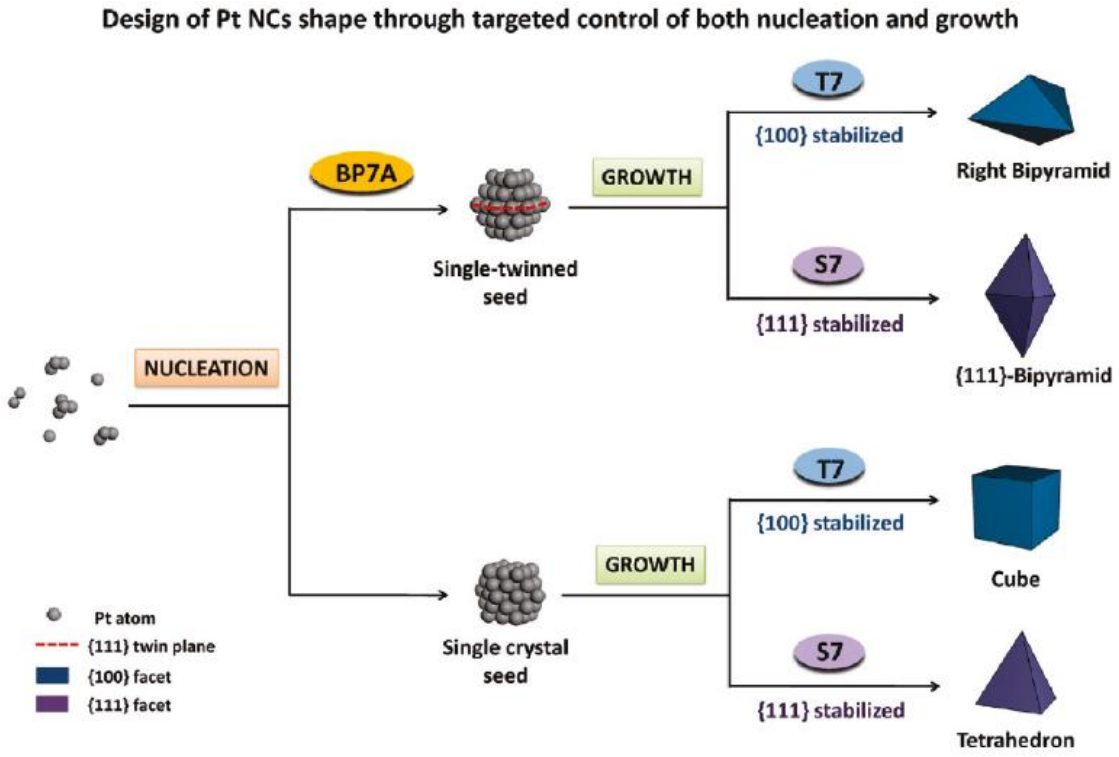


**Figure 1.9** Schematic Illustration on the rational design of Pt nanocrystals shapes through targeted control over both nucleation and growth using specific peptides.[91,92] (Reprinted with permission from ref91, Copyright [2011] American Chemical Society and from Ref 92, Copyright [2014] American Chemical Society)

Bioenabled approaches are not restricted to the 2D and branched morphologies. Recently APMNs with intriguing shapes, such as platonic cubes, tetrahedrons and bipyramids, have also been reported. Bio-combinatorial techniques such as phage display have been extensively employed for the screening and identification of a myriad of peptide sequences with specific binding affinity onto surface of inorganic materials.[78] In the innovative synthesis presented by

Huang's group,[91,92] a specific Pt-binding peptide BP7A was selected to stabilize and mediate the synthesis of single-twinned seeds, which was shaped into the right bipyramid and (111) bipyramid, respectively with the aid of T7 and S7 peptides(***Figure 1.9***). In sharp contrast, single crystalline seeds are produced in the absence of BP7A, which will evolve into tetrahedrons and nanocubes under the identical growth condition. Taken together, the rational design of biomimetic approach towards APMNs takes full advantage of the biopolymers' binding motifs to regulate the crystal structure of seed as well as the subsequent facet growth through selective surface passivation.

**1.5.2 Bio-templated ex-situ synthesis**

A rich variety of natural and recombinant proteins have so far been explored as biotemplates for the synthesis of Au NPs with highly ordered structures.[62-65,67] In a representative example, anisotropic Au NPs arrays have been integrated on the self-assembled protein clathrin Hub-His6 through a two-step, seed-mediated growth process.[64] In another study, a tetrapod shaped Au-protein supramolecular nanostructure is achieved through the coordination of as-prepared Au nanoclusters with the trimeric gp5-His6 protein.[62] Notably, rationally designed complex plasmonic nanostructures with well-defined shapes including polyhedral and extended 1D, 2D and 3D ordered arrays have been constructed with the aid of DNA origami.[72] During the synthesis, a precise number of NPs are patterned regularly on the specific sites of the sophisticated DNA motifs, the shape and size of which can be finely tuned using programmable molecular linkers and spacers. Similarly, Rosi and colleagues have developed a new paradigm for the construction of helical Au NPs chains and hollow Au globular superstructures using self-assembled peptide building blocks (***Figure 1.10***).[58,59,78,93,94]

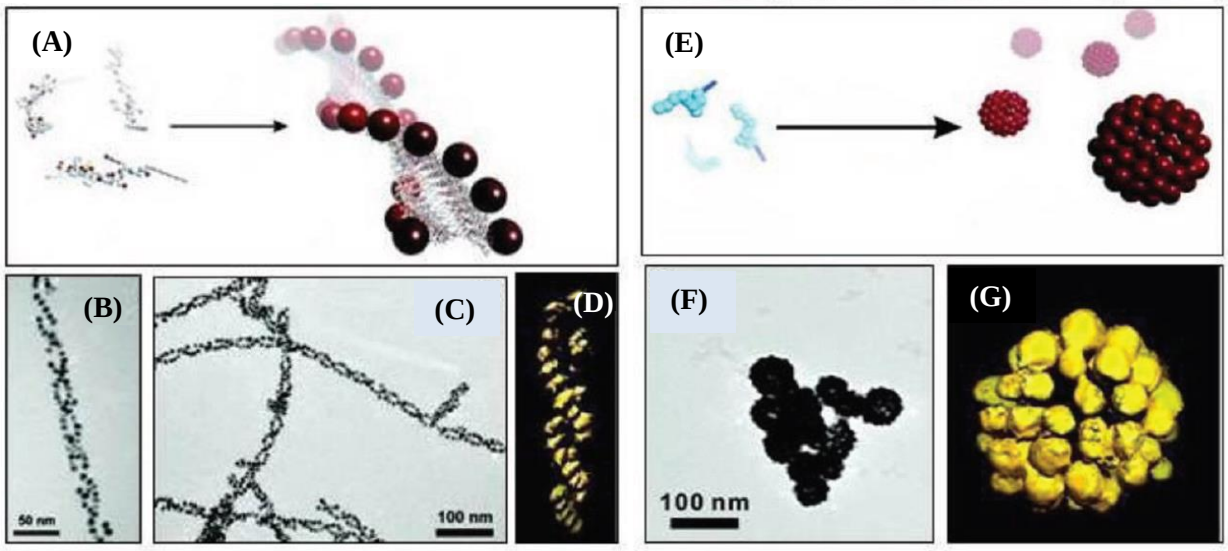


**Figure 1.10** Peptide-based formation of nanoparticle superstructures. (A) Formation scheme of a peptide double helix using the $C_{12}$-$PEP_{Au}$ sequence (B, C) TEM images of Au nanoparticle double helices using the peptide (D) Representative 3D image of the assembled structure achieved via tomography[93] (Reprinted with permission from ref29, Copyright [2010] Wiley) (E) Peptide-based assembly of Au nanoparticles to form hollow spherical superstructures using the C6-AA-PEPAu peptide (F) TEM analysis of the hollow nanospheres (G) 3D surface rendering of the tomographic volume.[58] (Reprinted with permission from ref58, Copyright [2010] American Chemical Society)

### 1.5.3 Biopolymer mediated overgrowth

It is well established that intricate hierarchical structures and bimetallic core-shell hetero-structures can be achieved by drawing on the seeded overgrowth method. Simply put, the crystallographic orientation of the well-facet seeds governs the post-deposition of either identical or secondary metal elements.[24] By harnessing different shaped seeds and fine-tuning of the experimental conditions, dumbbell shaped nanorods,[95] polyhedral Au@PdPt[96] and dendritic Pt NPs on Au NTs[97] have been previously synthesized.

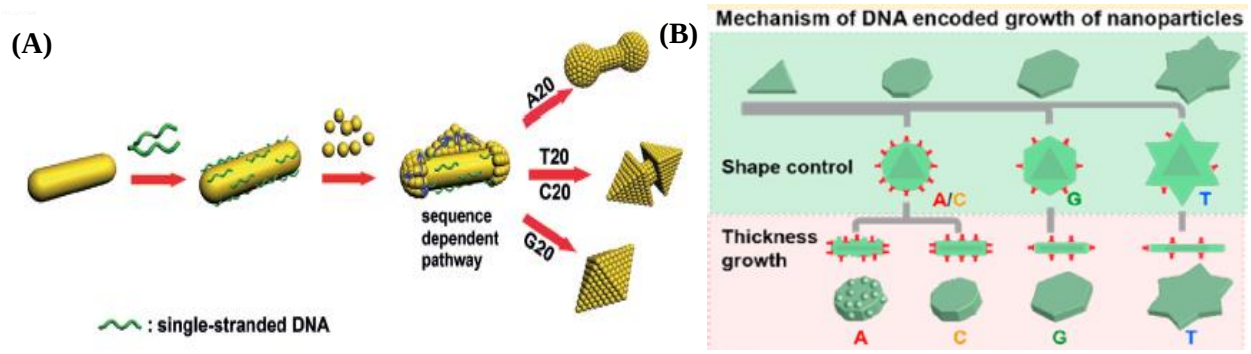


**Figure 1.11** (A) A proposed mechanism of overgrowth of AuNRs by homooligomeric DNA with different sequences[98] (Reprinted with permission from ref98, Copyright [2015] Wiley) (B) schematic representation of DNA-encoded growth of Au nanoprisms seeds into four shapes using different DNA strands (A20, T20, C20 and G20).[99] (Reprinted with permission from ref99, Copyright [2015] American Chemical Society)

Nevertheless, biomolecules mediated overgrowth are scarcely investigated until very recently. Lu's group employed nucleotides as sequence-programmable ligands to direct the overgrowth of Au NRs and Ag NTs.[98,99] In one case as shown in ***Figure 1.11A***, two distinctive shape evolution pathways are uncovered through kinetics study, leading to the formation of nanodumbbell and nanooctahedron.[98] When the overgrowth was performed in the presence of T20 or C20, intermediate products were obtained. This DNA-encoded overgrowth strategy allows for the fine-tuning of LSPR from visible to NIR region beyond 1000 nm. In an analogous synthesis, Au nanoprisms are used as the pristine seeds for the mechanistic investigation of the role of the DNA plays during the course of shape evolution.[99] A two-stage growth mechanism including the initial epitaxial growth and the followed-up thickening process was proposed (***Figure 1.11B***). In the first stage, a transition from nanoprisms to the nonagonal nanoplates, followed by hexagons, and eventually to six-pointed stars are strongly correlated to the binding affinity as well as the concentration of DNA ligands. In the second stage, the residual Au precursors along with the mobility of DNA bounded on the (111) facet have decisive implications for the thickening and roughing process.[99]

## 1.6 Distinctive properties of Bio-NPs hybrid system

### 1.6.1 Adsorption at the bio/abio interface

There has been a growing interest in the protein-coronas on the surface of NPs. Research conducted by Murphy's group reveals that the surface charge of NPs plays a significant role in dictating the protein adsorption on the NPs. As shown in the ***Figure 1.12A***, proteins from the simple cell culture media adsorb spontaneously to the surface of cationic Au NPs and the surface charge flips from positive to negative.[100] Notably, this adsorption process is reversible and the inherent dynamic feature as well as the composition of the protein corona further regulates the cellular uptake.[101]

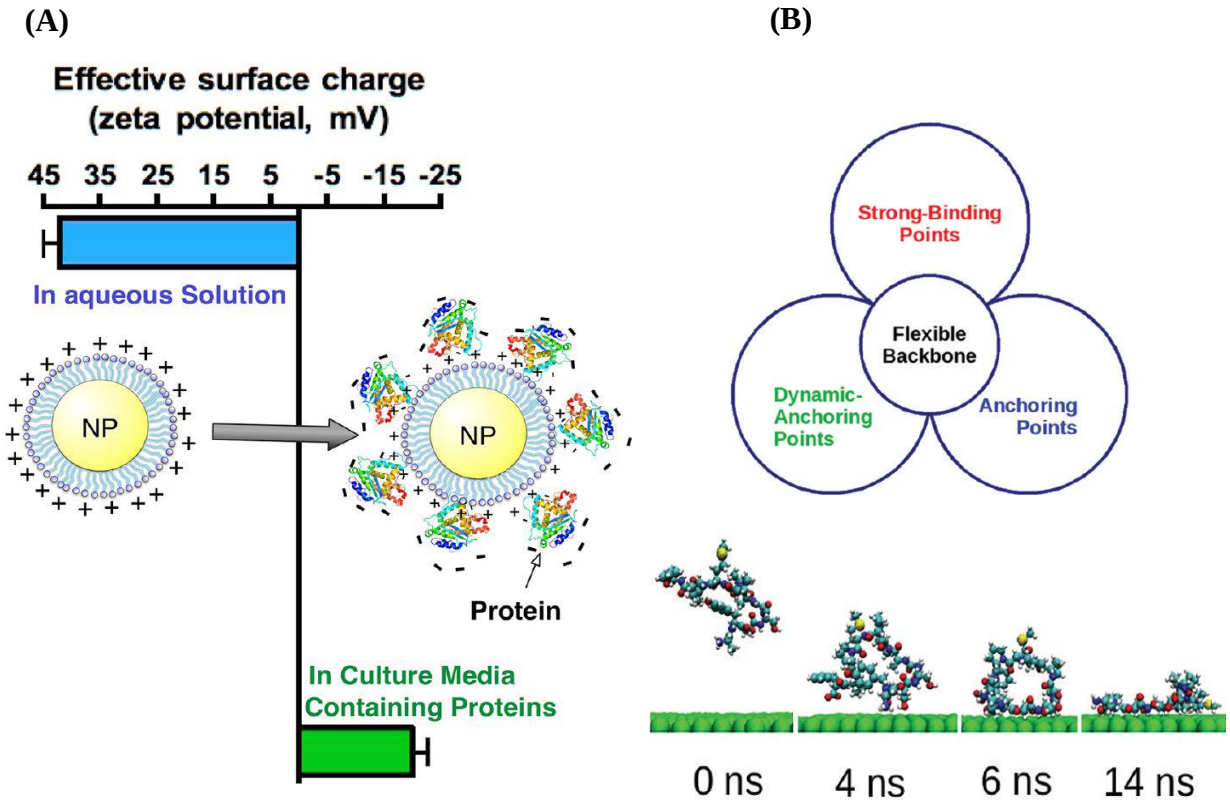


**Figure 1.12** (A) Cartoon demonstrating the adsorption of protein from biological media to the surface of initially cationic GNPs, and the resulting alteration of the surface charge in cellular media to a negative value, as measured by ζ potential analysis.[100] (Reprinted with permission from ref100, Copyright [2013] American Chemical Society) (B) Binding process of peptide onto gold surfaces.[102] (Reprinted with permission from ref102, Copyright [2012] American Chemical Society)

In additional to the surface charge, the shape of Au NPs affects the binding affinity of proteins onto NPs dramatically. For instance, BSA was used as the model protein to examine the binding strength onto the citrate-stabilized Au nanospheres (NSPs), Au NTs and Au NRs. Among these three types of Au NPs, Au NSPs show the highest binding affinity whereas the Au NTs rank the lowest.[103] Consistent results have also been found by probing the interaction between BSA and Au NSPs/Au NRs through fluorescence quenching and LSPR band shift indicating that BSA is prone to bind onto the ends of the GNRs.[104]

Due to the existence of resourceful peptides and proteins with versatile structures and functionalities, it is very challenging to find a set of widely accepted principles to delineate the adsorption behavior of biomolecules onto the NPs. Molecular dynamic simulation (MDS) is regarded as a powerful tool to study the binding process of peptides onto the gold surface.[102,105] Unlike the strong non-specific sulfur-gold bonding, the specific and high binding affinities originate from the cooperative interaction of the multiple amino acid residues. MDS results reveal that the overall binding process can be separated into four regimes: diffusion, anchoring, crawling and binding ***(Figure 1.12B)***. Accordingly, tyrosine, methionine, and phenylalanine are found to be the strong binding residues; serine and proline serve as anchoring sites, while glycine and alanine impart the flexibility to the peptide backbones and make them more amenable to conformational changes.[102]

### 1.6.2 Colloidal and morphological stability

APMNs are conventionally produced in the presence of charged surfactants, which significantly enhance their colloidal stability due to the elastic repulsion between adjacent NPs. Similarly, biopolymers bearing abundant polar moieties such as amines and carboxylate groups are able to efficiently prevent the agglomeration of NPs by conferring the net charges onto the

surface of APMNs and meanwhile lower their surface energy. The remarkable colloidal stability of Au and Ag nanoprisms prepared in the presence of repeat proteins or lignosulfonate has been confirmed through TEM, DLS and UV-Vis observations (Chapter 6 & Chapter 8).[90]

APMNs have a strong propensity to undergo shape transformation in response to the variations of temperature and the surrounding environment.[106] The thermodynamic driving force behind the shape change can be explained by the requirement to minimize the interfacial free energy at a fixed volume. For fcc metal NPs, the most thermodynamic favorable product is quasi-globular Wulff polyhedrons, such as truncated octahedron and cuboctahedron enclosed by a mixture of (100) and (111) facets.[107] APMNs can be considered to be trapped at the meta-stable states stabilized by the surface capping agent. Once the adsorbed surfactant is removed, the facets with lower surface energy will emerge at the cost of the high-energy facets so that the total interfacial energy reaches the minimum. Take Ag nanocubes as an example, the sharp corner will be rounded at elevated temperature. It is mainly because the original (100) facet is converted to (111) facet when surface capping agent, PVP, is released to the environment.[108] By the analogous mechanism, Ag nanobars will turn into Ag nanorices[109] after long-term storage.

Shape transformation can also be expedited by kinetics factors such as refluxing, heating and selective oxidative etching. For instance, Au NRs are shortened when exposed to HCl,[110] while Ag NTs will transform into round disks in the presence of halides ions.[111] The aforementioned shape evolution could be effectively circumvented by adding a sufficient amount of biopolymer stabilizers. On the other hand, the selective binding of biomolecules onto the specific facets is capable of driving the shape transformation towards desirable orientation, which may offer a compelling alternative for the synthesis of APMNs as well as a platform for plasmonic sensing of biomolecules.

### 1.6.3 Cytotoxicity and biocompatibility

Despite the fact that APMNs have great potentials in diagnostic and therapeutic applications, a comprehensive cytotoxicity profile need to be established before clinic implementations. In fact, the Au NPs cores are inert to the cells indicated by a number of *in vitro* studies.[112] However, the surface charge may cause many adverse effects, such as denaturation of proteins or severe cytotoxicity. Although there was an early concern that Au NPs with small diameter (<2 nm) may exhibit significant toxicity due to the high redox reactivity, recent *in vitro* and *in vivo* investigations demonstrated that Au NPs are not acutely toxic regardless of their size.[113] A toxicity assessment was then conducted by Murphy et al. in which Au NRs with different aspect ratio (1.5 - 4) and varied surface modification were studied as the model system.[51] They argue that the surface functionalization predominately affects the cytotoxicity rather than the morphology of the NPs. Moreover, it is found that the molecular origin of cytotoxicity mainly stemmed from the surface capping agent CTAB as compared with other positively charged polymeric surfactants.[100]

Considering the biosafety of NPs, it is of great importance to carefully design the surface chemistry. For instance, pre-treatment of NPs with a dense layer of fetal bovine serum (FBS) protein can remarkably reduce the cytotoxicity caused by nutriment depletion.[114] Recently, reactive oxygen species (ROS) on NPs has been found to trigger the cytotoxicity,[115] which could also be mitigated by protein coating to passivate the surface defects. Note that NPs with hydrophobic surfaces can raise potential biosafety hazard, i.e., cause damage to the cell membranes by interacting with the hydrophobic lipid bilayer. Functionalization of NPs with hydrophilic protein could therefore improve the biocompatibility. [114]

As the subject of nanotoxicity has been extensively investigated, more standard evaluation protocols revolving about the concerns such as dosage, operation, and impurity, is demanded so that toxicity profile obtained from individual labs could be accurately compared.[100]

### 1.6.4 Chiroptical properties

Biomolecules are optically active in the UV-region which is far from the LSPR band of Au and Ag NPs.[116] Intriguingly, when achiral NPs are functionalized with chiral biomolecule ligands such as helical peptides and double strand DNAs, a moderate and reproducible CD response was identified in the plasmon resonance region (***Figure 1.13A***).[57,117] Experimental observation and theoretical calculation presumes that the detected ellipticity of biomolecule-Au NPs complex in the visible region mainly derives from the dipolar interaction between chiral ligands and the plasmonic NPs.[116] In a broad sense, the chiroptical activity could be detected under the following circumstances (1) in-situ formation of an intrinsic chiral Au nanocluster in the presence of chiral ligands (2) electronic interaction between the chiral ligands and achiral metal core electrons, and (3) chiral arrangement of the ligands on an achiral metal core. [50]

In addition to that, a highly ordered biopolymer templates, particularly, DNA origami has enabled the construction of chiral plasmonic nanostructures composed of Au NPs arranged in a helical manner (***Figure 1.13B***).[118] The intensive CD signal is presumably attributed to the collective plasmonic coupling of Au NPs ensemble. The CD peak position along with the enhancement factor can be in turn finely tailored by adjusting the size of NPs as well as the distance between spacers. Moreover, a mirror CD profile can be observed for left-handed and right-handed assembly of Au NPs arrays, respectively.

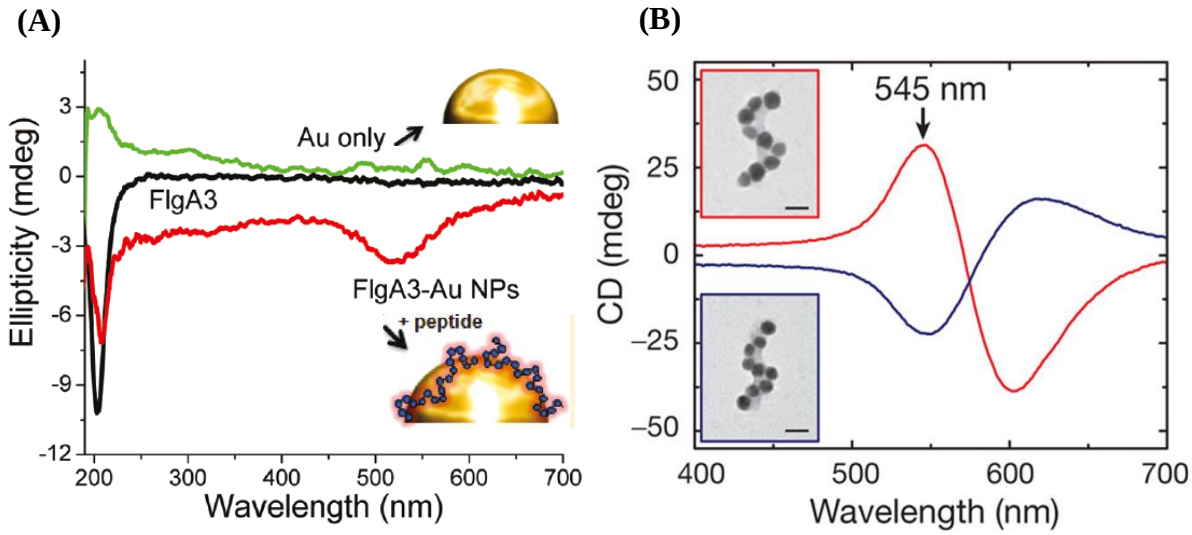


**Figure 1.13** (A) Chiroptical characterization of the FlgA3 binding to Au nanoparticles: CD spectra of the individual components (peptides and Au NPs), as well as the peptide-capped Au NPs.[56] (Reprinted with permission from ref56, Copyright [2011] American Chemical Society) (B) Circular dichroism of left-handed (red line) and right-handed (blue line) self-assembled gold nanohelices (16 nm) using DNA origami.[118] (Reprinted with permission from ref118, Copyright [2012] Nature Publishing Group)

## 1.7 References

(1) Hu, M.; Chen, J.; Li, Z.-Y.; Au, L.; Hartland, G. V.; Li, X.; Marquez, M.; Xia, Y. *Chem. Soc. Rev.* **2006**, *35*, 1084.
(2) Zhang, Q.; Tan, Y. N.; Xie, J.; Lee, J. Y. *Plasmonics* **2008**, *4*, 9.
(3) Dreaden, E. C.; Alkilany, A. M.; Huang, X.; Murphy, C. J.; El-Sayed, M. A. *Chem. Soc. Rev.* **2012**, *41*, 2740.
(4) Tokel, O.; Inci, F.; Demirci, U. *Chem. Rev.* **2014**, *114*, 5728.
(5) Xue, B.; Wang, D.; Zuo, J.; Kong, X.; Zhang, Y.; Liu, X.; Tu, L.; Chang, Y.; Li, C.; Wu, F.; Zeng, Q.; Zhao, H.; Zhao, H.; Zhang, H. *Nanoscale* **2015**, *7*, 8048.
(6) Leng, W.; Vikesland, P. J. *Anal. Chem.* **2013**, *85*, 1342.
(7) Lane, L. A.; Qian, X.; Nie, S. *Chem. Rev.* **2015**, *115*, 10489.
(8) Pastoriza-Santos, I.; Liz-Marzan, L. M. *J. Mater. Chem.* **2008**, *18*, 1724.
(9) Lohse, S. E.; Burrows, N. D.; Scarabelli, L.; Liz-Marzán, L. M.; Murphy, C. J. *Chem. Mater.* **2014**, *26*, 34.
(10) Jin, R.; Cao, Y.; Mirkin, C. A.; Kelly, K. L.; Schatz, G. C.; Zheng, J. G. *Science* **2001**, *294*, 1901.
(11) Millstone, J. E.; Park, S.; Shuford, K. L.; Qin, L.; Schatz, G. C.; Mirkin, C. A. *J. Am. Chem. Soc.* **2005**, *127*, 5312.
(12) Nelayah, J.; Kociak, M.; Stephan, O.; Garcia de Abajo, F. J.; Tence, M.; Henrard, L.; Taverna, D.; Pastoriza-Santos, I.; Liz-Marzan, L. M.; Colliex, C. *Nat. Phys.* **2007**, *3*, 348.
(13) Hammond, J.; Bhalla, N.; Rafiee, S.; Estrela, P. *Biosensors* **2014**, *4*, 172.

(14) Sun, Y.; Mayers, B.; Herricks, T.; Xia, Y. *Nano Lett.* **2003**, *3*, 955.
(15) Qian, Z.; Park, S.-J. *Chem. Mater.* **2014**, *26*, 6172.
(16) Gole, A.; Murphy, C. J. *Chem. Mater.* **2004**, *16*, 3633.
(17) Scarabelli, L.; Coronado-Puchau, M.; Giner-Casares, J. J.; Langer, J.; Liz-Marzán, L. M. *ACS Nano* **2014**, *8*, 5833.
(18) Xie, J.; Lee, J. Y.; Wang, D. I. C. *Chem. Mater.* **2007**, *19*, 2823.
(19) Kuo, C.-H.; Huang, M. H. *Langmuir* **2005**, *21*, 2012.
(20) Saverot, S.; Geng, X.; Leng, W.; Vikesland, P. J.; Grove, T. Z.; Bickford, L. R. *RSC Adv.* **2016**, *6*, 29669.
(21) Chen, Q.; Jia, Y.; Xie, S.; Xie, Z. *Chem. Soc. Rev.* **2016**, *45*, 3207.
(22) Quan, Z.; Wang, Y.; Fang, J. *Acc. Chem. Res.* **2013**, *46*, 191.
(23) Elechiguerra, J. L.; Reyes-Gasga, J.; Yacaman, M. J. *J. Mater. Chem.* **2006**, *16*, 3906.
(24) Tao, A. R.; Habas, S.; Yang, P. *Small* **2008**, *4*, 310.
(25) Liu, K.; Zhao, N.; Kumacheva, E. *Chem. Soc. Rev.* **2011**, *40*, 656.
(26) Bansal, V.; Li, V.; O'Mullane, A. P.; Bhargava, S. K. *CrystEngComm* **2010**, *12*, 4280.
(27) Aherne, D.; Ledwith, D. M.; Gara, M.; Kelly, J. M. *Adv. Funct. Mater.* **2008**, *18*, 2005.
(28) Murphy, C. J.; Sau, T. K.; Gole, A. M.; Orendorff, C. J.; Gao, J.; Gou, L.; Hunyadi, S. E.; Li, T. *J. Phys. Chem. B* **2005**, *109*, 13857.
(29) Lohse, S. E.; Murphy, C. J. *Chem. Mater.* **2013**, *25*, 1250.
(30) Wang, L.; Zhu, Y.; Xu, L.; Chen, W.; Kuang, H.; Liu, L.; Agarwal, A.; Xu, C.; Kotov, N. A. *Angew. Chem. Int. Ed.* **2010**, *49*, 5472.
(31) Xia, Y.; Ye, J.; Tan, K.; Wang, J.; Yang, G. *Anal. Chem.* **2013**, *85*, 6241.
(32) Chen, L.; Fu, X.; Lu, W.; Chen, L. *ACS Appl. Mater. Interfaces* **2013**, *5*, 284.
(33) Yang, X.; Yu, Y.; Gao, Z. *ACS Nano* **2014**, *8*, 4902.
(34) Wang, Y.; Yan, B.; Chen, L. *Chem. Rev.* **2013**, *113*, 1391.
(35) Geng, X.; Leng, W.; Carter, N. A.; Vikesland, P. J.; Grove, T. Z. *J. Chem. Mater. B* **2016**, *4*, 4182.
(36) Yang, Y.; Zhong, X.-L.; Zhang, Q.; Blackstad, L. G.; Fu, Z.-W.; Li, Z.-Y.; Qin, D. *Small* **2014**, *10*, 1430.
(37) Ma, W.; Sun, M.; Xu, L.; Wang, L.; Kuang, H.; Xu, C. *Chem. Commun.* **2013**, *49*, 4989.
(38) Adura, C.; Guerrero, S.; Salas, E.; Medel, L.; Riveros, A.; Mena, J.; Arbiol, J.; Albericio, F.; Giralt, E.; Kogan, M. J. *ACS Appl. Mater. Interfaces* **2013**, *5*, 4076.
(39) Bardhan, R.; Chen, W.; Perez-Torres, C.; Bartels, M.; Huschka, R. M.; Zhao, L. L.; Morosan, E.; Pautler, R. G.; Joshi, A.; Halas, N. J. *Adv. Funct. Mater.* **2009**, *19*, 3901.
(40) Wang, Y.; Black, K. C. L.; Luehmann, H.; Li, W.; Zhang, Y.; Cai, X.; Wan, D.; Liu, S.-Y.; Li, M.; Kim, P.; Li, Z.-Y.; Wang, L. V.; Liu, Y.; Xia, Y. *ACS Nano* **2013**, *7*, 2068.
(41) Xia, Y.; Xia, X.; Peng, H.-C. *J. Am. Chem. Soc.* **2015**, *137*, 7947.
(42) Jana, N. R.; Gearheart, L.; Murphy, C. J. *Langmuir* **2001**, *17*, 6782.
(43) Sau, T. K.; Murphy, C. J. *J. Am. Chem. Soc.* **2004**, *126*, 8648.
(44) Chen, S.; Carroll, D. L. *Nano Lett.* **2002**, *2*, 1003.
(45) Chen, S.; Fan, Z.; Carroll, D. L. *J. Phys. Chem. B* **2002**, *106*, 10777.
(46) Li, N.; Zhang, Q.; Quinlivan, S.; Goebl, J.; Gan, Y.; Yin, Y. *ChemPhysChem* **2012**, *13*, 2526.
(47) Niu, W.; Zhang, L.; Xu, G. *Nanoscale* **2013**, *5*, 3172.
(48) Zhang, H.; Jin, M.; Xiong, Y.; Lim, B.; Xia, Y. *Acc. Chem. Res.* **2013**, *46*, 1783.
(49) Personick, M. L.; Mirkin, C. A. *J. Am. Chem. Soc.* **2013**, *135*, 18238.

(50) Langille, M. R.; Personick, M. L.; Zhang, J.; Mirkin, C. A. *J. Am. Chem. Soc.* **2012**, *134*, 14542.
(51) Alkilany, A. M.; Nagaria, P. K.; Hexel, C. R.; Shaw, T. J.; Murphy, C. J.; Wyatt, M. D. *Small* **2009**, *5*, 701.
(52) Alkilany, A. M.; Murphy, C. J. *J. Nanopart. Res.* **2010**, *12*, 2313.
(53) Dickerson, M. B.; Sandhage, K. H.; Naik, R. R. *Chem. Rev.* **2008**, *108*, 4935.
(54) Delehanty, J. B.; Bradburne, C. E.; Susumu, K.; Boeneman, K.; Mei, B. C.; Farrell, D.; Blanco-Canosa, J. B.; Dawson, P. E.; Mattoussi, H.; Medintz, I. L. *J. Am. Chem. Soc.* **2011**, *133*, 10482.
(55) Naik, R. R.; Stringer, S. J.; Agarwal, G.; Jones, S. E.; Stone, M. O. *Nat. Mater.* **2002**, *1*, 169.
(56) Dickerson, M. B.; Jones, S. E.; Cai, Y.; Ahmad, G.; Naik, R. R.; Kröger, N.; Sandhage, K. H. *Chem. Mater.* **2008**, *20*, 1578.
(57) Slocik, J. M.; Govorov, A. O.; Naik, R. R. *Nano Lett.* **2011**, *11*, 701.
(58) Chen, C.-L.; Rosi, N. L. *J. Am. Chem. Soc.* **2010**, *132*, 6902.
(59) Song, C.; Zhao, G.; Zhang, P.; Rosi, N. L. *J. Am. Chem. Soc.* **2010**, *132*, 14033.
(60) Diamanti, S.; Elsen, A.; Naik, R.; Vaia, R. *J. Phys. Chem. C* **2009**, *113*, 9993.
(61) Li, Y.; Tang, Z.; Prasad, P. N.; Knecht, M. R.; Swihart, M. T. *Nanoscale* **2014**, *6*, 3165.
(62) Ueno, T.; Koshiyama, T.; Tsuruga, T.; Goto, T.; Kanamaru, S.; Arisaka, F.; Watanabe, Y. *Angew. Chem. Int. Ed.* **2006**, *45*, 4508.
(63) Niide, T.; Shimojo, K.; Wakabayashi, R.; Goto, M.; Kamiya, N. *Langmuir* **2013**, *29*, 15596.
(64) Hom, N.; Mehta, K. R.; Chou, T.; Foraker, A. B.; Brodsky, F. M.; Kirshenbaum, K.; Montclare, J. K. *J. Mater. Chem.* **2012**, *22*, 23335.
(65) Lin, Y.; Xia, X.; Wang, M.; Wang, Q.; An, B.; Tao, H.; Xu, Q.; Omenetto, F.; Kaplan, D. L. *Langmuir* **2014**, *30*, 4406.
(66) McMillan, R. A.; Howard, J.; Zaluzec, N. J.; Kagawa, H. K.; Mogul, R.; Li, Y.-F.; Paavola, C. D.; Trent, J. D. *J. Am. Chem. Soc.* **2005**, *127*, 2800.
(67) Mayavan, S.; Dutta, N. K.; Choudhury, N. R.; Kim, M.; Elvin, C. M.; Hill, A. J. *Biomaterials* **2011**, *32*, 2786.
(68) Schoen, A. P.; Schoen, D. T.; Huggins, K. N. L.; Arunagirinathan, M. A.; Heilshorn, S. C. *J. Am. Chem. Soc.* **2011**, *133*, 18202.
(69) Lan, X.; Chen, Z.; Liu, B.-J.; Ren, B.; Henzie, J.; Wang, Q. *Small* **2013**, *9*, 2308.
(70) Tan, L. H.; Xing, H.; Chen, H.; Lu, Y. *J. Am. Chem. Soc.* **2013**, *135*, 17675.
(71) Zhao, Y.; Xu, L.; Liz-Marzán, L. M.; Kuang, H.; Ma, W.; Asenjo-García, A.; García de Abajo, F. J.; Kotov, N. A.; Wang, L.; Xu, C. *J. Phys. Chem. Lett.* **2013**, *4*, 641.
(72) Tan, S. J.; Campolongo, M. J.; Luo, D.; Cheng, W. *Nat Nano* **2011**, *6*, 268.
(73) Schreiber, R.; Luong, N.; Fan, Z.; Kuzyk, A.; Nickels, P. C.; Zhang, T.; Smith, D. M.; Yurke, B.; Kuang, W.; Govorov, A. O.; Liedl, T. *Nat. Commun.* **2013**, *4*.
(74) Lo, P. K.; Karam, P.; Aldaye, F. A.; McLaughlin, C. K.; Hamblin, G. D.; Cosa, G.; Sleiman, H. F. *Nat. Chem.* **2010**, *2*, 319.
(75) Nykypanchuk, D.; Maye, M. M.; van der Lelie, D.; Gang, O. *Nature* **2008**, *451*, 549.
(76) Zou, L.; Qi, W.; Huang, R.; Su, R.; Wang, M.; He, Z. *ACS Sustain. Chem. Eng.* **2013**, *1*, 1398.
(77) Mahal, A.; Khullar, P.; Kumar, H.; Kaur, G.; Singh, N.; Jelokhani-Niaraki, M.; Bakshi, M. S. *ACS Sustain. Chem. Eng.* **2013**, *1*, 627.

(78) Briggs, B. D.; Knecht, M. R. *J. Phys. Chem. Lett.* **2012**, *3*, 405.
(79) Yu, L.; Banerjee, I. A.; Matsui, H. *J. Am. Chem. Soc.* **2003**, *125*, 14837.
(80) Xie, J.; Lee, J. Y.; Wang, D. I. C.; Ting, Y. P. *Small* **2007**, *3*, 672.
(81) Geng, X.; Grove, T. Z. *RSC Adv.* **2015**, *5*, 2062.
(82) Shankar, S. S.; Rai, A.; Ankamwar, B.; Singh, A.; Ahmad, A.; Sastry, M. *Nat. Mater.* **2004**, *3*, 482.
(83) Liu, B.; Xie, J.; Lee, J. Y.; Ting, Y. P.; Chen, J. P. *J. Phys. Chem. B* **2005**, *109*, 15256.
(84) Shao, Y.; Jin, Y.; Dong, S. *Chem. Commun.* **2004**, 1104.
(85) Xie, J.; Lee, J. Y.; Wang, D. I. C. *J. Phys. Chem. C* **2007**, *111*, 10226.
(86) Au, L.; Lim, B.; Colletti, P.; Jun, Y.-S.; Xia, Y. *Chem. Asian J.* **2010**, *5*, 123.
(87) Li, C.; Bolisetty, S.; Mezzenga, R. *Adv. Mater.* **2013**, *25*, 3694.
(88) Jiang, F.; Hsieh, Y.-L. *Biomacromolecules* **2014**, *15*, 3608.
(89) Singh, V.; Khullar, P.; Dave, P. N.; Kaur, G.; Bakshi, M. S. *ACS Sustain. Chem. Eng.* **2013**, *1*, 1417.
(90) Geng, X.; Roth, K. L.; Freyman, M. C.; Liu, J.; Grove, T. Z. *Chem. Commun.* **2016**, *52*, 9829.
(91) Ruan, L.; Chiu, C.-Y.; Li, Y.; Huang, Y. *Nano Lett.* **2011**, *11*, 3040.
(92) Ruan, L.; Ramezani-Dakhel, H.; Lee, C.; Li, Y.; Duan, X.; Heinz, H.; Huang, Y. *ACS Nano* **2014**, *8*, 6934.
(93) Chen, C.-L.; Rosi, N. L. *Angew. Chem. Int. Ed.* **2010**, *49*, 1924.
(94) Chen, C.-L.; Zhang, P.; Rosi, N. L. *J. Am. Chem. Soc.* **2008**, *130*, 13555.
(95) Song, J. H.; Kim, F.; Kim, D.; Yang, P. *Chem. Eur. J.* **2005**, *11*, 910.
(96) Kang, S. W.; Lee, Y. W.; Park, Y.; Choi, B.-S.; Hong, J. W.; Park, K.-H.; Han, S. W. *ACS Nano* **2013**, *7*, 7945.
(97) Leary, R. K.; Kumar, A.; Straney, P. J.; Collins, S. M.; Yazdi, S.; Dunin-Borkowski, R. E.; Midgley, P. A.; Millstone, J. E.; Ringe, E. *J. Phys. Chem. C* **2016**, *120*, 20843.
(98) Song, T.; Tang, L.; Tan, L. H.; Wang, X.; Satyavolu, N. S. R.; Xing, H.; Wang, Z.; Li, J.; Liang, H.; Lu, Y. *Angew. Chem. Int. Ed.* **2015**, *54*, 8114.
(99) Tan, L. H.; Yue, Y.; Satyavolu, N. S. R.; Ali, A. S.; Wang, Z.; Wu, Y.; Lu, Y. *J. Am. Chem. Soc.* **2015**, *137*, 14456.
(100) Alkilany, A. M.; Lohse, S. E.; Murphy, C. J. *Acc. Chem. Res.* **2013**, *46*, 650.
(101) Ritz, S.; Schöttler, S.; Kotman, N.; Baier, G.; Musyanovych, A.; Kuharev, J.; Landfester, K.; Schild, H.; Jahn, O.; Tenzer, S.; Mailänder, V. *Biomacromolecules* **2015**, *16*, 1311.
(102) Yu, J.; Becker, M. L.; Carri, G. A. *Langmuir* **2012**, *28*, 1408.
(103) Chaudhary, A.; Gupta, A.; Khan, S.; Nandi, C. K. *Phys. Chem. Chem. Phys.* **2014**, *16*, 20471.
(104) Iosin, M.; Toderas, F.; Baldeck, P. L.; Astilean, S. *J. Mol. Struct.* **2009**, *924–926*, 196.
(105) Tang, Z.; Palafox-Hernandez, J. P.; Law, W.-C.; E. Hughes, Z.; Swihart, M. T.; Prasad, P. N.; Knecht, M. R.; Walsh, T. R. *ACS Nano* **2013**, *7*, 9632.
(106) Xia, Y.; Xiong, Y.; Lim, B.; Skrabalak, S. E. *Angew. Chem. Int. Ed.* **2009**, *48*, 60.
(107) Frenken, J. W. M.; Stoltze, P. *Phys. Rev. Lett.* **1999**, *82*, 3500.
(108) Chen, J.; McLellan, J. M.; Siekkinen, A.; Xiong, Y.; Li, Z.-Y.; Xia, Y. *J. Am. Chem. Soc.* **2006**, *128*, 14776.
(109) Xiong, Y.; Cai, H.; Wiley, B. J.; Wang, J.; Kim, M. J.; Xia, Y. *J. Am. Chem. Soc.* **2007**, *129*, 3665.

(110) Tsung, C.-K.; Kou, X.; Shi, Q.; Zhang, J.; Yeung, M. H.; Wang, J.; Stucky, G. D. *J. Am. Chem. Soc.* **2006**, *128*, 5352.
(111) Tang, B.; Xu, S.; An, J.; Zhao, B.; Xu, W.; Lombardi, J. R. *Phys. Chem. Chem. Phys.* **2009**, *11*, 10286.
(112) Li, N.; Zhao, P.; Astruc, D. *Angew. Chem. Int. Ed.* **2014**, *53*, 1756.
(113) Bar-Ilan, O.; Albrecht, R. M.; Fako, V. E.; Furgeson, D. Y. *Small* **2009**, *5*, 1897.
(114) Yang, S.-T.; Liu, Y.; Wang, Y.-W.; Cao, A. *Small* **2013**, *9*, 1635.
(115) Lewinski, N.; Colvin, V.; Drezek, R. *Small* **2008**, *4*, 26.
(116) Govorov, A. O.; Fan, Z.; Hernandez, P.; Slocik, J. M.; Naik, R. R. *Nano Lett.* **2010**, *10*, 1374.
(117) Shemer, G.; Krichevski, O.; Markovich, G.; Molotsky, T.; Lubitz, I.; Kotlyar, A. B. *J. Am. Chem. Soc.* **2006**, *128*, 11006.
(118) Kuzyk, A.; Schreiber, R.; Fan, Z.; Pardatscher, G.; Roller, E.-M.; Hogele, A.; Simmel, F. C.; Govorov, A. O.; Liedl, T. *Nature* **2012**, *483*, 311.

# Chapter 2. Facile, tunable and SERS-enhanced HEPES gold nanostars

Scott E. Saverot, Xi Geng, Weinan Leng, Peter J. Vikesland, Tijana Z. Grove

and Lissett R. Bickford

Reprinted with permission from X. Geng, and T.Z Grove, *RSC Adv.*, **2016**, *6*, 29669-29673.


**Attributions:** SS initiated the project, synthesized the Au nanostars, performed UV-Vis test and prepared the draft paper. XG performed morphological characterization and SERS test. XG also provided constructive input on experimental design, data analysis and writing. WL and PJV offered technical assistance on SERS analysis. LRB and TZG supervised the project and made further contribution through editing the manuscript.

## 2.1 Abstract

Gold nanoparticles have shown promise as effective tools in biomedicine for drug delivery, imaging, and photo thermal therapy. We present the preparation of gold nanostars (Au NSTs) through a two-step approach utilizing a common Good's buffer, HEPES, as a weak reducing agent. Au NSTs with tunable branches up to 30 nm in length were produced in a two-step synthesis. We have investigated the effect of the ionic strength on the Au NST growth and branch length. Au NSTs were found to be near-infrared responsive and provide an augmented SERS signal, with an enhancement factor, defined as the magnitude of SERS signal amplification, of approximately $10^7$. The unique branched morphology of Au NSTs confers optical properties advantageous for *in vivo* biomedical applications.

## 2.2 Introduction

Gold nanoparticles are studied for their localized surface plasmon resonance (LSPR), and the collective resonant electron oscillations that may be excited by exposure to an electromagnetic field.[1] LSPR is tunable through nanoparticles' size, shape, and composition. LSPR in the near-infrared (NIR) region, where the absorbance of biomolecules reaches a minimum[2,3] is advantageous for *in vivo* imaging because of a deeper tissue penetration and a better signal to noise ratio.[4-7] Noble metal nanostructures demonstrate a phenomenon known as surface-enhanced Raman scattering (SERS) that results in an enhanced Raman scattering signal for surface associated molecules by several orders of magnitude.[8-10] This capability is due to the excitation of the surface plasmon of nanoparticles and an increased polarizability of the target molecules under incident radiation as new chemical bonds are formed with the metallic surface.[8-11] As a result, much attention has been placed into tuning nanoparticles' shape-dependent optical properties and creating "hot spots" (areas with strongly enhanced electromagnetic fields) typical at junctions and sharp tips.[9,11,12]

Gold star-shaped nanoparticles, nanostars (Au NSTs), have received attention as capable platforms for NIR and infrared absorption and SERS applications due to their many branches and sharp tips.[3,4,11,12] Particles with a greater number of longer branches produce enhanced peak resonance.[3,13,14] Many studies have been conducted utilizing Au NSTs' unique properties. Notably Yuan et al. fabricated strong NIR resonant SERS Au NST probes and Gao et al. designed multifunctional Au NST based nanocomposites for NIR, SERS and magnetic resonance techniques.[15,16]

Au NSTs are commonly synthesized in a buffer composed of 4-(2-hydroxyethyl)-1-piperazineethanesulfonic acid (HEPES) through one-pot methods.[3-5,12,17-19] HEPES buffer is a zwitterionic organic buffer agent, utilized in cell culture, desired for its maximal solubility in

water, low permeability to cell membranes, and minimal salt and temperature effects.[4] Based on the original published procedure, HEPES-mediated Au NSTs were reported to have a peak at 688 nm.[4] Although the entire IR region consists of wavelengths between 700 nm and 2500 nm.[2,20,21] for biomedical purposes we are interested in the biological NIR window. This window extends between 650 nm and 900-950 nm dependent upon tissue type,[5-7] a range in which water and hemoglobin have their lowest absorption. Thus, it stands to reason that reported HEPES-mediated Au NSTs are minimally NIR sensitive.

To serve as effective biomedical tools, nanoparticles must be well-characterized.[17,22] One-pot reactions, valued for simplicity and use of weak reducing agents, do not offer sufficient precision in controlling branch growth, thus yielding effectively highly polydisperse samples. It is critical to optimize methods to yield suspensions with low polydispersity to maintain performance and predictability in nanoparticle use.[17,22] Seed-mediated approaches reported to date have overcome this inconsistency of one-pot reactions. However, they often require adding surfactants such as cetrimonium bromide, dimethylformamide, polyvinyl pyrrolidone, some of which are known to be cytotoxic, that need to be removed prior to application.[3,4,14,15,23,24] Therefore, there is a need for a robust biocompatible method for Au NST synthesis. Towards this goal, we report a tunable and green synthesis of NIR-sensitive and SERS-functional Au NSTs. Both nanoparticle size and branch length can be controlled in this simple, two-step approach.

Herein, we describe a two-step synthesis of Au NSTs that resembles seed-mediated approaches while making no effort to separate gold seeds and the growth solution. In this two-step procedure, gold nuclei are introduced at low precursor concentrations after which gold ions is increased through addition of the fresh precursor to promote growth on existing particles. We investigate the effect of solution ionic strength and consider the halide's effects on Au NST

formation and stability. Lastly, we investigate the SERS properties of these Au NSTs using the conventional Raman reporter, 4-mercaptobenzoic acid (4-MBA).

## 2.3 Experimental

### 2.3.1 Gold nanostar synthesis

A 2 mM hydrogen tetrachloroaurate trihydrate ($HAuCl_4 \cdot 3H_2O$, Sigma Aldrich) stock solution was prepared in Milli-Q water in amber bottles and allowed to age for 3 days prior to synthesis. HEPES buffer was prepared fresh with Milli-Q water at a final concentration of 150 mM and the pH adjusted to 7.4 through the addition of 1 M sodium hydroxide (NaOH) solution. In a typical experiment, 666 μL of HEPES was mixed with 333 μL of 0.15 mM $HAuCl_4$ solution, with no stirring at room temperature (25 °C) and was allowed to react for 80 minutes. At this time, 833 μL of 0.15 mM $HAuCl_4$ was added under the same conditions to the reaction and allowed to react overnight. The process was scalable up to ten times volume. Resulting suspensions were centrifuged at 4,000 rpm for 15 min to remove excess HEPES solution. The one-step procedure is identical to that previously described,[4] with modified amount of $HAuCl_4$ added to constitute the total volume (1.166 mL) and allowed to react overnight. In ionic strength studies, 6 M solutions of NaCl and $NaNO_3$ in Milli-Q water were added to prepared HEPES buffer at different concentrations (5, 10, 25, 50 mM) prior to synthesis under similar two-step conditions.

### 2.3.2 Nanoparticle characterization

UV-vis spectrophotometry analysis was performed using a Cary 60 UV-vis spectrophotometer (Agilent). Transmission electron microscopy (TEM) analysis was performed on a Philips EM420 at an accelerating voltage of 120 kV. TEM samples were prepared by applying 10 μL of nanoparticle suspension (0.5 mg/mL) onto 200 mesh carbon-coated Cu grids

(Ted Pella), followed by drying overnight prior to imaging. The particle-size distribution was estimated by measuring the size of approximately 100 nanoparticles in different grid regions using ImageJ software. Crystal structure of Au NSTs were examined using JEOL 2100 field thermionic emission high resolution (HR-TEM) equipped with a silicon drifted detector-based EDS system, where 300 mesh ultrathin grids (EM Science) were used as sample supports.

### 2.3.3 Colloidal stability

Nanoparticles were suspended in Milli-Q water at an OD of 0.3. Colloidal stability was monitored weekly, over 3 weeks, using a UV-vis spectrophotometer. Sample absorbance spectra were normalized to the initial spectra, post synthesis.

### 2.3.4 4MBA-tagged SERS preparation

Au NSTs were conjugated to 4-mercaptobenzoic acid (4-MBA) according to a modified protocol adapted from Li et al.[11] Briefly, 20 µL of 10 mM 4-MBA dissolved in ethanol was added to a solution of the above mentioned Au NSTs and the resultant solution was agitated for five hours (Rotoflex). The solution was then centrifuged at 9000 rpm for 30 min to remove excess 4-MBA and re-suspended in Milli-Q water. Although SERS signal form as prepared NSTs was greatly enhanced, it was impossible to quantify the enhancement factor (EF). Since Au NSTs are anisotropic, it is difficult to accurately estimate number and density of 4-MBA molecules attached to the NSTs' surface. Assembling NSTs into SERS substrates circumvents that uncertainty and we went ahead with that strategy to measure EF.

### 2.3.5 SERS measurement

The purified Au NST colloidal suspension was drop-casted onto an aluminum foil substrate and dried overnight to form a thin layer of Au NST substrate. Then, 10 µl of 0.1 mM 4-MBA ethanol solution was applied onto the as-prepared Au NST substrate and dried overnight before use.

SERS spectra were collected with a WITec alpha 500R using a 785 nm excitation source. Backscattered light was collected using 10X and 100X objectives at integration times ranging from 50 ms to 1 s. The signal was dispersed using a 300 groove/mm grating and the dispersed light was collected by a Peltier cooled charge coupled device (CCD). We assumed that a monolayer of 4-MBA was attached onto the surface of the Au NST substrate.

**Table 1.** SERS Analysis Parameters

| **Parameter** | Value | Description |
|---|---|---|
| **V** | $\pi \times \left(\frac{d}{2}\right)^2 \times h$ | Excitation volume of the 785nm laser (diameter and focal depth dependent) |
| **ρ** | 1.5 g $cm^{-3}$ | Density of 4-MBA |
| $\mathbf{h_{10X}}$ | 17.4 μm | Focal depth of laser at 10X |
| $\mathbf{h_{100X}}$ | 1.9 μm | Focal depth of laser at 100X |
| $\mathbf{d_{10X}}$ | 1.6 μm | Diameter of laser spot size at 10X |
| $\mathbf{d_{100X}}$ | 0.5 μm | Diameter of laser spot size at 100X |
| **M** | 154.2 g $mol^{-1}$ | Molecular weight of 4-MBA |
| $\mathbf{N_A}$ | $6.02 \times 10^{23}\ mol^{-1}$ | Avogadro constant |
| **f** | 0.5 | Occupation factor for assumed monolayer of 4-MBA molecules |
| **A** | 0.54 $nm^2$ | Footprint of the 4-MBA molecule |

The pure 4-MBA control spectrum was obtained through the drop casting of 4-MBA in ethanol in similar manner described above. All reported SERS data is an average of 100 collected spectra over a 2000 × 500 μm scan area of the substrate. The enhancement factor (EF) was calculated using the following equation: $EF = (I_{SERS}/I_{bulk}) \times (N_{Bulk}/N_{SERS})$, where the peak at 1590 $cm^{-1}$ was selected for the EF evaluation.[11,25] The terms $I_{SERS}$ and $I_{Bulk}$ are the intensities of the same Raman band in the SERS and bulk Raman spectra, respectively.[11] We further define the terms $N_{Bulk}$ and $N_{SERS}$ as: $N_{Bulk} = \left(\frac{V \times \rho}{M}\right) \times N_A$ and $N_{SERS} = (f \times \pi \times \left(\frac{d}{2}\right)^2)/A$, respectively. Further experimental parameters can be found in Table 1.

## 2.4 Results and Discussion

***Figure 2.1a*** shows the typical absorption spectra of Au NSTs synthesized through one-step or two-step method. Both spectra feature an absorption peak near 530 nm and a NIR absorption peak above 740 nm. The two-step procedure resulted in red-shifted NIR peaks between 760 and 815 nm whereas one-step methods yielded particles with a range between 720-780 nm. Particle size and aspect ratio are known to govern the optical properties of nanoparticles.[3,4,26,27] Gold nanoparticles with elongated features present a longitudinal plasmon resonance that red-shifts relative to the LSPR of spherical gold nanoparticles (520 nm).[1,4,26] TEM analysis of the recovered Au NSTs show that the two-step approach produced particles with a greater number of branches of increased length compared to the one-step synthesis (***Figure 2.1b,c***). The two-step method produced Au NSTs with average branch length of 20.7 nm ± 7.7 nm compared to the one-step with average branches of 14.4 nm ± 4.5 nm (***Figure S1***). However, TEM analysis considers a limited sample size and can misrepresent particle homogeneity. To address this, the quality of NST preparation and procedure repeatability was evaluated from LSPR peaks. From DLS measurements, an average estimated hydrodynamic diameter of Au NSTs is 61 nm (***Figure S2***), consistent with the measurement of Au NSTs from tip to tip in TEM images. The synthetic procedure is very robust and the yield could reach up to 80%, which means 80% of the total number falls into the category of branched Au NSTs. Additionally, the synthesis could be further scale up to 100 mL without compromising the quality of Au NSTs.

We next investigated the mechanism of Au NST formation. Gold seeds were prepared through a first addition of a low concentration (0.15 mM) of $HAuCl_4$ to prepared HEPES buffer. The second addition was introduced after 80 minutes of reaction time, after which typical Au NST structures were formed over the course of the day as observed in TEM images (***Figure S3b***). We surmise that upon the second addition of precursor, the gold seed to gold precursor

ratio is achieved that favors deposition upon already present particles. After one-day, Au NSTs exhibited characteristic long branches. A kinetic scan of the typical reaction over one-day is shown in ***Figure S3a***. We hypothesize that low concentrations and a low gold seed to gold precursor ratios deter the production of additional nuclei, favoring deposition upon existing nuclei and growth of anisotropic nanoparticles. Operating within the confines of the slow growth rate, Au NSTs were synthesized without the need of additional surfactants or coordinating ligands.

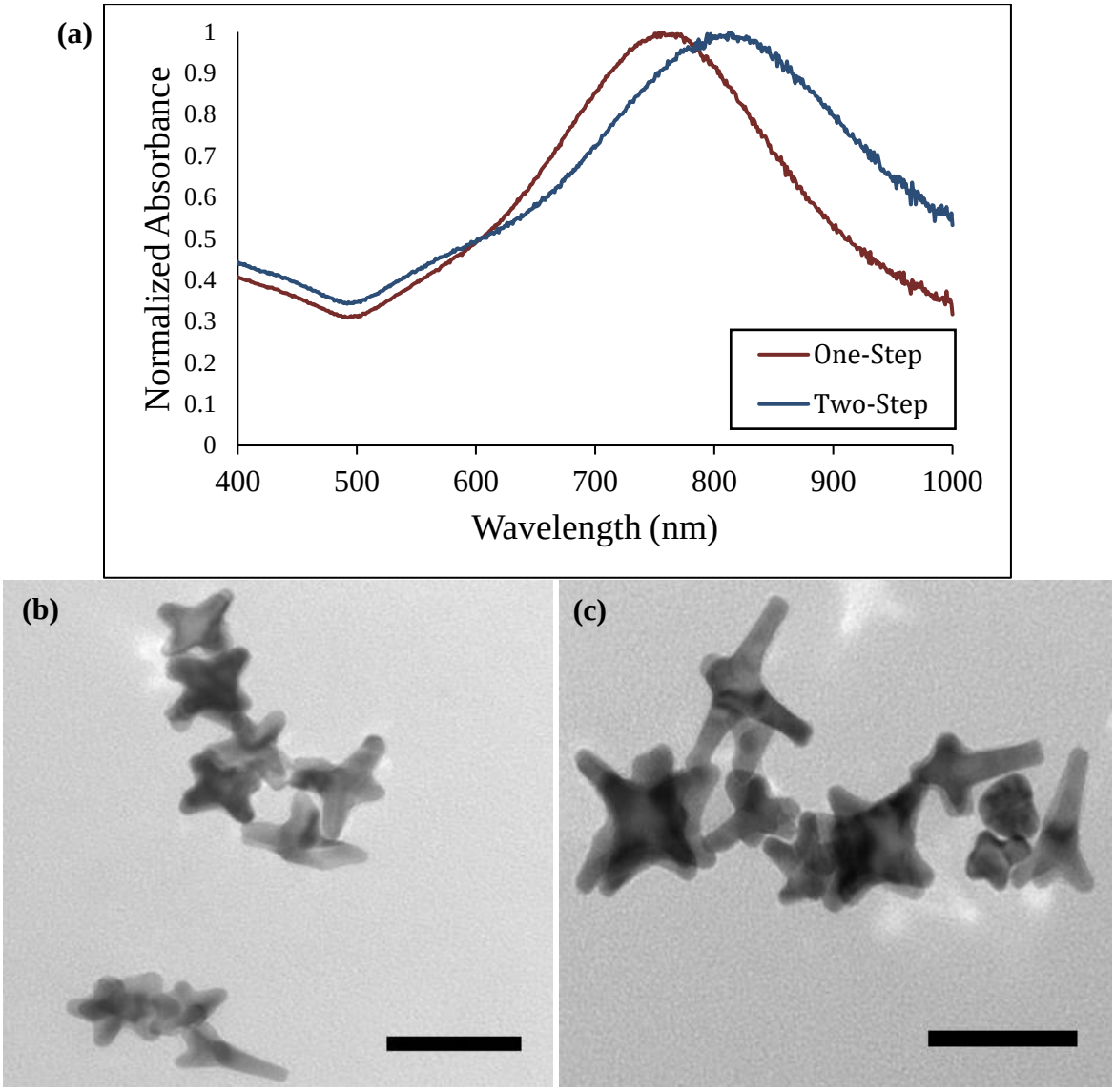

**Figure 2.1** (a) LSPR of Au NSTs prepared using one-step and two-step procedures. (b) TEM images of Au NSTs prepared using the one-step synthesis approach and (c) Au NSTs prepared using the two-step approach (Scale bar = 50 nm).

Colloidal stability of Au NSTs in D.I. water was analyzed over three weeks by observing changes in LSPR peaks, as these are more informative measures of physical changes to particles.[28] Au NSTs are strikingly stable experiencing only a minor (18%) loss in absorbance intensity (***Figure S4a***) over the three-week period while maintaining branched morphology without any significant agglomeration and change in branch length (***Figure S4b***). Similarly, incubation of as-prepared Au NSTs in 1× PBS over six hours resulted in a loss of only 6% absorbance intensity (***Figure S5***). It is important to note that surface of these NSTs has not been altered and that for any biological application PEG or targeting ligand would be added to the surface through standard coupling strategies. Nevertheless, presented data indicate that Au NSTs are fairly stable in solution without any surface functionalization.

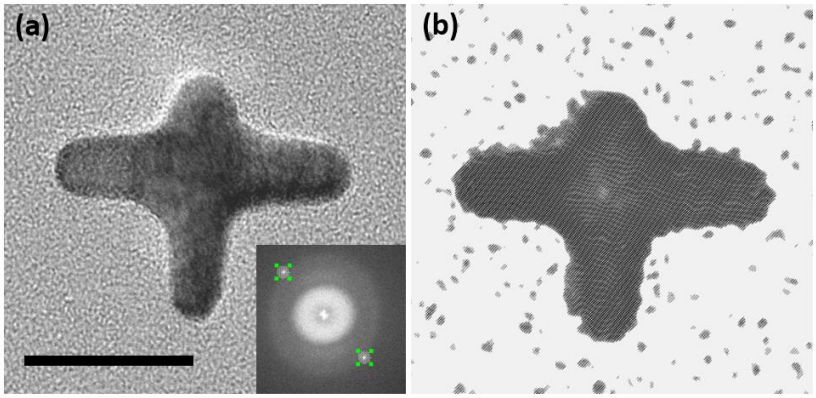


**Figure 2.2** (a) HR-TEM image of representative Au NST (inset = FFT diffraction pattern). (b) HR-TEM image of the inverse FFT, from corresponding diffraction pattern. (scale bar = 20 nm)

In the fast Fournier Transform (FFT) patterns from HR-TEM images two symmetrical diffraction spots are observed (***Figure 2.2a***), consistent with the single crystalline structure of Au NSTs. The lattice spacing between the (111) planes is about 0.236 nm, which is similar that of bulk gold.[29] The inverse FFT image in ***Figure 2.2b*** is equivalent to the image in the ***Figure 2.2a***

suggesting that the entire Au NST, including the four tips and the central region of the NST, are contributing to the FFT pattern. Identical FFT patterns for different tips can be seen in ***Figure S6***.

The effects of the ionic strength on nanoparticle stability and aggregation are well described and understood.[30-33] In particular, the addition of salt is a particle independent method to affect the repulsive forces between charged particles.[31] Notably, increases in ionic strength through salt addition have been shown to increase particles' hydrodynamic diameter as well as, increase aggregation, and decrease stability.[30,32,33] Herein, we investigate the effects of varying ionic strengths through salt additions during Au NST synthesis. We observed a modest shift in particle LSPR with increasing concentrations of $NaNO_3$ (***Figure 2.3a***). Additionally, for the highest concentration tested, Au NST branch length increased as seen in ***Figure 2.3a***. Against our chemical intuition, the increase in the ionic strength does not give rise to significant aggregation.

**(a)**

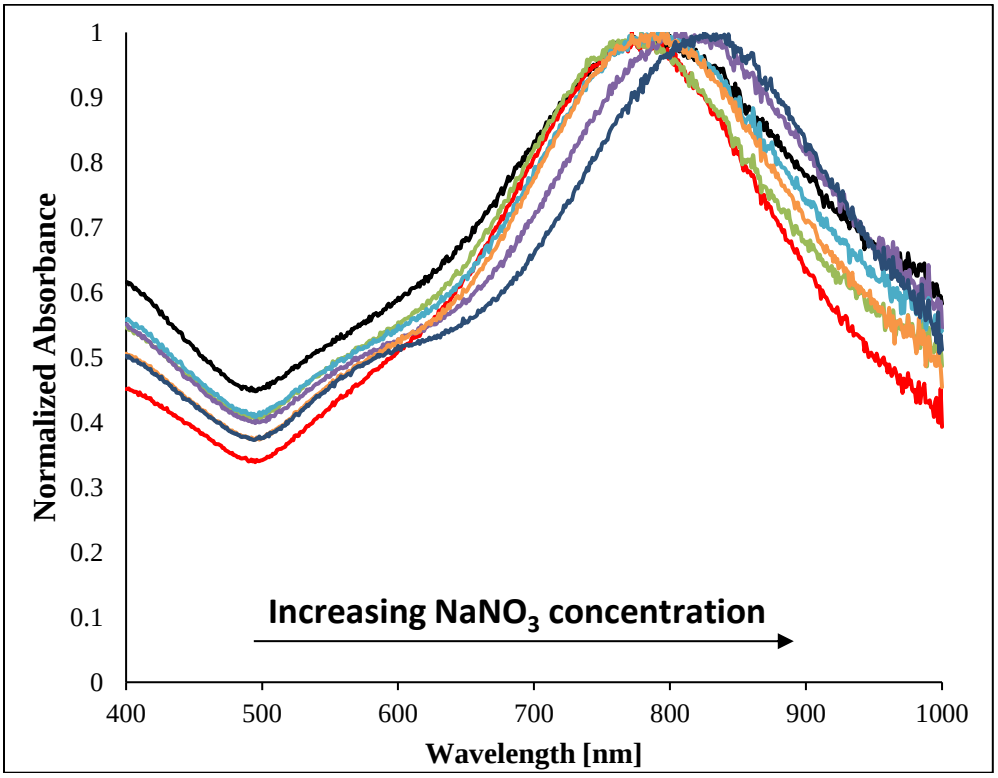

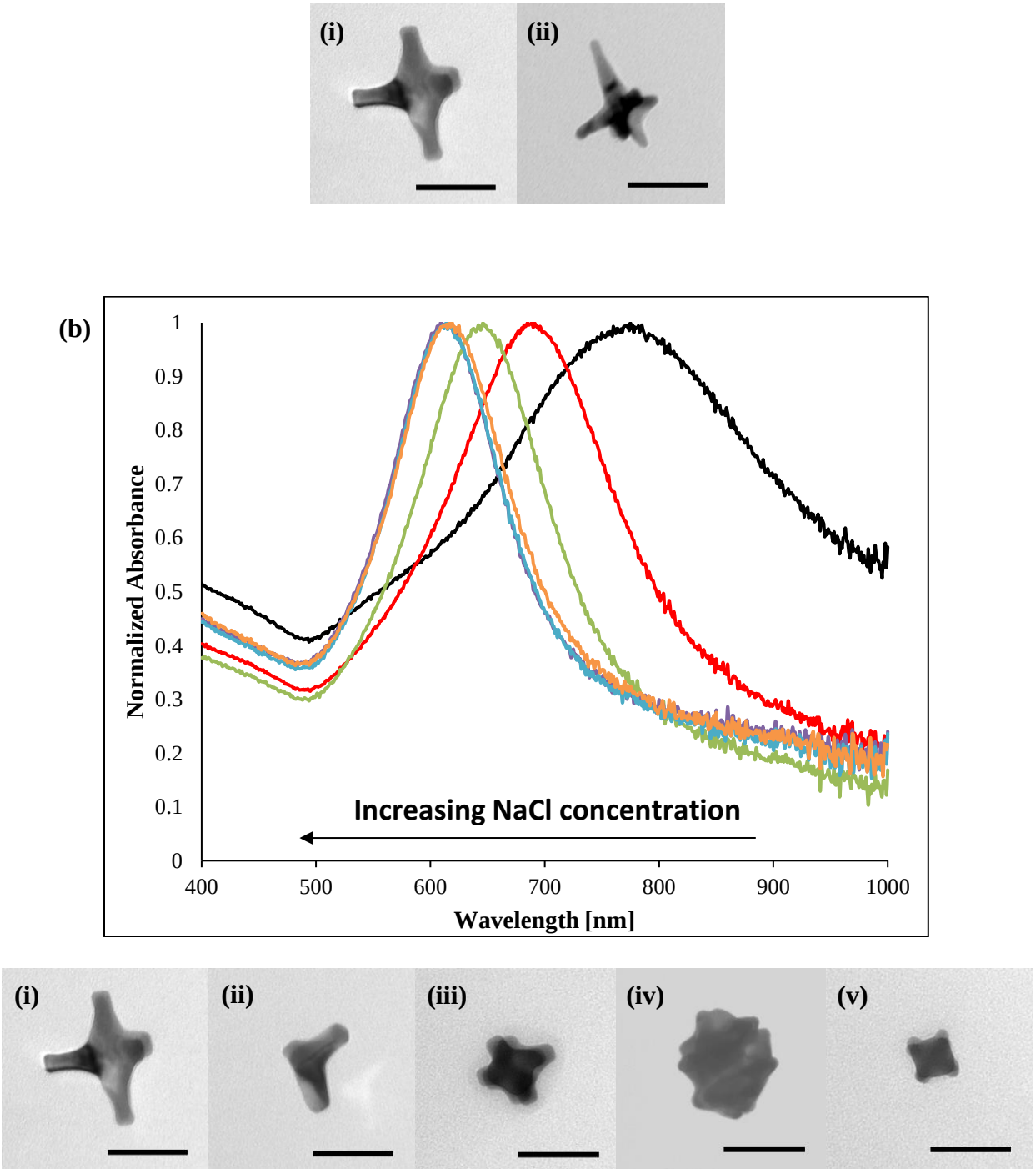


**Figure 2.3** (a) The LSPR of Au NSTs synthesized through the two-step approach in the presence of $NaNO_3$ at: 0, 10, 25, 50, 75, 100, 500 mM from left to right. TEM images (i, ii) correspond to 0 and 50 mM $NaNO_3$ respectively. (scale bar = 50 nm). (b) The LSPR of Au NSTs synthesized through the two-step approach in the presence of NaCl at: 0, 10, 25, 50, 75, 100 mM from right

to left. TEM images (i-v) correspond to 0, 10, 25, 50, 75 mM of NaCl respectively (scale bar = 50 nm).

To pinpoint the effector ion, we conducted a similar study with sodium chloride (NaCl) salt. ***Figure 2.3b*** shows the result of NaCl addition to reaction mixture. Increasing concentrations of NaCl elicited blue-shifting in particle's LSPR. Particles formed in the presence of high concentrations of NaCl have a NIR peak near 615 nm. TEM images show the length of Au NSTs arms could be modulated by the concentration of NaCl, indicating that sodium or chloride ions had an effect in precursor deposition on gold seeds (***Figure 2.3b***). Comparing results from $NaNO_3$ and NaCl additions in the same ionic strength range, we conclude that the chloride ions dominate the morphological evolution of nanoparticles rather than the effect of ionic strength. This is consistent with published reports that the addition of halides such as chloride and bromide may significantly slow the growth kinetics which may also hinder the elongation of braches on the <111> direction.[13] Thus in the case of NaCl addition, the preferential binding of chloride ions onto the gold surfaces inhibits tip growth resulting in the blue-shifting of the NIR peak and LSPR consistent with less anisotropic morphologies. At the same time, although sodium and nitrate ions affect the ionic strength, they do not impart any specific ion effect and thus may only impose minor influence onto the morphology of Au NSTs.

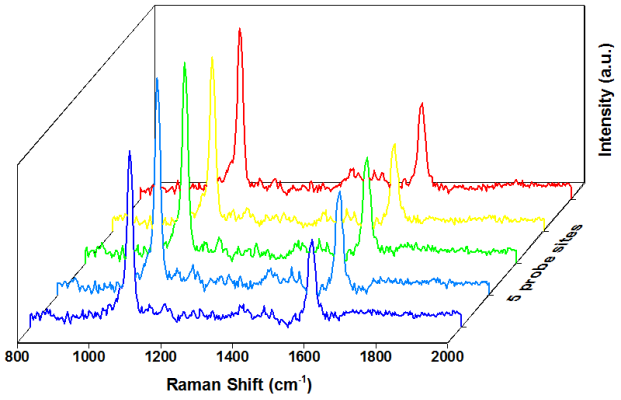


**Figure 2.4** The baseline corrected SERS spectroscopy of 4-MBA tagged Au NSTs at 5 different locations.

The SERS performance of the Au NSTs was examined through measurement of the Raman spectra of 4-MBA deposited onto self-assembled Au NST substrate (***Figure 2.4***). For comparison, the Raman spectrum of pure 4-MBA is shown in ***Figure S7***. The EF value is estimated to $10^7$. Details of calculation are presented in Section 2.2.5. We attribute this enhancement to the well-defined tips of Au NSTs as observed in TEM images. The value of EF is likely underestimated because of the incomplete surface coverage. Nevertheless, SERS signal of 4-MBA in several locations on the substrate is highly reproducible indicating the homogenous self-assembly of Au NSTs and 4-MBA deposition.

## 2.5 Conclusions

We demonstrate the facile, green synthesis of Au NSTs for SERS applications. The absorption peak of Au NSTs can be tuned between 615 nm and 815 nm by simply adjusting reaction conditions. The HR-TEM analysis confirms the formation of monocrystalline particles with multiple branches up to 30 nm in length. We investigated the effect of ionic strength upon Au NST growth, noting the undesirable effects of chloride ions. Au NSTs were found to exhibit enhanced SERS performance, with an enhancement factor of approximately $9.8\times10^6$. By virtue of their exhibited sensitivity to both NIR and SERS, these prepared Au NSTs could be well suited as biosensors, reporters or targeted biomedical treatments. Further studies to evaluate performance of these NSTs in SERS imaging and photo thermal therapy are undergoing in our laboratories.

## 2.6 Acknowledgements

The authors would like to thank Chris Winkler from the Nanoparticle Characterization and Fabrication Laboratory (NCFL) for assistance with nanoparticles characterization and imaging.

## 2.7 References


(1) Juvé, V.; Cardinal, M. F.; Lombardi, A.; Crut, A.; Maioli, P.; Pérez-Juste, J.; Liz-Marzán, L. M.; Del Fatti, N.; Vallée, F. *Nano Lett.* **2013**, *13*, 2234.
(2) Cai, W.; Gao, T.; Hong, H.; Sun, J. *Nanotechnol. Sci. Appl.* **2008**, 10.2147/NSA.S3788.
(3) Ng, V. W. K.; Berti, R.; Lesage, F.; Kakkar, A. *J. Mater. Chem. B* **2013**, *1*, 9.
(4) Xie, J.; Lee, J. Y.; Wang, D. I. C. *Chem. Mater.* **2007**, *19*, 2823.
(5) Becker, A.; Hessenius, C.; Licha, K.; Ebert, B.; Sukowski, U.; Semmler, W.; Wiedenmann, B.; Grotzinger, C. *Nat. Biotechnol.* **2001**, *19*, 327.
(6) Jain, P. K.; El-Sayed, I. H.; El-Sayed, M. A. *Nano Today* **2007**, *2*, 18.
(7) Smith, A. M.; Mancini, M. C.; Nie, S. *Nat. Nanotechnol.* **2009**, *4*, 710.
(8) Moskovita, M. In *Surface-Enhanced Raman Scattering: Physics and Applications*; Kneipp, K., Moskovits, M., Kneipp, H., Eds.; Springer: 2006.
(9) Kwon, K.; Lee, K. Y.; Lee, Y. W.; Kim, M.; Heo, J.; Ahn, S. J.; Han, S. W. *J. Phys. Chem. C* **2007**, *111*, 1161.
(10) Talley, C. E.; Jusinski, L.; Hollars, C. W.; Lane, S. M.; Huser, T. *Anal. Chem.* **2004**, *76*, 7064.
(11) Li, J.; Zhou, J.; Jiang, T.; Wang, B.; Gu, M.; Petti, L.; Mormile, P. *Phys. Chem. Chem. Phys.* **2014**, *16*, 25601.
(12) Xie, J.; Zhang, Q.; Lee, J. Y.; Wang, D. I. C. *ACS Nano* **2008**, *2*, 2473.
(13) Lohse, S. E.; Burrows, N. D.; Scarabelli, L.; Liz-Marzán, L. M.; Murphy, C. J. *Chem. Mater.* **2014**, *26*, 34.
(14) Hsiangkuo, Y.; Christopher, G. K.; Hanjun, H.; Christy, M. W.; Gerald, A. G.; Tuan, V.-D. *Nanotechnology* **2012**, *23*, 075102.
(15) Yuan, H.; Liu, Y.; Fales, A. M.; Li, Y. L.; Liu, J.; Vo-Dinh, T. *Anal. Chem.* **2013**, *85*, 208.
(16) Gao, Y.; Li, Y.; Chen, J.; Zhu, S.; Liu, X.; Zhou, L.; Shi, P.; Niu, D.; Gu, J.; Shi, J. *Biomaterials* **2015**, *60*, 31.
(17) Dam, D. H. M.; Culver, K. S. B.; Kandela, I.; Lee, R. C.; Chandra, K.; Lee, H.; Mantis, C.; Ugolkov, A.; Mazar, A. P.; Odom, T. W. *Nanomedicine*, *11*, 671.
(18) Dam, D. H. M.; Lee, J. H.; Sisco, P. N.; Co, D. T.; Zhang, M.; Wasielewski, M. R.; Odom, T. W. *ACS Nano* **2012**, *6*, 3318.
(19) Chen, R.; Wu, J.; Li, H.; Cheng, G.; Lu, Z.; Che, C.-M. *Rare Metals* **2010**, *29*, 180.
(20) Palantavida, S.; Tang, R.; Sudlow, G. P.; Akers, W. J.; Achilefu, S.; Sokolov, I. *J. Mater. Chem. B* **2014**, *2*, 3107.
(21) Manickavasagan, A. In *Imaging with Electromagnetic Spectrum: Applications in Food and Agriculture*; Manickavasagan, A., Jayasuriya, H., Eds.; Springer: 2014.
(22) Clancy, M. K. In *Cancer Theranostics*; Wang, X. C. a. S., Ed.; Oxford: 2014.
(23) Khoury, C. G.; Vo-Dinh, T. *J. Phys. Chem. C* **2008**, *112*, 18849.
(24) Ray, P. C.; Yu, H.; Fu, P. P. *J. Environ. Sci. Health C: Environ. Carcinog. Ecotoxicol. Rev.* **2009**, *27*, 1.
(25) Xue, B.; Wang, D.; Zuo, J.; Kong, X.; Zhang, Y.; Liu, X.; Tu, L.; Chang, Y.; Li, C.; Wu, F.; Zeng, Q.; Zhao, H.; Zhao, H.; Zhang, H. *Nanoscale* **2015**, *7*, 8048.
(26) Nikoobakht, B.; El-Sayed, M. A. *Chem. Mater.* **2003**, *15*, 1957.
(27) Nehl, C. L.; Liao, H.; Hafner, J. H. *Nano Lett.* **2006**, *6*, 683.
(28) Ray, T. R.; Lettiere, B.; de Rutte, J.; Pennathur, S. *Langmuir* **2015**, *31*, 3577.

(29) Khanal, S.; Casillas, G.; Bhattarai, N.; Velázquez-Salazar, J. J.; Santiago, U.; Ponce, A.; Mejía-Rosales, S.; José-Yacamán, M. *Langmuir* **2013**, *29*, 9231.
(30) Lin, S.; Wiesner, M. R. *Langmuir* **2012**, *28*, 11032.
(31) Burns, C.; Spendel, W. U.; Puckett, S.; Pacey, G. E. *Talanta* **2006**, *69*, 873.
(32) Badawy, A. M. E.; Luxton, T. P.; Silva, R. G.; Scheckel, K. G.; Suidan, M. T.; Tolaymat, T. M. *Environ. Sci. Technol.* **2010**, *44*, 1260.
(33) Pamies, R.; Cifre, J. G. H.; Espín, V. F.; Collado-González, M.; Baños, F. G. D.; de la Torre, J. G. *J. Nanopart. Res.* **2014**, *16*, 2376.

## 2.8 Supplemental Information

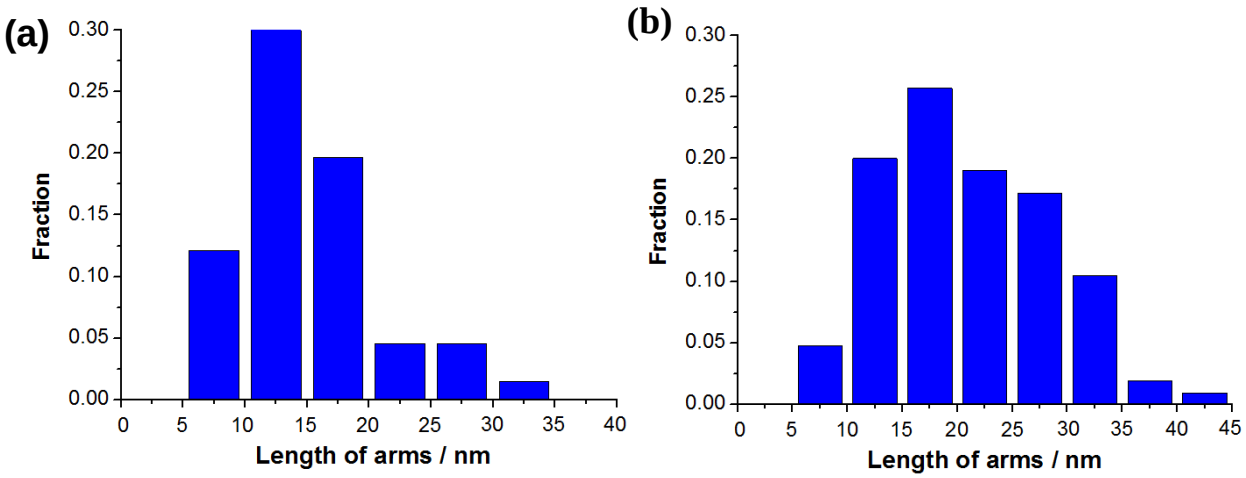


**Figure S1**. Histograms depicting Au NST branch length from TEM analysis of (a) one-step and (b) two-step reactions.

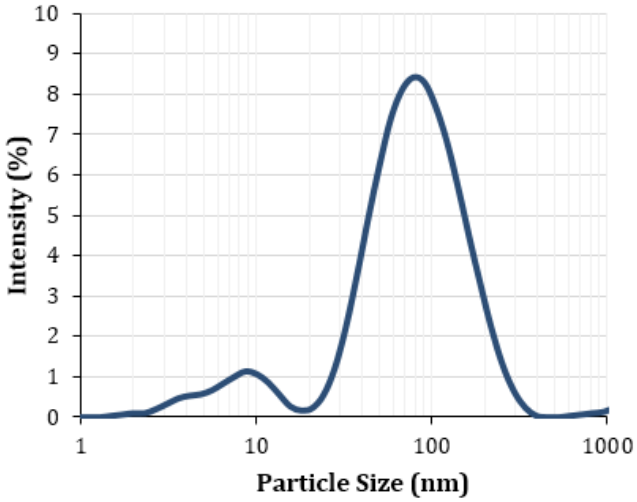


**Figure S2**. Hydrodynamic size of the Au NSTs prepared through the two-step reaction.

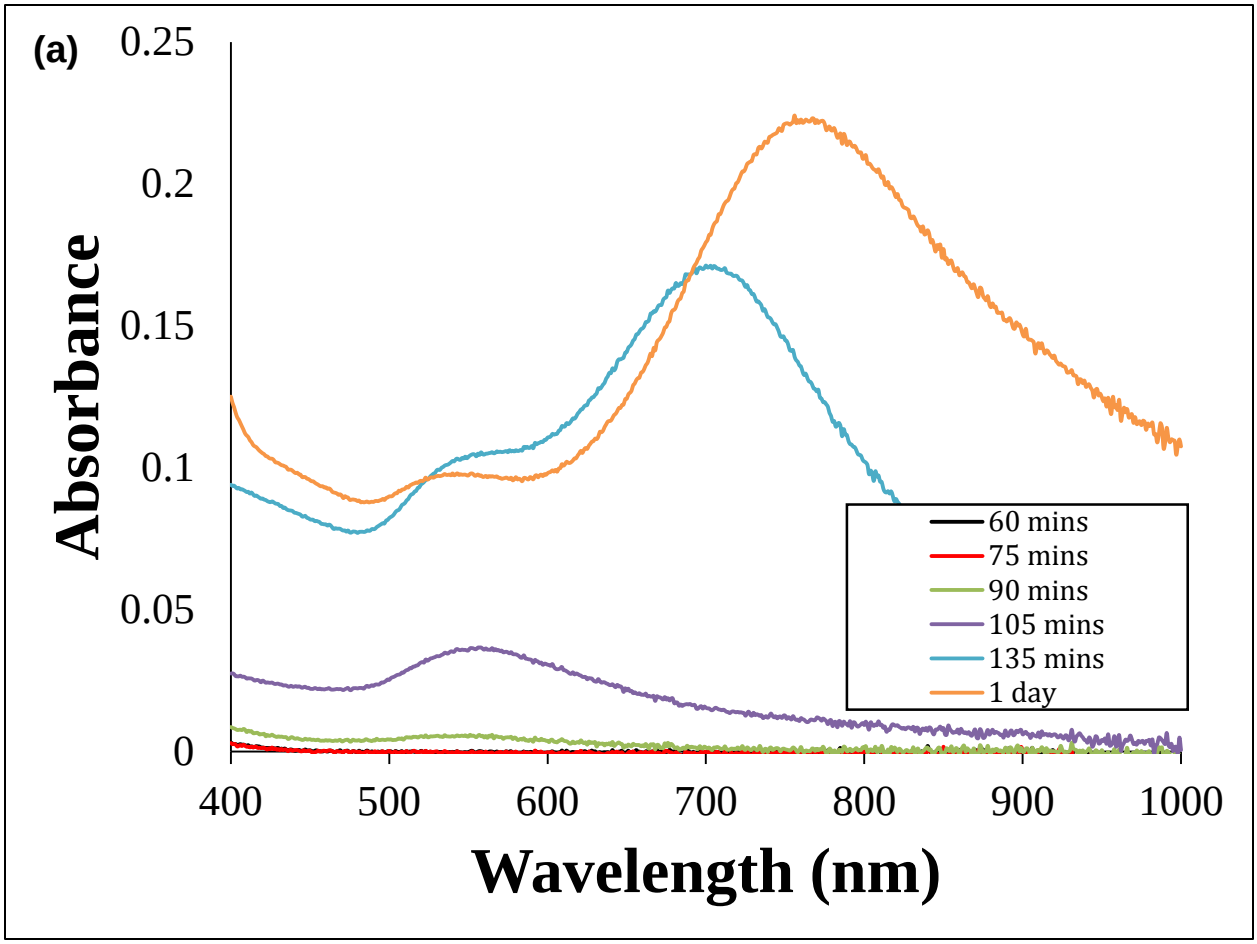


**(b)**

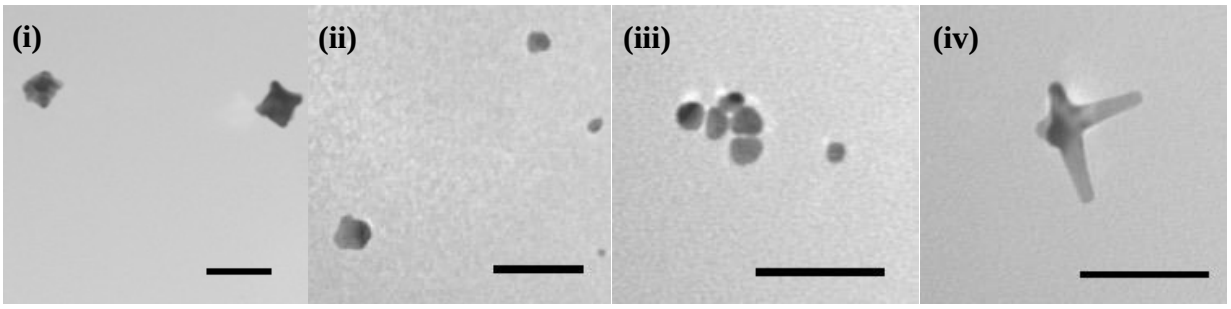


**Figure S3**. (a) Evaluation of the LSPR during Au NST formation. Values indicate elapsed time since the first addition of $HAuCl_4$ to HEPES. The second addition occurs 80 minutes after the start of the reaction. (b) TEM images of Au NSTs prepared using a two step approach. Images correspond to time after the start of the reaction: (i) 75 mins (ii) 105 mins (iii) 135 mins (iv) one day (scale bar = 50 nm).

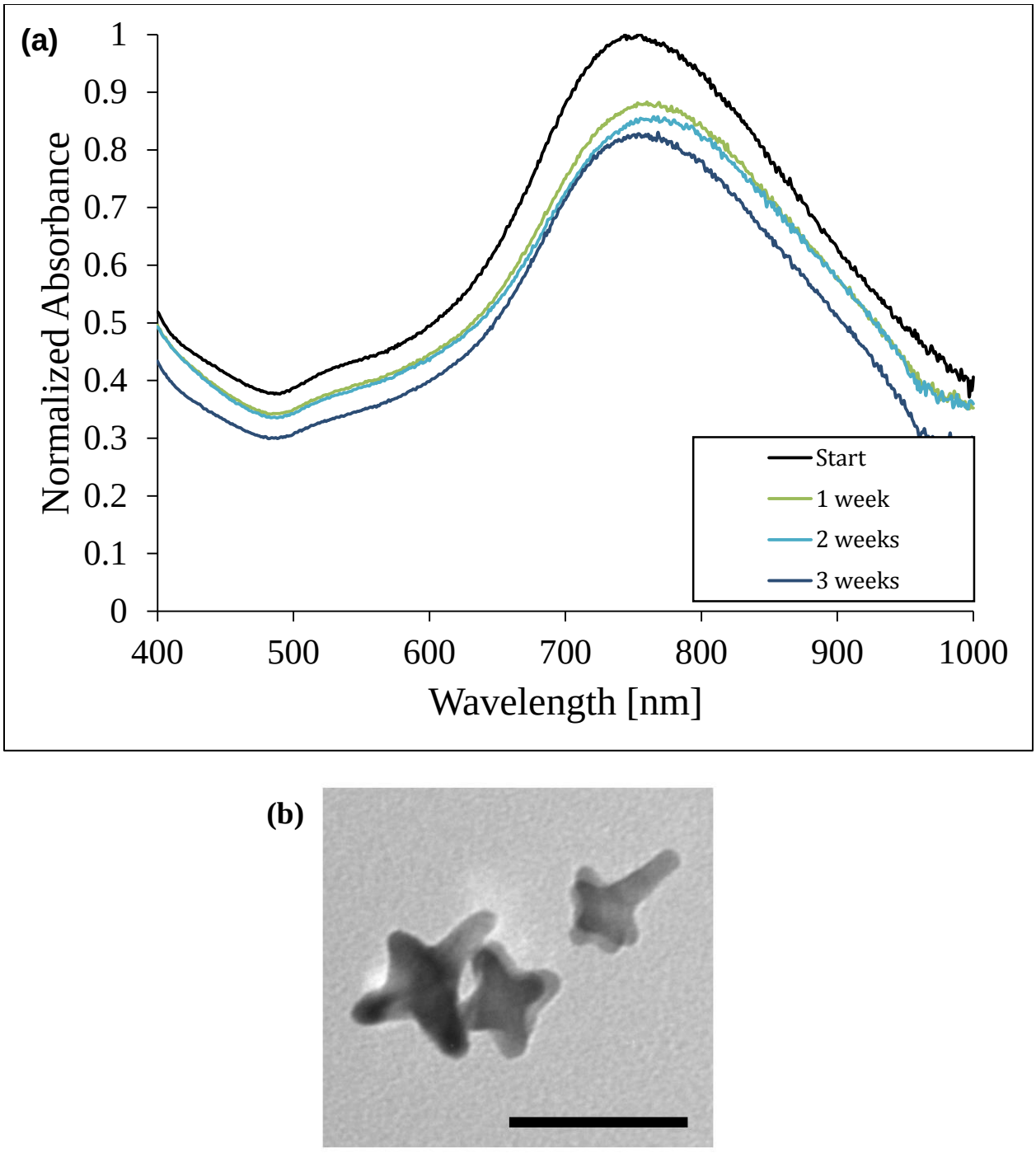


**Figure S4.** (a) UV-Vis spectra of Au NSTs in D.I. water. Reported values are normalized by the O.D. of the nanoparticle suspension. (b) Representative TEM image of Au NSTs sample, prepared using two-step synthesis, after three-week suspension in D.I. water (scale bar = 50 nm).

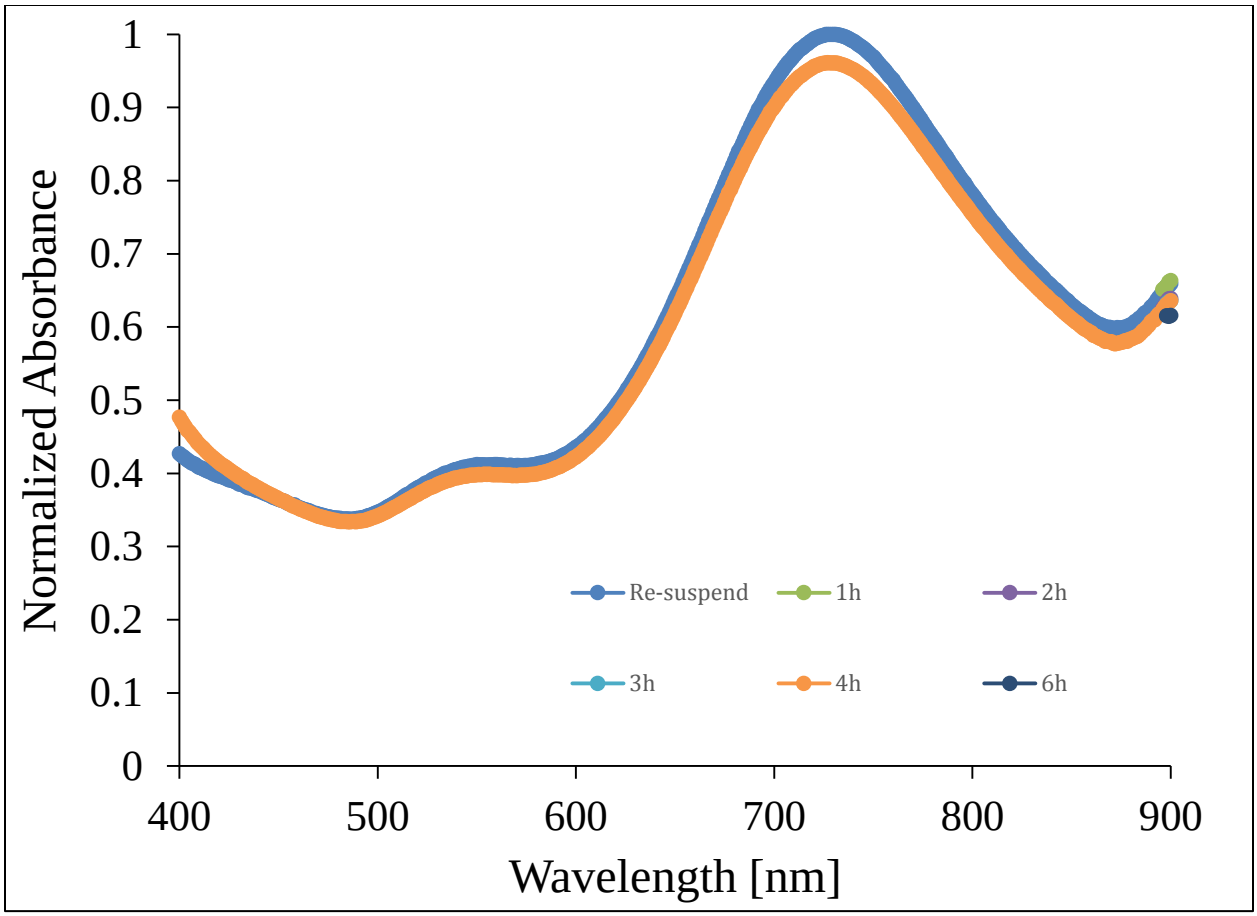


**Figure S5**. UV-Vis spectra of Au NSTs re-suspended in 1× PSB. Reported values are normalized by the O.D. of the nanoparticle suspension.

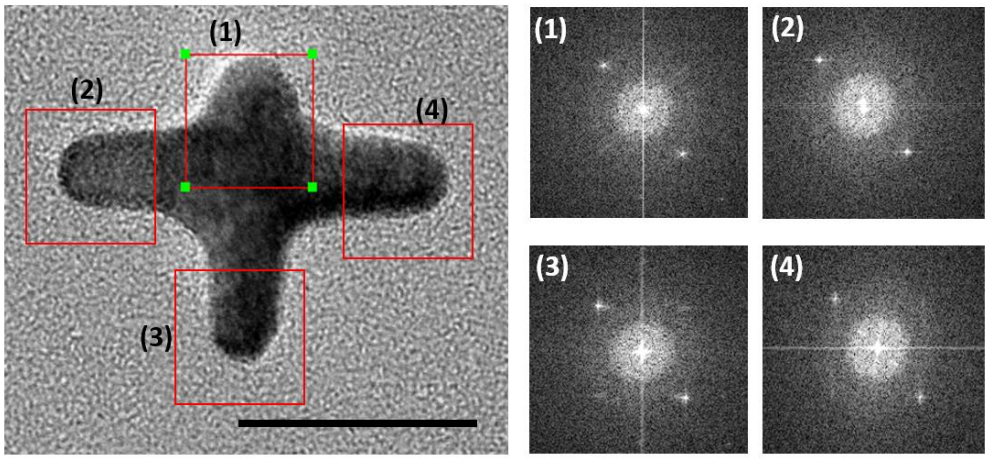


**Figure S6**. FFT diffraction of single Au NST at its four arms. Each arm exhibits an identical FFT pattern.

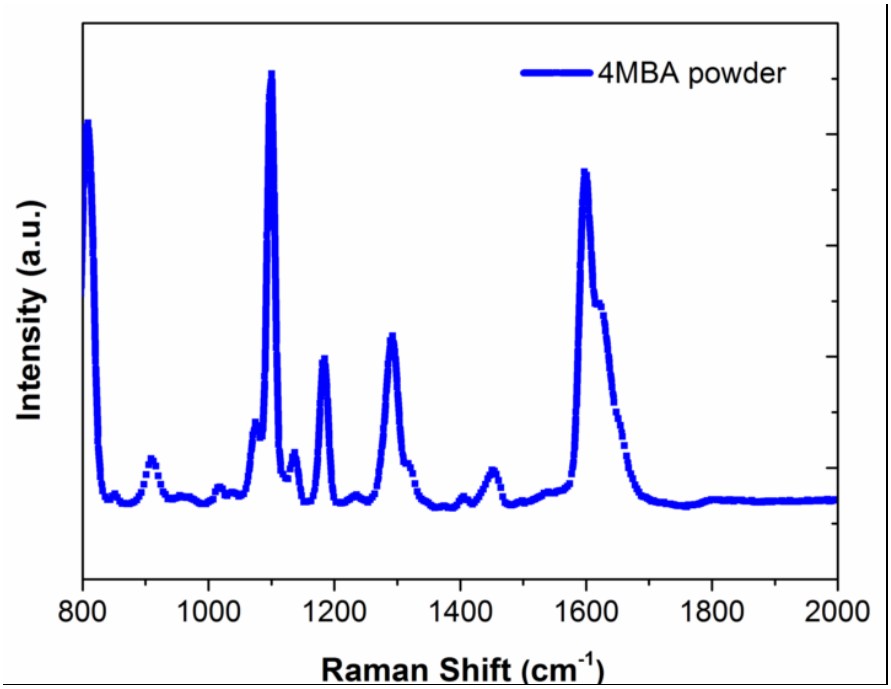


**Figure S7**. Raman signal of pure 4-MBA powder.

# Chapter 3. Repeat-protein mediated synthesis of gold nanoparticle: Effect of protein shape on the morphological and optical properties

Xi Geng and Tijana Z. Grove

Reprinted with permission from X. Geng, and T.Z Grove, *RSC Adv.*, **2015**, *5*, 2062-2069.


**Attributions:** XG performed all experiments and was the primary writer of the manuscript. TZG supervised the research project and provided technical insight during experimentation and data analysis, TZG also assisted in writing and editing the manuscript.

## 3.1 Abstract

Repeat proteins have recently emerged as promising candidates for the modular design of biohybrid platforms with a high degree of tunability. Consensus sequence tetratricopetide repeat (CTPR) proteins with increasing number of repeats were designed to probe the effects of protein shape on the morphology and resulting physicochemical properties of plasmonic gold nanoparticles. In a synthetic procedure analogous to the biomineralization processes in nature, CTPRs with 3, 6, or 18 tandem repeats were used as both the stabilizing and shape-directing agent. The electronic microscopy and spectroscopic studies indicate that both the $[HAuCl_4]$/[CTPR] ratio and the CTPR shape have dramatic implications on the morphology and plasmon absorbance of the as-synthesized Au NPs. Induced plasmon ellipticity and fluorescence quenching data provide further evidence for the molecular interaction between CTPR and Au NPs or $HAuCl_4$ species. Overall, this work elucidated the effects of CTPR protein shape on the morphology and plasmonic properties of Au NPs, which will further guide the rational design of modular protein based bioconjugate frameworks for colorimetric and enantiomeric biosensors.

## 3.2 Introduction

Over the past few decades, versatile synthetic approaches towards inorganic nanoparticles with well-defined structures and precisely tailored physicochemical properties have been extensively studied and developed.[1] An area of growing interest is the harnessing of biomolecules for the synthesis and assembly of nanoparticles under mild ambient conditions for biosensing and catalysis.[2,3] Bioenabled strategies draw inspiration from nature where materials with unique structures, compositions, and functions are achieved in the process of biomineralization through the interaction of inorganic material with bioscaffold such as peptides[4-10], proteins[11-17] and nucleic acids.[18-24]

In particular, extensive research has focused on the biomimetic synthesis of Au NPs as the fundamental building blocks for the construction of catalytic, optoelectronic and biosensing devices.[12,25,26] To date, a broad spectrum of natural and recombinant proteins were exploited as biotemplates for the synthesis of Au NPs with tailored structures.[11-14,16] In a representative example, anisotropic Au NPs arrays have been integrated on the self-assembled protein clathrin Hub-His6 through a two-step, seed-mediated growth process. In another study, a tetrapod shape was achieved through the coordination of in-situ prepared Au nanoclusters with the trimeric gp5-His6 protein.[11] More recently, proteins were used for the directed growth of highly fluorescent Au nanoclusters with discrete sizes.[27] While these examples illustrate new avenues for the synthesis of inorganic nanoparticles and their assemblies, a thorough understanding of the structure and function of proteins as well as the interactions at the bio-abio interface is one of the key steps to tuning the size, shape, composition, and functionality of the final biohybrid nanomaterials.

In this work we exploit designed repeat proteins for bioenabled synthesis of chirooptical Au NPs. Repeat proteins are composed of multiple tandem repeats of small structural motif.

Their modular architecture is based on well-defined local interactions between neighboring repeats. The structure, stability, and function of repeat proteins can be modulated in a predictable manner by simple combination of repeats with desired properties,[28] making this class of proteins especially well-suited for biotechnological applications.

Protein arrays consisting of multiple repeats of the 34 amino acid helix-turn-helix **c**onsensus sequence **t**etratrico**p**eptide **r**epeat, CTPR, have recently emerged as promising candidates for the modular design of biohybrid platforms with a high degree of tunability.[29-34] The simplest repeat protein system is one in which all the repeats within a protein are identical, such as the CTPRn protein array, where n stands for the number of tandem repeats. Such CTPRn protein can therefore be treated as a simple homopolymeric molecule, where the monomer is a single repeat helix-turn-helix motif 34 amino acids in length. CTPRn arrays form a superhelical structure, where eight repeats (n=8) comprise one full turn of the superhelix.[35]

The advantage of the modular architecture is that it is possible to design proteins that are chemically identical but differ in size and shape. Herein, we use this property of repeat proteins to explore the effects of protein shape on size distribution, morphology, and plasmonic optical properties of Au NPs. Although much is known about how protein and peptide primary sequences affect the nucleation and growth of Au NPs,[8] the influence of protein structure and shape is not well understood. To this end, we engineered CTPRn arrays, where n= 3, 6, or 18, with identical surface chemistry, but distinct shapes expressed as aspect ratio (***Figure 3.1c***). These proteins were then used in the one-step synthesis of CTPR-Au NPs conjugates.

In this report, we present a green synthesis strategy for the fabrication of repeat protein-stabilized Au NPs. CTPR proteins with varied number of repeating units were employed as both the stabilizer and structure-directing agent for the construction of protein-Au NPs conjugates.

Direct interactions between protein and Au precursor were observed in fluorescence quenching experiments. The shape and particle size of Au NPs is closely correlated to the concentration and the length of the CTPRn array as seen in TEM images.

Accordingly, the plasmon absorption of the resultant CTPR-stabilized Au NPs could be tuned spanning a wide wavelength range. Circular dichroism analysis further demonstrated that CTPR proteins retained their secondary structure after conjugation with Au NPs. Interestingly, induced chirality was also detected in the region of the plasmonic absorption of CTPR-Au NPs.

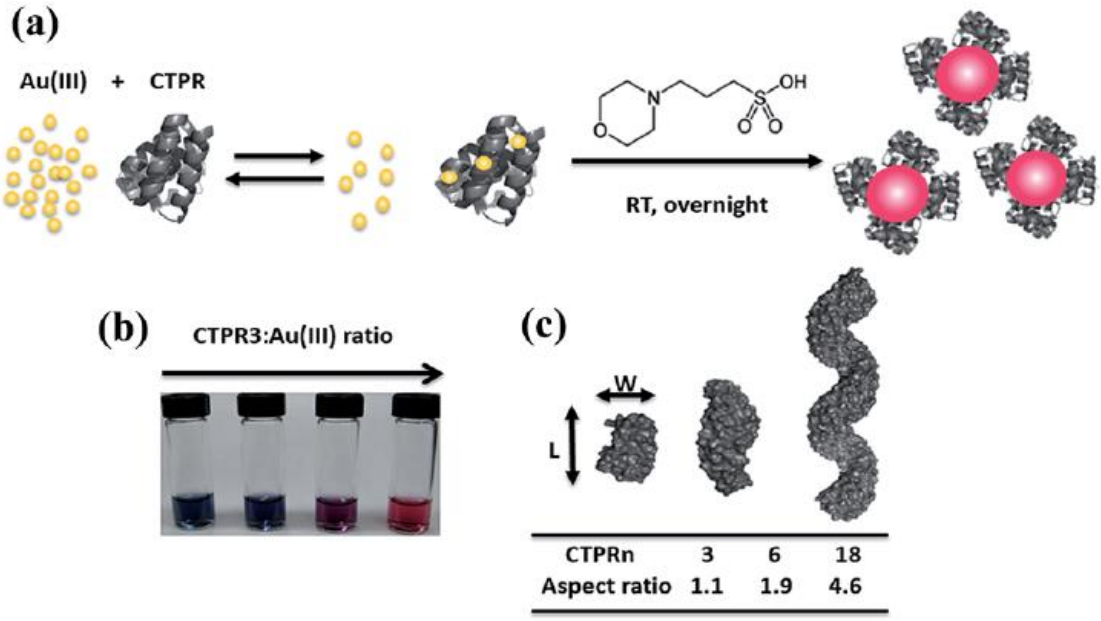


**Figure 3.1** (a) Schematic illustration of the synthesis of CTPR stabilized Au NPs. Gold precursor ions are mixed with CTPR protein at predefined concentration ratios followed by the addition of the reducing agent. (b) Photograph of CTPR3 stabilized Au colloids. Localized surface plasma resonance (LSPR) blue-shifts with increasing [CTPR3]:[Au(III)] ratio. (c) Cartoon representation of CTPR3, 6 and 18 with different aspect ratios but identical surface residues. This cartoon was prepared from X-ray coordinates[35] using Pymol. (http://www.pymol.org/)

## 3.3 Experimental

### 3.3.1 Chemicals

Chloroauric acid (99.9%) was purchased from Strem Chemicals Inc. 3-(N-morpholino)propanesulfonic acid (MOPS) were acquired from MP biomedicals, LLC. Other reagents were purchased from Sigma-Aldrich and Fisher Chemicals. All reagents were used as received without further purification. Deionized water (18 MΩ/cm, Millipore Milli-Q) was exclusively used for preparing all aqueous solutions and for all the rinsing procedures.

### 3.3.2 Expression of CTPR proteins

CTPR proteins with 3, 6 and 18 tandem repeating units were synthesized through recombinant bacterial expression technology as described previously (***Figure S1***).[29,31] Synthetic genes for the desired protein in pPROEx vector, coding for N-terminal $(His)_6$ tag and ampicillin resistance, were transformed into E.Coli BL21(DE3) cells and cultured overnight at 37°C on agar plates. One single colony was selected and incubated overnight in 50 mL of Luria−Bertani (LB) media containing 100 μg/mL of ampicillin. 10ml of overnight cultures were then dispensed into 1 L of LB media supplemented with 100 μg/mL ampicillin. The cells were grown in an incubator-shaker (250 rpm) at 37 °C until the optical density ($OD_{600}$) reached 0.6-0.8. Expression of CTPR3 was induced with 1mM isopropyl β-D-thiogalactoside (IPTG) followed by 5 h expression at 37 °C, whereas CTPR6 and 18 were expressed at 18 °C for 16 h in an analogous manner. The cells were harvested by centrifugation at 5,000 rpm for 20 min and the pellets were frozen at -80 °C until purification.

### 3.3.3 Purification of CTPR proteins

The cell pellets were resuspended in lysis buffer consisting of 50 mM Tris, 300mM sodium chloride and 0.1 wt% Tween 20. After 2 min sonication at 30% power using a microtip and Mison sonicator, lysed cells were centrifuged at 16,000 rpm for 30 min and the protein supernatant was purified using standard Ni-NTA affinity purification protocol. The N-terminal

hexahistidine tag was then cleaved from the CTPR proteins using TEV protease. The collected proteins were further purified by Akta Prime Plus size exclusion chromatography using Superdex 75 16/600 or 200 16/600 Prep Grade column in 150mM sodium chloride and 50 mM sodium phosphate buffer at pH 8 with a flow rate of 0.5ml/min. As a final step, the aqueous solutions of CTPRs were dialyzed against 10mM phosphate buffer three times at 4 °C using a dialysis membrane with molecular weight cutoff of 3k or 10k Da.

### 3.3.4 Preparation of CTPR-stabilized gold nanoparticles

The protein-Au NP conjugates were synthesized via the approach depicted in ***Figure 3.1a***. In a typical procedure, 100µl of 10mM phosphate buffer solution of CTPRn was added into 0.5 ml of 0.4 mM aqueous solution of chloroauric acid. Subsequently, 0.4 ml of 100 mM MOPS pH 7.4 was added to the solution at ambient conditions. A series of CTPR-Au NPs samples were prepared in the same way where the concentration of $HAuCl_4$ and MOPS was held constant, while the ratio of $[HAuCl_4]$/ [CTPR] was adjusted to 1000, 400, 100 and 20. The samples are denoted as CTPRn-Au-m, where n is the number of tandem CTPR repeats and m is the ratio of $[HAuCl_4]$/[CTPR] (n = 3, 6, 18; m = 1k, 400, 100, 20).

### 3.3.5 Instrumentations

The transmission electron microscopy (TEM) analysis was performed on a Philips EM420 at an accelerating voltage of 120 kV. TEM samples were prepared by applying a 7 µl sample solution on 300 mesh carbon-coated Cu grids (EM Science), followed by drying overnight before observation. The particle-size distribution was estimated by measuring the size of approximately 100 NPs at different regions using Image J.

The UV-Vis spectra of CTPR-Au NPs were monitored using an Agilent Cary 100 Bio UV-Vis spectrophotometer. All UV-vis measurements were conducted in 1cm path length quartz

cuvette at room temperature. The fluorescence quenching experiments were carried out at room temperature and 50 °C on an Agilent Cary Eclipse fluorimeter using the 1 cm path length quartz cuvette. Briefly, 2 μM CTPR3 protein was titrated every 10min with 2 μl of 2 mM $HAuCl_4$ aqueous solution.

Circular dichroism data were acquired using samples containing 0.5-2 μM protein on a Jasco J-815 CD spectrometer. Far UV CD (190nm-280nm) spectra were recorded at 25 °C to assess the secondary structure of CTPR proteins. Each sample was recorded three times from 190-260 nm in a 2 mm pathlength quartz cuvette, and averaged. Data were collected using a 1 nm bandwidth, 2 nm data pitch, and a data integration time of 1 s. The CD intensities are expressed in terms of [θ] and were normalized to units of mean residue ellipticity for all samples ($deg \times cm^2 \times dmol^{-1}$). The induced chirality of CTPR-Au samples was recorded by monitoring the ellipticity in the visible region (400 nm - 650 nm) using a 10 mm pathlength cuvette.

## 3.4 Results and Discussion

### 3.4.1 Design and construction of CTPR stabilized Au NPs

Our strategy for repeat-protein enabled synthesis of Au NPs is illustrated in ***Figure 3.1***. In this work we exploit the modular construction of CTPR proteins to explore the effects of protein shape and concentration on size distribution and morphology of plasmonic Au NPs. CTPRn arrays are composed of tandem repeats of a basic structural unit, 34 amino acids in length. In contrast to globular proteins, repeat proteins have no interactions between residues at large distance in the primary structure, which makes them much easier to engineer. The stability of individual CTPR units can be rationally manipulated, and the stability of CTPRn arrays can be predicted based on the behavior of the units from which they are composed.[28,31] This unprecedented level of control and predictability of both the structure and thermodynamic

stability means that CTPR units can be mixed and matched in a modular and predetermined fashion to design proteins with the desired properties.[36] CTPRn arrays (n=3, 6, or 18, ***Figure 3.1c***) were used in one-pot synthesis of Au NP under ambient conditions. This synthetic scheme in ***Figure 3.1a*** is analogous to the typical biomineralization process in nature where the metal ions are first sequestered with a bioscaffold at predefined concentration ratios. As observed in photographs in Figure 1b, colloidal plasmonic Au NPs are formed upon addition of a mild reducing agent, MOPS.

In a typical protein-directed synthesis, Au ions are reduced either by a strong reducing agent or by the reductive functional groups in proteins which are typically activated by increasing the pH of the solutions to alkaline. [11,27] However, the harsh reaction conditions involved in these processes often lead to an irreversible conformational change of the proteins.[37] A milder synthetic method is therefore required to preserve the structure of the proteins in the protein-directed approach. Notably, the use of Good's buffers has been explored for Au NPs synthesis that could be performed under extremely mild conditions.[16,38-41] This is crucial for one-step synthesis and functionalization of NPs with biomolecules that often do not tolerate organic solvents, wide pH range, and elevated temperatures. In the absence of CTPR protein, flower-like Au nanoparticles were generated using MOPS as the reducing agent (***Figure 3.2a***). The mean particle size was estimated to be 33.3±9.7 nm. It has been observed previously that the tertiary amine of either the piperazine or the morpholine group is capable of reducing the metal ions through formation of nitrogen centered radicals.[41] Despite the reports that piperazine ring is essential for the surface ligand mediated growth of highly branched nanoparticles, it is evident from our data that the morpholine group serves as a shape-directing agent to promote the agglomeration of primary Au seeds and the ensuing branched NP growth.

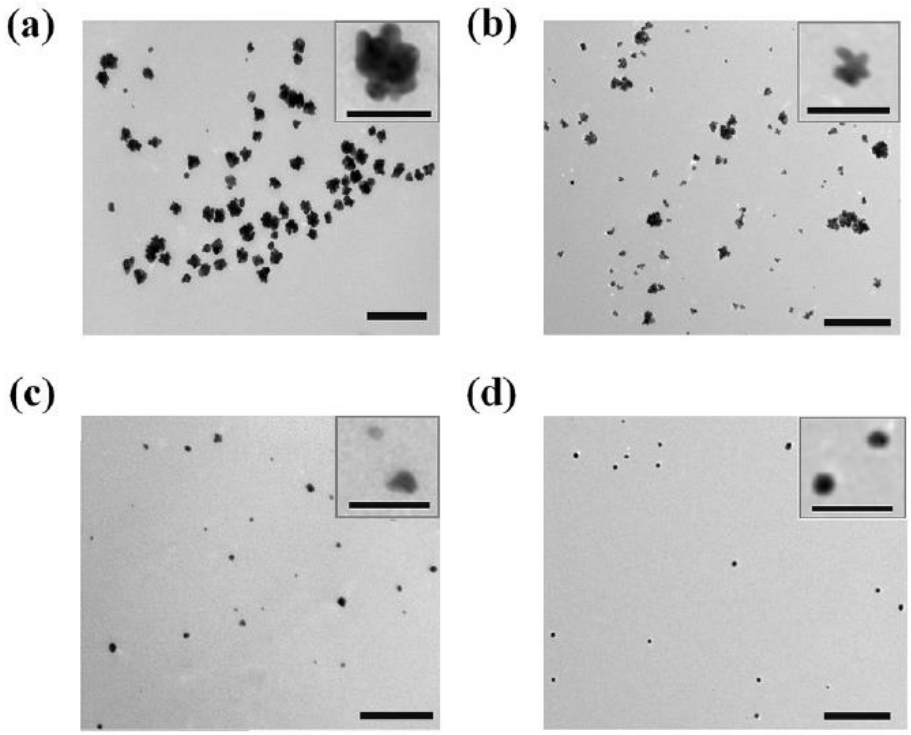


**Figure 3.2** TEM images. Au NPs synthesized as described using [$HAuCl_4$] = 0.2 mM and (a) no CTPR3 added (b) CTPR3-Au-1k (c) CTPR3-Au-100 (d) CTPR3-Au-20. (Scale bar = 200 nm) Inset: magnified TEM images with scale bar = 50 nm.

The TEM images of CTPR3-stabilized Au NPs prepared with different [$HAuCl_4$]/[CTPR3] ratios in MOPS buffer are shown in the ***Figure 3.2b-d.*** In the presence of the low concentration of CTPR3, branched or multipod-like Au NPs were produced (***Figure 3.2b***). As the concentration of protein increases, nanoparticles become less agglomerated and more spherical (***Figure 3.2d***). We speculate that the Au(III) ions are coordinated by the protein surface residues to form stable CTPR3-$HAuCl_4$ complexes thereby providing potential nucleation sites for the in-situ reduction of Au by MOPS.[42] Subsequently, the growth of Au NPs is partially suppressed by capping the Au core with CTPR3 corona. However, the excess amount of Au(III) ions located in the vicinity of the initial Au-CTPR3 complex favors the rapid growth of individual Au NPs as well as the inevitable aggregation of adjacent small Au NPs formed at the initial stage of the reaction. Although the mean particle size does not change dramatically as a

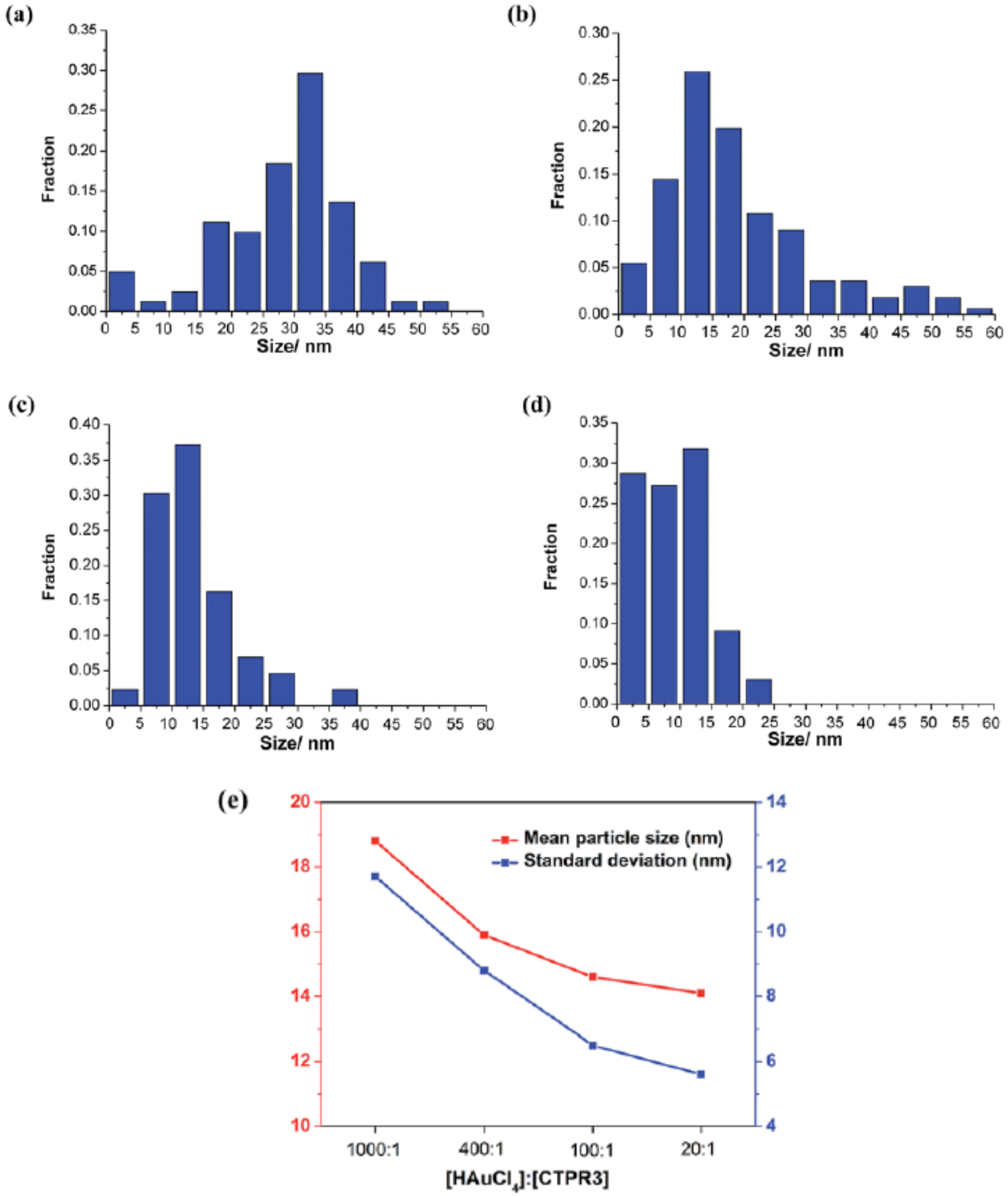


**Figure 3.3** Histograms of the size distribution of (a) Au NPs in the absence of CTPR3 (b) CTPR3-Au-1k (c) CTPR3-Au-100 (d) CTPR3-Au-20 (e) Mean particle size and standard deviation of CTPR3-Au NPs.

function of protein concentration, the size distribution becomes much narrower (***Figure 3.3e***). Agglomerated nanoclusters and highly branched NPs gradually disappeared, whereas the Au polyhedron and nanospheres are produced as CTPR3 concentration increases. We propose that increasing the amount of CTPR3 depletes the Au(III) at individual nucleation sites and hampers the overgrowth of Au NPs. In addition, CTPR protein also acts as an efficient stabilizer to inhibit the secondary nucleation and the agglomeration of Au NPs. It is noteworthy that CTPR3 template does not contain cysteine (thiols) or histidine (imidazole) residues that have been previously observed to bind metal NP surfaces.[43,44] However, Hill et al. reported that resilin-mimetic protein uses tyrosine (Tyr) residues for organization of Au NPs on its surface.[16] Recent molecular dynamics simulations also revealed strong binding affinity of Tyr for Au NPs.[45] Thus we reasoned that CTPR protein, where each repeat contains seven aromatic Tyr and one tryptophan (Trp) residues, will interact with gold species during the biomimetic synthesis. To gain more insight into the molecular level interactions of CTPRn arrays and gold, we have performed fluorescence quenching experiments.

### 3.4.2 Molecular interaction between CTPR and Au(III) and Au NPs

Each CTPR repeat contains six tyrosine and one tryptophan for total of 21, 42, and 126 surface-exposed aromatic residues for CTPR3, CTPR6, and CTPR18 respectively. Thus all CTPR proteins exhibit excitation and emission peaks at 275 and 338 nm respectively. Conveniently, these aromatic side-chains are built-in fluorescent probes of protein-ligand interactions. The pronounced quenching of CTPR3 fluorescence (***Figure 3.4a***) confirms that both Au(III) ions and Au NP interact with the protein surface, consistent with the proposed reaction scheme in ***Figure 3.1a***. To closer inspect the molecular mechanism of fluorescence quenching, we titrated Au(III) ions into the solution of CTPR3 and observed fluorescence

quenching as a function of Au(III) concentration ***Figure 3.4b.*** The fluorescence signal was corrected due to the inner filter effect by multiplying the observed fluorescence $F_{obs}$ with appropriate factors as shown in the equation:

$$F_{ideal}(\lambda_{ex},\lambda_{em}) = F_{obs}(\lambda_{ex},\lambda_{em})CF_p(\lambda_{ex})CF_s(\lambda_{em}) \quad (1)$$

$$= F_{obs}(\lambda_{ex},\lambda_{em})10^{(A_{ex}+A_{em})/2}$$

where $CF_p$ , $CF_s$ represents the correction factors for the total absorbance $A_{ex}$ and emission $A_{em}$ at the wavelength of $\lambda_{ex}$, $\lambda_{em}$, respectively.[46]

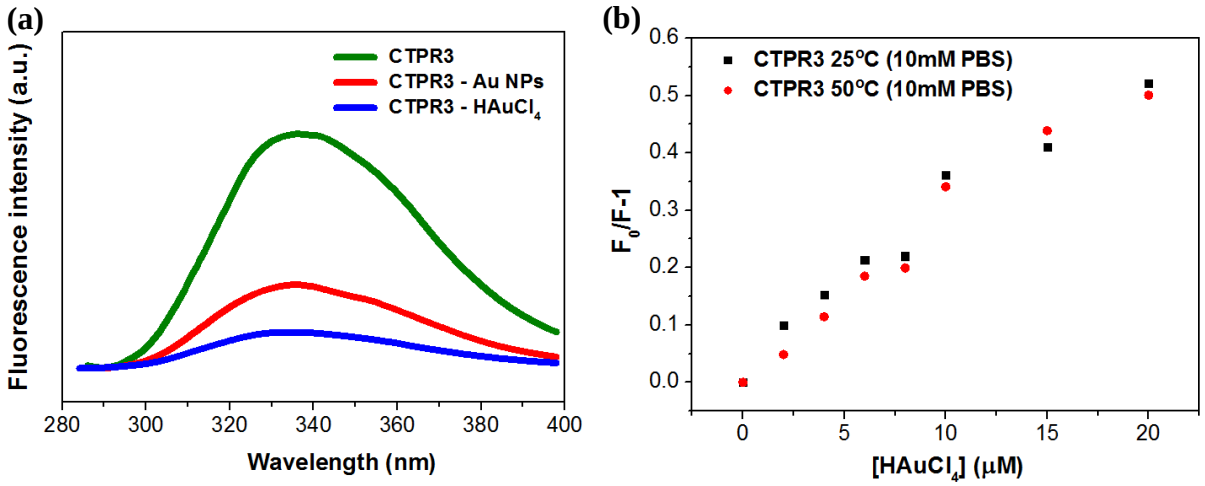


**Figure 3.4** Fluorescence spectra of (a) CTPR3, CTPR3-$HAuCl_4$ (100:1), CTPR3-Au-100 colloidal solution (b) Corrected fluorescence quenching profile of CTPR3 by $HAuCl_4$ in 10mM PBS at 25°C and 50°C. (Error bars are smaller than symbols.)

Because CTPR proteins are stable under a relatively broad range of temperatures,[28] we can readily change the solution conditions to further probe binding of Au(III) to CTPR. To distinguish between a collisional and static mechanism of fluorescence quenching, we performed identical titration experiments at room temperature and 50 °C. For a purely collisional mechanism of fluorescence quenching we expected to observe a steeper quenching curve due to the faster diffusion rate at elevated temperatures. Conversely, for purely static fluorescence quenching, the quenching curve will have a flattened slope arising from the dissociation of

weekly bound fluorophore-quencher complex at elevated temperatures.[47] The slope of the quenching curve does not change with the temperature implying that the interaction of Au(III) with CTPR could be explained by a combination of static and dynamic quenching.

The Stern-Volmer quenching constant, $K_{SV,}$ was estimated to be $2.7\times10^{4}$ $M^{-1}$ by fitting the data in ***Figure 3.4b*** to equation (2). Approximating that the fluorescence lifetime, $\tau_{0,}$ for biomacromolecules is around $5\times10^{-9}$ s,[16] the bimolecular quenching constant, $k_{q,}$ for CTPR3 and Au(III) ions was calculated to be $5.3\times10^{12}$ $M^{-1}s^{-1}$. This value is two orders of magnitude higher than $2\times10^{10}$ $M^{-1}s^{-1}$ for a typical diffusion controlled quenching process consistent with the formation of the complex between CTPR3 and Au(III) species.

$$[\frac{F_0}{F}] = 1 + K_{sv}[Q], \qquad K_{sv} = k_q\tau_0[Q] \tag{2}$$

**3.4.3 Effects of increasing length of CTPRn array on the growth and optical properties of Au NPs**

One may make an argument that extending a protein sequence could simply increase the number of Au binding sites. Indeed, studies of the mechanism and kinetics of NP formation using tyrosine-based oligopeptides clearly showed that with increasing number of amino acid residues, the size of the NPs increased and polydispersity decreased.[48] However, the relationship between protein length and morphologies of NPs is more elusive. For this purpose, CTPR arrays with increasing numbers of repeats were used in the synthesis of Au NPs. Previous hydrodynamic studies of CTPR arrays established that these proteins behave as rigid rods in solution, i.e. their molecular dimensions in solutions are identical to that observed in the high-resolution crystal structure.[34] Thus we will describe the protein shape with the aspect ratio calculated from the X-ray coordinates.

Increasing the protein concentration in the reaction mixture results in a transition of NP morphology from larger branched aggregates towards smaller globular particles regardless of CTPR array aspect ratio (***Figure S2***). However, distinct oligomeric nanostructures including fused dimer and trimers are observed for CTPR6-Au-20 samples (***Figure 3.5***). These morphologies were not observed in the presence of same concentration of CTPR3 or CTPR18. This result implies that CTPR6 may serve as a scaffold for the controlled arrangement of one-dimensional nanostructures analogous to what has been previously achieved with the DNA origami.[18,20,21] Additionally, we also observed that further increase in the concentration of the total amount of CTPR repeat does not lead to the smaller particle size and narrower size distribution for CTPR18-Au-100 as compared to CTPR3-Au-100, and CTPR6-Au-100 (***Table S2***).

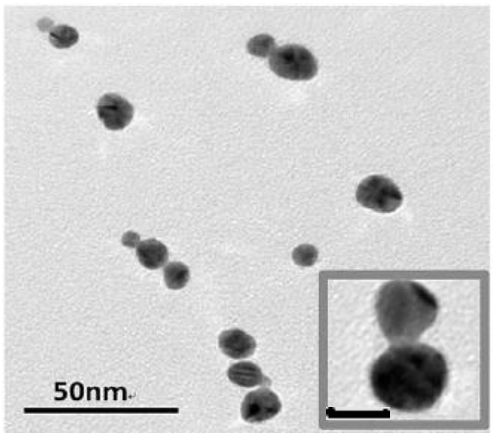


**Figure 3.5** CTPR6-Au-20 oligomers. (Inset: fused CTPR-Au NPs, scale bar = 10 nm).

UV-vis spectroscopy was used to monitor the surface plasmon resonance band of CTPR-Au NP. A bathochromic shift was observed as the protein concentration decreases (***Figure 3.6***). For instance, CTPR3-Au-1k displayed a wavelength of maximum absorbance $\lambda_{max}$ at 591 nm. Upon the addition of an increased amount of CTPR3, the $\lambda_{max}$ changed to 532 nm for CTPR3-Au-20, which is the characteristic absorption of spherical Au NPs. It is well-established that the

longitudinal localized surface plasmon resonance (LSPR) is determined by the size as well as the aspect ratio of anisotropic NPs.[49, 50] The substantial LSPR red-shift for Au prepared in the presence of low concentration of CTPR could be ascribed to the morphological features such as elongated shapes, branched tips, etc.[38] This result is in good agreement with the representative TEM images showing branched or agglomerated morphologies at low protein concentrations. Likewise, the $\lambda_{max}$ of CTPR6 or CTPR18 capped Au followed a similar concentration dependence trend. As shown in ***Figure 3.6a-b*** and ***S3***, narrower SPR peaks and substantial decrease in $\lambda_{max}$ were obtained when the Au NPs were prepared under the condition of low [$HAuCl_4$]/[CTPR] ratio, i.e. increased protein concentration.

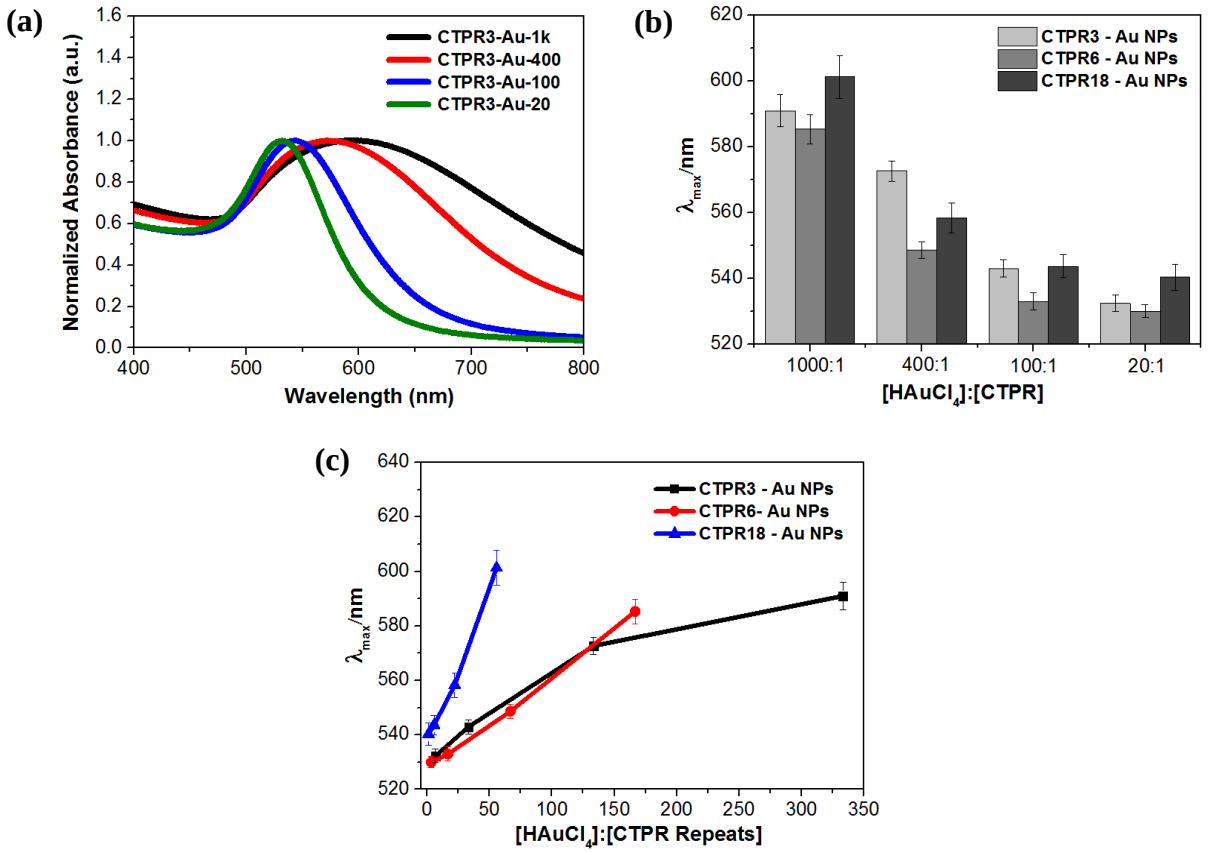


**Figure 3.6** (a) Normalized UV-vis spectra of Au NPs synthesized in the presence of CTPR3: CTPR3-Au-1k, CTPR3-Au-400, CTPR3-Au-100 and CTPR3-Au-20 NPs (b) Maximum plasmon absorption wavelength of CTPR-Au NPs as a function of [$HAuCl_4$]/[CTPR] and (c) as a function of [$HAuCl_4$]/[number of CTPR repeats]. (e.g. the concentration of [number of CTPR repeats] equals 3 fold of [CTPR3], since each CTPR3 protein is composed of 3 repeats.)

We further investigated the influence of the protein aspect ratio on the SPR of Au NPs by plotting the $\lambda_{max}$ as a function of the ratio of [$HAuCl_4$]/[CTPR repeats]. If variation in morphology and UV-Vis spectra are due only to increased number of nucleation sites, we expect the normalized data to follow an identical concentration trend for CTPR3, CTPR6, and CTPR18. However, two different trends of LSPR band variation were identified. As seen in the ***Figure 3.6c***, $\lambda_{max}$ is more sensitive to the protein concentration for CTPR18 in comparison with CTPR3 and CTPR6. This SPR shift dependence for CTPR18-Au may be correlated to the large aspect ratio of 4.6 and the elongated superhelical structure adopted by CTPR18.[30] We propose that more spherical CTPR3 and 6, aspect ratio of 1.1 and 1.9 respectively, are anchored in a more efficient manner onto the surface of Au NPs to suppress rapid growth and aggregation.

### 3.4.4 Long term colloidal stability of CTPR-stabilized Au NPs

The colloidal stability of the CTPR-decorated Au NPs was evaluated by monitoring the UV-vis spectra of CTPR3-Au-100 samples placed at 4 $^{o}$C for 3 months. As shown in the ***Figure S4a,*** only a minor loss in the LSPR intensity was identified whereas no noticeable shift or broadening of LSPR peak occurred. In addition, TEM analysis also confirmed that the Au NPs were well-dispersed and no self-aggregation behavior was found for the CTPR3-Au-100 sample (***Figure S4b***). Thus, CTPR proteins stabilized Au NPs exhibited remarkably high colloidal stability in MOPS buffer.

### 3.4.5 Circular dichroism measurements

CTPRn arrays displayed the characteristic CD spectrum of an α-helical protein, with minimum at 222 nm and 208 nm (***Figure 3.7a).*** The mean residue ellipticity (MRE) remains nearly constant upon addition of $HAuCl_4$ or addition of MOPS. More importantly, no signals characteristic of β-sheet or random coil structures were identified in the CD spectrum. This result

suggests that the metal ion coordination does not cause distortion of the secondary structure implying that the bioactivity of CTPR could be kept intact during the Au NP synthesis and finally when bound to the nanoparticle surface.

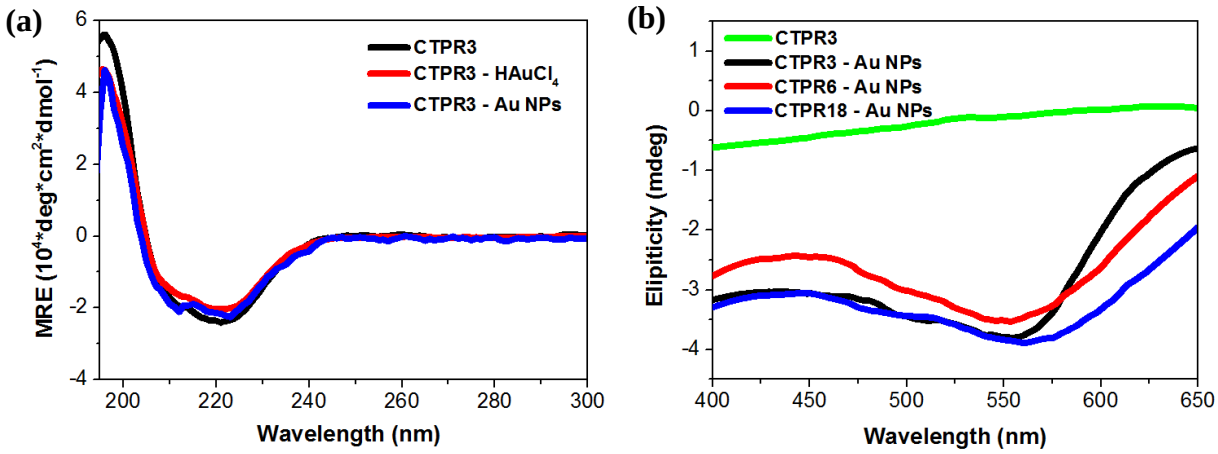


**Figure 3.7** CD spectra of (a) CTPR3, CTPR3-$HAuCl_4$ (1:100), CTPR3-Au-100 in the UV region and (b) CTPR3 control, CTPR3-Au-100, CTPR6-Au-100 and CTPR18-Au-100 samples in the visible light region.

In addition, the complexation of Au NPs with CTPR-3, 6, 18 induced a CD response at the plasmon resonance frequency region (ca. 550nm) as shown in the ***Figure 3.7b.*** As suggested previously,[50] the optical activity of Au NPs capped with chiral ligands is generally attributed to three reasons: (1) in-situ formation of an intrinsic chiral Au nanocluster in the presence of chiral ligands (2) electronic interaction between the chiral ligands and achiral metal core electrons, and (3) chiral arrangement of the ligands on an achiral metal core. Since the plasmonic CD bands of CTPR-Au NPs disappear after ligand exchange with achiral 2-mercaptoethanol, we ruled out in-situ formation of chiral Au nanoclusters. We surmise that the negative ellipticity of CTPR-Au NPs complex in the visible spectrum region may result from the dipolar interaction between chiral protein ligands and the plasmonic NPs.[50-52] Induced CD signals at the plasmonic absorption region have been previously demonstrated for peptides with specific Au binding affinity.[6] Exploration of CTPR-Au NPs for the development of biosensors based on the

plasmonic chirality is currently underway in our group. It is important to note that the application of these functionalized NPs is limited to aqueous solutions with physiological pH and ambient conditions. And further study of the environmental impacts on the stability and optical properties of CTPR-Au NPs is also of great interest to us.

## 3.5 Conclusions

In summary, we have developed a green-chemistry route for the preparation of Au NPs using Good's buffer and modular repeat proteins. TEM and UV-vis analysis indicated that the morphology as well as the LSPR absorbance of Au NPs can be adjusted by varying the ratio of $[HAuCl_4]$/[CTPR] in conjunction with the protein length. This study exemplifies the pivotal role of protein shape in tuning the morphology-dependent optical properties of protein-stabilized Au NPs. CD spectroscopic studies suggested that CTPR retained its secondary structure after coordinating with Au (III) or Au NPs. Moreover, the obtained CTPR-Au conjugates exhibited chirality in the visible light region indicating the strong molecular interaction between the CTPR proteins and Au NPs. This repeat protein-directed synthetic method enabled the facile fabrication of Au NPs with tailored morphology, LSPR and optical activity and may find potential applications in chiral biosensing and catalysis.

## 3.6 Acknowledgements

The authors would like to thank Nanoscale Characterization and Fabrication Lab (NCFL) for the use of TEM facility. We are grateful to Prof. Aitziber L. Cortajarena for insightful comments and suggestions. We acknowledge members of Grove's group for useful discussion of the manuscript. This work was in part supported by the JFC grants from Institute for Critical Technology and Applied Science (ICTAS), Virginia Polytechnic Institute and State University.

## 3.7 References


(1) Saha, K.; Agasti, S. S.; Kim, C.; Li, X.; Rotello, V. M. *Chem. Rev.* **2012**, *112*, 2739.
(2) Dickerson, M. B.; Sandhage, K. H.; Naik, R. R. *Chem. Rev.* **2008**, *108*, 4935.
(3) Delehanty, J. B.; Bradburne, C. E.; Susumu, K.; Boeneman, K.; Mei, B. C.; Farrell, D.; Blanco-Canosa, J. B.; Dawson, P. E.; Mattoussi, H.; Medintz, I. L. *J. Am. Chem. Soc.* **2011**, *133*, 10482.
(4) Naik, R. R.; Stringer, S. J.; Agarwal, G.; Jones, S. E.; Stone, M. O. *Nat. Mater.* **2002**, *1*, 169.
(5) Dickerson, M. B.; Jones, S. E.; Cai, Y.; Ahmad, G.; Naik, R. R.; Kröger, N.; Sandhage, K. H. *Chem. Mater.* **2008**, *20*, 1578.
(6) Slocik, J. M.; Govorov, A. O.; Naik, R. R. *Nano Lett.* **2011**, *11*, 701.
(7) Chen, C.-L.; Rosi, N. L. *J. Am. Chem. Soc.* **2010**, *132*, 6902.
(8) Song, C.; Zhao, G.; Zhang, P.; Rosi, N. L. *J. Am. Chem. Soc.* **2010**, *132*, 14033.
(9) Diamanti, S.; Elsen, A.; Naik, R.; Vaia, R. *J. Phys. Chem. C* **2009**, *113*, 9993.
(10) Li, Y.; Tang, Z.; Prasad, P. N.; Knecht, M. R.; Swihart, M. T. *Nanoscale* **2014**, *6*, 3165.
(11) Ueno, T.; Koshiyama, T.; Tsuruga, T.; Goto, T.; Kanamaru, S.; Arisaka, F.; Watanabe, Y. *Angew. Chem. Int. Ed.* **2006**, *45*, 4508.
(12) Niide, T.; Shimojo, K.; Wakabayashi, R.; Goto, M.; Kamiya, N. *Langmuir* **2013**, *29*, 15596.
(13) Hom, N.; Mehta, K. R.; Chou, T.; Foraker, A. B.; Brodsky, F. M.; Kirshenbaum, K.; Montclare, J. K. *J. Mater. Chem.* **2012**, *22*, 23335.
(14) Lin, Y.; Xia, X.; Wang, M.; Wang, Q.; An, B.; Tao, H.; Xu, Q.; Omenetto, F.; Kaplan, D. L. *Langmuir* **2014**, *30*, 4406.
(15) McMillan, R. A.; Howard, J.; Zaluzec, N. J.; Kagawa, H. K.; Mogul, R.; Li, Y.-F.; Paavola, C. D.; Trent, J. D. *J. Am. Chem. Soc.* **2005**, *127*, 2800.
(16) Mayavan, S.; Dutta, N. K.; Choudhury, N. R.; Kim, M.; Elvin, C. M.; Hill, A. J. *Biomaterials* **2011**, *32*, 2786.
(17) Schoen, A. P.; Schoen, D. T.; Huggins, K. N. L.; Arunagirinathan, M. A.; Heilshorn, S. C. *J. Am. Chem. Soc.* **2011**, *133*, 18202.
(18) Lan, X.; Chen, Z.; Liu, B.-J.; Ren, B.; Henzie, J.; Wang, Q. *Small* **2013**, *9*, 2308.
(19) Tan, L. H.; Xing, H.; Chen, H.; Lu, Y. *J. Am. Chem. Soc.* **2013**, *135*, 17675.
(20) Zhao, Y.; Xu, L.; Liz-Marzán, L. M.; Kuang, H.; Ma, W.; Asenjo-García, A.; García de Abajo, F. J.; Kotov, N. A.; Wang, L.; Xu, C. *J. Phys. Chem. Lett.* **2013**, *4*, 641.
(21) Tan, S. J.; Campolongo, M. J.; Luo, D.; Cheng, W. *Nat. Nanotechnol.* **2011**, *6*, 268.
(22) Schreiber, R.; Luong, N.; Fan, Z.; Kuzyk, A.; Nickels, P. C.; Zhang, T.; Smith, D. M.; Yurke, B.; Kuang, W.; Govorov, A. O.; Liedl, T. *Nat. Commun.* **2013**, *4*.
(23) Lo, P. K.; Karam, P.; Aldaye, F. A.; McLaughlin, C. K.; Hamblin, G. D.; Cosa, G.; Sleiman, H. F. *Nat. Chem.* **2010**, *2*, 319.
(24) Nykypanchuk, D.; Maye, M. M.; van der Lelie, D.; Gang, O. *Nature* **2008**, *451*, 549.
(25) Zou, L.; Qi, W.; Huang, R.; Su, R.; Wang, M.; He, Z. *ACS Sustain. Chem. Eng.* **2013**, *1*, 1398.
(26) Mahal, A.; Khullar, P.; Kumar, H.; Kaur, G.; Singh, N.; Jelokhani-Niaraki, M.; Bakshi, M. S. *ACS Sustain. Chem. Eng.* **2013**, *1*, 627.
(27) Xie, J.; Zheng, Y.; Ying, J. Y. *J. Am. Chem. Soc.* **2009**, *131*, 888.
(28) Cortajarena, A. L.; Regan, L. *Protein Sci.* **2011**, *20*, 336.

(29) Kajander, T.; Cortajarena, A. L.; Main, E. R. G.; Mochrie, S. G. J.; Regan, L. *J. Am. Chem. Soc.* **2005**, *127*, 10188.
(30) Grove, T. Z.; Osuji, C. O.; Forster, J. D.; Dufresne, E. R.; Regan, L. *J. Am. Chem. Soc.* **2010**, *132*, 14024.
(31) Cortajarena, A. L.; Yi, F.; Regan, L. *ACS Chem. Biol.* **2008**, *3*, 161.
(32) Grove, T. Z.; Regan, L.; Cortajarena, A. L. *J. R. Soc. Interface* **2013**, *10*.
(33) Mejias, S. H.; Sot, B.; Guantes, R.; Cortajarena, A. L. *Nanoscale* **2014**.
(34) Cortajarena, A. L.; Lois, G.; Sherman, E.; O'Hern, C. S.; Regan, L.; Haran, G. *J. Mol. Biol.* **2008**, *382*, 203.
(35) Kajander, T.; Cortajarena, A. L.; Mochrie, S.; Regan, L. *Acta Crystallogr. Sect. D* **2007**, *63*, 800.
(36) Grove, T. Z.; Forster, J.; Pimienta, G.; Dufresne, E.; Regan, L. *Biopolymers* **2012**, *97*, 508.
(37) Yu, Y.; Luo, Z.; Teo, C. S.; Tan, Y. N.; Xie, J. *Chem. Commun.* **2013**, *49*, 9740.
(38) Xie, J.; Lee, J. Y.; Wang, D. I. C. *Chem. Mater.* **2007**, *19*, 2823.
(39) Xie, J.; Zhang, Q.; Lee, J. Y.; Wang, D. I. C. *ACS Nano* **2008**, *2*, 2473.
(40) Park, J.; Choi, S.; Kim, T.-I.; Kim, Y. *Analyst* **2012**, *137*, 4411.
(41) So, M.-H.; Ho, C.-M.; Chen, R.; Che, C.-M. *Chem. Asian. J* **2010**, *5*, 1322.
(42) Roth, K. L.; Geng, X.; Grove, T. Z. *J. Phys. Chem. C* **2016**, *120*, 10951.
(43) Aldeek, F.; Safi, M.; Zhan, N.; Palui, G.; Mattoussi, H. *ACS Nano* **2013**, *7*, 10197.
(44) Hou, J.; Szaflarski, D. M.; Simon, J. D. *J. Phys. Chem. B* **2013**, *117*, 4587.
(45) Yu, J.; Becker, M. L.; Carri, G. A. *Langmuir* **2011**, *28*, 1408.
(46) Zhao, X.; Liu, R.; Chi, Z.; Teng, Y.; Qin, P. *J. Phys. Chem. B* **2010**, *114*, 5625.
(47) Lakowicz, J. R. *Principles of Fluorescence Spectroscopy*; Springer: Singapor, 2006.
(48) Si, S.; Bhattacharjee, R. R.; Banerjee, A.; Mandal, T. K. *Chem. Eur. J.* **2006**, *12*, 1256.
(49) Nikoobakht, B.; El-Sayed, M. A. *Chem. Mater.* **2003**, *15*, 1957.
(50) Link, S.; El-Sayed, M. A. *J. Phys. Chem. B* **1999**, *103*, 4212.
(51) Govorov, A. O. *J. Phys. Chem. C* **2011**, *115*, 7914.
(52) Schaaff, T. G.; Whetten, R. L. *J. Phys. Chem. B* **2000**, *104*, 2630.

## 3.8 Supplemental Information

**Table S1**. Molecular design of recombinant CTPRn proteins with different lengths and aspect ratios but same surface exposed residues.

Consensus sequence of CTPR protein: 34 amino acid residues
**AEAWYNLGNAYYKQGDYQKAIEYYQKALELDPNN**

| Recombinant CTPRs | # of amino acid residues | Mw (kDa) | Aspect ratio |
|---|---|---|---|
| n=3 | 107 | 12.5 | 1.1 |
| n=6 | 213 | 25 | 1.9 |
| n=18 | 629 | 74.1 | 4.6 |

**Table S2**. Particle size of Au NPs synthesized in the presence of CTPR3 protein with different ratios of [$HAuCl_4$]/[CTPR].

| Au sample | [$HAuCl_4$]:[CTPR] | Size (nm) |
|---|---|---|
| MOPS-Au | 0 | 33.3±9.7 |
| CTPR3-Au-1000 | 1000:1 | 18.8±11.7 |
| CTPR3-Au-400 | 400:1 | 15.9±8.8 |
| CTPR3-Au-100 | 100:1 | 14.6±6.5 |
| CTPR3-Au-20 | 20:1 | 14.1±5.6 |
| CTPR6-Au-1000 | 1000:1 | 16.9±7.6 |
| CTPR6-Au-400 | 400:1 | 13.9±5.7 |
| CTPR6-Au-100 | 100:1 | 12.3±5.1 |
| CTPR6-Au-20 | 20:1 | 11.2±4.1 |
| CTPR18-Au-1000 | 1000:1 | N/A |
| CTPR18-Au-400 | 400:1 | 16.5±8.8 |
| CTPR18-Au-100 | 100:1 | 13.8±8.3 |

**CTPR 3 6 18 Marker**

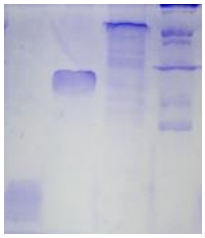

**Figure S1**. SDS-PAGE gel of CTPR3, 6, 18 stained with coomassie blue.

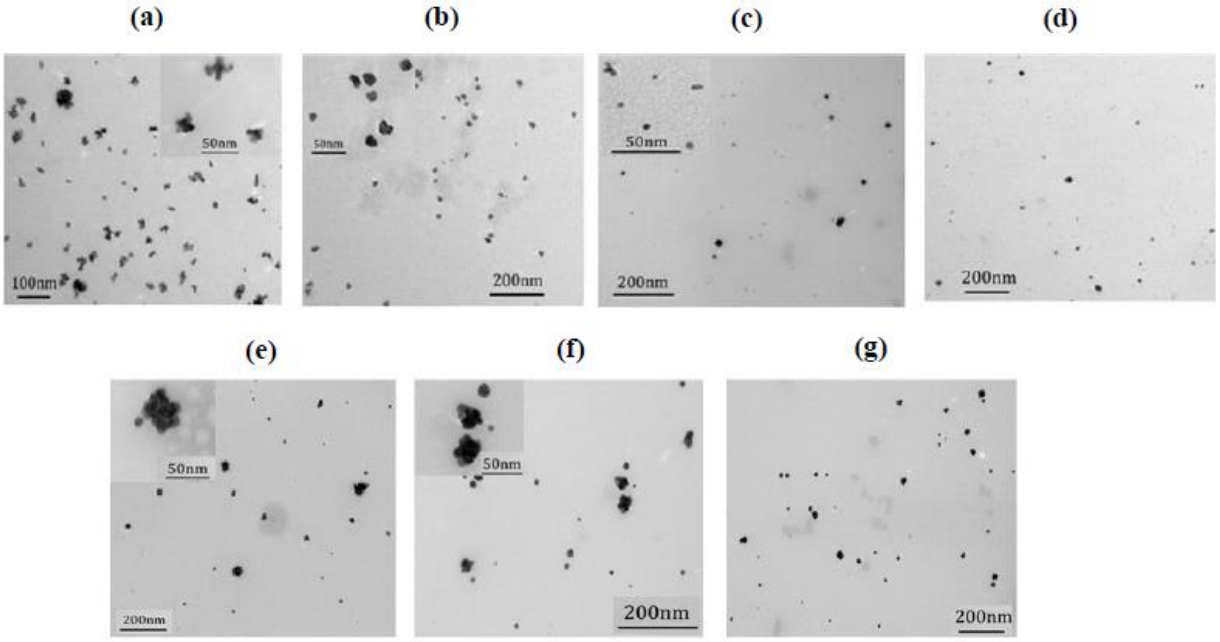


**Figure S2**. TEM images (a) CTPR6-Au-1k (b) CTPR6-Au-400 (c) CTPR6-Au-100 (d) CTPR6-Au-20 (e) CTPR18-Au-1k (f) CTPR18-Au-400 (g) CTPR18-Au-100.Scale bar = 200 nm. (inset showing magnified CTPR-Au NPs, scale bar = 50 nm)

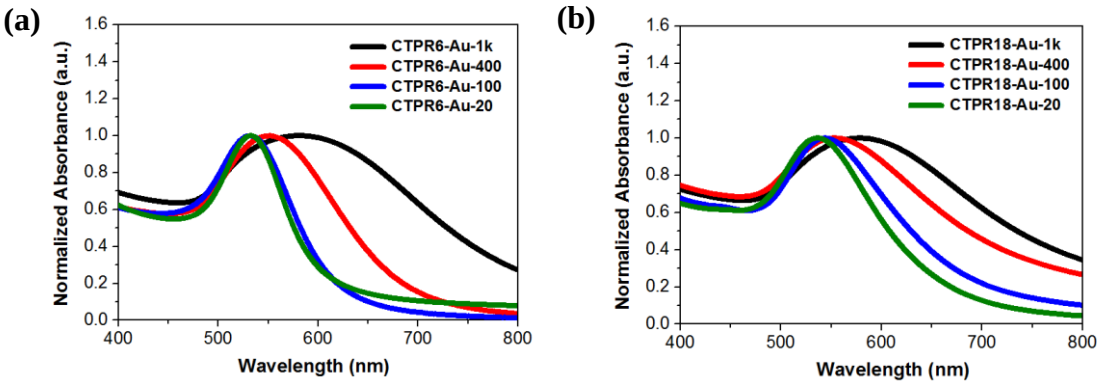


**Figure S3**. UV-vis spectra of (a) CTPR6-Au NPs and (b) CTPR18-Au NPs prepared with different ratio of $[HAuCl_4]$/[CTPR].

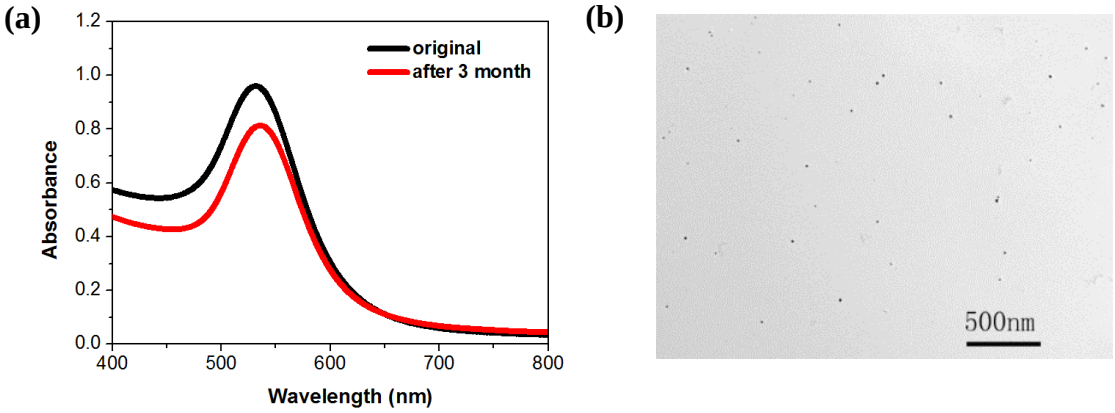


**Figure S4**. (a) UV-vis spectra and (b) TEM images of CTPR3-Au-100 after store at 4 °C for 3 months.

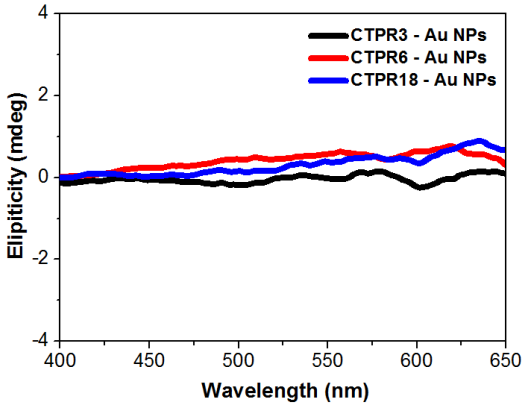


**Figure S5**. CD spectra of CTPR-Au-100 samples after ligand exchange using 2-mercaptoethanol.

# Chapter 4. Bioinorganic interface: mechanistic studies of protein-directed nanomaterial synthesis

Kristina L. Roth, Xi Geng and Tijana Z. Grove

Reprinted with permission from K. L. Roth, X. Geng, and T. Z. Grove, *J. Phys. Chem. C*, **2016**, *120*, 10951-10960. 

**Attributions:** KLR performed fluorescence quenching and 2D NMR experiments. KLR was the primary writer of the manuscript. XG make contribution to the fluorescence quenching and morphological characterization. XG also engaged in the discussion and revision of the manuscript. TZG supervised the research project and provided technical insight during experimentation and data analysis, TZG also assisted in writing and editing the manuscript.

## 4.1 Abstract

Proteins and peptides have attracted much attention as templates for one-pot synthesis of biocompatible gold nanoparticles. While numerous natural and *de novo* protein sequences have been used, the actual mechanism of nanoparticle nucleation and growth from the protein matrix is not well understood. In this study we utilized engineered consensus tetratricopeptide repeat protein (CTPR) to probe the bioinorganic interface during gold nanoparticle synthesis. The binding of CTPR to gold ions and the gold nanoparticle surface was investigated using fluorescence spectroscopy and heteronuclear single quantum coherence NMR spectroscopy to provide residue-specific measurements. This work provides a foundation for the rational design of proteins for synthesis of tailored functional nanomaterials for biological, medical, and optical applications.

## 4.2 Introduction

In the past two decades, much scientific interest has focused on gold nanoparticles (NPs) due to their optical and electronic properties attractive for biological and medical applications, including imaging, diagnostics, and phototherapy.[1,2] Since optical and electronic properties of NPs depend on size, shape, composition, and surface functionalization, the synthetic procedures that produce gold NPs in a variety of shapes with tunable sizes have been at the forefront of research interest.[3-5] It is now widely recognized that in addition to size and shape, the surface chemistry of gold NPs is crucial for specific biomedical requirements such as cellular uptake, targeting capabilities, and cytotoxicity.[6] Thus, synthetic methods that allow for simultaneous control over NP size, shape, and biocompatible surface chemistries are of great interest for nanomedicine. Synthetic approaches that utilize biopolymers are one possible solution. Plant extracts, polysaccharides, proteins, and peptides have all been used to synthesize metallic NPs *in vitro*.[7-10] Such syntheses are performed under mild aqueous conditions, eliminating the need for aggressive reducing agents, high temperatures, and polymeric surfactants.[11] These advantages have led to a growing interest in the rational design of biomolecules that allow for control in synthesis and assembly of gold NPs.

In nature, inorganic materials are synthesized and assembled in the process of biomineralization, which consists of crystal nucleation followed by the crystal growth in a biomolecular matrix, most often proteins.[7,12] However, the complex process of biomineralization is not fully understood.[7,8] Mimicking the biomineralization process, the Mann group synthesized various inorganic NPs (iron sulphide, manganese oxide, and uranyl oxyhydroxide) *in vitro* using a cage protein, ferritin, as a template.[13] Since then the use of peptides[14,15] and proteins[16] in NP synthesis have been an active area of research. A one-pot synthesis of gold nanoplates performed using algal extract demonstrated that a 28k Da protein found in the extract acted as both the

reducing and shape-directing agent, albeit sequence and identity of this protein are unknown,.[17] Common proteins like BSA have also been employed in biomimetic gold NP synthesis.[18,19] Recently, our group has reported the use of a consensus tetratricopeptide repeat protein (CTPR) in a bio-enabled synthesis strategy to form gold NPs.[20] Due to their modular structure and ease of engineering, repeat proteins have attracted the interest of the biotechnology community.[21-29]

Further investigations into the nucleation, growth, and morphogenesis steps occurring during biomineralization will allow for development and control over NPs synthesized using protein scaffolds. Identifying the role of protein sequence[9,30-32] and protein secondary structure[33-35] on biomineralization has been an ongoing task. The Aldinger group found that the kinetics and thermodynamics of crystalline oxide growth is dependent on amino acid identity, with glutamic acid demonstrating the slowest crystal growth.[9] The ability of the aromatic rings on tryptophan and tyrosine to reduce metal ions has been clearly demonstrated by Mandal and colleagues.[36-38]Along with identity the sequence of amino acid residues play a role in NP size, shape, and aggregation.[39] Additionally, studies of specific peptide motifs, important in calcification, found that the secondary structure of a bioscaffold is important for biomineraliazation.[33] Understanding the components and molecular mechanisms that initiate and promote hierarchical deposition of metal ions has significant implications for the development of a variety of nanotechnologies.

In this work, we use a designed repeat protein, CTPR3, as a model biomineralization matrix (***Figure 4.1***). We investigate molecular details of the initial binding step between CTPR3 and chloroauric acid (complexation step in ***Figure 4.2***) along with the protein orientation and interaction with the gold NP surface. Gold NPs were selected for their interesting optical properties and significant biomedical applications. The CTPR scaffold is a *de novo* (i.e. synthetic sequence not present in nature) protein with a 34 amino acid helix-turn-helix motif (***Figure 4.1***).

The advantage of engineered proteins is that the synthetic sequence can be tuned for a particular application, while a well-defined protein fold is preserved.[20,21,23,24,26] The simplest repeat protein system is one in which all the repeats within a protein are identical as in CTPR3, which has three CTPR repeats in tandem for a total of 3*34 amino acids. In the process of NP synthesis, CTPR3 has a dual role – it acts as a template by binding gold ions in the nucleation step, but it is also a surfactant that binds to the NP surface to prevent further growth and agglomeration (***Figure 4.2***).

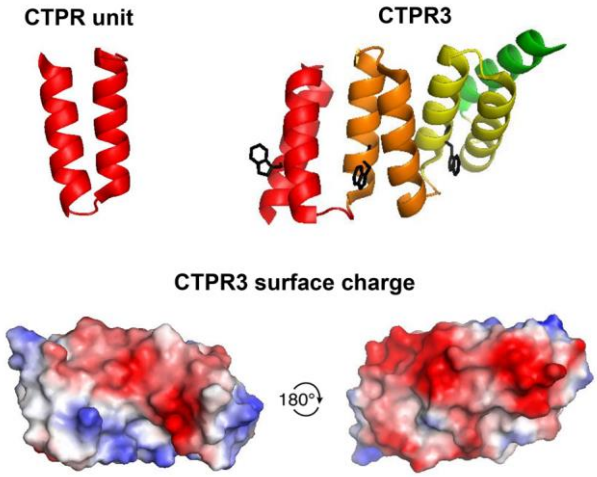


**Figure 4.1** Top: One helix-turn-helix unit of CTPR is shown in red along with the structure of CTPR3 with tryptophan side chains displayed in black for each repeat. Bottom: An electrostatic potential map of CTPR3 with the surface charge shown, color range deep red to deep blue corresponds to an electrostatic potential range from -108 to + 108 kT/e, where k is Boltzmann's constant, T is absolute temperature, and e is the charge of a proton. All figures were prepared from X-ray coordinates (PDB 1NA0) using Pymol.

The sequence of CTPR3 contains no histidine, methionine, or cysteine amino acids, which are known strong binders for gold and are commonly used to immobilize proteins to gold surfaces.[40-44] The repeating structure of CTPR3 allowed us to probe effects of amino acid identity versus their surrounding chemical environments. Since each repeat contains exactly the same sequence, the same positions in the primary and secondary protein structure for each repeat will be the same. However, in different repeats the same residues will experience different chemical surroundings due to the repeat packing. For example, CTPR3 contains one tryptophan

residue per repeat (***Figure 4.1***). In the structure of CTPR3, each one of the tryptophan residues is in a different environment. Therefore, the CTPR3 scaffold allows for the analysis of the effect of both identity and chemical environment of the amino acid and their importance in nucleation and NP growth.

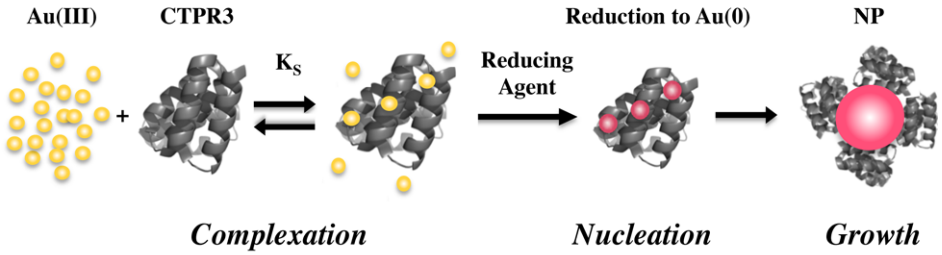


**Figure 4.2** Scheme of gold nanoparticle synthesis using protein as a template.

## 4.3 Experimental Methods

### 4.3.1 CTPR3 and $^{15}$N-CTPR3 expression and purification

The CTPR3 and $^{15}$N-CTPR3 proteins were expressed and purified using a previously reported method.[45,46] Briefly, the plasmid pProExHtam containing genes coding for CTPR3, N-terminal $His_6$-tag, and a TEV protease cleavage site, were transformed into BL21 (DE3) cells and cultured overnight at 37 °C on an agar plate. A single colony was cultured overnight in 50 mL of LB media at 37 °C. A 1:100 dilution of the overnight culture was added to 1 L of LB media. The cells were grown to an $OD_{600}$ of 0.6-0.8 and then induced with 1mM isopropyl β-D-1-thiogalactopyranoside (IPTG) followed by expression for 5 hours at 30°C. The cells were collected by centrifugation and resuspended in lysis buffer containing 50 mM Tris, 300 mM sodium chloride, and 0.1 wt% Tween20. Half a tablet of Complete EDTA-free protease inhibitor cocktail (Roche, Basel, Switzerland) and lysozyme (1 mg/mL) was added to the suspension and incubated for 30 min at 0 °C, then microtip sonicated (Branson) at 30% power for 1 min with 10 second pulses. Lysed cells were centrifuged and the supernatant was collected and purified using

standard Ni-NTA affinity purification techniques. The eluted CTPR3 was incubated with TEV protease in 50 mM Tris-HCl, 1 mM BME pH 7.6 buffer at 4 °C overnight to cleave the $His_6$-tag. The $His_6$-tag free CTPR3 was collected through a Ni-NTA column as a flow-through fraction. CTPR3 was further purified using size exclusion chromatography using a HiLoad 16/600 Superdex 75 (GE Healthcare Life Sciences) column. The protein was dialyzed into 10 mM $Na_2HPO_4$ pH 7.6 for further experiments.

Similar expression and purification methods were used for $^{15}$N-CTPR3. Minimal media containing $^{15}NH_4Cl$ was used in place of LB media. At the final purification step with size exclusion chromatography 150 mM NaCl, 50 mM $Na_2HPO_4$ pH 6.3 buffer was used to eliminate the need for dialysis.

**4.3.2 Fluorescence spectroscopy**

Fluorescence spectra were recorded on a Cary Eclipse Fluorometer using $\lambda_{ex}$ = 275nm, excitation slit 5 nm and emission slit 10 nm. All of $HAuCl_4$ into CTPR3 titrations were performed using 5 µM CTPR3 in 10 mM $Na_2HPO_4$ pH 7.6 in a 10 mm path-length cuvette. Ionic strengths of the solutions were adjusted using NaCl. A 1 mM $HAuCl_4$ in 10 mM $Na_2HPO_4$ pH 7.6 solution was titrated into the protein, mixed, and equilibrated for 10 min before recording the fluorescence. To account for the inner filter effect Equation 1 was used to correct each observed fluorescence intensity.

$$F_{ideal}(\lambda_{ex},\lambda_{em}) = F_{obs}(\lambda_{ex},\lambda_{em})CF_p(\lambda_{ex})CF_s(\lambda_{em}) \quad (1)$$
$$= F_{obs}(\lambda_{ex},\lambda_{em})10^{(A_{ex}+A_{em})/2}$$

$CF_p$ and $CF_s$ represent the correction factors for the total absorbance, $A_{ex}$ and $A_{em}$, at the wavelengths $\lambda_{ex}$ and $\lambda_{em}$ respectively. The molar extinction coefficients of $HAuCl_4$ at 275 and 340 nm were determined experimentally (***Figure S1***).

### 4.3.3 HSQC NMR

NMR spectra were obtained using a Bruker Avance II 600 MHz spectrometer. The 0.5 mM $^{15}$N-CTPR3 sample was prepared in 150 mM NaCl, 50 mM $Na_2HPO_4$, 10% $D_2O$ at pH 6.3. A 0.25 M solution of $HAuCl_4$ in 150mM NaCl, 50 mM $Na_2HPO_4$ at pH 6.3 was titrated into the CTPR3 with 30 min incubation after each addition at 20°C. The CTPR3 NH crosspeaks were assigned based on previously published assignments for CTPR3.[47] All data was processed with TopSpin (Bruker) and analyzed with Sparky.[48]

### 4.3.4 Nanoparticle synthesis

Nanoparticles were synthesized by combining 0.1 mM CTPR3 and 1.3 mM $HAuCl_4$ in 5 mM $Na_2HPO_4$ pH 7 buffer. The ionic strength was adjusted to 238.75 mM using either NaCl or $NaNO_3$. The samples were prepared in NMR tubes and left at room temperature in the dark for 3 weeks.

### 4.3.5 TEM

The images were obtained using a Phillips EM420 with an accelerating voltage of 120 kV. In order to remove salt from the samples they were first centrifuged at 10,000 rpm for 2 min and the supernatant was removed. The pelleted NPs were resuspended in DI $H_2O$. Samples were prepared by depositing 10 µL of the NP solution on a 300 mesh carbon coated copper grid (EM Science) and left to dry overnight.

## 4.4 Results and Discussion

### 4.4.1 Fluorescence spectroscopy

The process of biomineralization occurs through an initial crystal nucleation step followed by crystal growth (***Figure 4.2***). Varying conditions in any of the steps will alter the NP size and morphology. The initial complexation step, i.e. binding of the metal ion to the

bioscaffold, regulates the rate of crystal growth and crystal morphology through the modulation of the local concentration.[49] In a recent report by Smeets et al., the initial growth rate of calcium carbonate was enhanced by binding of calcium ions to a negatively charged polymer where the ions become locally concentrated.[49] Although many current biotechnology studies focus primarily on the synthesis of NPs with tunable shape and size[16,19,50,51], the nature of the biomolecule interaction with metal ions is yet to be determined. One goal of this study is to determine the molecular interactions occurring during the initial complexation step between gold ions and CTPR3. Deeper insight into the bioinorganic interface in NP synthesis will enable design of new biomolecular templates with increased control of complexation and nucleation resulting in regulation of NP morphology.

This study probed the molecular level interactions of CTPR3 and gold ions. At pH 7 CTPR3 has a net negative charge of -15, with most of the negative residues positioned on the convex face (***Figure 4.1***).[45] Due to this polyanion characteristic, we hypothesized that the binding of CTPR3 to gold ions is dependent on ionic strength. Thus, by varying the ionic strength the ratio of free to bound metal ions changes. To probe the role of electrostatic interactions in Au(III) binding to CTPR3 and resulting morphology of NPs we have measured $K_S$ (***Figure 4.2***) as a function of total ionic strength.

### 4.4.2 CTPR3 and gold ion interaction monitored by steady-state fluorescence

Steady-state fluorescence is a commonly used technique to evaluate protein interactions with the surface of metallic NPs.[52,53] The intensity of the intrinsic fluorescence of the protein will change when the local environment of the protein is altered. Metals and especially metal nanoparticles efficiently quench chromophores. Therefore, monitoring the changes in intensity of

the intrinsic protein emission as a function of metal ion or NP concentration can offer insight into the binding mechanism between metals and proteins.

4A shows the fluorescence spectra of CTPR3 with an increasing concentration of gold ions. The emission spectra of CTPR3 exhibits an emission maximum at 340 nm upon excitation at 275 nm due to 6 tyrosine and 1 tryptophan residues in each of the three repeats. The emission intensity systematically decreases upon the progressive addition of the chloroauric acid in the buffered solution (***Figure 4.3A***). It is important to note here that during this process CTPR3 remains fully folded without any change in the secondary structure composition.[20] Thus, we have attributed this emission quenching to direct complexation between CTPR3 and Au(III).

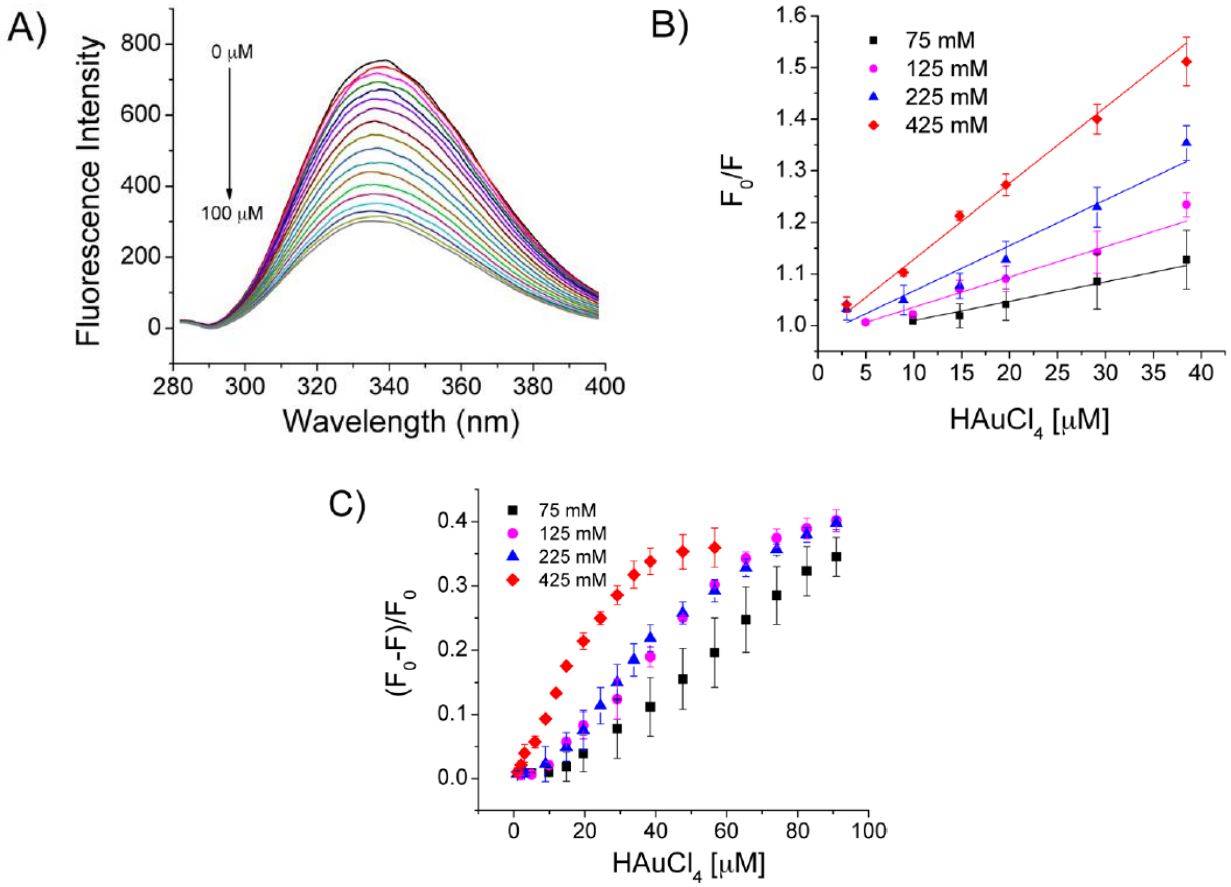


**Figure 4.3** (A) Fluorescence spectra of 5 μM CTPR3 titrated with $HAuCl_4$ at an ionic strength of 225 mM. (B) Fluorescence quenching of CTPR3 as a function of increasing concentration of $HAuCl_4$. Each data point is the mean of three independent observations. (C) Plot of $(F_0\text{-}F)/F_0$ versus $HAuCl_4$ concentration for increasing ionic strengths.

Each repeat in CTPR3 contains seven negative and two positive surface-exposed residues. Due to the high charge of the protein surface we initially predicted that electrostatic interactions played an important role in the binding of gold ions to CTPR3. To test this, we varied the ionic strength of the buffered protein solution from 75-425 mM to monitor the effect of charge screening on molecular interaction. It can be seen that the same CTPR3 to $HAuCl_4$ ratio (1:3) exhibits different quenching of the fluorescence signal depending on the ionic strength of the solution. At the same point during the titration the solution with low ionic strength, 125 mM, displays the highest fluorescent signal. As ionic strength is increased, there is an increase in quenching due to more favorable interactions between CTPR3 and the gold ions.

Quenching of biomacromolecule emission can occur through a variety of processes: static and binding related quenching, collisional quenching, or the inner filter effect. To eliminate inner filter effect, all emission data is corrected for the competitive absorption and reabsorption of light by Au(III) and Au NP at the excitation and emission wavelengths (see materials and methods section). The quenching data was analyzed using the Stern-Volmer equation (Equation 2) shown below.

$$[\frac{F_0}{F}] = 1 + K_{sv}[Q] = \ 1 + k_q\tau_0[Q] \qquad (2)$$

$F_0$ and F are the fluorescence intensities in the absence and presence of quencher, $k_q$ is the biomolecular quenching constant, and $\tau_0$ is the lifetime of CTPR3 in the absence of quencher.

The plot of the Stern-Volmer equation in the presence of increasing concentration of Au(III) is shown in ***Figure 4.3B***. A linear relationship between $F_0/F$ and $HAuCl_4$ concentration is indicative of a single population of fluorophore, implying that all tyrosine and tryptophan residues have the same accessibility to the quencher. The value of the Stern-Volmer quenching

constant ($K_{SV}$) was determined from the slope of the line. Further, the bimolecular quenching constant $k_q$, related to the availability of the fluorophore to the quencher, or simply the efficiency of quenching, can be calculated from the $K_{SV}$ and the fluorescence lifetime of the CTPR3 in the absence of the quencher. The lifetime of CTPR3 in the absence of quencher, $\tau_0 = 3.82 \pm 0.05$ ns (***Figure S3***) was measured using time resolved fluorescence spectroscopy. The calculated $k_q$ value of $9.71 \pm 0.97 \times 10^{11}$ $M^{-1}s^{-1}$ for CTPR3 and Au(III) at an ionic strength of 75 mM is almost two orders of magnitude greater than the previously reported value for a diffusionally controlled collisional quenching constant ($1.00 \times 10^{10}$ $M^{-1}s^{-1}$), confirming the possibility of a static quenching mechanism. As predicted, the increase in ionic strength and subsequent increase in charge screening results in higher $k_q$ values (Table 4.1).

**Table 4.1** Stern-Volmer constant ($K_{sv}$) and biomolecular quenching constant ($k_q$) as a function of ionic strength.

| Ionic Strength (mM) | Ksv ($M^{-1}$) | kq ($M^{-1}$ $s^{-1}$) |
|---|---|---|
| **75** | $3.71 \times 10^3$ | $9.71 \times 10^{11}$ |
| **125** | $6.26 \times 10^3$ | $1.64 \times 10^{12}$ |
| **225** | $1.16 \times 10^4$ | $3.03 \times 10^{12}$ |
| **425** | $1.46 \times 10^4$ | $3.83 \times 10^{12}$ |

Static quenching is often associated with the ground-state complex formation between the fluorophore and the quencher. Quenching of the emission intensity is either due to the excited-state energy transfer in the complex, or due to the change in the conformation and microenvironment of the fluorophore. In either case, temperature increase would favor complex dissociation and less quenching. Conversely, at a higher temperature an increase in diffusion would increase the probability of collision and favor a collisional quenching mechanism. In an attempt to further elucidate the mechanism of CTPR3 emission quenching in the presence of Au(III), we have performed quenching experiments at 25 °C and 50 °C. CTPR3 remains folded

at this temperature.[54] The plot of $F_0/F$ versus $HAuCl_4$ concentration for both temperatures is a straight line with an identical slope indicating a combination of collisional and static quenching mechanisms that ultimately result in gold ion association with CTPR3 (***Figure S4***).

The Stern-Volmer equation strictly applies only to a collisional quenching mechanism. Therefore, to evaluate the association constant between CTPR3 and Au(III), we plotted fraction of complexed gold ions, $(F_0\text{-}F)/F_0$, versus total $HAuCl_4$ concentration (***Figure 4.3C***). The sigmoidal shape of the binding isotherms at varying ionic strengths suggests the presence of cooperative binding. The binding of gold ions to CTPR3 is possibly a multi-associative event where Au(III) is interacting with more than one site on the surface of the protein and the $K_{obs}$ is a composite of the binding constants from the multiple binding site. Thus, the binding isotherms could not be treated with either a single binding site model or multiple independent sites model. To further evaluate the degree of cooperativity of the complex formation we used the Hill equation:

$$\log[\frac{F_0 - F}{F}] = \log K_a + n \log[Q] \qquad (3)$$

where $F_0$ and F are the same as in Equation 2, $K_a$ is the binding constant, and the Hill coefficient, n, indicates the degree of cooperativity in binding. For non-cooperative interactions n = 1 and the binding isotherm can be fitted to a multiple independent sites model. A Hill coefficient less than 1 indicates negative cooperativity, whereas n larger than 1 indicates positive cooperativity. The double logarithmic plot (***Figure 4.4***) has a sigmoidal shape at all ionic strengths indicating multiple non-equivalent binding sites on the CTPR3 protein surface in which the gold ions bind in partial cooperativity. Although we were unable to determine the macroscopic $K_S$, it is evident that binding is ionic strength dependent and that CTPR3 has multiple binding sites for the gold ion.

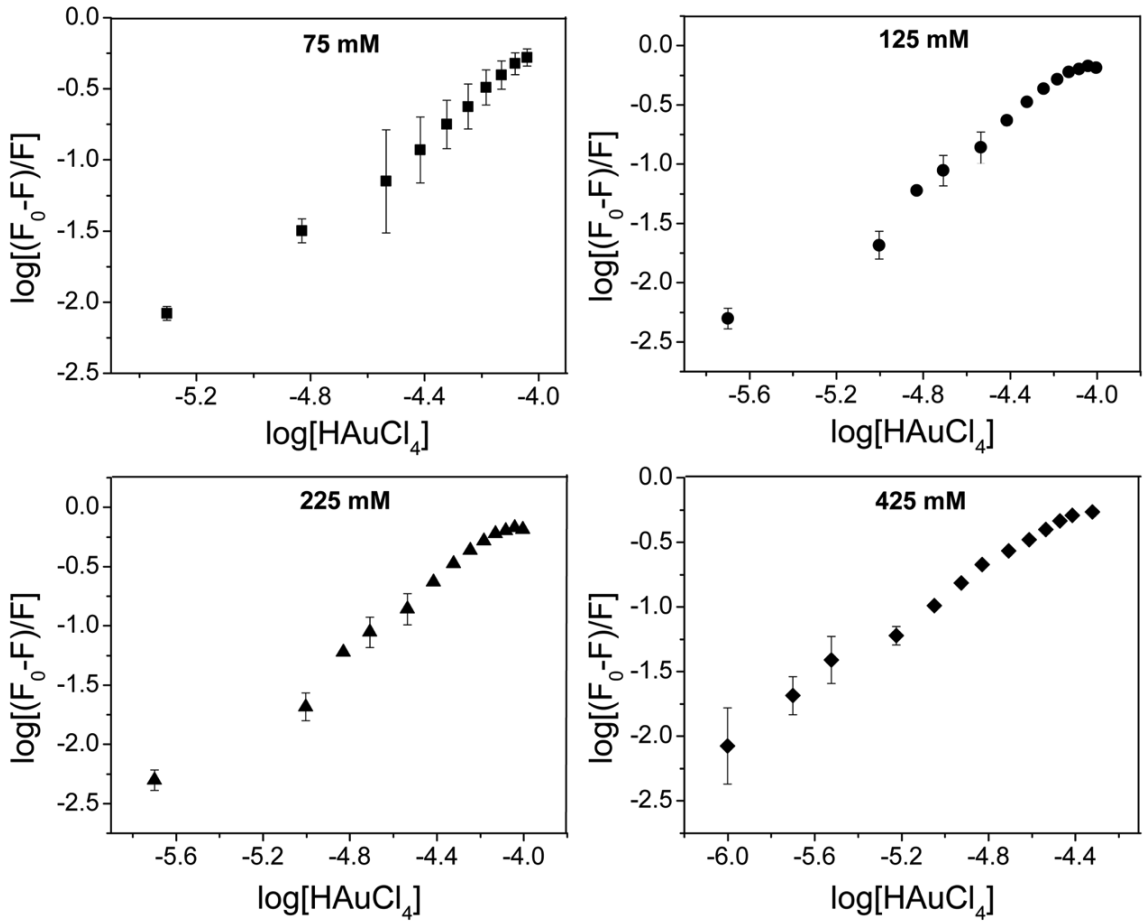


**Figure 4.4** Hill plots depicting the binding curves from Au(III) and CTPR3 at varying ionic strengths.

### 4.4.3 Ionic strength dependent NP growth

Fluorescence quenching data clearly shows that the interaction between gold ions and CTPR3 is ionic strength dependent. Consequently, the complexation equilibrium will be affected by ionic strength; e.g. at high ionic strengths the equilibrium will be shifted towards the ion-bound form of the protein. To test how change in the complexation equilibrium ($K_S$) affects NP growth and morphology, we have synthesized gold NPs at a 1:13 molar ratio of CTPR3 to $HAuCl_4$ in 5 mM $Na_2HPO_4$ with a final adjusted pH of 6.8 and $\mu$ = 8.75 mM due to the phosphate alone. In two other samples the ionic strength was adjusted to 238.75 mM with either

NaCl or $NaNO_3$. The NPs were synthesized at room temperature in the dark using NMR tubes as the reaction vessel. After 3 days the high ionic strength solutions were the first to develop a light purple color and after 10 days the solution with $\mu$ = 8.75 mM also appeared purple. The color of all the samples stopped changing after 3 weeks (***Figure S5***). Size and morphology of the resulting NPs was analyzed from TEM images (***Figure 4.5***). Small 10 nm NPs that form clusters are formed from the solution with low ionic strength whereas larger, well-dispersed NPs are formed at the higher ionic strengths.

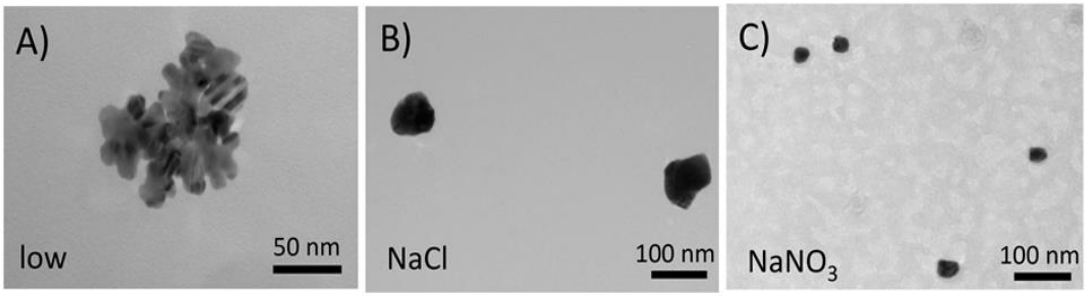


**Figure 4.5** (A) TEM image of gold NPs in 8.75 mM ionic strength sample. (B) TEM of gold NPs in 238.75 mM ionic strength sample adjusted with NaCl. (C) TEM of gold NPs in 238.75 mM ionic strength adjusted with $NaNO_3$.

Considering a constant CTPR3 and phosphate concentration in all samples, the difference in NP morphology can be related to the presence of salt ions in solution. At the low ionic strength the complexation equilibrium is shifted towards more free gold ions in solution. The higher amount of free gold ions leads to a higher number of seeds in solution and therefore a larger number of smaller NPs are formed (***Figure 4.5A***). Assuming that the interaction between CTPR3 and gold NPs is also weaker at the low ionic strength, less protein will coat the NP surface resulting in NP agglomeration and the clustered morphology. In contrast, in the samples with high ionic strengths complexation equilibrium is shifted towards the ion-bound form of the protein resulting in the formation of larger spherical NPs (***Figure 4.5B***). The stronger interaction between the NPs and CTPR3 also increases the colloidal stability of the NPs resulting in a well-

dispersed system. However, NPs prepared with $NaNO_3$ are smaller, around 35 nm (***Figure 4.5C***), than NPs prepared in the presence of NaCl, which are around 60 nm.

Effects of halide ions on the NP growth are well established, but effects of the ionic strength are not well understood.[55,56] We can speculate that the observed difference in NP size is due to chloride ions and CTPR3 competition for binding the gold surface. Presumably, in the $NaNO_3$ solutions the surface of the growing NP is covered with protein, which slows the diffusion and hinders subsequent deposition of gold ions, resulting in overall smaller NPs.

### 4.4.4 CTPR3 and gold ion interaction probed by NMR

To probe the interaction between CTPR3 and gold ions with a single-residue resolution we used a $^{1}H$-$^{15}N$ HSQC NMR experiment. $HAuCl_4$ was titrated into 0.5 mM of $^{15}N$-labeled CTPR3 at protein to $HAuCl_4$ ratios of 1:2, 1:4, 1:6, 1:8, and 1:10. The peaks observed in this experiment correspond to the NH group on the backbone of CTPR3. A change in the chemical environment of an amino acid results in a shift of the corresponding NH peak. The chemical shift perturbation (d) was determined from the change in peak position along the $^{1}H$ and $^{15}N$ axis using the following equation[57],

$$d = \sqrt{\frac{1}{2}[\delta_H^2 + (\alpha \cdot \delta_N^2)]} \qquad (4)$$

where $\delta_H$ and $\delta_N$ represent the change in the observed shift from the free state, and $\alpha$ is a scaling factor. The scaling factor for our experiment was calculated to be 0.147 taking into account the range of $^{15}N$ and $^{1}H$ shifts.[57]

The peaks found in the spectrum are narrow and are well dispersed, consistent with the HSQC spectrum of a folded protein. Overall, the peaks seen in the spectrum for CTPR3 and $HAuCl_4$ (1:10) overlap with the spectrum for pure CTPR3 indicating no change in secondary

structure during the titration. However, a few discrete peaks display a shift as $HAuCl_4$ is titrated into the protein solution. The corresponding residues are considered to be discrete binding sites for gold ions. ***Figure 4.6A*** shows the chemical shift perturbation (d) for each assigned amino acid in the CTPR3 sequence. The solid line indicates the average of d plus one standard deviation; all peaks above the line are considered a major peak shift indicating a large change in the NH chemical environment. The residues that show a major shift are W12, G16*, N17, Y25, A62*, N76, Y87, Y99, A103*, and L106. The three amino acids denoted with an asterisk are not surface exposed and will be discussed later. A surface model of CTPR3 with amino acids colored cyan for a chemical shift perturbation considered strong is seen in ***Figure 6B***. When plotted on the protein surface the residues with strong interaction to the gold ions do not constitute a contiguous patch but are isolated sites. The interaction of gold ions with isolated residues is consistent with the existence of multiple binding sites on CTPR3.

It is important to restate that CTPR3 does not contain histidine, cysteine, and methionine residues which are known to form strong bonds with metal surfaces.[58,59] The absence of these amino acids allows us to probe the interaction of gold ions with amino acids not as well studied. Non-covalent gold binding favors amino acids with aromatic side groups through π-metal interactions.[60-62] As expected, three tyrosine (Y) residues and one tryptophan (W), all of which have aromatic side chains, are interacting strongly with the gold ions. Additionally, two asparagines (N) are involved in gold ion binding. Theoretical and experimental data shows that Au(I) and Au(III) can exhibit properties similar to a hydrogen bond acceptor; thus it is feasible that asparagine acts as a hydrogen bond donor to the Au(III).[63] Leucine 106 is the only amino acid that shows a significant peak shift but has a side chain without aromaticity or charge. The

interaction between L106 and Au(III) could possibly be driven by spatial proximity to other binding residues and not any inherent feature of leucine.

The major perturbation shift exhibited by the three non-surface exposed residues cannot be explained by a direct interaction between the metal ion and amino acid side chain. However, these residues are in the *i*+4 position from the surface exposed W12 and Y99, both found to be strong interaction sites. Thus, it is feasible that the large perturbations seen for G16 and A103 are a result of the change in the environment from hydrogen bonding through the alpha helix. The 58th residue, in the *i*+4 position from A62, does not have a peak assignment on the HSQC spectrum. However, position 58 in CTPR3 is an aspartic acid which favors gold binding due to its charge, so an interaction with Au(III) resulting in the shift of A62 is plausible.[64]

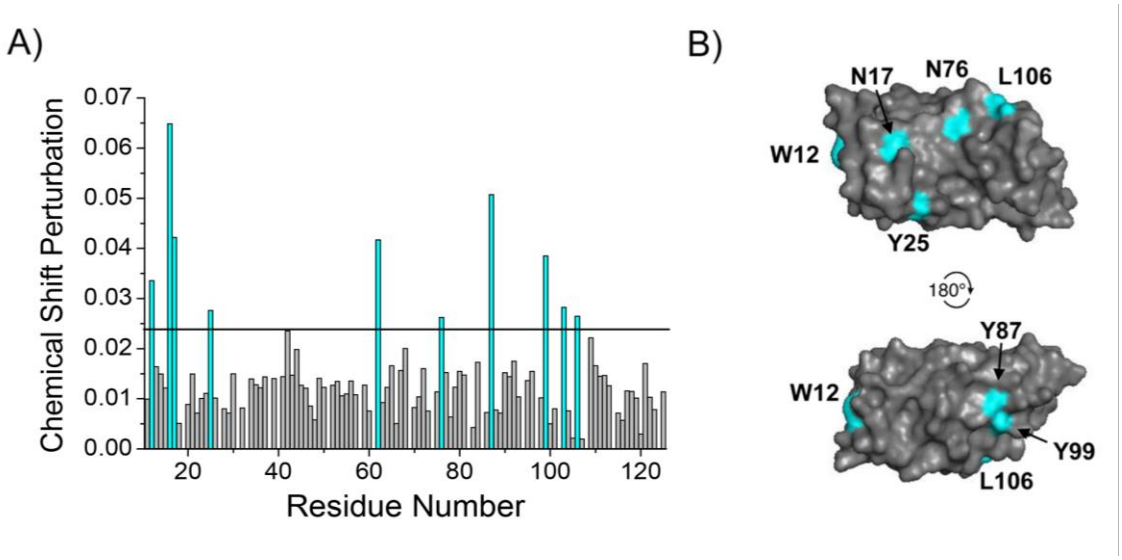


**Figure 4.6** (A) Monitoring the interaction between CTPR3 and Au(III) by NMR chemical shift perturbations. The solid line represents the average plus one standard deviation; positions above one standard deviation are colored cyan. (B) A surface model of CTPR3 where residues that bind gold ions are colored cyan. All figures were prepared from X-ray coordinates (PDB 1NA0) using Pymol.

While amino acid identity plays an important role in protein-gold ion interactions, the chemical environment of the side chain is crucial for complex formation. CTPR3 has three tryptophan residues in its sequence but only one of them binds Au(III). The shift for tryptophan

residues are shown in ***Figure 4.7A***; the red spectrum corresponds to CTPR3 and the purple spectrum to a 1:10 CTPR3 to $HAuCl_4$ solution. While the peaks for W46 and W80 overlap during the titration, indicating no change in chemical environment, the peak corresponding to W12 does shift. Examining the tryptophan residues in a space-filling model of CTPR3 (***Figure S7***) illustrates that the side chain of only W12 is available for π interactions, while W46 and W80 are sandwiched between neighboring residue's side chains. This indicates that in addition to the identities of the residue the overall orientation of the side chain are important in gold ion binding. Not only accessibility, but also the orientation of the side chain is a major factor in ion binding and needs to be taken into consideration when designing protein and peptide scaffolds for biomineralization.

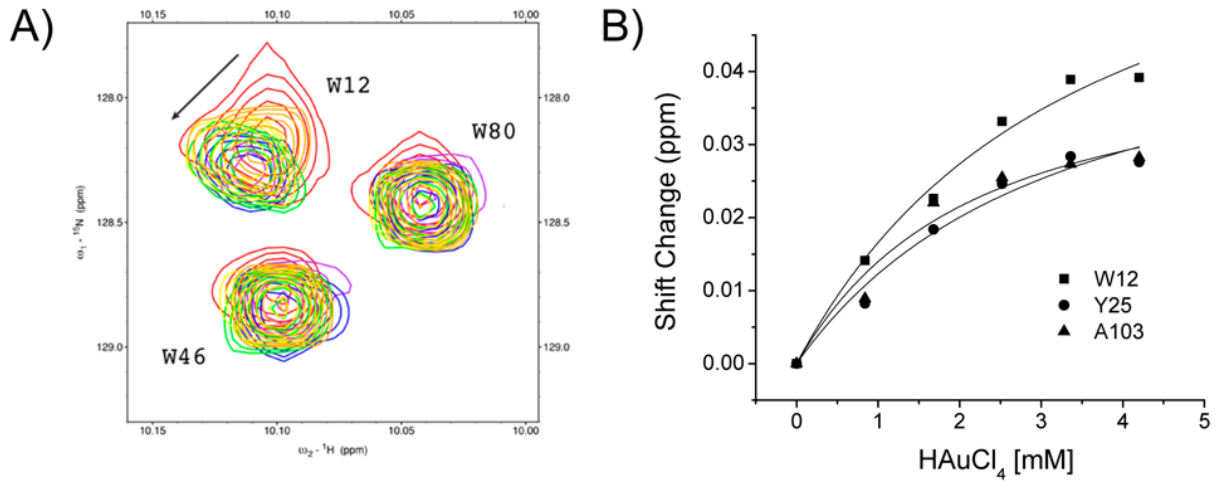


**Figure 4.7** (A) Overlay of three tryptophan peaks from the $^{1}H$-$^{15}N$ HSQC titration experiment, the red spectrum corresponds to pure CTPR3 and purple to 1:10 CTPR3 to $HAuCl_4$. Direction of peak shift for W12 denoted with arrow. (B) Binding isotherms for three residues determined from the NMR titration of CTPR3 with $HAuCl_4$.

The dissociation constant for W12, Y25, and A103 at an ionic strength of 225mM was determined from plotting the change in chemical shift as a function of ligand concentration (***Figure 4.7B***).[57] W12, Y25, and A103 have a $K_d$ of 3.1 ± 1.0, 1.8 ± 0.9, and 2.8 ± 1.3 mM respectively. Interestingly, all three interacting residues have similar binding. The low $K_d$ values

are due to weaker intermolecular forces occurring between the protein side chains and Au(III), such as π-metal interactions and hydrogen bonding. However, the macroscopic binding constant for cooperative multiple binding sites will be the product of individual events and thus higher in magnitude.

### 4.4.5 Protein orientation on gold NP surface

Gold NPs were formed *in situ* (***Figure 4.8A***) in a 1:12 molar ratio of CTPR3 to $HAuCl_4$ at pH 6 without addition of any external reducing agents. A $^{1}H$-$^{15}N$ HSQC experiment was then performed with this sample. The premise of this experiment is that protein relaxation parameters will charge if protein is bound to the NPs. Overlaying the NP/CTPR3 and pure CTPR3 spectra (***Figure S6***) shows no major change in peak positions, indicating the protein is still folded in the presence of NPs consistent with the results of CD spectroscopy (***Figure S2***).

When comparing the spectra of pure CTPR3 and CTPR3/NP there is an overall decrease in signal strength for all residues in the protein, consistent with signal being quenched in presence of NPs. However, some residues have a larger relative change in signal intensity than others. Residues located close to the NP surface exhibit restricted diffusion resulting in longer effective rotational correlation time and therefore a lower signal intensity.[65] Even though CTPR3 is in fast exchange with the NP surface there is a preferred face of the protein that interacts with the NP surface. ***Figure 4.8B*** compares the peak intensities of CTPR3/NPs to the solution containing pure CTPR3. All residues with a change in relative peak intensity below the black line (the average minus one standard deviation) are considered major changes. A surface model of CTPR3 is shown in ***Figure 4.8C*** with the Au(III) binding residues in cyan, the residues bound to the gold surface in magenta, and N17 which binds both the metal ion and gold NP surface in yellow.

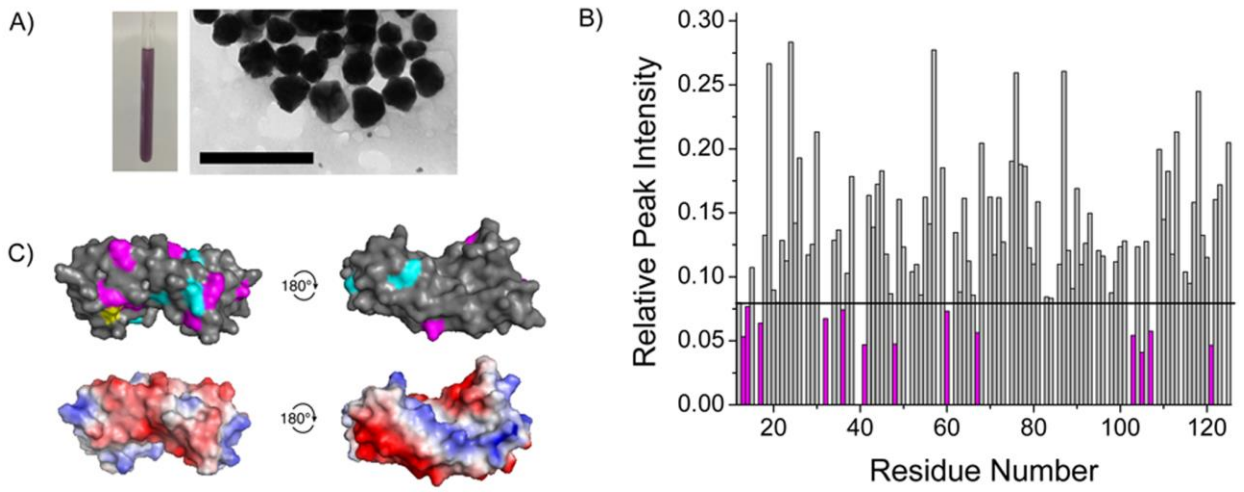


**Figure 4.8** (A) Picture of the NMR sample after NP formation and the corresponding TEM image of the NPs, scale bar 200 nm. (B) Relative peak intensity ($F_{CTPR3+NP}/F_{CTPR3}$) of $^{1}H$-$^{15}N$ HSQC of CTPR3 to CTPR3 after NP formation. Solid line represents average plus one standard deviation. Positions experiencing major reduction in intensity are colored maroon. (C) Top: CTPR3 surface model with residues binding Au(III) colored in cyan, residues binding gold surface in magenta, and N17 that interact with both in yellow. Bottom: An electrostatic potential map of CTPR3 with the surface charge shown, color range deep red to deep blue corresponds to an electrostatic potential range from -108 to + 108 kT/e, where k is Boltzmann's constant, T is absolute temperature, and e is the charge of a proton. All figures were prepared from X-ray coordinates (PDB 1NA0) using Pymol.

Interestingly, all residues interacting with the gold NP surface are localized on the more negative face of the protein, analogous to the trend seen with gold ions. The proximity of residues that bind to Au(III) to the NP surface indicates the importance of the initial Au(III) complexation step in determining the conformation of a protein on a NPs surface. Understanding this connection between initial ion complexation and final orientation of a protein on a metal NP surface will allow for control of the protein orientation in sensing and imaging applications.

## 4.5 Conclusions

We have used CTPR3, an engineered repeat protein, to probe a mechanism of protein assisted NP formation. Two different techniques, fluorescence quenching and heteronuclear 2D NMR, were used to observe CTPR3 interaction with both gold ions and gold NPs. We observed that the initial complexation step between gold ions and CTPR3 is ionic strength dependent.

Moreover, size and morphology of NPs can be tuned by adjusting the ionic strength. We ascertained the importance of residue identity, chemical environment, and orientation for gold ion-protein binding. Furthermore, we found that NPs preferentially interact with the negatively charged face of CTPR3 as observed in 2D NMR. The detailed understanding of protein-ion and protein-NP interactions will enable rational deign of proteins for biomimetic synthesis of metallic NPs. Knowledge of protein behavior in the presence of metal ions and NPs will facilitate design and implementation of biologically functional nanomaterials.

## 4.6 Acknowledgements

The authors would like to acknowledge Narasimhamurthy Shanaiah for his help with the NMR titration experiment; William Maza for his help with time resolved fluorescence, and the Nanoscale Characterization and Fabrication Lab (NCFL) for the use of the TEM facility. We appreciate the members of the Grove lab for their insightful discussion.

## 4.7 References

(1) Huang, X.; El-Sayed, M. A. *J. Adv. Res.* **2010**, *1*, 13.
(2) Zhang, X. *Cell Biochem. Biophys.* **2015**.
(3) Murphy, C. J.; Sau, T. K.; Gole, A. M.; Orendorff, C. J.; Gao, J.; Gou, L.; Hunyadi, S. E.; Li, T. *J. Phys. Chem. B* **2005**, *109*, 13857.
(4) Skrabalak, S. E.; Chen, J.; Sun, Y.; Lu, X.; Au, L.; Cobley, C. M.; Xia, Y. *Acc. Chem. Res.* **2008**, *41*, 1587.
(5) Ha, T. H.; Koo, H.-J.; Chung, B. H. *J. Phys. Chem. C* **2007**, *111*, 1123.
(6) Dykman, L.; Khlebtsov, N. *Chem. Soc. Rev.* **2012**, *41*, 2256.
(7) Schulz, A.; Wang, H.; van Rijn, P.; Boker, A. *J. Mater. Chem.* **2011**, *21*, 18903.
(8) Arakaki, A.; Shimizu, K.; Oda, M.; Sakamoto, T.; Nishimura, T.; Kato, T. *Org. Biomol. Chem.* **2015**, *13*, 974.
(9) Durupthy, O.; Bill, J.; Aldinger, F. *Cryst. Growth Des.* **2007**, *7*, 2696.
(10) Galloway, J. M.; Staniland, S. S. *J. Mater. Chem.* **2012**, *22*, 12423.
(11) Chiu, C. Y.; Ruan, L.; Huang, Y. *Chem. Soc. Rev.* **2013**, *42*, 2512.
(12) Prasad Shastri, V. *MRS Bull.* **2015**, *40*, 473.
(13) Meldrum, F. C.; Wade, V. J.; Nimmo, D. L.; Heywood, B. R.; Mann, S. *Nature* **1991**, *349*, 684.
(14) Hwang, L.; Zhao, G.; Zhang, P.; Rosi, N. L. *Small* **2011**, *7*, 1939.
(15) Li, Y.; Tang, Z.; Prasad, P. N.; Knecht, M. R.; Swihart, M. T. *Nanoscale* **2014**, *6*, 3165.
(16) Xie, J.; Zheng, Y.; Ying, J. Y. *J. Am. Chem. Soc.* **2009**, *131*, 888.

(17) Xie, J.; Lee, J. Y.; Wang, D. I.; Ting, Y. P. *Small* **2007**, *3*, 672.
(18) Lin, J.; Zhou, Z.; Li, Z.; Zhang, C.; Wang, X.; Wang, K.; Gao, G.; Huang, P.; Cui, D. *Nanoscale Res. Lett.* **2013**, *8*, 170.
(19) Singh, A. V.; Bandgar, B. M.; Kasture, M.; Prasad, B. L. V.; Sastry, M. *J. Mater. Chem.* **2005**, *15*, 5115.
(20) Geng, X.; Grove, T. Z. *RSC Adv.* **2015**, *5*, 2062.
(21) Carter, N. A.; Grove, T. Z. *Biomacromolecules* **2015**, *16*, 706.
(22) Grove, T. Ž.; Kostić, N. M. *J. Am. Chem. Soc.* **2003**, *125*, 10598.
(23) Grove, T. Z.; Osuji, C. O.; Forster, J. D.; Dufresne, E. R.; Regan, L. *J. Am. Chem. Soc.* **2010**, *132*, 14024.
(24) Grove, T. Z.; Forster, J.; Pimienta, G.; Dufresne, E.; Regan, L. *Biopolymers* **2012**, *97*, 508.
(25) Grove, T. Z.; Regan, L.; Cortajarena, A. L. *J. R. Soc. Interface* **2013**, *10*.
(26) Parker, R.; Mercedes-Camacho, A.; Grove, T. Z. *Protein Sci.* **2014**, *23*, 790.
(27) Mejias, S. H.; Sot, B.; Guantes, R.; Cortajarena, A. L. *Nanoscale* **2014**.
(28) King, N. P.; Bale, J. B.; Sheffler, W.; McNamara, D. E.; Gonen, S.; Gonen, T.; Yeates, T. O.; Baker, D. *Nature* **2014**, *510*, 103.
(29) Phillips, J. J.; Millership, C.; Main, E. R. G. *Angew. Chem. Int. Ed.* **2012**, *51*, 13132.
(30) Baumgartner, J.; Antonietta Carillo, M.; Eckes, K. M.; Werner, P.; Faivre, D. *Langmuir* **2014**, *30*, 2129.
(31) Gebauer, D.; Verch, A.; Börner, H. G.; Cölfen, H. *Cryst. Growth Des.* **2009**, *9*, 2398.
(32) Masica, D. L.; Schrier, S. B.; Specht, E. A.; Gray, J. J. *J. Am. Chem. Soc.* **2010**, *132*, 12252.
(33) Shiba, K.; Minamisawa, T. *Biomacromolecules* **2007**, *8*, 2659.
(34) He, G.; Dahl, T.; Veis, A.; George, A. *Nat. Mater.* **2003**, *2*, 552.
(35) Hume, J.; Chen, R.; Jacquet, R.; Yang, M.; Montclare, J. K. *Biomacromolecules* **2015**, *16*, 1706.
(36) Si, S.; Mandal, T. K. *Chem. Eur. J.* **2007**, *13*, 3160.
(37) Bhattacharjee, R. R.; Das, A. K.; Haldar, D.; Si, S.; Banerjee, A.; Mandal, T. K. *J. Nanosci. Nanotechnol.* **2005**, *5*, 1141.
(38) Si, S.; Bhattacharjee, R. R.; Banerjee, A.; Mandal, T. K. *Chem. Eur. J.* **2006**, *12*, 1256.
(39) Slocik, J. M.; Stone, M. O.; Naik, R. R. *Small* **2005**, *1*, 1048.
(40) Feyer, V.; Plekan, O.; Tsud, N.; Chab, V.; Matolin, V.; Prince, K. C. *Langmuir* **2010**, *26*, 8606.
(41) Xue, Y.; Li, X.; Li, H.; Zhang, W. *Nat. Commun.* **2014**, *5*.
(42) Djalali, R.; Chen, Y. F.; Matsui, H. *J. Am. Chem. Soc.* **2003**, *125*, 5873.
(43) Niide, T.; Shimojo, K.; Wakabayashi, R.; Goto, M.; Kamiya, N. *Langmuir* **2013**, *29*, 15596.
(44) Ueno, T.; Koshiyama, T.; Tsuruga, T.; Goto, T.; Kanamaru, S.; Arisaka, F.; Watanabe, Y. *Angew. Chem. Int. Ed. Engl.* **2006**, *45*, 4508.
(45) Cortajarena, A. L.; Kajander, T.; Pan, W.; Cocco, M. J.; Regan, L. *Protein Eng. Des. Sel.* **2004**, *17*, 399.
(46) Main, E. R.; Xiong, Y.; Cocco, M. J.; D'Andrea, L.; Regan, L. *Structure* **2003**, *11*, 497.
(47) Main, E. R. G.; Stott, K.; Jackson, S. E.; Regan, L. *Proc. Natl. Acad. Sci.* **2005**, *102*, 5721.
(48) Goddard, T. D.; Kneller, D. G. *SPARKY 3*; University of California: San Francisco.

(49) Smeets, P. J.; Cho, K. R.; Kempen, R. G.; Sommerdijk, N. A.; De Yoreo, J. J. *Nat. Mater.* **2015**, *14*, 394.
(50) Yang, T.; Li, Z.; Wang, L.; Guo, C.; Sun, Y. *Langmuir* **2007**, *23*, 10533.
(51) Xie, J.; Lee, J. Y.; Wang, D. I. C. *J. Phys. Chem. C* **2007**, *111*, 10226.
(52) Cañaveras, F.; Madueño, R.; Sevilla, J. M.; Blázquez, M.; Pineda, T. *J. Phys. Chem. C* **2012**, *116*, 10430.
(53) Selva Sharma, A.; Ilanchelian, M. *J. Phys. Chem. B* **2015**, *119*, 9461.
(54) Cortajarena, A. L.; Regan, L. *Protein Sci.* **2011**, *20*, 336.
(55) Lohse, S. E.; Burrows, N. D.; Scarabelli, L.; Liz-Marzán, L. M.; Murphy, C. J. *Chem. Mater.* **2014**, *26*, 34.
(56) Langille, M. R.; Personick, M. L.; Zhang, J.; Mirkin, C. A. *J. Am. Chem. Soc.* **2012**, *134*, 14542.
(57) Williamson, M. P. *Prog. Nucl. Magn. Reson. Spectrosc.* **2013**, *73*, 1.
(58) Sigal, G. B.; Bamdad, C.; Barberis, A.; Strominger, J.; Whitesides, G. M. *Anal. Chem.* **1996**, *68*, 490.
(59) Pensa, E.; Cortés, E.; Corthey, G.; Carro, P.; Vericat, C.; Fonticelli, M. H.; Benítez, G.; Rubert, A. A.; Salvarezza, R. C. *Acc. Chem. Res.* **2012**, *45*, 1183.
(60) Zhou, J. C.; Wang, X.; Xue, M.; Xu, Z.; Hamasaki, T.; Yang, Y.; Wang, K.; Dunn, B. *Mater. Sci. Eng. C* **2010**, *30*, 20.
(61) Ramezani, F.; Amanlou, M.; Rafii-Tabar, H. *Amino Acids* **2014**, *46*, 911.
(62) Yu, J.; Becker, M. L.; Carri, G. A. *Langmuir* **2012**, *28*, 1408.
(63) Schmidbaur, H.; Raubenheimer, H. G.; Dobrzanska, L. *Chem. Soc. Rev.* **2014**, *43*, 345.
(64) Joshi, H.; Shirude, P. S.; Bansal, V.; Ganesh, K. N.; Sastry, M. *J. Phys. Chem. B* **2004**, *108*, 11535.
(65) Lin, W.; Insley, T.; Tuttle, M. D.; Zhu, L.; Berthold, D. A.; Král, P.; Rienstra, C. M.; Murphy, C. J. *J. Phys. Chem. C* **2015**, *119*, 21035.

## 4.8 Supplemental Information

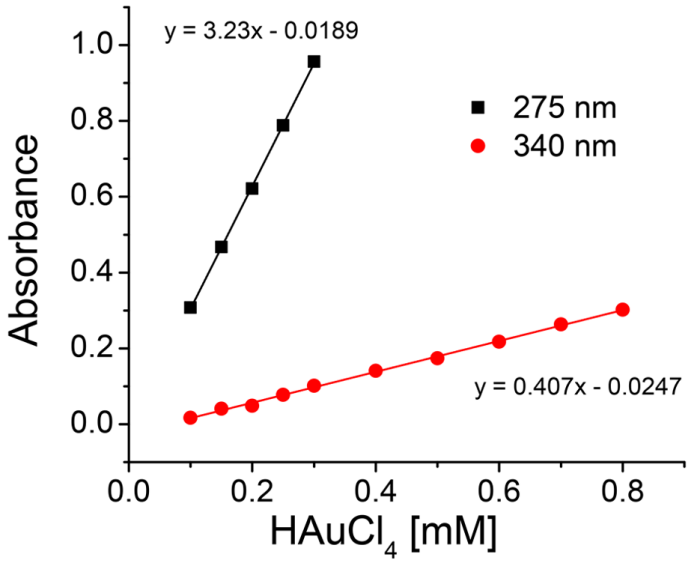


**Figure S1**. Beer-Lambert plots for $HAuCl_4$ at 275 and 340 nm.

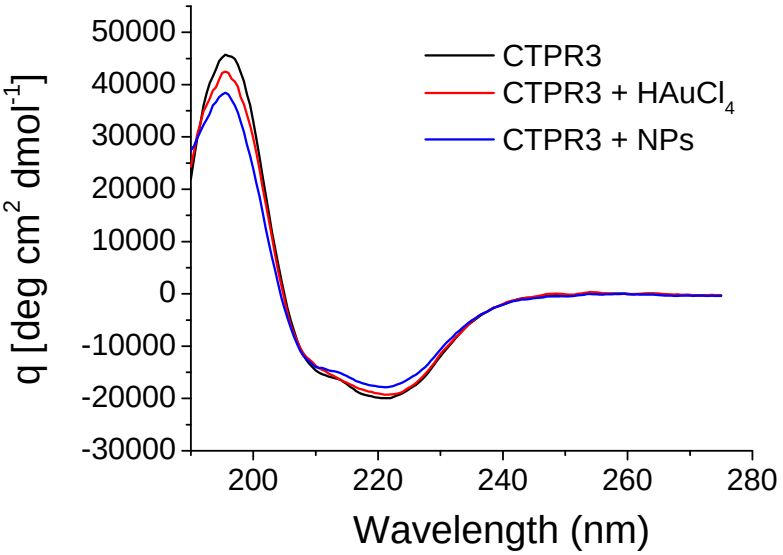


**Figure S2**. Circular dichroism (CD) spectra of CTPR3 (black), CTPR3 after titration with $HAuCl_4$ (red), and CTPR3 after formation of NPs (blue).

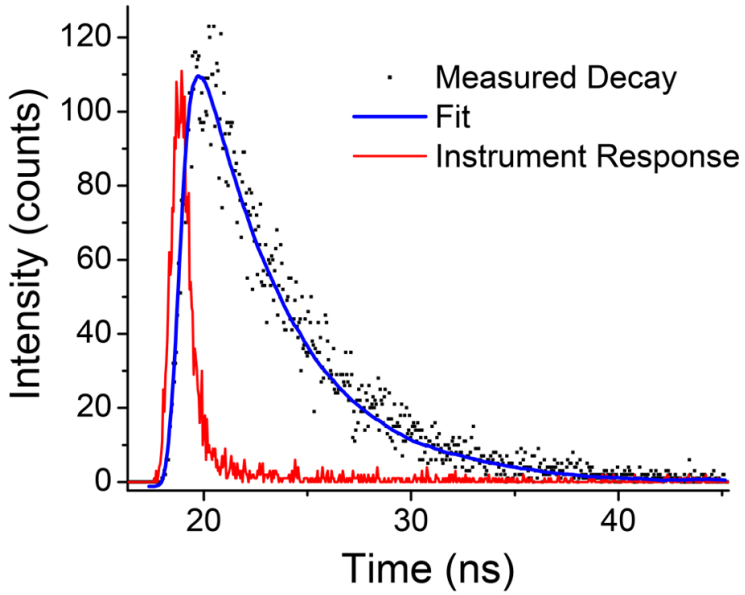


**Figure S3**. Time resolved fluorescence of CTPR3.

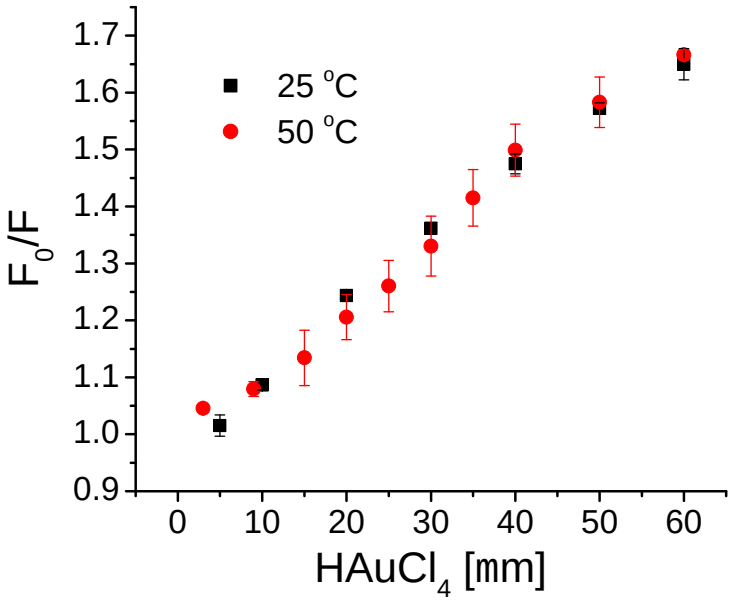


**Figure S4**. Fluorescence quenching of CTPR3 by $HAuCl_4$ at 25 °C and 50 °C.

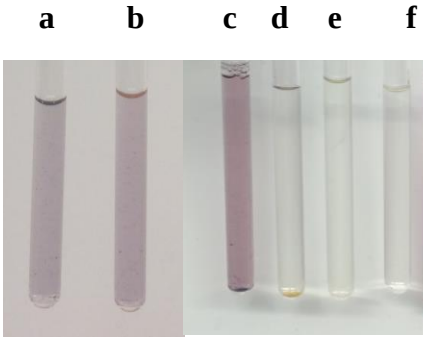


**Figure S5**. Images of NMR tubes after 3 weeks with $HAuCl_4$ in 5 mM $Na_2HPO_4$ (a & d), 5 mM $Na_2HPO_4$ and 230 mM NaCl (b & e), and 5 mM $Na_2HPO_4$ and 230 mM $NaNO_3$ (c & f). Samples a, b, and c also have CTPR3 in a 13:1 $HAuCl_4$ to CTPR3 ratio.

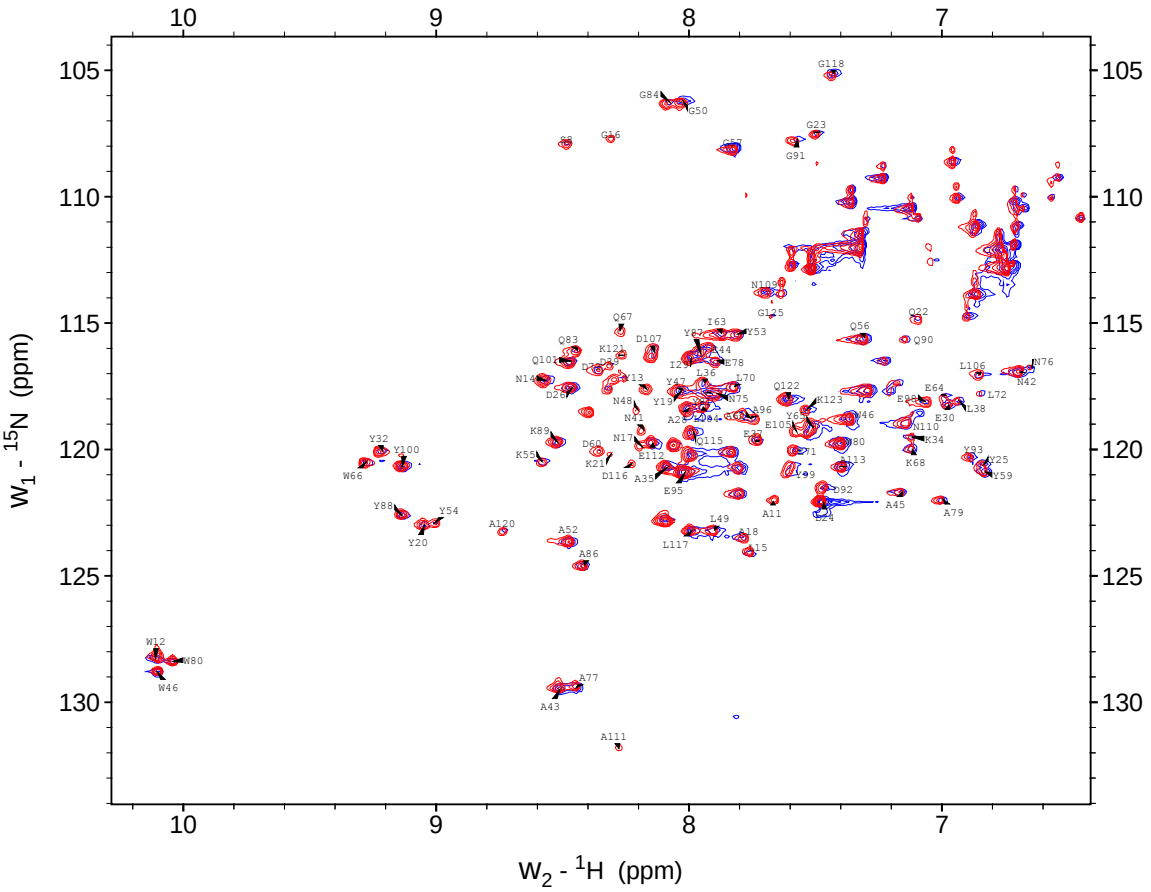


**Figure S6**. Overlay of $^{1}H$-$^{15}N$ HSQC spectra of CTPR3 (red) and CTPR3 sample after NP formation (blue).

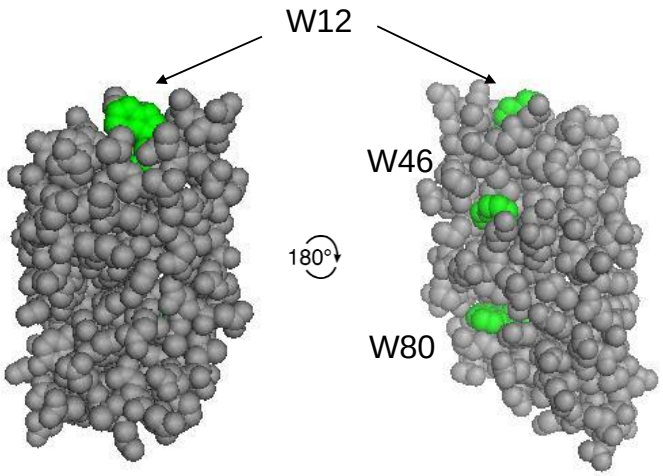


**Figure S7**. A space-filling model of CTPR3 with tryptophan residues in green.

# Chapter 5. Protein-aided formation of triangular silver nanoprisms with enhanced SERS performance

Xi Geng, Weinan Leng, Nathan A. Carter, Peter J. Vikesland and Tijana Z. Grove

Reprinted with permission from X. Geng, W. Leng, N. A. Carter, P. J. Vikesland, and T.Z Grove, *J. Mater. Chem. B*, **2016**, *4*, 4182-4190. 

**Attributions:** XG initiated the project, performed all the experiments as well as wrote the manuscript. WL and PJV offered technical assistance on SERS analysis. NAC assisted in SEM characterization. TZG supervised the project and edited the manuscript.

## 5.1 Abstract

In this work, we present a modified seed-mediated synthetic strategy for the growth of silver nanoprisms with low shape polydispersity, narrow size distribution and tailored plasmonic absorbance. During the seed nucleation step, consensus sequence tetratricopeptide repeat (CTPR) proteins are utilized as potent stabilizers to facilitate the formation of planar-twinned Ag seeds. Ag nanoprisms were produced in high yield in a growth solution containing ascorbic acid and CTPR-stabilized Ag seeds. Note that the percent yield were defined by the ratio of intact and truncated silver nanoprisms to the total number of Ag NPs, which is estimated based on the TEM and SEM observations. From the time-course UV-Vis and transmission electron microscopy (TEM) studies, we postulate that the growth mechanism is the combination of facet selective lateral growth and thermodynamically driven Ostwald ripening. The resultant Ag nanotriangles (NTs) exhibit excellent surface enhanced Raman spectroscopy (SERS) performance. The enhancement factor (EF) measured for 4-mercapto benzoic acid (4-MBA) reporter is estimated to be $3.37 \times 10^5$ in solution and $2.8 \times 10^6$ for SERS substrate.

## 5.2 Introduction

Plasmonic metallic NPs such as Au and Ag NPs have received immense attention due to their tailored localized surface plasmon resonance (LSPR) band in the visible and near infrared (NIR) regions.[1,2] Since the electromagnetic field induced by LSPR of NPs is strongly dependent upon the local dielectric environment, plasmonic NPs have been widely exploited for the molecular sensing, bioimaging and therapeutic applications.[3,4] Furthermore, the coupling of electromagnetic filed between adjacent NPs results in a significant amplification of the spectroscopic signals allowing for the implementation of plasmon-enhanced spectroscopic tools and other advanced optoelectronic devices.[5-7]

Optical, electronic, and catalytic properties of NPs are determined by their composition, crystal structures, as well as their geometric features.[1,8] The anisotropy at the nanoscale results in the unprecedented physical and chemical properties. Therefore, over the past two decades, remarkable progress has been made in the colloidal synthesis of a myriads of anisotropic NPs including nanowires,[9,10] nanorods,[11] nanoprisms[12,13] branched NPs,[14-16] etc. For example, the advent of Ag nanoprisms in the early 2000 has sparked tremendous research interest on the subject of 2D plate-like plasmonic nanostructures.[12] Discrete dipole approximation (DDA) simulation and UV-Vis spectral investigations have unambiguously confirmed dual LSPR modes corresponding to dipole and quadrupole.[12,17] The in-plane dipole LSPR is conveniently regulated by the aspect ratio of nanoparticle (edge length/thickness). Moreover, electron energy-loss spectroscopy (EELS) mapping identified the plasmonic hot spots at the sharp tips of the nanoprisms. These plasmonic hot-spots imbibe nanoprisms with the ultra-high chemical sensitivity that enables chemical and biological sensors for glucose, $Hg^{+}$, and DNA.[18-20]

Furthermore, the massive field enhancement of these tips facilitates the fabrication of high-performance surface enhanced Raman spectroscopy (SERS) probes.[5]

Hitherto, a wide variety of colloidal routes have been developed to prepare well-defined Ag nanoprisms.[21,22] Photo-induced approach through selective plasmon excitation triggers the transformation of Ag nanospheres into NTs with low polydispersity. [5,12,23,24] Despite high-precision control over the shape and size distribution of NPs, photochemical routes are time and energy-consuming processes that typically demand laser radiation and can only proceed at low concentration thus limiting yields. By contrast, thermal approaches, either in aqueous or organic solutions, provide simple and rapid routes towards high-yield production of Ag NTs. Particularly, ligand-assisted chemical reduction methods are easier to perform and have been widely adopted. For example polyvinyl pyrrolidone (PVP) and polyacrylamide (PA) with terminal hydroxyl groups serve as reductant and shape directing agent due to their excellent solubility and specific binding affinity to the metallic nanocrystals.[25,26] The fine shape control is realized by adjusting the ratio between metal precursor and the reducing agent.[26] Organic solvents such as dimethylformamide (DMF) and n-methyl-2-pyrrolidone (NMP) have also been used for the formation of Ag NTs at elevated temperatures.[27,28] In a seminal works by Mirkin and Yin's groups, $H_2O_2$ in synergy with citrate ions was used to selectively etch the facets of less-stable nanocrystals thereby promoting the nucleation of plate-like structures as well as the reconstruction of Ag NTs.[29,30]

Seed-mediated growth, proposed by Murphy et al. in their pioneering works on gold nanorods and nanospheres with tunable size [11,31] has been successfully extended to prepare well-defined Ag nanoprisms with low shape and size polydispersity. [13,32-36] Although multi-step protocols sacrifice the convenience of the traditional one-pot synthesis, the exquisite control over

the growth kinetics, and thus shape and size, is achieved by isolating the growth step from the initial nucleation of seeds. Notwithstanding that the underlying reasons by which the growth proceeds along one favourable orientation have not been indisputably addressed, seeded growth is believed to boost the symmetry breaking event during the course of shape evolution.[37] Synthetic polymers such as PVP, sodium polystyrene sulfonate (PSSS), and polyvinyl alcohol (PVA) have been widely used as the stabilizer and shape directing agents to aid the seeded-growth of 2D Ag nanoprisms.[38] Recently, Ag nanoprisms with large lateral dimension (~5 μm) and high aspect ratio (~400) have been realized by means of successive epitaxial deposition over multiple cycles.[39,40]

Biopolymer-assisted approaches have recently opened up the potential of the green-synthesis of anisotropic NPs at ambient conditions. [41-43] For instance, single crystalline Au nanoprisms have been prepared using plant extracts such as lemongrass,[44] and brown seaweed.[45] Additionally, the so-called shape directing proteins, albeit sequence and structure unknown, were isolated from the algal extract to produce Au nanoplates with distinctive triangular or hexagonal shapes.[42] However, research so far has been focused onto the one-pot biomimetic methods, which typically generate gold nanoprisms with rather large size and high shape polydispersity. Only few attempts have been made on the bio-assisted seeded growth of shape-selective noble NPs with improved morphological yield.[46,47]

Previously, our group has demonstrated that the morphology and optical properties of noble metal NPs could be modulated by the concentration and the structure of the CTPR proteins.[48] CTPR is a *de novo* protein sequence based on the tertratricopeptide repeat family.[49] CTPR, and repeat proteins in general are composed of the repeating structural motif. In the CTPR protein that motif is helix-turn-helix motif with 34 amino acids in length. If all repeats

have identical sequence, as is the case for CTPR, protein can be treated as a simple homopolymeric molecule, where the monomer is a single repeat.[50] Extending number of CTPR repeats results in a superhelical structure, where eight repeats (n = 8) comprise one full turn of the superhelix.[51,52] In this work, we use CTPR protein consisting of three repeats, which is the smallest stable molecule.[51] The sequence of CTPR protein and the circular dichroism (CD) spectrum indicative of the helical structure is shown in the Supporting information ***Figure S1***. The $^{1}H$-$^{15}N$ HSQC NMR and fluorescence quenching studies have been carried out in our lab to interrogate interaction between CTPR protein and noble metals.[53] Binding of the Au(III) to the CTPR is driven by overall electrostatics, with tryptophan, tyrosine and asparagine side chains coordinating metal ion. Guided by that knowledge, we hypothesized that CTPR will similarly interact with silver ions and thus exert control over the kinetics, crystalline structure and preferential growth of silver NPs.

In the present study, we developed a modified protocol for seed-mediated synthesis of 2D anisotropic Ag nanoprisms (***Scheme 1***). Herein, engineered repeat proteins, CTPRs, were used to prepare well-dispersed Ag seeds with inherent twinning defects. These spherical nuclei then direct the lateral growth of well-defined Ag nanoprisms with tunable size and optical properties. Time-course UV-Vis and TEM studies provided insights into the mechanism for the NPs evolution, whilst the roles of the protein has also been elucidated. As-prepared Ag nanoprisms exhibited remarkable SERS performance both in solution and on the solid substrate.

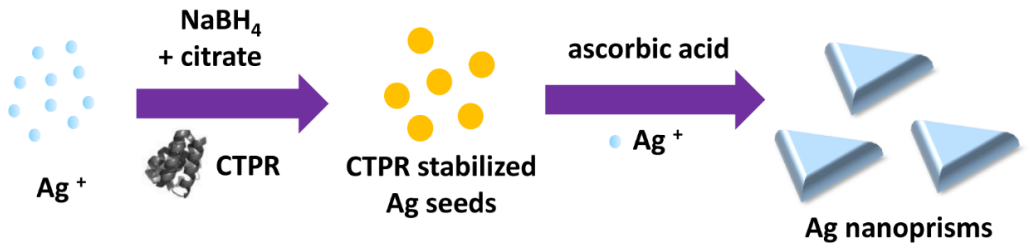


**Scheme 5.1** Schematic illustration of synthetic procedures for triangular Ag nanoprisms.

## 5.3 Experimental

### 5.3.1 Chemicals and reagents

Silver nitrate (>99.5%) was purchased from Fluka. Lysozyme was obtained from (Calbiochem) EMD Millipore Corporation. All other chemical reagents were acquired from Sigma-Aldrich and Fisher Chemicals and were used as received without further purification. Deionized water (18 MΩ/cm, Millipore Milli-Q) was exclusively used for preparing all aqueous solutions and for all rinsing procedures.

### 5.3.2 Expression and purification of CTPR proteins

CTPR proteins were synthesized through recombinant bacterial expression technology as described previously (***Figure S1***).[54,55] Synthetic genes for the desired protein in pPROEx vector, coding for N-terminal $(His)_6$ tag and ampicillin resistance, were transformed into *E .Coli* BL21(DE3) cells and cultured overnight at 37 °C on agar plates. A single colony was selected and incubated overnight in 50 mL of Luria−Bertani (LB) media containing 100 μg/mL of ampicillin. 10 ml of overnight cultures were then dispensed into 1 L of fresh LB media supplemented with 100 μg/mL ampicillin. The cells were grown in an incubator-shaker (250 rpm) at 37 °C until the optical density ($OD_{600}$) reached 0.8. Expression of CTPR3 and CTPR3 with terminal cysteine (CTPR3-cys) was induced with 1mM isopropyl β-D-thiogalactoside (IPTG) followed by 5 h expression at 37 °C, whereas CTPR6 and 18 were expressed at 18 °C for 16 h in an analogous manner. The cells were harvested by centrifugation at 5,000 rpm for 20 min and pellets were frozen at -80 °C until purification.

The cell pellets were re-suspended in lysis buffer consisting of 50 mM Tris, 300 mM sodium chloride and 0.1 wt% Tween 20. After 2 min sonication at 30% power using a microtip and Mison sonicator, lysed cells were centrifuged at 16,000 rpm for 30 min and protein

supernatant was purified using standard Ni-NTA affinity purification protocol. The N-terminal hexa-histidine tag was then cleaved from the CTPR proteins using TEV protease. The collected proteins were further purified by Akta Prime Plus size exclusion chromatography using Superdex 75 16/600 or 200 16/600 Prep Grade column in 150 mM sodium chloride and 50 mM sodium phosphate buffer at pH 8 with a flow rate of 0.5 ml/min. As a final step, the aqueous solutions of proteins were dialyzed against 10mM phosphate buffer three times at 4 °C using a dialysis cassette with molecular weight cutoff of 3.5k or 10k Da.[55]

### 5.3.3 Preparation of CTPR-stabilized Ag seeds and Ag prisms

Silver seeds were prepared by adding 5 ml 0.5 mM $AgNO_3$ at the rate of 2 mL/min using a syringe pump (KD Scientific) under vigorous agitation to the aqueous solutions of trisodium citrate (5 mL, 2.5 mM), $NaBH_4$ (0.3 mL, 10 mM) and CTPR proteins (0.125 mL 0.1-2 mg/ml) in a glass vial. In the ensuing step, fixed amount of CTPR-stabilized Ag seeds (10-200 μl) were added into the 5 mL 0.15 mM ascorbic acid aqueous solution, followed by the dropwise addition of 3 ml 0.5 mM $AgNO_3$ at the rate of 1 mL/min under stirring. A series of Ag seeds and Ag NPs were prepared in this manner under ambient condition by adjusting the concentration of both reactants and capping agents. BSA, lysozyme and CTPR proteins with different terminal functionalities and varied length (number of repeats) were employed as stabilizer and potential shape directing agents (***Figure S1***). The as-prepared Ag colloidal solution was centrifuged at 10,000 rpm for 20 min and the resultant pellets were rinsed with DI water to remove the residue stabilizer and reducing agent. After several purification cycles, the Ag NTs were re-dispersed into DI water for later SERS measurement.

### 5.3.4 Instrumentations

TEM and High resolution TEM (HR-TEM) analysis was performed on a Philips EM420 at an accelerating voltage of 120 kV and JEOL 2100 at 200 kV, respectively. TEM samples were prepared by applying a 7 μl sample solution on 300 mesh ultrathin carbon-coated Cu grids (EM Science), followed by drying overnight before observation. The thickness, as well as the size of Ag prisms, was measured from TEM images using Image J. The morphology of Ag NPs is also characterized using ZEISS 1550VP field emission scanning electron microscopy (FESEM). The UV-Vis spectra of Ag NPs were monitored using an Agilent Cary 100 Bio UV-Vis spectrophotometer. All UV-Vis measurements were conducted in 1cm path length PMMA cuvette at room temperature. SERS spectra were collected with a WITec alpha 500R using a 785 nm excitation source. Briefly, 10 μl of 10 mM 4MBA solutions were added into the 0.99 ml of purified Ag colloidal solutions, followed by incubating on a benchtop shaker for 12 h. The liquid samples were injected into a quartz cuvette (pathlength = 2 mm) for SERS analysis. The self-assembled Ag NTs SERS substrate was fabricated by drop casting of purified Ag NTs colloidal solution onto the Si wafer and then dried at ambient condition. 5 μl of 10 mM 4MBA solution was subsequently transferred onto the SERS substrate. Backscattered light was collected using 100× objectives at integration times of 1 s. The signal was dispersed using a 1200 groove/mm grating and the dispersed light was collected by a Peltier-cooled charge-coupled device (CCD). All SERS spectra reported for the cuvettes or substrates are average of 100 spectra collected over the identical focal area.[6]

## 5.4 Results and Discussion

Seeded-mediated synthesis of NPs is a versatile and robust methods that decouples growth stage from the initial nucleation thereby allowing for the precise control over the size and shapes of NPs.[37,56] In the presence of seed nanocrystals, the deposition of metal atoms onto the

pre-existing seeds is more favorable than homogenous nucleation due to the lower activation energy. With the aid of surfactant, the NP evolution is dictated by the crystal structure of seed as well as the surfactant templating effect.

### 5.4.1 Morphological characterization of CTPR-stabilized Ag seeds and Ag nanoprisms

In the seed-nucleation step, spherical Ag NPs with the particle size ranging from 3-5 nm were produced in the presence of sodium citrate and CTPR3 protein, where 3 stands for three tandem repeats of the 34 amino acid sequence (***Figure 5.1***). Additionally, a large number of Ag nanoclusters (<2 nm) were formed through rapid reduction of $AgNO_3$ by $NaBH_4$ (***Figure 5.1a***). Golden yellow colloidal solution of CTPR3-stabilized Ag NP has the extinction peak at 408 nm. The distinctive twinning boundaries, which is regarded as one of the key prerequisites for the subsequent epitaxial growth of 2D planar nanoprisms have been observed in HR-TEM images of Ag seeds (***Figure 5.1a inset)*** .[57] The as-prepared Ag seeds were kept in the dark till further use to

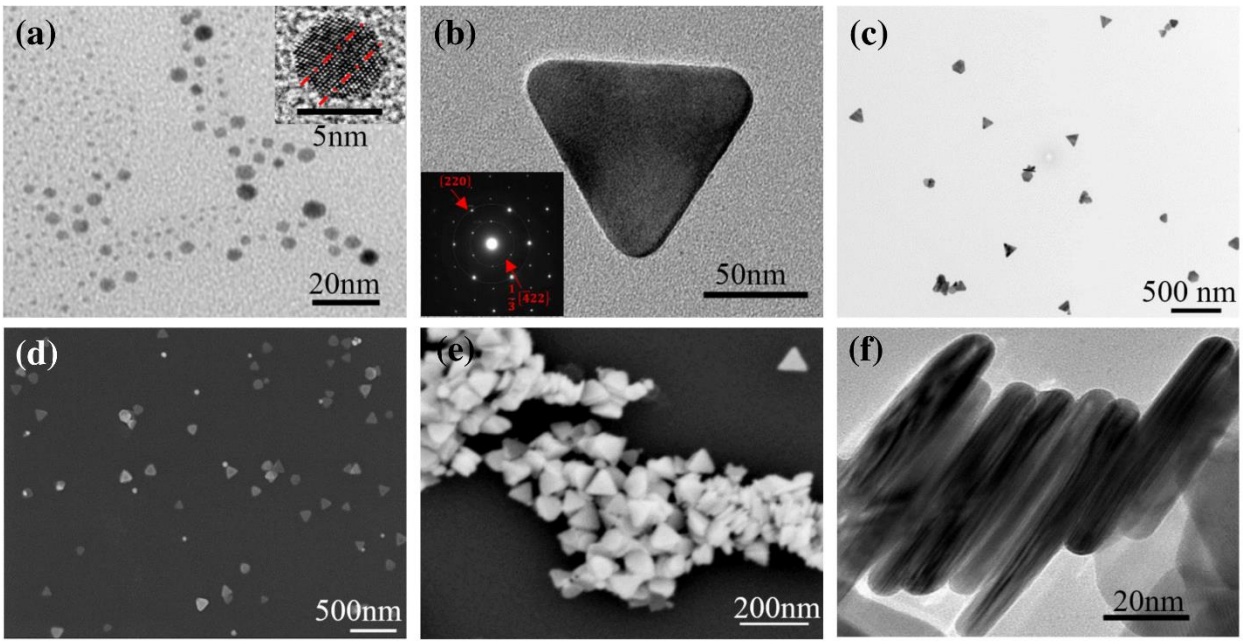


**Figure 5.1** (a) TEM image of CTPR3-Ag seeds (inset: HR-TEM of twinning nanocrystal) (b) HR-TEM image and selective area diffraction (SAED) pattern of Ag NT (c) TEM image and (d) SEM image of Ag NTs prepared using 20 µl CTPR3-Ag seed. Thickness of Ag nanoprisms was determined from SEM (e) and TEM (f) images.

circumvent the interference such as homogeneous nucleation arising from the residual $NaBH_4$. In the subsequent step, fast seed addition and dropwise $AgNO_3$ injection into the reaction mixture enabled the rapid growth of high-quality anisotropic nanoprisms **(*Figure 5.1b*).**[13]

Single crystalline structure of Ag prisms with the lattice spacing of 0.144 nm was confirmed by HR-TEM and selected area diffraction (SAED) pattern indexed as (220), whilst the flat top face was ascertained by the weak SAED diffraction spots corresponding to the forbidden 1/3 (422) specific for planar Ag or Au NTs (***Figure 5.1b inset***).[12] The average length of NTs is approximately 102.8 ± 18.9 nm as illustrated in the representative TEM and SEM images of Ag NTs (***Figure 5.1c-e***). The thickness of Ag NTs is estimated to be 8.8 ± 2.0 nm from the images of vertically stacked NTs (***Figure 5.1e, 1f***). The synthetic route is robust and reproducible - over 85% of the NPs are NTs or partially truncated NTs before any purification process. The absence of CTPR3 during the seed growth step results in a poor yield of Ag NTs under same experimental conditions.

### 5.4.2 Mechanistic investigation on the formation of Ag NTs

#### 5.4.2.1 Effect of citrate

We further investigated if citrate can be omitted from the seed-growth step and if CTPR3 solely could be used to adequately regulate the growth of Ag seeds. The LSPR intensity of Ag nanospheres increased by 20% in the absence of citrate but is accompanied by a broadening of the full with at the half maximum (FWHM) of the plasmon absorption peak, indicative of higher polydispersity (***Figure S2a)***. However, NPs prepared with these seeds lack dipolar in-plane LSPR absorbance at the NIR region indicating that these seed are inefficient in activating the formation of Ag prisms (***Figure S2b)***. In fact, NPs with variety of shapes including the spheres, nanorods and nanoprisms are produced under this condition (***Figure S2c***). Our observation is in

a good agreement with the earlier literature reporting that the citrate anions are critical for the transformation of spherical Ag NPs to Ag NTs.[58] Both CTPR and citrate are thus indispensable for the high-yield production of Ag NTs through seed-mediated process. Since only very low quantities of citrate or CTPR3 are present during the seeded-growth step, face-selective growth of Ag NTs is primarily driven by the innate planar twinning defects of Ag seeds rather than the strong absorbance of capping agents on the (111) facets of the Ag NTs. Moreover, we have also carried out the control experiment in which 23 μg/ml CTPR was added during the growth step instead of the seed nucleation step. The present CTPR in this step dramatically reduced the reaction kinetics leading to poor yield of Ag nanoparticles that were primarily nanospheres.

**5.4.2.2 Effect of ascorbic acid**

Since the shape-control in the synthesis of anisotropic Ag NPs is typically achieved by adjusting the ratio of ascorbic acid (AA) to metal precursors, Ag crystal growth was performed under the condition of varied concentration of AA. The $\lambda_{max}$ of LSPR red shifted slightly to ca. 850 nm when the ratio of AA to Ag was doubled (***Figure S3a)***. This result can be rationalized by the extended edge length arising from the accelerated lateral deposition of Ag(0) atoms onto the edge of Ag NTs with high surface energy. With the further increase in [AA]/[$Ag^+$] ratio and thus the reaction rate, the self-nucleation process could not be efficiently inhibited,[56] resulting in a thermodynamically favourable products such as cuboctahedra or quasi-globular Ag NPs enclosed by a mixture of both (111) and (100) facets. Excess of AA is also considered to induce undesirable defects onto the Ag NTs such as dislocations and stacking faults leading to the deformation of NTs and gradual damping of the LSPR intensity (***Figure S3a-b***). According to the UV-Vis profile and TEM images, the ratio of [AA]/[$Ag^+$] in the range from 0.5 to 1 is needed for the high-yield of well-defined nanoprisms with intact outlines.

### 5.4.2.3 Morphology development

During the course of the reaction outlined in the ***Figure 5.2***, the transformation of ultrafine spherical Ag seeds to 2D nanoprisms with rounded edges and eventually Ag NTs was revealed by the gradual color change from pale yellow to ruby red, then blue and finally purple. To elucidate the underlying growth mechanism, parallel experiments were performed in which fixed volume of $Ag^+$ precursors was added to the solution of CTPR3-Ag seeds followed by rapid injection of 0.5 ml 25 mM citrate to suppress continuous growth, i.e. quench reaction. As shown in the ***Figure 5.2***, the initial injection of 0.05 ml $AgNO_3$ was rapidly reduced by the excess of AA promoting the enlargement of the spherical Ag seed and leading to the formation of small 2D Ag NPs with disk-like or triangular contour. Addition of 0.1 ml $Ag^+$ led to the lateral growth of the NPs on the relatively high-energy facets such as (110) and (100). Concurrently, a large amount of small Ag nanoclusters (stage II) is produced. Intriguingly, only triangles or disks with the size around 40nm are observed after addition of 0.2 ml of $AgNO_3$, whereas quasi-spherical Ag NPs and majority of nanoclusters almost disappeared (stage III). This is likely due to the Ostwald ripening, i.e. small nanoclusters or nanospheres composed of a large number of surface atoms are etched by $O_2$ provided during the vigorous agitation, followed by the condensation onto the adjacent larger NPs, preferentially at the higher edge sites.[59] As clearly seen in the ***Figure 5.2 inset***, some protrusions and fused small hemi-spheres are identified on the top and the edge of the Ag NTs. Further increase in the precursor amount allows for the continuous lateral deposition of Ag(0) onto the Ag prisms in a face-selective manner and the round disks are converted to NTs (stage IV). The structural transition from small triangles to round disks and finally back into large triangular nanoprisms have been previously observed by Yin et al.[60] The

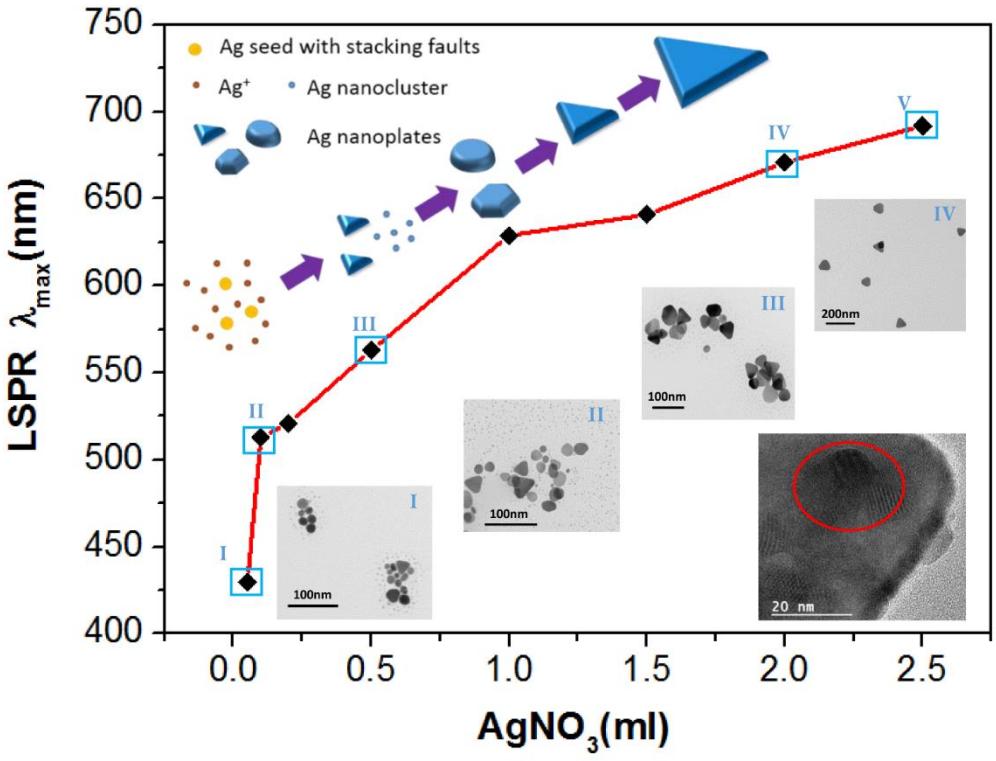


**Figure 5.2** Mechanism of Ag NTs formation. LSPR wavelength and TEM images corresponding to different injection volume of 0.5 mM $AgNO_3$. Inset: HR-TEM of protrusions fused onto the nanoprisms.

individual edge of small triangles formed at the early stage are composed of one hcp facet sandwiched by one (111) and one (100) fcc facets of varied thickness.[35] The preferential deposition of Ag on (100) sub-facets leads to the formation of intermediates such as truncated hexagonal nanoplates or round disks possessing a mixture of (100) and (111) bounded edges. The shape evolution ceases when all the (100) facets disappear, accompanied by the formation of intact triangles. The observed LSPR red shift of the $\lambda_{max}$ - 408 nm→430 nm→513 nm→623 nm - is consistent with the proposed mechanism and shape evolution from the small Ag seeds to bigger Ag nanospheres to small 2D nanoprisms and finally larger NTs (***Figure 5.2 and S4***). We surmise that following two mechanisms act in concert: (1) atom by atom deposition of newly reduced Ag(0) onto the

high-energy edges of preformed nanoprisms; and (2) dissolution and merging of tiny spherical NPs and nanoclusters onto the anisotropic 2D NTs.[61]

**5.4.2.4 Effect of CTPR3 sequence on the Ag seeds and Ag NTs.**

To further explore the distinct role of CTPR3, control experiments were performed in which commercially available Bovine Serum Albumin (BSA) and lysozyme were utilized as stabilizers in the synthesis of Ag seed. Additionally, we also prepared Ag seed in the absence of CTPR3 as shown in the ***Figure S5a***. Well-dispersed Ag seeds were prepared in the presence of BSA, even though the FWHM of UV-vis absorbance is broader than for seeds prepared with CTPR3 indicating the higher size polydispersity. In sharp contrast, severe agglomeration of lysozyme-Ag NPs occurs resulting in a broad hump in the UV-vis spectra (***Figure S5a***).

Next, we proceeded with NT synthesis. 20 μl of as-prepared Ag seeds stabilized with either CTPR3, BSA, or lysozyme were used in reaction as described. Whereas the colloidal solution synthesized using CTPR3-Ag seeds exhibit strong absorbance peaks at the NIR region (793 nm), ascribed to the characteristic in-plane dipolar LSPR band for Ag NPs (***Figure S5b***), no apparent LSPR bands were identified in the NIR region of colloidal solutions prepared using other seeds. This observation is consistent with TEM images where NPs prepared with CTPR3 seeds are well-defined NTs with narrow size distribution (***Figure S5c***) but variety of shapes is present when using other Ag seeds (***Figure S5d-f***).

The observed effect of protein used on Ag NP synthesis can be rationalized by closer inspection of protein physicochemical properties. CTPR3 and BSA have similar pI values, 4.5 and 4.7, respectively but BSA has almost five times larger molecular weight. Additionally, CTPR3 does not contain any thiols whereas BSA does. On the other hand CTPR3 and lysozyme are similar size, but lysozyme has pI of 11.35. Thus we suggest that neither thiols nor positive

charge are favourable for the growth of NTs. The cysteine or disulphide moieties - present in both BSA and lysozyme – have strong binding affinities for Ag and potentially inhibit both the growth of low-energy (111) top facet and the lateral growth of high energy (110), (100) facets on the edges. Concurrently, the positive charges and sulfhydryl and disulphide functionalities may also leads to the undesirable assembly of NPs as shown in the ***Figure S5d-e***.

To date, a series of amino acid residues have been extensively exploited to modify the surface properties or regulate the growth of metal NPs.[62-65] In particular, terminal poly-histidine and cysteine tag is often deliberately engineered into the protein or peptide for the controlled assembly or patterning of NPs.[66-70] To better understand the tolerance of described synthetic strategy to modifications of CTPR3, we performed Ag NTs synthesis using either CTPR3 with N-terminal poly-histidine tag or CTPR3 with engineered C-terminal cysteine. Although the UV-vis spectra of colloidal solution containing Ag seeds is identical in all cases (***Figure S6a***), the intensity of LSPR peaks is noticeably lower for Ag NTs prepared via CTPR3-cys-Ag seed in contrast to its counterparts (***Figure S6b***). Ag NPs with large size and shape polydispersity are generated in reaction with CTPR3-cys Ag seeds similar to the observation for BSA-Ag seeds (***Figure S6c***). Conversely, reaction with poly-histidine CTPR3 seeds resulted in the formation of fully-developed triangles with small degree of truncations and snips (***Figure S6d***).

Although the specific interactions between CTPR3 and Ag NPs are yet not known, we hypothesize that abundant aromatic residues, i. e. tyrosine and tryptophan in CTPR sequence play the role analogous to polystyrene sulfonate or aromatic surfactant, such as benzyldimethylhexadecylammonium chloride[10] in promoting the growth of high-quality Ag seeds. Rather than through facet-selective adsorption or so-called surfactant templating mechanism, the precise shape control is attained primarily due to the nature of twinned crystal

seeds setting stage for the plate-like structures during the growth stage. CTPR sequence also contains negatively charged aspartate residues that have been shown to be advantageous for the high yield synthesis of nanoplates.[65] Furthermore, the electrostatic repulsion due to surface charges precludes the NP fusion process during the seed formation and the initial NT growth step,[24] thus improving the colloidal stability and reducing the polydispersity. In contrast to our previous findings that protein shape may exert an appreciable impact on the growth and morphology of gold NPs,[48] the morphology as well as the optical properties of Ag NTs are independent or the size and shape of the CTPR repeat protein. (***Figure S6a, b, e***)

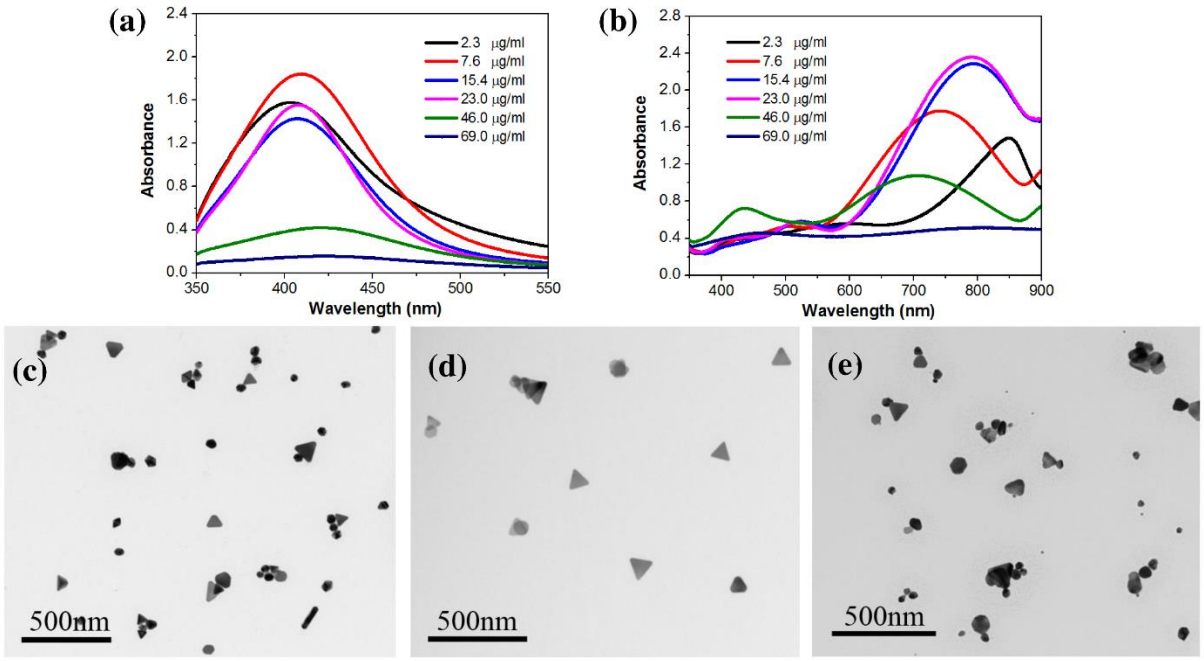


**Figure 5.3** UV-vis of (a) Ag seeds prepared with the increasing CTPR3 concentration (b) Ag NPs prepared using the corresponding CTPR-Ag seeds; (c, d, e)TEM images of Ag NPs prepared using 20 μl CTPR3-Ag seed (2.3 μg/ml; 15.4 μg/ml; 46 μg/ml of protein).

**5.4.2.5 Effect of CTPR3 concentration.**

Since CTPR3 has been confirmed to improve the quality of the Ag seeds as well as the overall morphological yield of the Ag NTs, we explored the optimal CTPR3 concentration. With the increase in the CTPR3 concentration from 2.3 μg/ml to 15.4 μg/ml, the LSPR band of

CTPR3-bound Ag seeds was slightly narrowed (***Figure 5.3a***). Further increase in CTPR3 concentration caused dramatic attenuation of the LSPR intensity, potentially as a consequence of complexation between $Ag^+$ and CTPR leading to the slow reaction. Ag seeds prepared in the presence of lower concentration of CTPR3 (2.3 μg/ml-23 μg/ml) are indeed more favourable for the subsequent NT formation (***Figure 5.3b, d***).

When Ag NPs are prepared using CTPR3-Ag seed with low concentration of CTPR3 (2.3 μg/ml), not only Ag triangles but tetrahedron, octahedron, and pentatwins bounded with (111) facets are concurrently produced (***Figure 5.3c***). The larger shape polydispersity is probably due to the poor quality of seeds containing defects like multi-fold twining structures. Contrary to that, excessive amount of CTPR3 (>46 μg/ml) may significantly slow down the nucleation rate of Ag seeds and cause detrimental effect on the follow-up synthesis of Ag NTs. Indeed, small-sized quasi-globular NPs and NTs with irregular contours are observed in the TEM images (***Figure 5.3e***). This observation implies that the suppression of growth is no longer limited to the (111) on the top faces but also takes place on reactive concave and convex facets at edges. The appearance of vast number of small nanoclusters around the NPs also indicate that the hypothesized Ostwald ripening is to some extent halted under such circumstance. Therefore, CTPR3 concentration ranging from 15.4 to 23 μg/ml is proposed as the optimal concentration during the seed nucleation step.

A small shift (408 nm →415 nm) and minor loss in LSPR intensity (11%) for Ag seeds occurred after storage in the dark for two weeks (***Figure S2a***). Although LSPR of NTs undergoes a slight blue shift (793 nm → 765 nm), the yield and the morphology of the Ag NTs resembles that of Ag NTs prepared using fresh Ag seeds (***Figure S2b, 2d)***. Overall, both CTPR3-functionalized Ag seeds and the resultant Ag NTs exhibit excellent colloidal stability and

structural integrity at ambient condition since no significant precipitation or peak broadening occurs during the storage. The long-term colloidal stability could be further improved by storing NPs in oxygen and halide free environment and by applying extra capping agent.

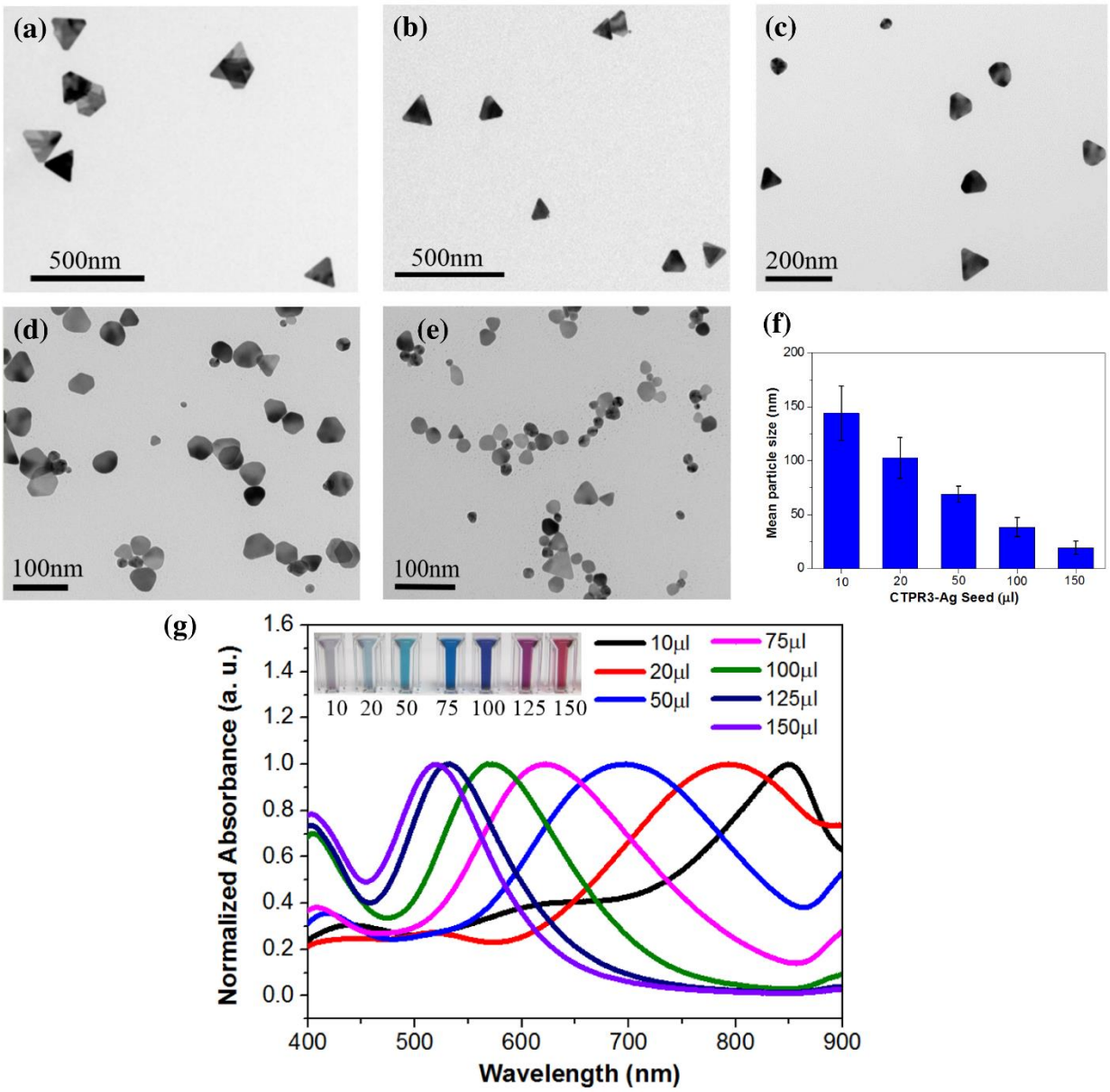


**Figure 5.4** TEM images of selected samples prepared using (a) 10, (b) 20, (c) 50, (d) 100, and (e) 150 µl CTPR3-Ag seed, (f) Mean particle size vs volume of seeds, (g) UV-Vis spectra and the photographic images of the collodial Ag NTs solutions obtained using different volume of seeds.

### 5.4.3 Tailoring morphology and plasmon bands of Ag nanoprisms through adjusting the amount of CTPR3-Ag seeds

One striking advantage of the seed-mediated protocol is that the LSPR could be conveniently tuned to span a broad spectral range, from visible to NIR region (500-900 nm), through the variation of the quantities of Ag seeds used during the growth step.[35] Precise control over the LSPR is attainable when less seeds (<100 μl) are used. Otherwise, bimodal absorbance profile is observed, attributed to the competitive growth between isotropic nanospheres and facet-selected NTs in the presence of a large number of nuclei (***Figure 5.4g***). The LSPR features are strongly dependent upon the morphological features of the Ag NTs including their edge length, thickness as well as the sharpness of the vertexes.[21] As the total number of seeds increased, the mean particle size declined steadily and the resultant Ag NPs underwent a progressive shape transition from triangular nanoprisms to round disks ***(Figure 5.4a-e)***. The remarkable change in the shape and size consequently bring about the dramatic blue shift of LSPR absorbance as shown in the ***Figure 5.4g***.

### 5.4.4 SERS performance and EF calculation

The SERS performance of the Ag NTs was investigated using 4-MBA as reporter molecules. As illustrated in the ***Figure 5.5a***, 4MBA tagged Ag NTs exhibited two intense peaks at 1078 and 1590 $cm^{-1}$, which could be assigned to the characteristic aromatic ring-breathing mode.[71] The enhancement factor (EF) was estimated using the equation (1) for SERS probe in the solution and equation (2) for SERS substrate:

$$EF = (I_{SERS}/I_{Sol}) \times (C_{Sol}/C_{SERS}) \quad (1)$$

$$EF = (I_{SERS}/I_{bulk}) \times (N_{Bulk}/N_{SERS}) \quad (2)$$

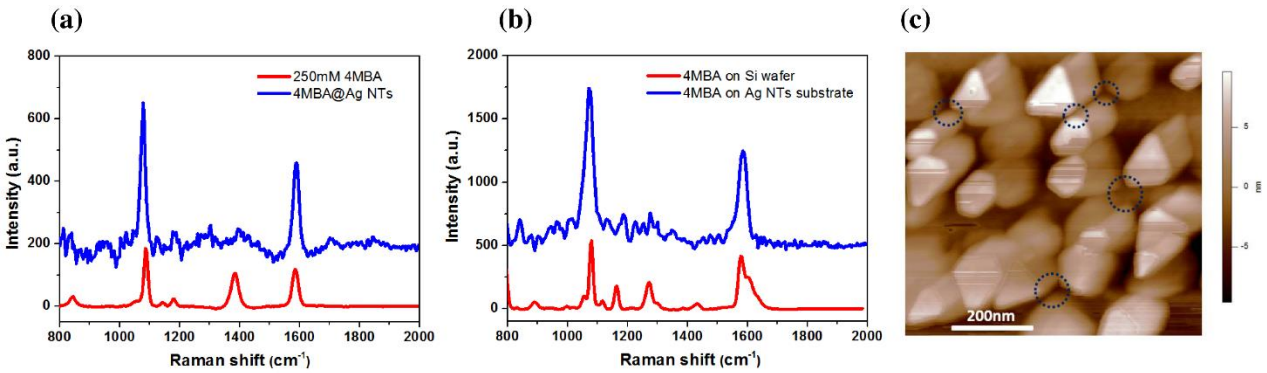


**Figure 5.5**. Raman spectra of (a)250 mM 4MBA in the solution containing 1M NaOH and 4MBA-taged Ag NTs colloidal solution. (b)4MBA on Si wafer and on the Ag NTs SERS substrate (c) Representative AFM images of SERS substrate prepared by drop casting Ag NTs onto the silicon wafer.

where $I_{SERS}$ and $I_{Sol}$ are the peak intensities of 1078 $cm^{-1}$ for the 4MBA@Ag solution and 0.5 M 4MBA solution in 1M NaOH, $C_{SERS}$ ($N_{SERS}$) and $C_{Sol}$ ($N_{Sol}$) are the concentration(number) of SERS sample and ordinary 4MBA. Assuming that a monolayer of 4MBA molecule with a footprint of 0.54$nm^2$ is adsorbed onto the Ag prisms in solution, the EF value is estimated to be $3.37\times10^5$. This value could be slightly underestimated due to the incomplete surface coverage (SI for detailed calculation).[5] Alternatively, we can also evaluate the EF for SERS substrate by making comparison between the SERS signal of 4MBA on Ag NTs substrate and the Raman signal of the 4MBA bulk sample on Si wafer (***Figure 5.5b***). By using identical measurement parameters including the accumulation time and laser focal volume, the EF value is estimated to $2.8\times10^6$. Previous study has shown that 63 hot spots per million SERS sites contribute 24% of the overall signal intensity.[72] As compared with other SERS surfaces,[73,74] Ag NTs-based SERS substrate may exhibit the following features. (a) As indicated in both ***Figure 5.5c*** and ***Figure S7***, a few bowtie–like structures are observed in which two Ag NTs are facing tip to tip with a few nanometer gap. This well-oriented bowtie patterning has been previously shown to make a great enhancement on Raman signals.[75] (b) Additionally, the close packing of adjacent Ag NTs may

also provide a number of potential hot spots that may significantly amplify the electromagnetic field thereby obtaining higher EF value.[5] Thus we hypothesized that the near-filed coupling between adjacent NPs with sharp tips will generate a large number of hot spots further augmenting the EF value. Undoubtedly, the as-prepared Ag prisms with well-defined morphologies and sharp vertices can serve as highly active SERS-tags or substrate materials for the sensing and detection of trace amount of analytes.

## 5.5 Conclusions

In summary, CTPR repeat proteins have been explored for the bio-enabled synthesis of anisotropic Ag nanoparticles. We presented a facile and rapid synthetic strategy for the preparation of Ag nanoprisms at ambient condition based on a CTPR-assisted seed-growth. Through the systematic study of various experimental parameters, we found that the presence of CTPR3 is pivotal for the production of well-dispersed planar-twinned seeds necessary for the high-yield growth of Ag nanotriangles with low polydispersity. The well-defined Ag nanoprisms are fabricated using ca. 23 μg/ml CTPR3 during the seed nucleation step while the AA to $AgNO_3$ ratio ranging from 0.5-1 is preferred during the NTs growth step. Furthermore, we provide insights in the mechanism of the Ag NTs generation. The facet selective epitaxial growth and thermodynamically driven Ostwald ripening act concurrently to yield ca. 100 nm edge-length and 8nm thickness Ag NTs. Plasmon absorbance ranging from visible to NIR region can be tailored by adjusting amount of CTPR3-stabilized seed in the reaction. These Ag NTs exhibit excellent SERS performance. The EF using 4-MBA reporter molecule is estimated to be $3.37 \times 10^5$ for Ag NT based SERS probe in solution and $2.8 \times 10^6$ for solid substrate.

## 5.6 Acknowledgements

The authors would like to thank Dr. Guoliang Liu and Clayton Scruggs for insightful comments, suggestions, and discussion on this research work. Author acknowledge ICTAS Nanoscale Characterization and Fabrication Lab (NCFL) for the use of AFM, TEM, and SEM. This work was in part supported by the JFC ICTAS grant number 119106 to TZG.

## 5.7 References

(1) Pastoriza-Santos, I.; Liz-Marzan, L. M. *J. Mater. Chem.* **2008**, *18*, 1724.
(2) Zhang, Q.; Tan, Y. N.; Xie, J.; Lee, J. Y. *Plasmonics* **2008**, *4*, 9.
(3) Dreaden, E. C.; Alkilany, A. M.; Huang, X.; Murphy, C. J.; El-Sayed, M. A. *Chem. Soc. Rev.* **2012**, *41*, 2740.
(4) Tokel, O.; Inci, F.; Demirci, U. *Chem. Rev.* **2014**, *114*, 5728.
(5) Xue, B.; Wang, D.; Zuo, J.; Kong, X.; Zhang, Y.; Liu, X.; Tu, L.; Chang, Y.; Li, C.; Wu, F.; Zeng, Q.; Zhao, H.; Zhao, H.; Zhang, H. *Nanoscale* **2015**, *7*, 8048.
(6) Leng, W.; Vikesland, P. J. *Anal. Chem.* **2013**, *85*, 1342.
(7) Lane, L. A.; Qian, X.; Nie, S. *Chem. Rev.* **2015**, *115*, 10489.
(8) Lohse, S. E.; Burrows, N. D.; Scarabelli, L.; Liz-Marzán, L. M.; Murphy, C. J. *Chem. Mater.* **2014**, *26*, 34.
(9) Sun, Y.; Mayers, B.; Herricks, T.; Xia, Y. *Nano Lett.* **2003**, *3*, 955.
(10) Qian, Z.; Park, S.-J. *Chem. Mater.* **2014**, *26*, 6172.
(11) Gole, A.; Murphy, C. J. *Chem. Mater.* **2004**, *16*, 3633.
(12) Jin, R.; Cao, Y.; Mirkin, C. A.; Kelly, K. L.; Schatz, G. C.; Zheng, J. G. *Science* **2001**, *294*, 1901.
(13) Scarabelli, L.; Coronado-Puchau, M.; Giner-Casares, J. J.; Langer, J.; Liz-Marzán, L. M. *ACS Nano* **2014**, *8*, 5833.
(14) Xie, J.; Lee, J. Y.; Wang, D. I. C. *Chem. Mater.* **2007**, *19*, 2823.
(15) Kuo, C.-H.; Huang, M. H. *Langmuir* **2005**, *21*, 2012.
(16) Saverot, S.; Geng, X.; Leng, W.; Vikesland, P. J.; Grove, T. Z.; Bickford, L. R. *RSC Adv.* **2016**, *6*, 29669.
(17) Millstone, J. E.; Park, S.; Shuford, K. L.; Qin, L.; Schatz, G. C.; Mirkin, C. A. *J. Am. Chem. Soc.* **2005**, *127*, 5312.
(18) Xia, Y.; Ye, J.; Tan, K.; Wang, J.; Yang, G. *Anal. Chem.* **2013**, *85*, 6241.
(19) Chen, L.; Fu, X.; Lu, W.; Chen, L. *ACS Appl. Mater. Interfaces* **2013**, *5*, 284.
(20) Yang, X.; Yu, Y.; Gao, Z. *ACS Nano* **2014**, *8*, 4902.
(21) Millstone, J. E.; Hurst, S. J.; Métraux, G. S.; Cutler, J. I.; Mirkin, C. A. *Small* **2009**, *5*, 646.
(22) Yu, H.; Zhang, Q.; Liu, H.; Dahl, M.; Joo, J. B.; Li, N.; Wang, L.; Yin, Y. *ACS Nano* **2014**, *8*, 10252.
(23) Jin, R.; Charles Cao, Y.; Hao, E.; Metraux, G. S.; Schatz, G. C.; Mirkin, C. A. *Nature* **2003**, *425*, 487.
(24) Xue, C.; Mirkin, C. A. *Angew. Chem. Int. Ed.* **2007**, *46*, 2036.

(25) Xiong, Y.; Siekkinen, A. R.; Wang, J.; Yin, Y.; Kim, M. J.; Xia, Y. *J. Mater. Chem.* **2007**, *17*, 2600.
(26) Xiong, Y.; Washio, I.; Chen, J.; Cai, H.; Li, Z.-Y.; Xia, Y. *Langmuir* **2006**, *22*, 8563.
(27) Pastoriza-Santos, I.; Liz-Marzán, L. M. *Nano Lett.* **2002**, *2*, 903.
(28) Kim, M. H.; Yoon, D. K.; Im, S. H. *RSC Adv.* **2015**, *5*, 14266.
(29) Metraux, G. S. M., Chad A. *Adv. Mater.* **2005**, *27*, 2685.
(30) Zhang, Q.; Li, N.; Goebl, J.; Lu, Z.; Yin, Y. *J. Am. Chem. Soc.* **2011**, *133*, 18931.
(31) Jana, N. R.; Gearheart, L.; Murphy, C. J. *Langmuir* **2001**, *17*, 6782.
(32) Sau, T. K.; Murphy, C. J. *J. Am. Chem. Soc.* **2004**, *126*, 8648.
(33) Chen, S.; Carroll, D. L. *Nano Lett.* **2002**, *2*, 1003.
(34) Chen, S.; Fan, Z.; Carroll, D. L. *J. Phys. Chem. B* **2002**, *106*, 10777.
(35) Aherne, D.; Ledwith, D. M.; Gara, M.; Kelly, J. M. *Adv. Funct. Mater.* **2008**, *18*, 2005.
(36) Li, N.; Zhang, Q.; Quinlivan, S.; Goebl, J.; Gan, Y.; Yin, Y. *ChemPhysChem* **2012**, *13*, 2526.
(37) Niu, W.; Zhang, L.; Xu, G. *Nanoscale* **2013**, *5*, 3172.
(38) Le Beulze, A.; Duguet, E.; Mornet, S.; Majimel, J.; Tréguer-Delapierre, M.; Ravaine, S.; Florea, I.; Ersen, O. *Langmuir* **2014**, *30*, 1424.
(39) Zhang, Q.; Hu, Y.; Guo, S.; Goebl, J.; Yin, Y. *Nano Lett.* **2010**, *10*, 5037.
(40) Zeng, J.; Xia, X.; Rycenga, M.; Henneghan, P.; Li, Q.; Xia, Y. *Angew. Chem. Int. Ed.* **2011**, *50*, 244.
(41) Yu, L.; Banerjee, I. A.; Matsui, H. *J. Am. Chem. Soc.* **2003**, *125*, 14837.
(42) Xie, J.; Lee, J. Y.; Wang, D. I. C.; Ting, Y. P. *Small* **2007**, *3*, 672.
(43) Naik, R. R.; Stringer, S. J.; Agarwal, G.; Jones, S. E.; Stone, M. O. *Nat. Mater.* **2002**, *1*, 169.
(44) Shankar, S. S.; Rai, A.; Ankamwar, B.; Singh, A.; Ahmad, A.; Sastry, M. *Nat. Mater.* **2004**, *3*, 482.
(45) Liu, B.; Xie, J.; Lee, J. Y.; Ting, Y. P.; Chen, J. P. *J. Phys. Chem. B* **2005**, *109*, 15256.
(46) Jiang, F.; Hsieh, Y.-L. *Biomacromolecules* **2014**, *15*, 3608.
(47) Singh, V.; Khullar, P.; Dave, P. N.; Kaur, G.; Bakshi, M. S. *ACS Sustain. Chem. Eng.* **2013**, *1*, 1417.
(48) Geng, X.; Grove, T. Z. *RSC Adv.* **2015**, *5*, 2062.
(49) Main, E. R. G.; Stott, K.; Jackson, S. E.; Regan, L. *Proc. Natl. Acad. Sci. U.S.A.* **2005**, *102*, 5721.
(50) Carter, N. A.; Grove, T. Z. *Biomacromolecules* **2015**, *16*, 706.
(51) Kajander, T.; Cortajarena, A. L.; Mochrie, S.; Regan, L. *Acta Cryst. D* **2007**, *63*, 800.
(52) Cortajarena, A. L.; Wang, J.; Regan, L. *FEBS J.* **2010**, *277*, 1058.
(53) Roth, K. L.; Geng, X.; Grove, T. Z. *J. Phys. Chem. C* **2016**, *120*, 10951.
(54) Kajander, T.; Cortajarena, A. L.; Main, E. R. G.; Mochrie, S. G. J.; Regan, L. *J. Am. Chem. Soc.* **2005**, *127*, 10188.
(55) Cortajarena, A. L.; Yi, F.; Regan, L. *ACS Chem. Biol.* **2008**, *3*, 161.
(56) Xia, Y.; Xia, X.; Peng, H.-C. *J. Am. Chem. Soc.* **2015**, *137*, 7947.
(57) Personick, M. L.; Mirkin, C. A. *J. Am. Chem. Soc.* **2013**, *135*, 18238.
(58) Sun, Y.; Xia, Y. *Adv. Mater.* **2003**, *15*, 695.
(59) Wang, L.; Wu, X.; Li, X.; Wang, L.; Pei, M.; Tao, X. *Chem. Commun.* **2010**, *46*, 8422.
(60) Goebl, J.; Zhang, Q.; He, L.; Yin, Y. *Angew. Chem. Int. Ed.* **2012**, *51*, 552.
(61) Radha, B.; Kulkarni, G. U. *Cryst. Growth Des.* **2011**, *11*, 320.

(62) Swami, A.; Kumar, A.; D'Costa, M.; Pasricha, R.; Sastry, M. *J. Mater. Chem.* **2004**, *14*, 2696.
(63) Roy, B.; Mukherjee, S.; Mukherjee, N.; Chowdhury, P.; Sinha Babu, S. P. *RSC Adv.* **2014**, *4*, 34487.
(64) Annadhasan, M.; Muthukumarasamyvel, T.; Sankar Babu, V. R.; Rajendiran, N. *ACS Sustain. Chem. Eng.* **2014**, *2*, 887.
(65) Shao, Y.; Jin, Y.; Dong, S. *Chem. Commun.* **2004**, 1104.
(66) Ueno, T.; Koshiyama, T.; Tsuruga, T.; Goto, T.; Kanamaru, S.; Arisaka, F.; Watanabe, Y. *Angew. Chem. Int. Ed.* **2006**, *45*, 4508.
(67) Hom, N.; Mehta, K. R.; Chou, T.; Foraker, A. B.; Brodsky, F. M.; Kirshenbaum, K.; Montclare, J. K. *J. Mater. Chem.* **2012**, *22*, 23335.
(68) Xie, J.; Lee, J. Y.; Wang, D. I. C. *J. Phys. Chem. C* **2007**, *111*, 10226.
(69) McMillan, R. A.; Howard, J.; Zaluzec, N. J.; Kagawa, H. K.; Mogul, R.; Li, Y.-F.; Paavola, C. D.; Trent, J. D. *J. Am. Chem. Soc.* **2005**, *127*, 2800.
(70) Bhattacharjee, Y.; Chakraborty, A. *ACS Sustain. Chem. Eng.* **2014**, *2*, 2149.
(71) Li, J.; Zhou, J.; Jiang, T.; Wang, B.; Gu, M.; Petti, L.; Mormile, P. *Phys. Chem. Chem. Phys.* **2014**, *16*, 25601.
(72) Fang, Y.; Seong, N.-H.; Dlott, D. D. *Science* **2008**, *321*, 388.
(73) Hong, X.; Wang, D.; Li, Y. *Chem. Commun.* **2011**, *47*, 9909.
(74) Zhang, L.-f.; Zhang, C.-y. *Nanoscale* **2013**, *5*, 6074.
(75) Zhou, H.; Yu, F.; Guo, C. F.; Wang, Z.; Lan, Y.; Wang, G.; Fang, Z.; Liu, Y.; Chen, S.; Sun, L.; Ren, Z. *Nanoscale* **2015**, *7*, 9153.

## 5.8 Supplemental Information

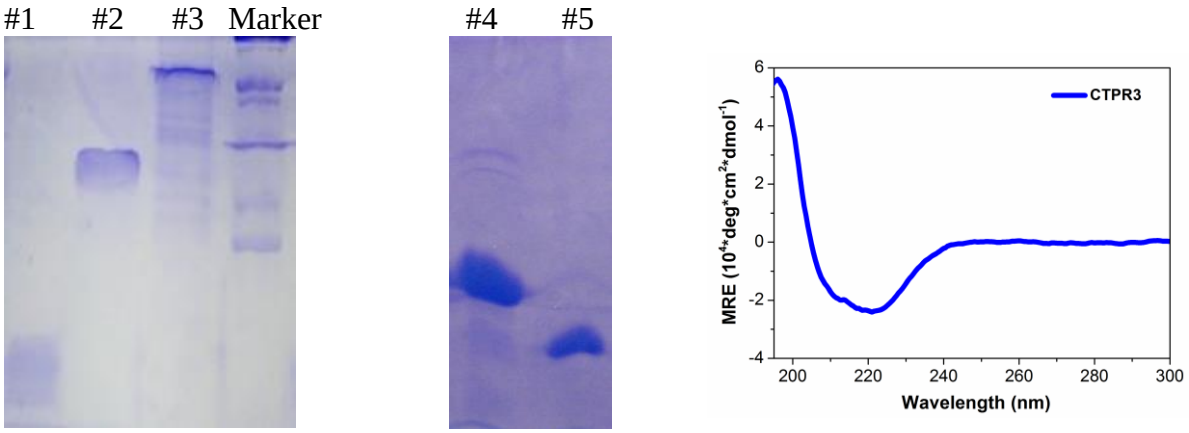


**AEAWYNLGNAYYKQGDYQKAIEYYQKALELDPNN**

**Figure S1.** (a) 15% SDS-PAGE gel of CTPR3 (lane 1), CTPR6 (lane 2), CTPR18 (lane 3), MW marker (lane 4). (b) 15% SDS-PEGE gel of CTPR3-cys (lane 1) and CTPR3 without (His)6-tag (lane 2). (c) Circular dichroism (CD) spectrum of CTPR3 protein (MRE: The mean residue ellipticity). Bottom: Single letter amino acid sequence of the CTPR repeat. CTPRn proteins are created by repeating this sequence n times (n=3, 6, 18).

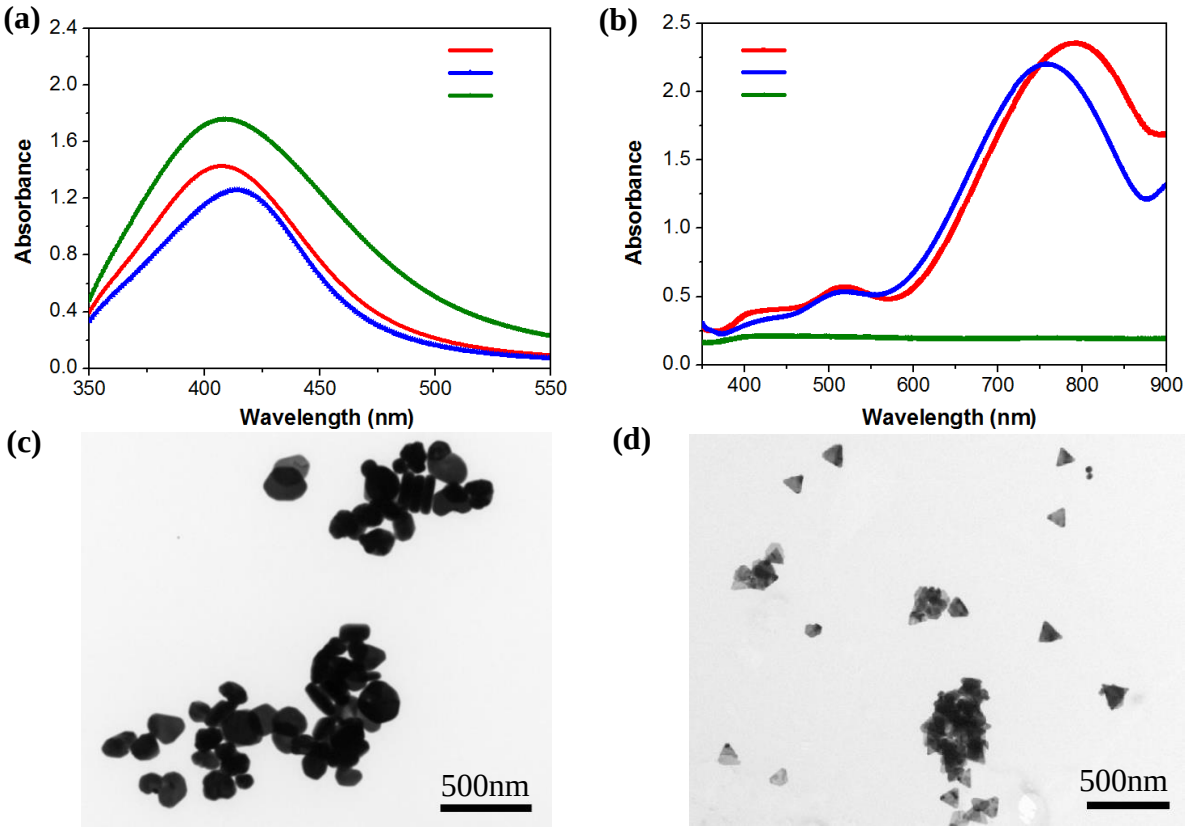


**Figure S2.** (a) UV-Vis spectra of freshly made Ag seed (red), seed stored at r.t in the dark for 2 weeks (blue), and seed prepared in the absence of citrate (green). (b) UV-Vis of nanoparticles prepared using freshly made Ag seed (red), seed stored at r.t in the dark for 2 weeks (blue), and seed prepared in the absence of citrate (green). (c,d) TEM images of Ag NPs prepared using 20µl seed prepared in the absence of citrate (left), and seed stored at r.t in the dark for 2 weeks (rigth).

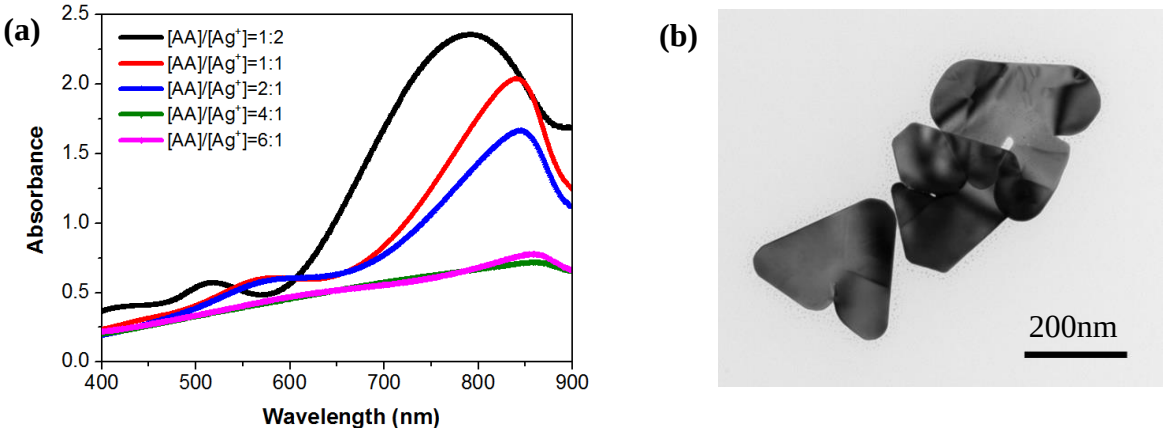


**Figure S3**. (a) UV-Vis spectra of Ag NPs prepared using 20 µl CTPR3-Ag seed with the increasing ratio of ascorbic acid [AA]/[$Ag^+$]. (b) TEM images of Ag NPs prepared using [AA]:[$Ag^+$] = 4:1.

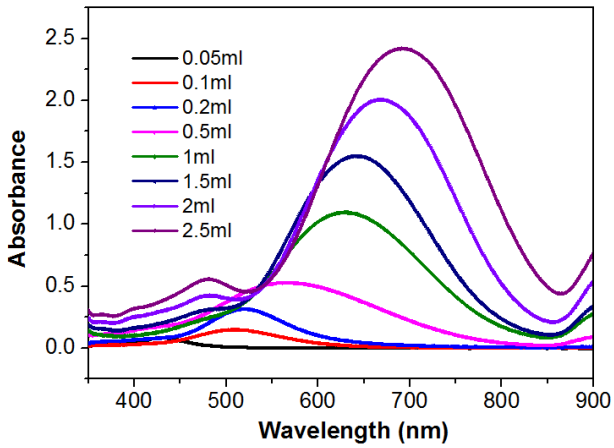


**Figure S4.** UV-vis of Ag NPs prepared with the increasing volume of 0.5 mM $AgNO_3$ aqueous solution

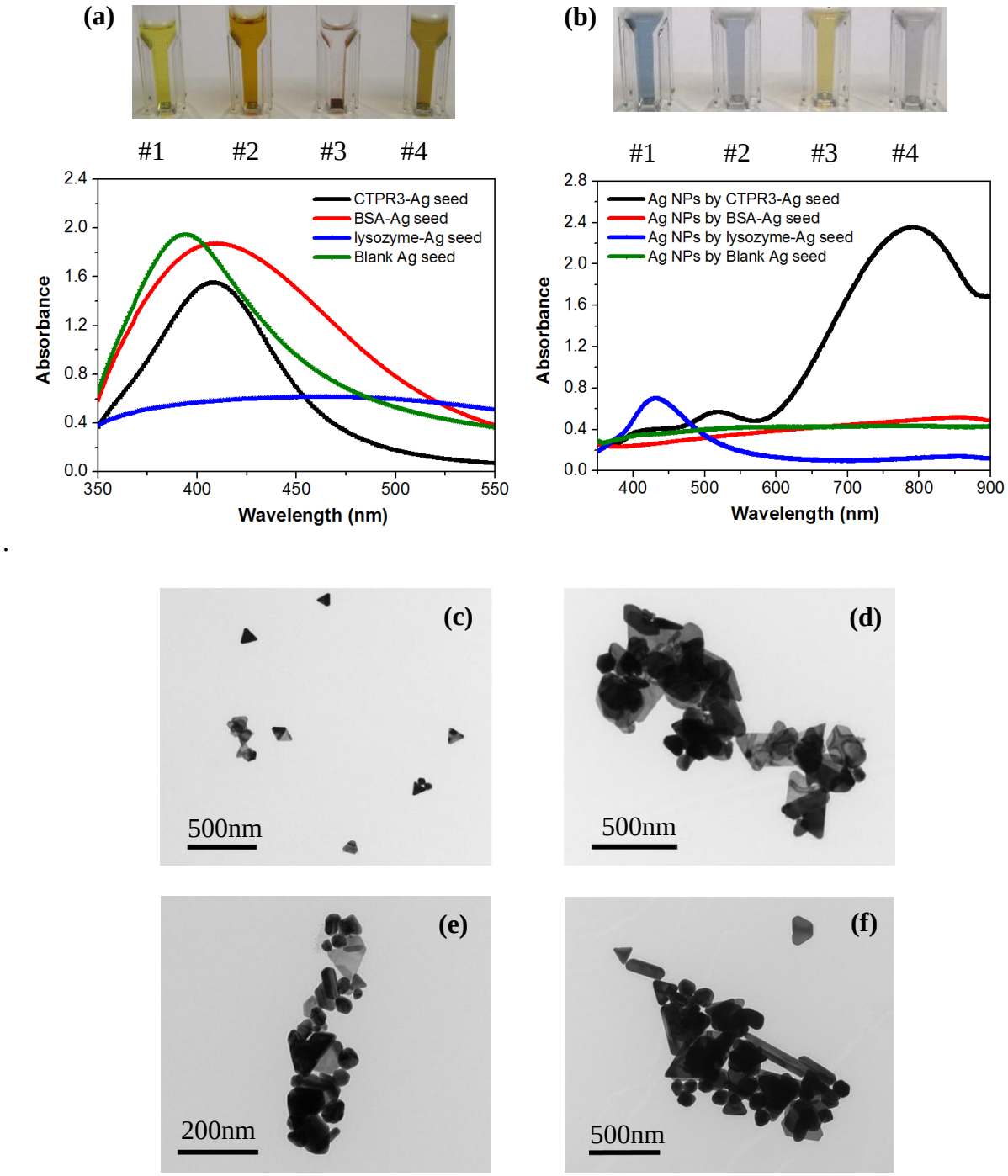


**Figure S5.** (a) UV-vis spectra and photgraphic images of Ag seeds solutions prepared in the absence of protein (green, #4), in the presence of CTPR3 (black, #1), BSA (red, #2), and lysozyme (blue, #3). (b) UV-vis spectra and photographic images of Ag NPs soluitons synthesized using 20 µl different types of seeds (color scheme and numbering same as in a). (c-f) TEM images of Ag NPs synthesized using 20 µl seeds #1-#4, respectively.

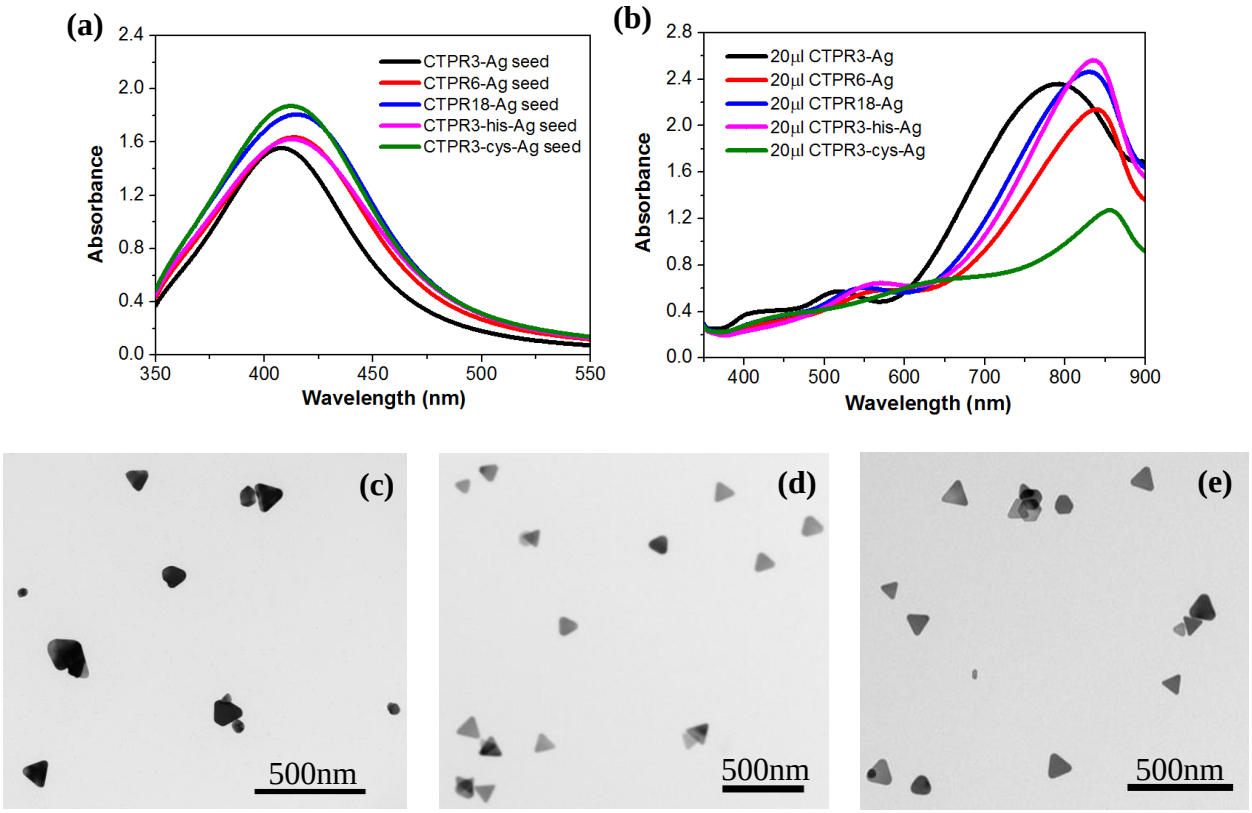


**Figure S6.** (a)UV-Vis spectra of Ag-seeds prepared in the presence of CTPR3 (black), CTPR6 (red), CTPR18 (blue), CTPR3-his (magenta), and CTPR3-cys (green). (b) UV-Vis spectra of Ag nanoprisms prepared using 20 µl of the corresponding seeds (coloring same as in a). (c-e) TEM images of Ag nanoprisms prepared using CTPR3-cys, CTPR3-his and CTPR18 respectively.

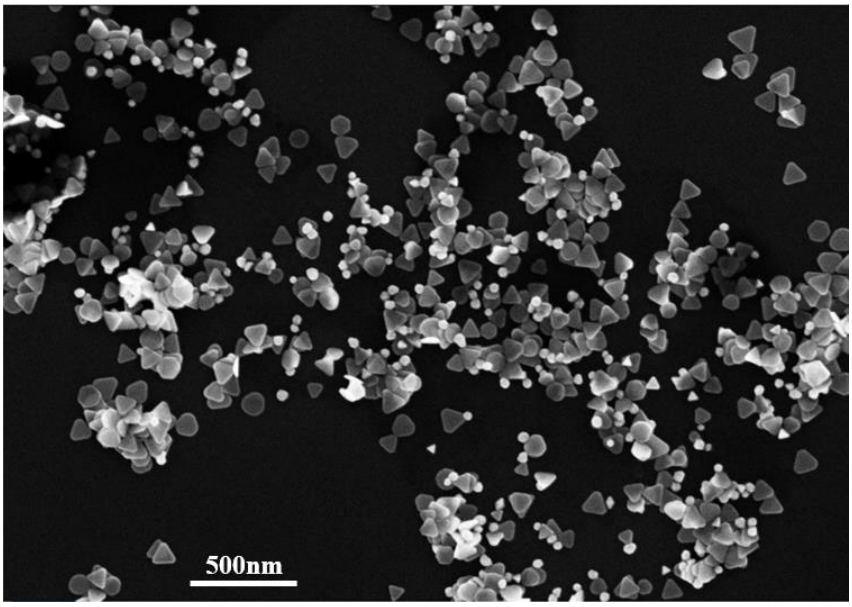


**Figure S7**. SEM image of Ag NTs-based SERS substrate.

**Enhancement factor (EF) is calculated as follows:**

**<u>For Ag nanoprisms in the solutions:</u>**

$$EF = (I_{SERS}/I_{Sol}) \times (C_{Sol}/C_{SERS})$$

Where $I_{SERS}$ and $I_{Sol}$ are the peak intensities of 1078cm$^{-1}$ for the 4MBA@Ag solution and 0.5M 4MBA solution in 1M NaOH, $C_{SERS}$ and $C_{Sol}$ are the concentration of 4MBA on Ag nanoprisms and in solution.

The volume of one Ag NT can be calculated by

$V_{NT} = \sqrt{3}a^2h/4$ , $a$=102.8nm, $h$=8.8nm, $\rho_{Ag}$= 10.5g/cm$^3$

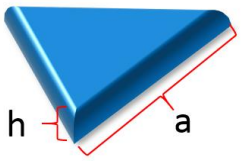


*Molecular weight of Ag= 107.87g/mol*

$V_{NT}$ = 40269nm$^2$,

The surface area of one Ag NT can be calculated by

$S_{NT} = \frac{\sqrt{3}a^2}{2} + 3ah$=1.187*10$^4$ nm$^2$

Weight of one silver NT: $W_{NT}= V_{NT} * \rho_{Ag}$ = 4.23 *10$^{-16}$ g

Weight of Ag NTs in the growth solution $W_{total}$= 0.5mM * 107.87g/mol * 3ml = 1.618 *10$^{-4}$ g

Since 1ml of the Ag NTs solution was used for the SERS measurement, the concentration of Ag NTs

$C_{total}$= 1ml/$V_{total}$* $W_{total}$ / $W_{NT}$ = 1ml/(5ml + 3ml + 0.075ml +0.02ml) * 1.618 *10$^{-4}$g/4.23 *10$^{-16}$ g

$$C_{total} = \frac{1ml * W_{total}}{V_{total} * W_{NT} * N_A} = \frac{1ml * 1.618 * 10^{-4}g}{(5+3+0.075+0.02)ml * 4.23 * 10^{-16}g * 6.02 * 10^{23}}$$

$$= 7.85 * 10^{-11}M$$

$$C_{SERS} = C_{total} * \frac{S_{NT}}{0.54\ nm^2} = 7.85 * 10^{-11}\ M * \frac{1.187 * 10^4}{0.54} = 1.73 * 10^{-6}\ M$$

Accumulation time was 1s for both condition and we assumed the 4-MBA with footprint of 0.54nm$^2$ was adsorbed as monolayer, then

$$EF = \left(\frac{I_{SERS}}{I_{Sol}}\right) \times \left(\frac{C_{Sol}}{C_{SERS}}\right) = \left(\frac{448}{192}\right) \times \left(\frac{0.25\ M}{1.73 * 10^{-6}\ M}\right) = 3.4 * 10^5$$

**For Ag nanoprisms as SERS substrate:**

$$EF = \left(\frac{I_{SERS}}{I_{Bulk}}\right) \times \left(\frac{N_{Bulk}}{N_{SERS}}\right) = \left(\frac{I_{SERS}}{I_{Bulk}}\right) \times \left(\frac{\delta_S * A}{\rho_S * f * A}\right)$$

Where $\delta_S$ and $\rho_S$ is the surface density of molecules on the regular substrate and Ag NTs SERS substrate, A is laser focal area, f is the occupied factor which is approximate to be 0.5.

10μl of 2M 4MBA suspension was deposited onto the Si wafer to form a thin film with the diameter of approximately 4mm, thus

$$\delta_S = \frac{V_{4MBA} * M_{4MBA} * N_A}{\pi d^2/4} = \frac{10\mu l * 2\ M * \ 6.02 * 10^{23}/mol}{3.14 * (4mm)^2/4} = 9.60 * 10^{23}\ m^{-2}$$

$V_{4MBA}$ =10 μl, $M_{4MBA}$ =2 mol/L, $M_{4MBA}$= molecular weight of 4MBA,

$$\rho_S = \frac{1}{0.54nm^2} = 1.85 * 10^{18}\ m^{-2}$$

$$EF = \left(\frac{I_{SERS}}{I_{Sol}}\right) \times \left(\frac{N_{Bulk}}{N_{SERS}}\right) = \left(\frac{1240}{470}\right) \times \left(\frac{9.6 * 10^{23}\ m^{-2}}{0.5 * 1.85 * 10^{18}\ m^{-2}}\right) = 2.8 * 10^6$$

# Chapter 6. Seed-mediated biomineralization toward the high yield production of gold nanoprisms

Xi Geng, Kristina L. Roth, Megan F. Freyman, Jianzhao Liu, and Tijana Z. Grove

Reproduced with permission from the Royal Society of Chemistry. Geng, X., Roth, K.L., Freyman, M.F., Liu, J., Grove, T.Z., *Chem. Comm.*, **2016**, *52*, 9829-9832.

**Attributions:** XG explored the new synthetic methodologies through meticulous experimentation and data interpretation. KLR conducted DLS study and MTT assay, and wrote the corresponding sections. MFF assisted XG to perform the NPs synthesis and JL provided expertise on AFM image analysis. TZG gave insightful suggestions and made critical contributions when composing the manuscript.

## 6.1 Abstract

Gold nanotriangles (Au NTs) with tunable edge length were synthesized *via* a green chemical route in the presence of the designed consensus sequence tetratricopeptide repeat (CTPR) protein, halide anions ($Br^-$) and CTPR-stabilized Ag seeds. The well-defined morphologies, tailored plasmonic absorbance from visible-light to the near infrared (NIR) region, colloidal stability and biocompatibility are attributed to the synergistic action of CTPR, halide ions, and CTPR-stabilized Ag seeds.

## 6.2 Introduction

Over the past decade, tremendous attention and research efforts have been devoted to the synthesis of gold (Au) nanoplates. Because of their highly anisotropic structure and localized surface plasmon resonance (LSPR) properties, they are exceptionally well suited for biomedical applications such as biosensing,[1] diagnostics and therapeutics.[2] The

synthesis of planar Au nanoparticles (NPs) is typically achieved via cetyltrimethylammonium bromide/chloride (CTAB/CTAC)-based protocols.[3-10] However, biomedical applications necessitate tedious and stringent purification processes for the complete removal of toxic cationic surfactants.[11,12] A growing interest has thus been focused on the biocompatible and green synthetic approaches that mimic natural biomineralizaton process.[13] In previous studies, plant extracts,[14,15] amino acids,[16] bovine serum albumin (BSA)[17,18] amyloid fibril[19] and other shape directing proteins[20] have demonstrated dual functions as stabilizers and reducing agents to produce anisotropic Au nanoplates. In addition,[21,22] Good's buffers have been reported to generate gold nanocrystals at ambient condition.[23,24] However, one-pot synthetic strategies typically resulted in broad morphological distribution of NPs. Seed-mediated growth along with the addition of shape-directing halides has been invoked as the most potent tools for directing the anisotropic growth of noble metal NPs.[9,10,25-28] The exquisite shape control is mainly realized through kinetic control as well as the preferential binding to the low index facets. As demonstrated in the present work, the incorporation of seed-mediated techniques into conventional biomineralizaton has the potential to provide unprecedented control over NP size and shape while maintaining biocompatibility requirements. To our knowledge, this is the first report of the synergistic action of protein, halide and protein-stabilized seeds for the efficient formation of triangular Au nanoprisms with narrow morphological distribution, excellent colloidal stability and low cytotoxicity.

## 6.3 Results and Discussion

The details of the synthetic process are depicted in ***Scheme 6.1***. Briefly, the CTPR protein (***Figure S1***) and sodium bromide were employed as the shape directing agents, while 3-

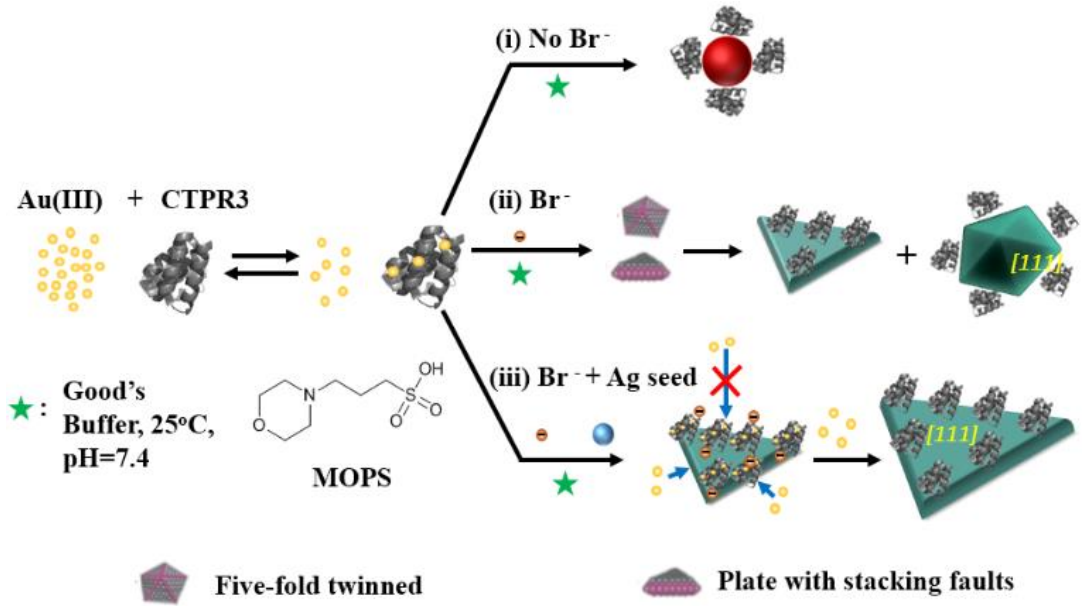


**Scheme 6.1** Schematic illustration of synthetic routes toward quasi-globular Au NPs (i), Au NPs bounded with (111) facets (ii) and Au triangular nanoprisms (iii).

(N-morpholino)propanesulfonic acid (MOPS) was used as a mild reducing agent.[29] CTPR protein is a *de novo* protein sequence based on the tetratricopeptide repeat family.[30] Repeat proteins have attracted attention of the biotechnology community for their modular structure and ease of engineering.[31-35] Although not specifically designed for biomineralizaton, CTPR proteins have demonstrated remarkable utility in the synthesis of noble metal nanoparticles[29,36] and nanoclusters.[37] In a typical synthetic procedure, CTPR3 was first mixed with gold precursor, followed by the addition of aqueous NaBr solution. Upon injection of MOPS, the solution rapidly turns colorless indicating the conversion of Au(III) to Au(I). The overall reduction will proceed from one hour up to a couple of days depending upon the concentration of CTPR3 and NaBr. In the presence of 10 μM CTPR3 protein, but without bromide ion (***Scheme 6.1-i***) small nanospheres (14.1 ± 5.6 nm) are produced (***Figure 6.1b***). In comparison, a mixture of Au nanoprisms, five-fold penta-twinned Au NPs (decahedrons) and Au nanospheres are produced in the presence of both CTPR3 and NaBr (***Scheme 6.1-ii, Figure 6.1c***). The formation of

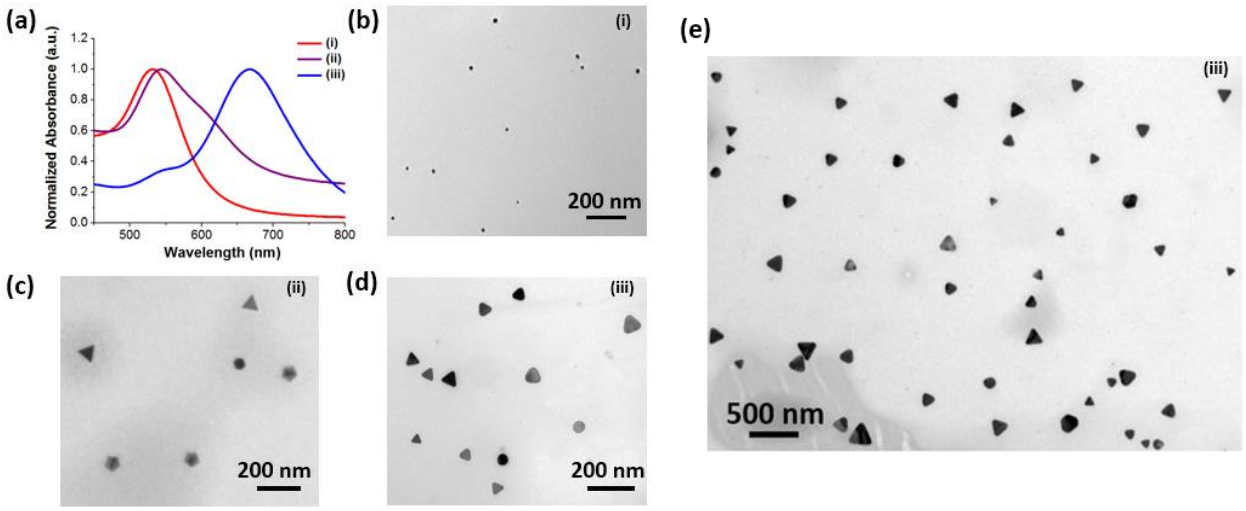


**Figure 6.1** (a) UV-Vis extinction spectra and (b-e) TEM images of Au NPs prepared using varied experimental conditions: (i) CTPR3 only, (ii) CTPR3 and NaBr, (iii) CTPR3, NaBr, and Ag seeds.

anisotropic Au NPs is consistent with the broad shoulder and asymmetric shape of the corresponding UV-Vis spectrum (***Figure 6.1a, ii***). In addition to Au NTs, the decahedrons with multi-fold twinning structure are also generated, as evidenced by the twin-grain boundaries and periodical fast Fourier transform (FFT) diffraction patterns (***Figure S4e-f***). Although the reaction condition depicted in ***Scheme 6.1-ii*** produces satisfactory yield of anisotropic Au NTs, their sizes and shapes are polydisperse (***Figure S5a***) due to the inherent drawbacks of one-pot synthesis such as unavoidable self-nucleation events and poor quality of seeds with diverse crystal structures.[38] Note that the percent yield were defined by the ratio of planar gold nanoprisms with curved and straight edges to the total number of Ag NPs, which is estimated based on the TEM observations. Aiming for high-yielding production of Au NTs with lower morphological polydispersity, CTPR3-stabilized Ag seeds (***Figure S2***) were deliberately added to promote the growth of Au NTs (***Scheme 6.1-iii and Figure 6.1e***). In a general sense, the addition of Ag seed will induce the catalytic deposition of Au(0) atoms onto the planar-twinned Ag surface without causing disruptive galvanic etching, particularly under the condition of

adequate amount of NaBr and CTPR3.[39,40] Once 10 µl of CTPR3-Ag seeds[36] with inherent stacking faults are introduced (Scheme 1-iii), the majority of NPs are Au NTs (***Figure 6.1d-e***). This morphological transition is accompanied by a pronounced red shift of the LSPR peak to 667 nm (***Figure 6.1a, iii***). Interestingly, efficient formation of Au NTs was also realized using 4-(2-hydroxyethyl)-1-piperazineethanesulfonic acid (HEPES) (***Figure S3***) implying that the choice of reducing agents potentially could be further extended to other biologically benign alternatives.

The single crystalline fcc structure Au NTs was identified by high resolution TEM (HRTEM) and hexagonal pattern of selected area electron diffraction (SAED) (***Figure S4a-b***). The measured interplanar spacing is 0.235 nm, consistent with the lattice parameter of Au (111) (***Figure S4a***). The composition of Au NTs was characterized using energy-dispersive X-ray spectroscopy (EDS) (***Figure S4c***). The smooth atomic force microscopy (AFM) profile is indicative of the planar top face of Au NTs (***Figure S4d***) with the measured between 8-15 nm, mainly depending on the amount of Ag seeds added.

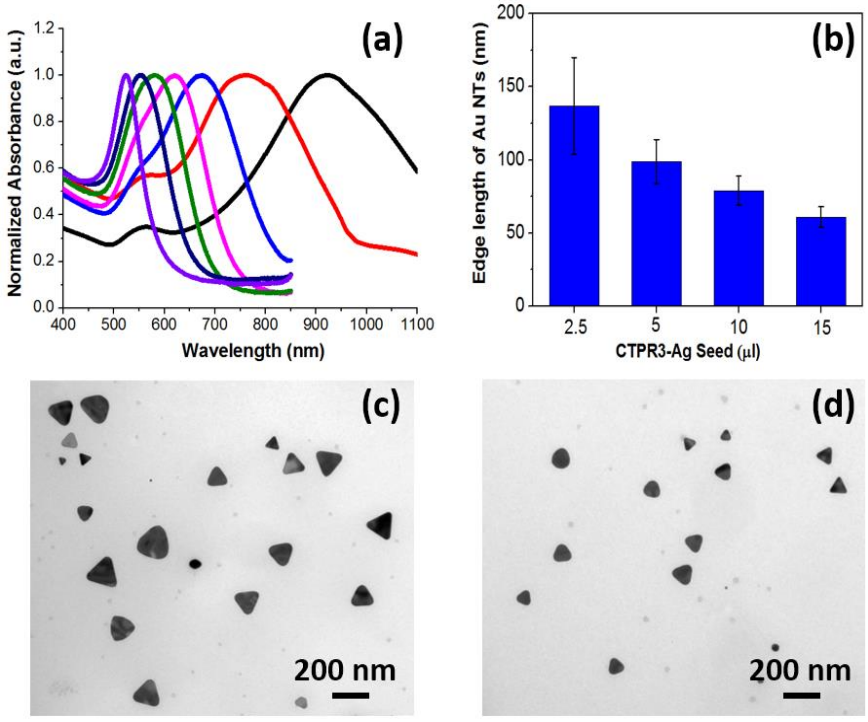

**Figure 6.2** (a) UV-Vis extinction spectra of Au NPs prepared in the presence of 2.5 µl (black), 5 µl (red), 10 µl (light blue), 15 µl (magenta), 20 µl (green), 25 µl (dark blue), 50 µl (violet) Ag seeds. (b) Edge length of Au NTs prepared using varied amount of Ag seeds. TEM images of Au NTs prepared using (c) 2.5 µl and (d) 5 µl Ag seeds.

It has been demonstrated that the LSPR features for Au NTs are closely associated with their edge length, thickness as well as the tips sharpness.[13] As shown in the ***Figure 6.2a***, the LSPR of Au NTs can be conveniently tuned to span a broad range from visible-light to near infrared (NIR) region by simply adjusting the amount of Ag seeds added in the initial growth stage. The shift in dipole plasmon resonance agrees very well with the change in the NT edge-length observed in TEM images. The edge length of the Au NTs could be finely tailored from 61 ± 7 to 137 ± 33 nm (***Figure 6.2b-d***). Notably, the yield of Au NTs is approximately 75% of the overall population without any purification process (***Figure S5b***), which will increase to 85 % by harvesting after sedimentation process (***Figure 6.1e*** and ***S5c***). In sharp contrast, Au NTs with broader size distribution (41 ± 14 nm) are obtained using one pot biomineralizaton without adding Ag seed. Intriguingly, the addition of Ag seeds also brings great benefits by significantly reducing the use of NaBr and CTPR without compromising the overall yield. A strong dipole LSPR peak was identified for the Au NTs sample prepared in the presence of 2 µM CTPR3 and 5 mM NaBr (***Figure S6***).

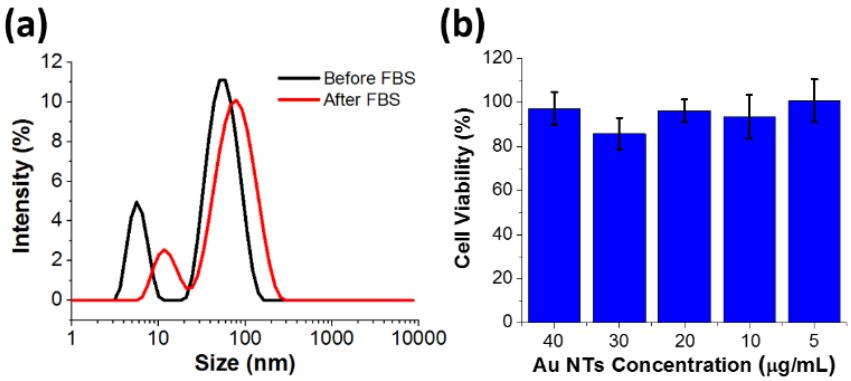

**Figure 6.3** (a) DLS of Au NTs before and after incubation with fetal bovine serum (FBS). (b) Percent of viable MBEC cells determined from MTT assay after incubation with varied concentrations of Au NTs (5-40 μg/ml).

Proteins and peptides could be used as efficient capping agents to grant excellent colloidal stability and interesting physicochemical properties to the functional nanomaterials.[41-43] We further explore the colloidal stability of the as-synthesized Au NTs and Au NTs in the fetal bovine serum (FBS). As shown in ***Figure 6.3a***, after Au NTs are incubated with FBS for 2 hours an increase in the hydrodynamic diameter of 30 nm is observed (***Table S1***). The increase in diameter can be attributed to adsorption of proteins from the FBS solution. It is important to note that the colloidal stability of CTPR3-stabilized is maintained during the centrifugation and re-dispersion processes and no agglomeration of NTs occurs after incubation with FBS. As expected, CTRP3-stabilized Au NTs have negative zeta potential due to the overall negative charge of the CTPR3. After incubation with FBS the zeta potential increases to -17.9 mV (***Table S1***), which is in agreement with previous reports of -20mV zeta potential for Au NPs after FBS incubation independent of the initial NP surface charge.[11,44] The protein corona can also serve as a protecting agent to lower the cytotoxicity of nanomaterials.[45] To that end, mouse brain endothelial cells (MBECs) were incubated with the as-prepared CTPR-stabilized Au NTs for 6 hours and cell viability was measured using MTT assay. For Au NT concentration range 5-40 μg $mL^{-1}$ no concentration dependent cell toxicity was observed (***Figure 6.3b***).

Even though the detailed growth mechanism is still elusive, we try to postulate a possible mechanism for the seed-mediated biomineralizaton. We have recently shown that the binding affinity of Au species to CTPR3 is driven mainly by metal-π interactions with tyrosine and tryptophan side chains and hydrogen bonding to asparagine side-chain.[46,47]

Moreover, the overall binding constant is ionic strength dependent. Interestingly, CTPR contains no cysteine or a specific gold binding sequence such as AG3.[48,49] To elucidate the roles of CTPR3 and bromide we first performed syntheses at the fixed ratio of $HAuCl_4$ and MOPS (0.2 mM: 40 mM), but either the concentration of CTPR3 or NaBr was adjusted. In the presence of 100 mM NaBr, the overall yield of anisotropic NPs increases as the concentration of CTPR3 increases. For instance, irregular sheet-like NPs are produced in the absence of CTPR3 (***Figure S7a***), limited number of Au NTs with rounded tips (< 10%) are generated when concentration of CTPR3 is less than 1μM (***Figure S7b***). But as the concentration of CTPR3 reaches 4 μM, 35% of the NP population are Au NTs (***Figure S7c***). Further increase in CTPR3 concentration up to 20 μM only slightly improved the overall yield of Au NTs at the cost of extended reaction time (>2 weeks). On the other hand, increasing the concentration of NaBr will also facilitate the growth of anisotropic Au NPs (***Figure S8a-b***), which is consistent with the previous report.[50] Nevertheless, when excess surface capping agent, either CTPR3 or NaBr is present, the reduction reaction will be dramatically inhibited and the free gold precursor will not be consumed efficiently to provide feedstock of Au(0) thereby hindering the growth of planar Au NTs. The yield of Au NTs declined and ill-defined NPs are formed by adding 300 mM NaBr (***Figure S8c***). We found that the highest yield of Au NTs was reached in the presence of 10 μM CTPR3 and 100 mM NaBr. Under optimized synthetic conditions, approximately 70% of NPs are bounded with (111) facets, among which Au NTs accounted for 75% of the entire population (***Figure S5a***). The prevalence of Au NTs and decahedrons implies that the coexistence of protein and NaBr promotes the nucleation of seeds with either planar or penta-twinned defects.

Herein we postulate that at the initial stage of the one-pot synthesis (***Scheme 6.1-ii***), Au nuclei with planar or penta-twinning structures are produced. The former will assemble into triangle-like pattern at the localized domain. This phenomenon was previously observed in the synthesis of Au nanoplates using extract of lemongrass and BSA.[14,51] Au NPs with corrugated and stepped edges are observed after 12 and 24 h consistent with the continuous deposition of gold atoms onto the triangle analogues (***Figure S9***). Interaction between CTPR3 and Au(III) is stronger at higher ionic strengths, thus as the concentration of NaBr increases more Au(III) ions will be complexed with the protein influencing the reduction kinetics.[47] At intermediate NaBr concentration there will be less free Au(III) ions accessible to the (111) faces with lower surface energy and chemical reactivity as compared with the stepped edges bearing high-density defects. CTPR3 $NH_2$ or $NH_3^+$ pendant groups may also interact with $Br^-$ and enhance the steric hindrance analogous to the zipping mechanism of CTAB.[52] The (111) faces are further passivated by the adsorption of $Br^-$ and CTPR3 via the surfactant templating or face-blocking process.[53] This scenario is supported by the compositional distribution of Br, O and N enriched on the (111) facets of Au NTs as shown in the ***Figure S10***. Eventually, the corrugated and stepped face gradually diminished whilst the Au NTs and decahedrons bounded with (111) faces are generated. Unfortunately, the broad distribution of crystallinity of nuclei along with the concomitant self-nucleation of isotropic NPs restrict the precise control over the size and shape. Once CTPR3-stabilized Ag seeds with innate planar twinning structure are added (***Scheme 6.1-iii***), the initial self-nucleation process will be appreciably circumvented. It has been well recognized that the twinned crystal seeds prompt the lateral growth of 2D planar nanostructures by providing low-energy re-

entrant groves.[13] Consequently, the as-reduced Au(0) will be predominantly deposited onto the facets - other than (111) - of planar twinned Ag nanocrystals in a rapid manner thereby improving the yield along with the quality of the Au NTs. As observed in STEM-EDX experiments, the trace amount of Ag element is evenly distributed over the entire area of the Au NTs rather than accumulated in the core (***Figure S10 and S11***). This observation is consistent with the dissolution and diffusion of Ag into the Au NTs, particularly when exposed to the light and under the condition of high halide concentration.

## 6.4 Conclusions

In summary, we developed a facile and high-yielding green methodology for the syntheses of anisotropic Au nanoprisms at ambient condition, in which NaBr, CTPR as well as CTPR-stabilized Ag seeds have imposed synergistic effects upon the morphology of the Au NPs. Indeed, since the CTPR sequence was not specifically designed or selected for binding Au, it is tempting to propose that the physico-chemical properties of biomolecules (e.g. pI, number of aromatic side-chains, etc.) are more important for efficient synthesis of anisotropic Au nanostructures than the actual specific binding motifs. Thus, this synthetic strategy can be further extended to a vast diversity of biomolecules as long as physico-chemical properties are optimized. One can then easily envision "designer coronas" where specific molecular recognition moieties can be incorporated into the engineered proteins or peptides to match a biomedical application.[54] Furthermore, this work demonstrates that the incorporation of seed-mediated growth into conventional biomineralizaton strategies yields noble metal NPs with unprecedented control over size and shape. Obtained Au NTs with well-defined morphologies exhibited

tailored plasmonic absorbance ranging from visible to NIR region. Reported NPs are colloidally stable and biocompatible thus holding great promises for versatile biosensing and biomedical applications.

## 6.5 Acknowledgements

The authors would like to thank Dr.Guoliang Liu for insightful comments, suggestions, and discussion on this research work. Author acknowledge ICTAS Nanoscale Characterization and Fabrication Lab (NCFL) for the use of AFM and TEM. This work was in part supported by the JFC ICTAS grant number 119106 to TZG.

## 6.6 References

(1) Beeram, S. R.; Zamborini, F. P. *ACS Nano* **2010**, *4*, 3633.
(2) Pelaz, B.; Grazu, V.; Ibarra, A.; Magen, C.; del Pino, P.; de la Fuente, J. M. *Langmuir* **2012**, *28*, 8965.
(3) Millstone, J. E.; Park, S.; Shuford, K. L.; Qin, L.; Schatz, G. C.; Mirkin, C. A. *J. Am. Chem. Soc.* **2005**, *127*, 5312.
(4) Millstone, J. E.; Métraux, G. S.; Mirkin, C. A. *Adv. Funct. Mater.* **2006**, *16*, 1209.
(5) Sau, T. K.; Murphy, C. J. *J. Am. Chem. Soc.* **2004**, *126*, 8648.
(6) Huang, Y.; Ferhan, A. R.; Gao, Y.; Dandapat, A.; Kim, D.-H. *Nanoscale* **2014**, *6*, 6496.
(7) Scarabelli, L.; Coronado-Puchau, M.; Giner-Casares, J. J.; Langer, J.; Liz-Marzán, L. M. *ACS Nano* **2014**, *8*, 5833.
(8) Chen, L.; Ji, F.; Xu, Y.; He, L.; Mi, Y.; Bao, F.; Sun, B.; Zhang, X.; Zhang, Q. *Nano Lett.* **2014**, *14*, 7201.
(9) Millstone, J. E.; Wei, W.; Jones, M. R.; Yoo, H.; Mirkin, C. A. *Nano Lett.* **2008**, *8*, 2526.
(10) Ha, T. H.; Koo, H.-J.; Chung, B. H. *J. Phys. Chem. C* **2007**, *111*, 1123.
(11) Alkilany, A. M.; Nagaria, P. K.; Hexel, C. R.; Shaw, T. J.; Murphy, C. J.; Wyatt, M. D. *Small* **2009**, *5*, 701.
(12) Alkilany, A. M.; Murphy, C. J. *J. Nanopart. Res.* **2010**, *12*, 2313.
(13) Millstone, J. E.; Hurst, S. J.; Métraux, G. S.; Cutler, J. I.; Mirkin, C. A. *Small* **2009**, *5*, 646.
(14) Shankar, S. S.; Rai, A.; Ankamwar, B.; Singh, A.; Ahmad, A.; Sastry, M. *Nat. Mater.* **2004**, *3*, 482.
(15) Liu, B.; Xie, J.; Lee, J. Y.; Ting, Y. P.; Chen, J. P. *J. Phys. Chem. B* **2005**, *109*, 15256.
(16) Shao, Y.; Jin, Y.; Dong, S. *Chem. Commun.* **2004**, 1104.
(17) Xie, J.; Lee, J. Y.; Wang, D. I. C. *J. Phys. Chem. C* **2007**, *111*, 10226.
(18) Au, L.; Lim, B.; Colletti, P.; Jun, Y.-S.; Xia, Y. *Chem. Asian J.* **2010**, *5*, 123.
(19) Li, C.; Bolisetty, S.; Mezzenga, R. *Adv. Mater.* **2013**, *25*, 3694.
(20) Xie, J.; Lee, J. Y.; Wang, D. I. C.; Ting, Y. P. *Small* **2007**, *3*, 672.
(21) Goswami, N.; Zheng, K.; Xie, J. *Nanoscale* **2014**, *6*, 13328.

(22) Goswami, N.; Yao, Q.; Luo, Z.; Li, J.; Chen, T.; Xie, J. *J. Phys. Chem. Lett.* **2016**, *7*, 962.
(23) Xie, J.; Lee, J. Y.; Wang, D. I. C. *Chem. Mater.* **2007**, *19*, 2823.
(24) Saverot, S.; Geng, X.; Leng, W.; Vikesland, P. J.; Grove, T. Z.; Bickford, L. R. *RSC Adv.* **2016**, *6*, 29669.
(25) Jana, N. R.; Gearheart, L.; Murphy, C. J. *Langmuir* **2001**, *17*, 6782.
(26) Niu, W.; Zhang, L.; Xu, G. *Nanoscale* **2013**, *5*, 3172.
(27) Personick, M. L.; Mirkin, C. A. *J. Am. Chem. Soc.* **2013**, *135*, 18238.
(28) Lohse, S. E.; Burrows, N. D.; Scarabelli, L.; Liz-Marzán, L. M.; Murphy, C. J. *Chem. Mater.* **2014**, *26*, 34.
(29) Geng, X.; Grove, T. Z. *RSC Adv.* **2015**, *5*, 2062.
(30) Main, E. R. G.; Stott, K.; Jackson, S. E.; Regan, L. *Proc. Natl. Acad. Sci. U.S.A.* **2005**, *102*, 5721.
(31) Mejias, S. H.; Lopez-Andarias, J.; Sakurai, T.; Yoneda, S.; Erazo, K. P.; Seki, S.; Atienza, C.; Martin, N.; Cortajarena, A. L. *Chem. Sci.* **2016**.
(32) Grove, T. Z.; Osuji, C. O.; Forster, J. D.; Dufresne, E. R.; Regan, L. *J. Am. Chem. Soc.* **2010**, *132*, 14024.
(33) Carter, N. A.; Grove, T. Z. *Biomacromolecules* **2015**, *16*, 706.
(34) Parker, Rachael N.; Grove, Tijana Z. *Biochem. Soc. Trans.* **2015**, *43*, 856.
(35) Cortajarena, A. L.; Yi, F.; Regan, L. *ACS Chem. Biol.* **2008**, *3*, 161.
(36) Geng, X.; Leng, W.; Carter, N. A.; Vikesland, P. J.; Grove, T. Z. *J. Chem. Mater. B* **2016**, *4*, 4182.
(37) Couleaud, P.; Adan-Bermudez, S.; Aires, A.; Mejías, S. H.; Sot, B.; Somoza, A.; Cortajarena, A. L. *Biomacromolecules* **2015**, *16*, 3836.
(38) Gao, C.; Goebl, J.; Yin, Y. *J. Chem. Mater. C* **2013**, *1*, 3898.
(39) Gao , C.; Lu , Z.; Liu , Y.; Zhang, Q.; Chi, M.; Cheng, Q.; Yin, Y. *Angew. Chem. Int. Ed.* **2012**, *51*, 5629.
(40) Qian, Z.; Park, S.-J. *Chem. Mater.* **2014**, *26*, 6172.
(41) Luo, Z.; Zheng, K.; Xie, J. *Chem. Commun.* **2014**, *50*, 5143.
(42) Song, X.-R.; Goswami, N.; Yang, H.-H.; Xie, J. *Analyst* **2016**, *141*, 3126.
(43) Yao, Q.; Yuan, X.; Yu, Y.; Yu, Y.; Xie, J.; Lee, J. Y. *J. Am. Chem. Soc.* **2015**, *137*, 2128.
(44) Ritz, S.; Schöttler, S.; Kotman, N.; Baier, G.; Musyanovych, A.; Kuharev, J.; Landfester, K.; Schild, H.; Jahn, O.; Tenzer, S.; Mailänder, V. *Biomacromolecules* **2015**, *16*, 1311.
(45) Caracciolo, G.; Palchetti, S.; Colapicchioni, V.; Digiacomo, L.; Pozzi, D.; Capriotti, A. L.; La Barbera, G.; Laganà, A. *Langmuir* **2015**, *31*, 10764.
(46) Yu, J.; Becker, M. L.; Carri, G. A. *Langmuir* **2012**, *28*, 1408.
(47) Roth, K. L.; Geng, X.; Grove, T. Z. *J. Phys. Chem. C* **2016**, *120*, 10951.
(48) Chen, C.-L.; Rosi, N. L. *Angew. Chem. Int. Ed.* **2010**, *49*, 1924.
(49) Briggs, B. D.; Knecht, M. R. *J. Phys. Chem. Lett.* **2012**, *3*, 405.
(50) Li, H.; Jo, J.; Wang, J.; Zhang, L.; Kim, I. *Cryst. Growth Des.* **2010**, *10*, 5319.
(51) Xue, Z.-H.; Hu, B.-B.; Dai, S.-X.; Du, Z.-L. *Mater. Chem. Phys.* **2010**, *123*, 278.
(52) Swami, A.; Kumar, A.; D'Costa, M.; Pasricha, R.; Sastry, M. *J. Mater. Chem.* **2004**, *14*, 2696.
(53) Xiao, J.; Qi, L. *Nanoscale* **2011**, *3*, 1383.
(54) Abadeer, N. S.; Murphy, C. J. *J. Phys. Chem. C* **2016**, *120*, 4691.
(55) Kajander, T.; Cortajarena, A. L.; Main, E. R. G.; Mochrie, S. G. J.; Regan, L. *J. Am. Chem. Soc.* **2005**, *127*, 10188.

(56) Aherne, D.; Ledwith, D. M.; Gara, M.; Kelly, J. M. *Adv. Funct. Mater.* **2008**, *18*, 2005.

## 6.7 Supplemental Information

## Experimental

### Expression of CTPR3 protein

CTPR proteins with 3 tandem repeating units were synthesized through recombinant bacterial expression technology.[35,55] Synthetic genes for the desired protein in pPROEx vector, coding for N-terminal $(His)_6$ tag and ampicillin resistance, were transformed into E.Coli BL21(DE3) cells and cultured overnight at 37 °C on agar plates. One single colony was selected and incubated overnight in 50 mL of Luria−Bertani (LB) media containing 100 μg/mL of ampicillin. 10ml of overnight cultures were then dispensed into 1 L of LB media supplemented with 100 μg/mL ampicillin. The cells were grown in an incubator-shaker (250 rpm) at 37 °C until the optical density ($OD_{600}$) reached 0.6-0.8. Expression of CTPR3 was induced with 1mM isopropyl β-D-thiogalactoside (IPTG) followed by 5h expression at 37°C. The cells were harvested by centrifugation at 5,000rpm for 20min and the pellets were frozen at -80°C until purification.

### Purification of CTPR3 protein

The cell pellets were resuspended in lysis buffer consisting of 50 mM Tris, 300mM sodium chloride and 0.1 wt% Tween 20. After 2 min sonication at 30% power using a microtip and Mison sonicator, lysed cells were centrifuged at 16,000 rpm for 30 min and the protein supernatant was purified using standard Ni-NTA affinity purification protocol. The collected proteins were further purified by Akta Prime Plus size exclusion chromatography using Superdex 75 16/600 Prep Grade column in 150 mM sodium chloride and 50 mM sodium phosphate buffer at pH 8 with a flow rate of 0.5ml/min. As a final step, the aqueous solutions of CTPRs were

dialyzed against 10 mM phosphate buffer three times at 4 °C using a dialysis membrane with molecular weight cutoff of 3k Da.

**Preparation of CTPR3-stabilized Ag seeds**[36,56]

Silver seeds were prepared by adding 5 ml 0.5 mM $AgNO_3$ at the rate of 2 mL/min using a syringe pump (KD Scientific) under vigorous agitation to the aqueous solutions of trisodium citrate (5 mL, 2.5 mM), $NaBH_4$ (0.3 mL, 10 mM) and CTPR proteins (0.125 mL 0.1-2 mg/ml) in a glass vial. The as-prepared Ag seeds were kept in the dark till further use to circumvent the interference such as homogeneous nucleation arising from the residual $NaBH_4$.

**Preparation of Au nanoprisms**

In a typical synthetic procedure, 0.1 ml CTPR3 (2 μM - 200 μM) was first mixed with 0.85 ml DI and 40 μl 10 mM $HAuCl_4$, followed by the addition of 0.2 ml 1M aqueous NaBr solution and (2.5 – 50 μl) CTPR3-stabilized Ag seed. Then, 0.8 ml 100 mM MOPS was injected into the solution. After 3 s of gentle shaking, the Au(III) was quickly converted to Au(I), and the solution was left undisturbed overnight. The as-prepared Au colloidal solution was centrifuged at 3,000 rpm for 10 min and the resultant pellets were rinsed with DI water to remove the residue stabilizer and reducing agent. After several purification cycles, the Au NTs were re-dispersed into DI water for later TEM characterization.

**Spectroscopic and morphological characterization**

TEM and High resolution TEM (HR-TEM) analysis was performed on a Philips EM420 at an accelerating voltage of 120 kV and JEOL 2100 at 200 kV, respectively. TEM samples were prepared by applying a 7 μl sample solution on 300 mesh ultrathin carbon-coated Cu grids (EM Science), followed by drying overnight before observation. The thickness, as well as the size distribution of Au NTs, was measured from atomic force microscope (AFM, Veeco BioScope II)

and TEM images using Image J. The UV-Vis spectra of Au NPs were monitored using Agilent Cary 100 Bio and UV-Vis-NIR spectrophotometer. All UV-Vis measurements were conducted in 1cm path length PMMA or quartz cuvette at room temperature.

**Dynamic light scattering (DLS) measurement**

The Au NTs colloidal solution (40 μg/mL) was incubated with 500uL undiluted Fetal bovine serum (FBS, Life Technologies) for 2 h at 37 °C under constant agitation. The Au NTs were centrifuged at 14,000 rpm for 20 min. The pellet was resuspended in water and washed two times by centrifuging at 14,000 rpm for 20 min. The final pellet was resuspened in 1 mL of 10mM NaBr. The average particle size and size distribution of the NPs was measured using a Malvern Zetasizer Nano-ZS, with five measurements taken for each sample. Zeta potential measurements were performed in a 10mM NaBr solution.

**MTT (3-(4, 5-dimethylthiazol-2-yl) 2, 5-diphenyl tetrazolium bromide) assay**

Mouse brain endothelial cells (MBEC) were seeded at 5,000 cells per well in a 96-well plate and incubated for 24 h at 37 °C in a 5% $CO_2$ incubator. Series of dilutions (40, 30, 20, 10, 5 μg/mL) of Au NTs in cell growth medium was added to the wells. A 1% Triton-X solution was used as a positive control. After 6 hours of incubation the nanoparticle solutions were removed and the cells washed with PBS. Then 10 μL of a 5 mg/mL MTT solution and 90 μL growth media were added to each well and further incubated for 4 hours. After 4 hours the media was removed and the formazan crystals were dissolved in 100 μL DMSO. The absorbance at 490 nm was measured using a microplate reader. Percent viability of the cells was calculated as the ratio of mean absorbance of triplicate readings with respect to mean absorbance of control wells.

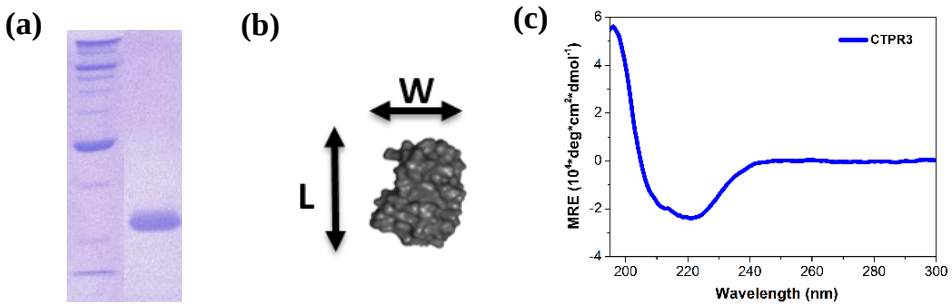


| Recombinant CTPRs | # of amino acid residues | Mw (kDa) | Aspect ratio(L/W) |
|---|---|---|---|
| n=3 | 107 | 12.5 | 1.1 |

CTPR3 is composed of the 3 tandem repeating motifs where each individual repeat is a 34 amino acids helix-turn-helix structure. CTPR3 protein is ~ 12k Da in size and carries overall negative charge. The 34 amino acid sequence is shown as follows:

**AEAWYNLGNAYYKQGDYQKAIEYYQKALELDPNN**

**Figure S1.** (a) 15% SDS-PAGE gel of Protein marker (left lane) and CTPR3 stained with coomassie blue (right lane). (b) Space-filling representation of the structure of CTPR3 protein drawn in Pymol. (c) Circular dichroism (CD) spectrum of CTPR3 protein (MRE: The mean residue ellipticity). Bottom: single letter amino acid sequence of the CTPR repeat. CTPRn proteins are created by repeating this sequence n times (n=3).

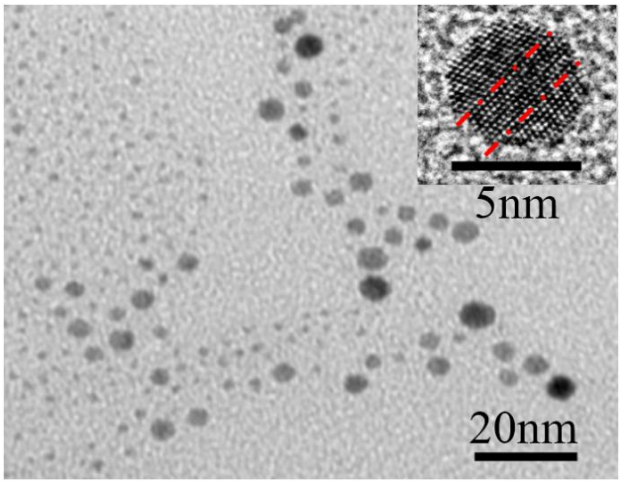


**Figure S2.** TEM image of CTPR3-stabilized Ag seeds (inset: HR-TEM of planar twinning nanocrystal).

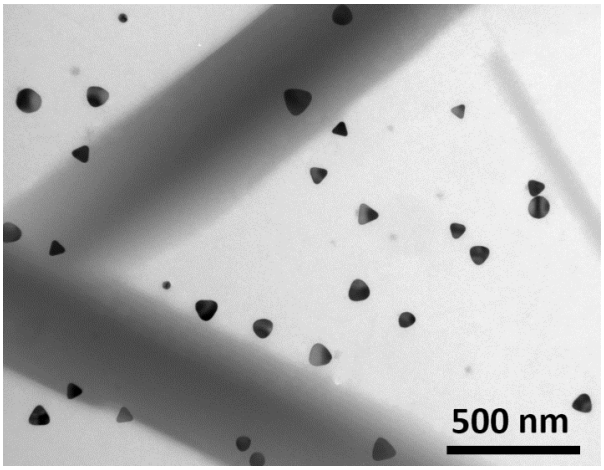


**Figure S3.** (a) TEM image of Au NTs prepared in the presence of 5 mM NaBr, 10 μM CTPR3, 40 mM HEPES and 5 μl Ag without any purificaiton.

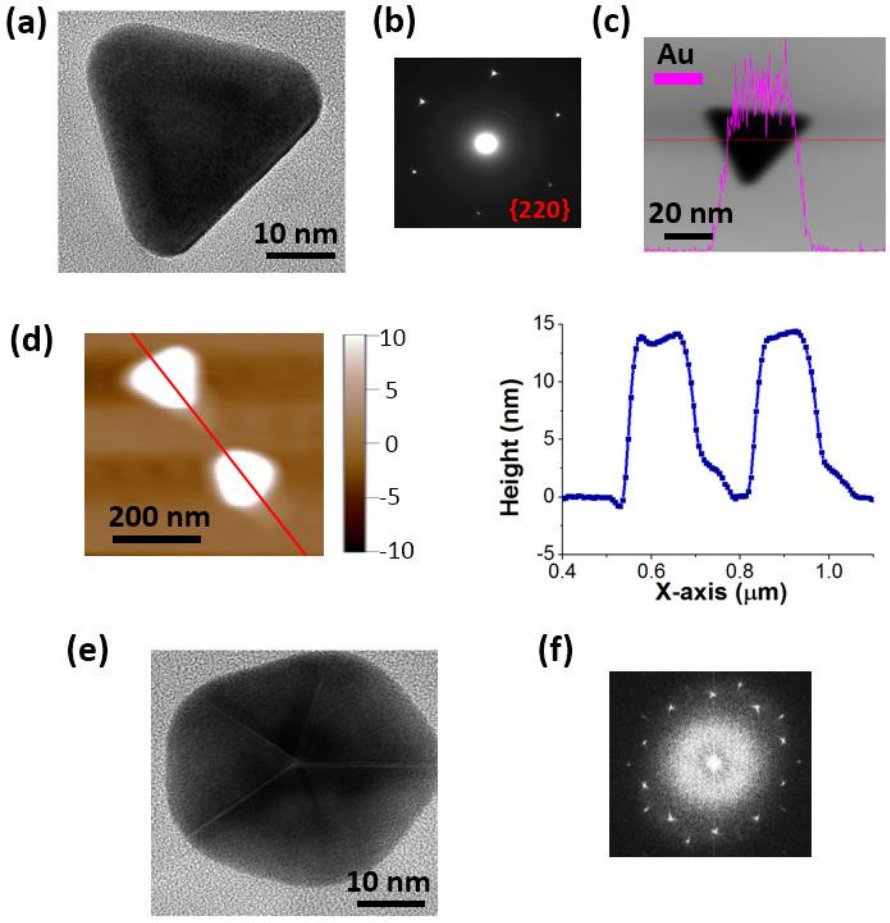


**Figure S4.** (a) HR-TEM images (b) SAED diffraction pattern (C) line scanning EDS characterization of Au NTs (d) AFM profile of Au NTs (e) HR-TEM image and (f) FFT diffraction pattern of Au decahedron.

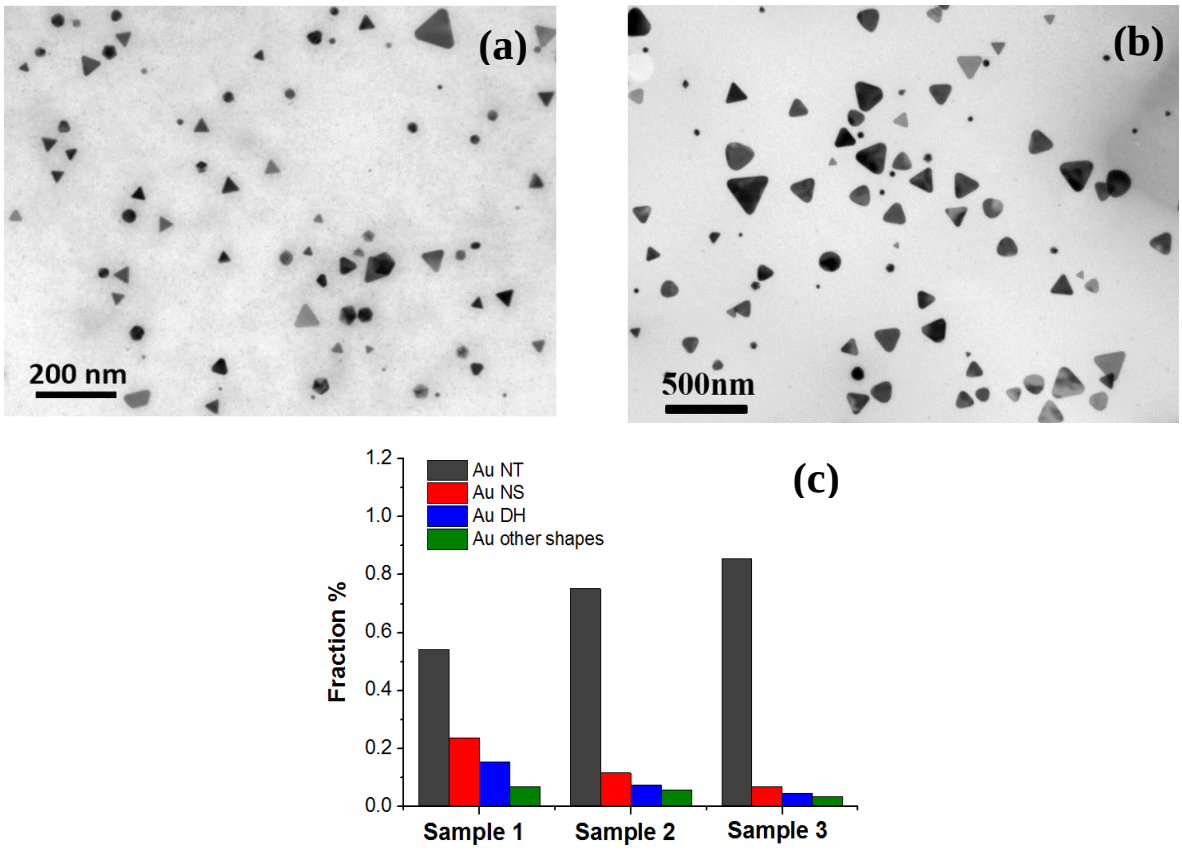


**Figure S5**. (a) TEM image of Au NTs prepared in the presence of 5 mM NaBr, 10µM CTPR3, 40 mM MOPS and 2.5 µl Ag seed without any purificaiton. (c) Histogram representing the distribution of Au NPs with different shapes. Sample 1 is prepared in the absence of Ag seed, Sample 2 and 3 is preapred using 2.5 µl Ag seed before and after purification, respectively. NTs: nanoprisms (dark gray); NS: nanospheres (red); DH: decahedrons (blue); Au with other shapes (green).

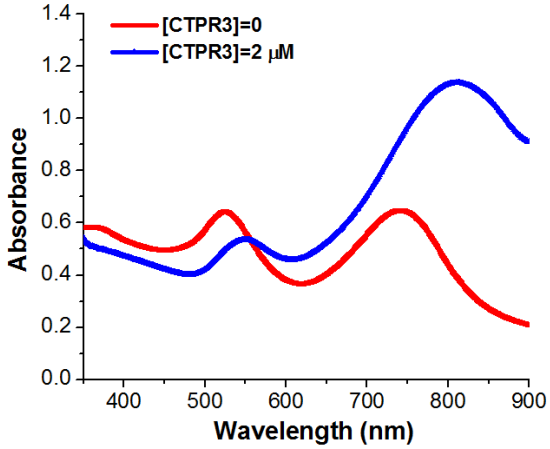


**Figure S6.** UV-Vis spectrum of Au NPs prepared in the absence of CTPR3(red) and in the presence of 2 µM CTPR3(blue) (NaBr = 5 mM and Ag seed = 5 µl).

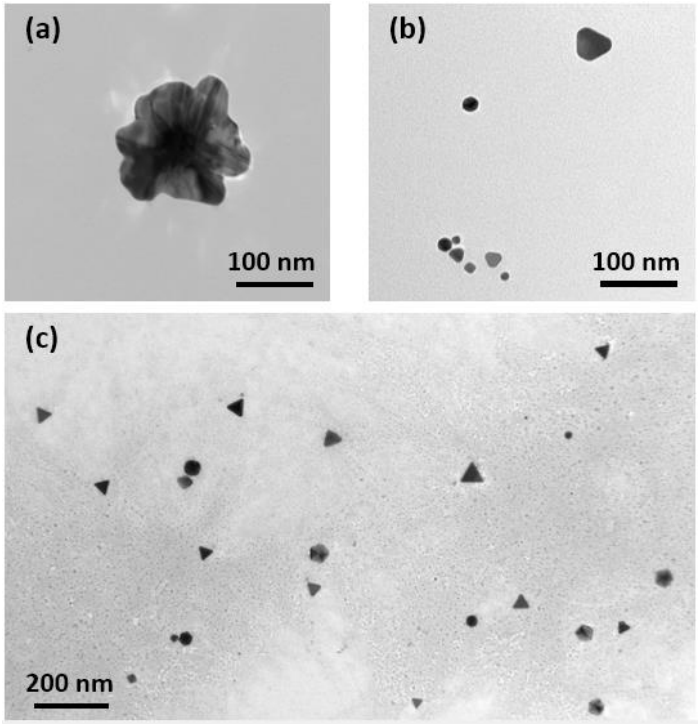


**Figure S7.** TEM images of Au NPs prepared in the presence of (a) 0 μM (b) 0.8 μM and (c) 4 μM CTPR3 ([NaBr] =100 mM).

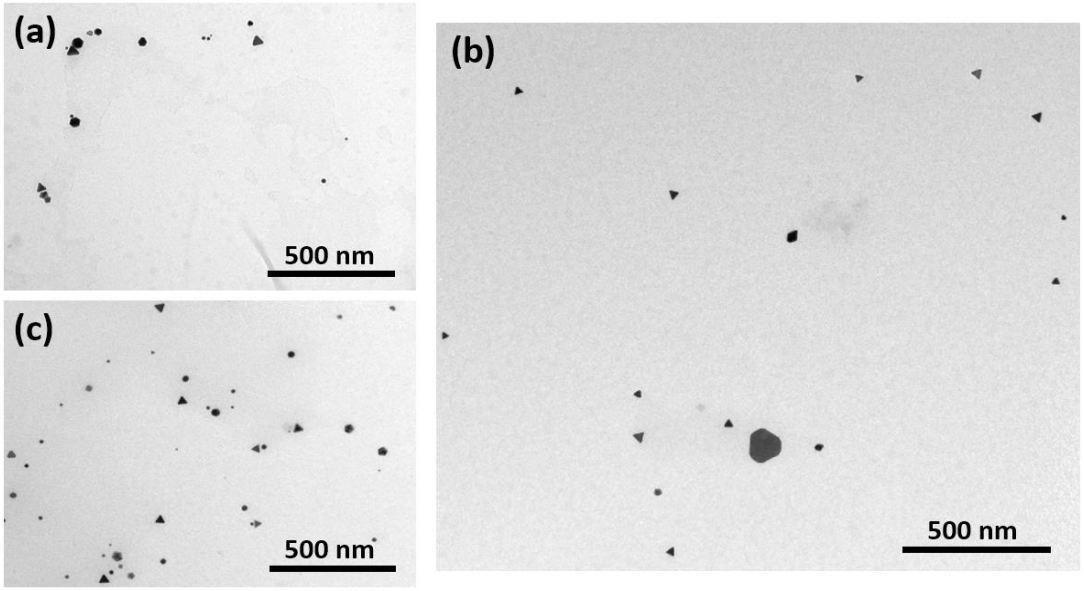


**Figure S8.** TEM images of Au NPs prepared in the presence (a) 10 mM, (b) 100 mM, and (c) 300 mM NaBr ([CTPR3] = 10 μM).

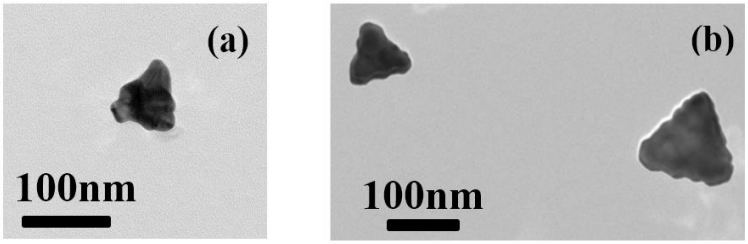


**Figure S9.** TEM image of Au NTs with corrugated and stepped edges, prepared in the presence of 100 mM NaBr and 10 μM CTPR3 (a) after 12 h and (b) after 1 day.

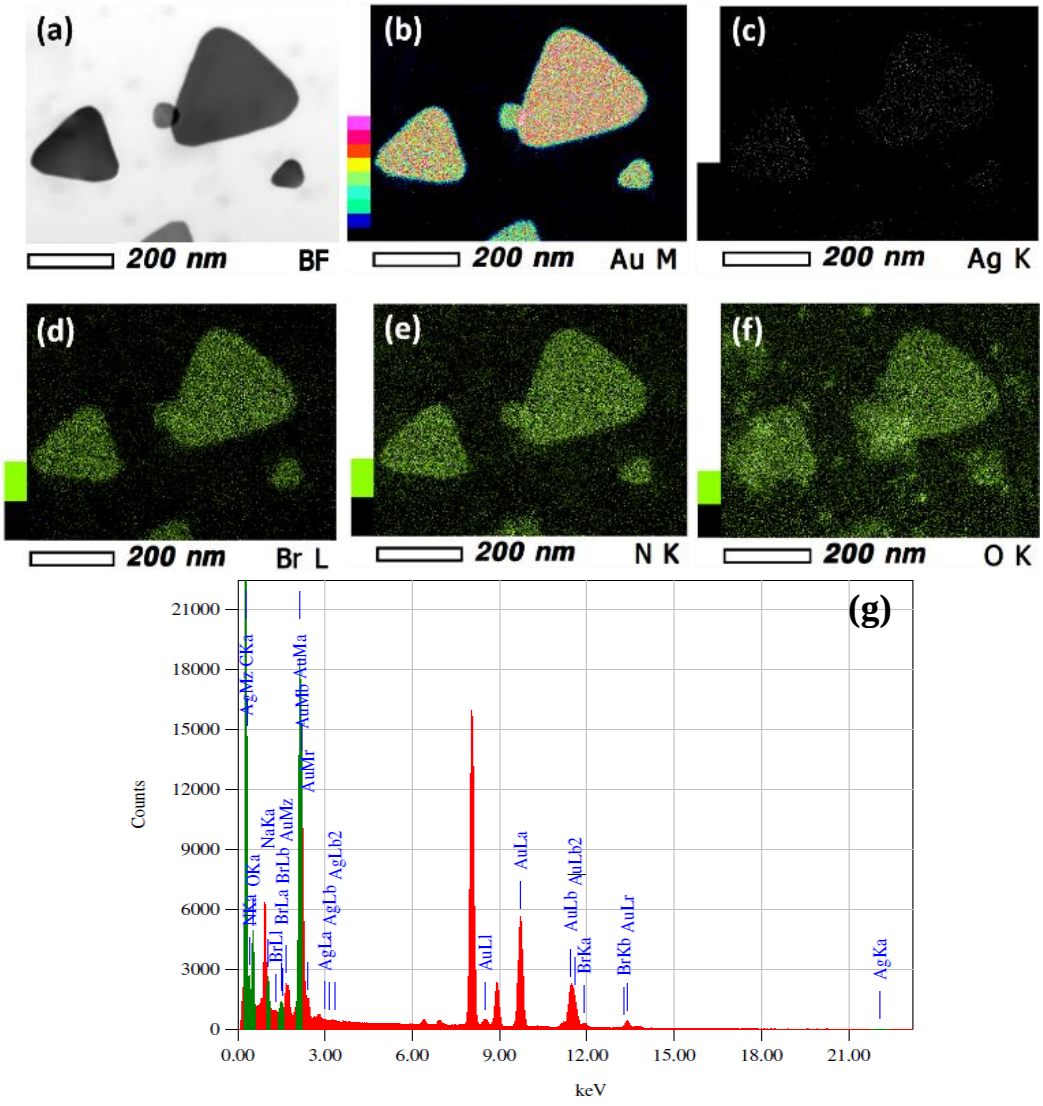


**Figure S10.** (a) TEM images of Au NTs prepared in the presence of 2.5 μl Ag seed. (b-f) Scanning TEM (STEM)-EDS mapping of Au, Ag, Br, N, O, respectively. (Warm color bands indicate higher intensity (g) EDS spectrum corresponding to Figure S10a.

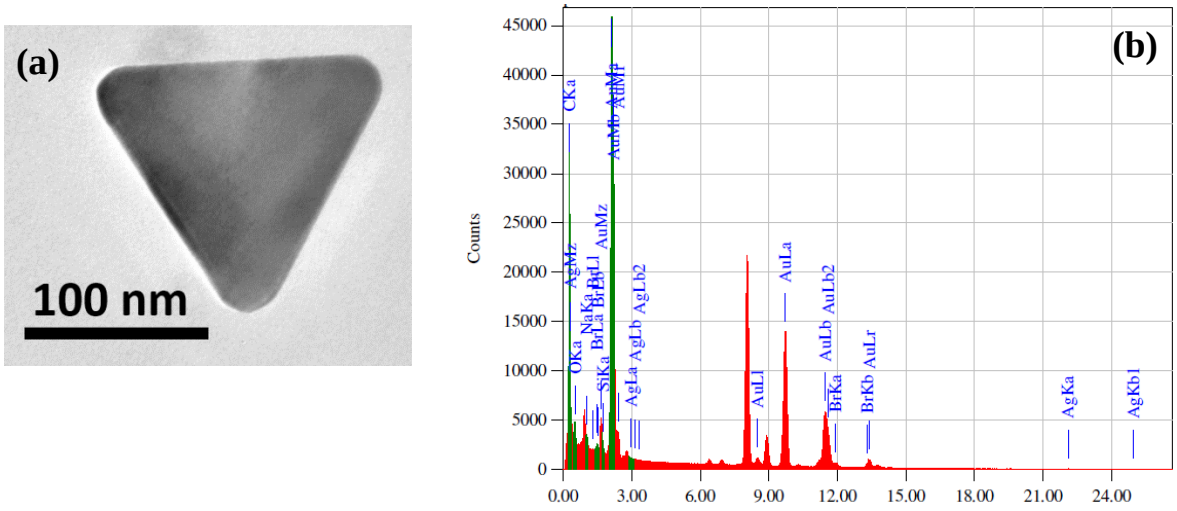


**Figure S11.** (a) TEM image and (b) STEM-EDS spectrum of single Au NT prepared in the presence of 5 mM NaBr, 10 µM CTPR3, 40 mM MOPS and 2.5 µl Ag seeds.

**Table S1.** The hydrodynamic size and zeta potential values of Au NTs before and after incubating with Fetal bovine serum (FBS).

| | Peak 1 Diameter | | Peak 2 Diameter | | ζ-Potential | |
|---|---|---|---|---|---|---|
| | before (nm) | after FBS (nm) | before (nm) | after FBS (nm) | before (mV) | after FBS (mV) |
| Au NTs | 6.05 ± 0.14 | 14.23 ± 1.37 | 59.87 ± 1.17 | 89.87 ± 3.01 | -27.02 | -17.90 |

# Chapter 7. Protein-directed synthesis of triangular silver and gold nanoprisms

Xi Geng, and Tijana Z. Grove

(Invited book chapter in *Methods in Molecular Biology Series*, A. K. Udit, Eds., Springer, 2017, under revision)

**Attributions**: XG was the primary writer of the manuscript. TZG assisted in writing and editing the manuscript.

## 7.1 Abstract

Anisotropic metallic nanoparticles, such as Au and Ag nanoprisms, have received tremendous attention for their application in catalysis, molecular sensing, signal amplification, bioimaging, and therapeutic applications due to their shape-dependent optical and physical properties. Herein, we present a protein-enabled synthetic strategy for the seeded growth of silver and gold nanoprisms with low shape polydispersity, narrow size distribution, and tailored plasmonic absorbance. During the initial seed nucleation step, consensus sequence tetratricopeptide repeat (CTPR) proteins are utilized as potent stabilizers to facilitate the formation of planar-twinned Ag seeds. High yield production of well-defined Ag/Au nanoprisms was achieved, respectively, by adding CTPR-stabilized Ag seeds into the growth solutions containing metal precursor, mild reducing agent, sodium halide, and additional CTPR.

## 7.2 Introduction

Over the past decade, tremendous attention and research efforts have been devoted to the synthesis of plasmonic metallic silver (Ag) and gold (Au) nanoplates. Such NPs are exceptionally well suited for biomedical applications such as biosensing,[1] diagnostics and

therapeutics[2] due to their highly anisotropic structure and localized surface plasmon resonance (LSPR) properties, Hitherto, a wide variety of colloidal routes have been developed to prepare well-defined Ag and Au nanoprisms.[3,4] For instance, photo-induced approach through selective plasmon excitation enabled the efficient conversion of Ag nanospheres into nanotriangles (NTs) with low polydispersity.[5-8] Thermal approaches using synthetic polymers with terminal hydroxyl groups and polar organic solvents provide simple and rapid routes towards high-yield production of Ag NTs.[9,10] On the other hand, the synthesis of planar Au nanoparticles (NPs) is typically achieved via cetyltrimethylammonium bromide/chloride (CTAB/CTAC)-based protocols.[11-18] In addition, seed-mediated growth along with the addition of shape-directing halides has been invoked as the most potent tools for directing the anisotropic growth of noble metal NPs.[17-22] The exquisite shape control is mainly realized through kinetic control as well as the preferential binding to the low index facets. However, a number of challenges remain. Despite high-precision control over the morphology of NPs, harsh experimental condition and energy-consuming processes including the elevated temperatures and hazardous chemicals are involved in a general sense. Furthermore, biomedical applications necessitate tedious and stringent purification processes for the complete removal of toxic cationic surfactants.[23,24]

A growing interest has thus been focused on the biocompatible and green synthetic approaches that mimic natural biomineralizaton process at ambient conditions.[3] In previous studies, a wide array of biopolymers have demonstrated dual functions as stabilizers and reducing agents to produce anisotropic Au and Ag nanoplates. [25-31] To our knowledge, current advances in biomimetic synthesis of anisotropic NPs are still centered on the one-pot biomimetic methods, which typically produce NPs with rather broader shape and size polydispersity. [25-30] In the recent work from our group we demonstrated that the incorporation of seed-mediated

techniques into conventional biomineralizaton yields the unprecedented control over NP size and shape while maintaining biocompatibility requirements.[32,33]

## 7.3 Materials

### 7.3.1 Chemicals and reagents

1. Silver nitrate ($AgNO_3$) (99 %).

2. Hydrogen tetrachloroaurate(III) hydrate (99%)

3. 3-(N-morpholino)propanesulfonic acid (MOPS) (MP biomedicals, LLC)

4. Isopropyl-β-D-thiogalactoside (IPTG) (purity >99%, IBI SCIENTIFIC)

5. Lysozyme (activity >23500 U/mg, CALBIOCHEM, EMD Chemicals, Inc.)

6. TEV protease (made in house)

7. All other chemical reagents including sodium citrate, sodium chloride, sodium bromide, sodium hydrogen phosphate, sodium borohydride, Tris, Tween 20, and ascorbic acid were acquired from Sigma-Aldrich and Fisher Chemicals and were used as received without further purification.

8. Deionized water (18 MΩ/cm, Millipore Milli-Q) was exclusively used for preparing all aqueous solutions and for all rinsing procedures.

### 7.3.2 Expression of CTPR proteins

CTPR proteins with 3, 6, and 18 tandem repeating units were synthesized through recombinant bacterial expression technology as described previously (***Figure 7.1, Table 7.1***).[34,35] Synthetic genes for the desired protein in pPROEx vector, coding for N-terminal $(His)_6$ tag and ampicillin resistance, were transformed into *E .Coli* BL21(DE3) cells and cultured overnight at 37 °C on agar plates. A single colony was selected and incubated overnight in 50 mL of Luria-Bertani (LB) media containing 100 μg/mL of ampicillin. 10 ml of overnight cultures were then

dispensed into 1 L of fresh LB media supplemented with 100 μg/mL ampicillin. The cells were grown in an incubator-shaker (250 rpm) at 37 °C until the optical density ($OD_{600}$) reached 0.8. Expression of CTPR3 and CTPR3 with terminal cysteine (CTPR3-cys) was induced with 1mM isopropyl β-D-thiogalactoside (IPTG) followed by 5 h expression at 37 °C, whereas CTPR6 and 18 were expressed at 18 °C for 16 h in an analogous manner. The cells were harvested by centrifugation at 5,000 rpm for 20 min and pellets were frozen at -80 °C until purification.

**Table 7.1** Molecular design of recombinant CTPRn proteins with different lengths and aspect ratios but same surface exposed residues.

| CTPRn | # of amino acid residues | MW (kDa) | Aspect ratio |
|---|---|---|---|
| n=3 | 107 | 12.5 | 1.1 |
| n=6 | 213 | 25 | 1.9 |
| n=18 | 629 | 74.1 | 4.6 |

Sequence of one CTPR repeat unit: **AEAWYNLGNAYYKQGDYQKAIEYYQKALELDPNN**

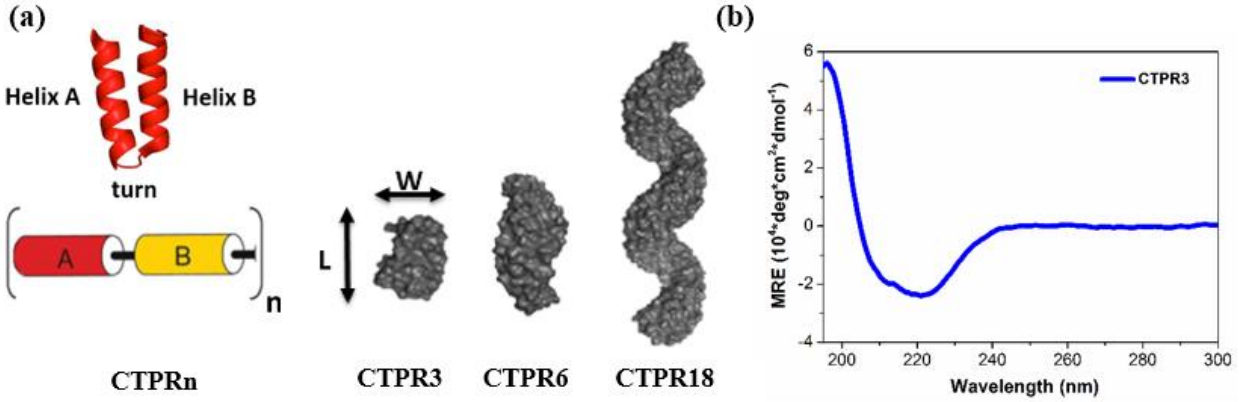


**Figure 7.1** (a) Cartoon representation of CTPRn structure and (b) Circular dichroism (CD) spectrum of CTPR protein (MRE: The mean residue ellipticity). Top: Single letter amino acid sequence of the CTPR repeat. CTPRn proteins are created by repeating this sequence n times (n=3, 6, 18).

### 7.3.3 Purification of CTPR proteins

Cell pellets were re-suspended in lysis buffer consisting of 50 mM Tris, 300 mM sodium chloride and 0.1 wt% Tween 20. After 2 min sonication at 30% power using a microtip and

Mison sonicator, lysed cells were centrifuged at 16,000 rpm for 30 min and protein was purified from supernatant using standard Ni-NTA affinity purification protocol. The N-terminal hexa-histidine tag was then cleaved from the CTPR proteins using TEV protease. Collected proteins were further purified using Akta Prime Plus size exclusion chromatography using Superdex 75 16/600 or Superdex 200 16/600 Prep Grade column in 150 mM sodium chloride and 50 mM sodium phosphate buffer at pH 8 with a flow rate of 0.5 ml/min. As a final step, the aqueous solutions of proteins were dialyzed against 10mM phosphate buffer three times at 4 °C using a dialysis cassette with molecular weight cutoff of 3.5k Da or 10k Da.[35]

## 7.4 Methods

All procedures should be done at room temperature unless specified otherwise.

### 7.4.1 Preparation of CTPR-stabilized Ag seeds

Silver seeds were prepared by adding 5 ml 0.5 mM $AgNO_3$ at the rate of 2 mL/min using a syringe pump (KD Scientific) under vigorous agitation to the aqueous solutions of trisodium citrate (5 mL, 2.5 mM), $NaBH_4$ (0.3 mL, 10 mM) and CTPR3 proteins (0.125 mL of 0.1-2 mg/ml) in a glass vial (***Figure 7.2***).

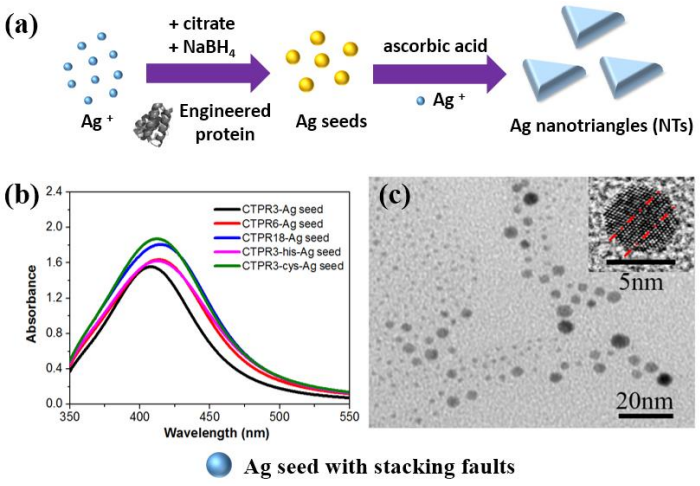


**Figure 7.2** (a) Schematic illustration of synthetic procedures for CTPR-stabilized Ag seeds and seeded growth of Ag nanoprisms. UV-Vis spectra (b) and TEM images (c) of CTPR3-Ag seeds

### 7.4.2 Seeded growth of Ag nanoprisms

In a typical synthesis, 20 µl of CTPR3-stabilized Ag seed solution as prepared in section **3.1** were added into the 5 mL of 0.15 mM ascorbic acid aqueous solution, followed by the dropwise addition of 3 ml of 0.5 mM $AgNO_3$ at the rate of 1 mL/min under stirring. Additionally, a series of Ag NPs were prepared in this manner under ambient condition by adjusting the concentration of protein stabilizer and ascorbic acid(***Figure 7.2a, Figure 7.3, Table 7.2***). The as-prepared Ag colloidal solution was centrifuged at 10,000 rpm for 20 min and the resultant pellets were rinsed with DI water to remove residual ascorbic acid. After two washing cycles, the Ag NTs were re-dispersed into DI water for later use.

(inset: HR-TEM of twinning nanocrystal)

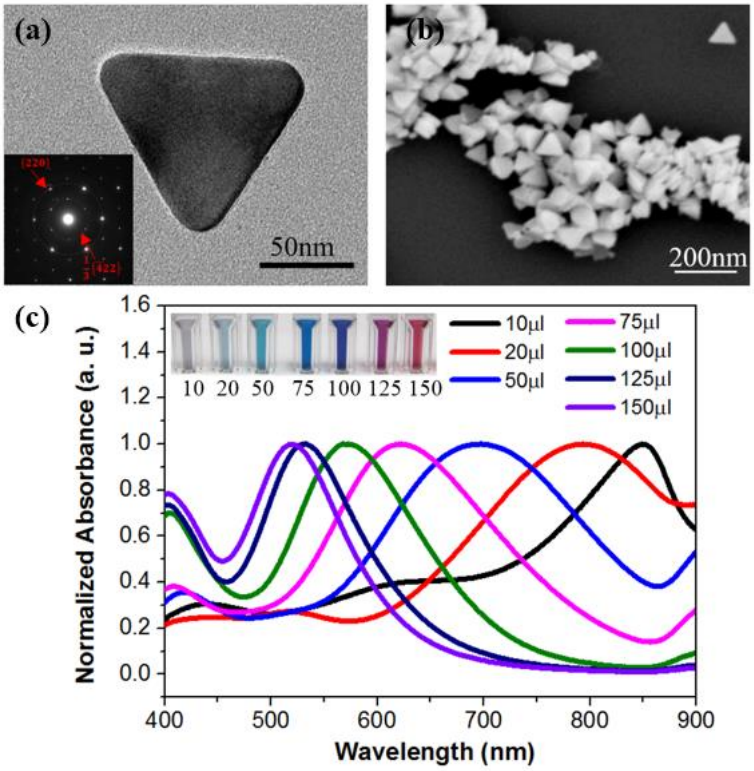


**Figure 7.3** (a) HR-TEM image and selective area diffraction (SAED) pattern of individual Ag NT(inset) (b) SEM image of Ag NTs prepared using 20µl CTPR3-Ag seed solution. (d) UV-Vis spectra and photographic images of the collodial Ag NTs obtained using different volumes of seed solution.

### 7.4.3 Seeded biomineralization of Au nanoprisms

0.1 ml of 80 μM CTPR3 was first mixed with 0.85 ml DI water and 40 μl of 10 mM $HAuCl_4$, followed by the addition of 0.2 ml of 1M aqueous NaBr solution and (2.5 – 50 μl) CTPR3-stabilized Ag seed solution. Then, 0.8 ml of 100 mM MOPS was injected into the solution. After 3s of gentle shaking, the Au(III) was quickly converted to Au(I) as observed by the change of color form pale yellow to clear, and the solution was left undisturbed overnight (***Figure 7.4a***). The as-prepared Au colloidal solution was centrifuged at 3,000 rpm for 10 min and the resultant pellets were rinsed with DI water to remove residual NaBr, CTPR and MOPS. After several purification cycles, the Au NTs were re-dispersed into DI water for subsequent TEM characterization.

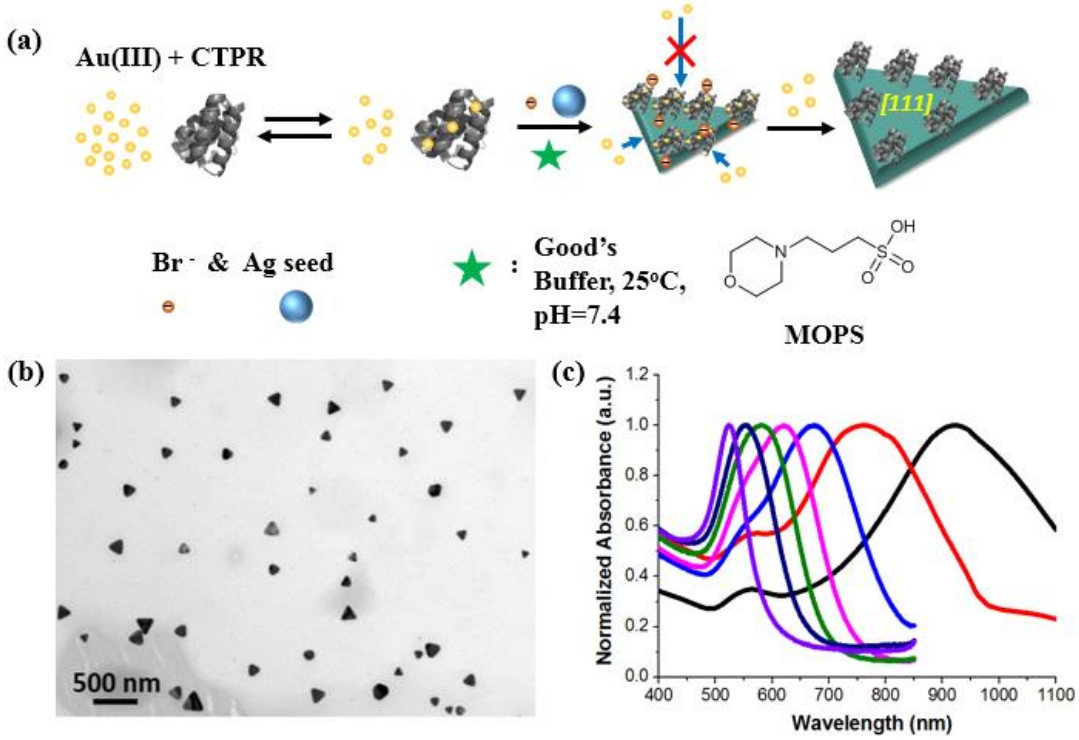


**Figure 7.4** (a) Schematic illustration of seeded biomineralization of triangular Au nanoprisms. (b) representative TEM image of the as-prepared Au NTs (c) UV-Vis spectra of Au NTs prepared in the presence of 2.5 μl (black), 5 μl (red), 10 μl (light blue), 15 μl (magenta), 20 μl (green), 25 μl (dark blue), 50 μl (violet) Ag seeds.

### 7.4.4 Instrumentation

#### 7.4.4.1 Spectroscopic (UV-Vis) characterization.

The UV-Vis spectra of Ag NPs were monitored using an Agilent Cary 100 Bio and Agilent UV-Vis-NIR spectrophotometer. All UV-Vis measurements were conducted in 1cm path length PMMA or quartz cuvette at room temperature.

#### 7.4.4.2 Morphological characterization.

TEM and high resolution TEM (HR-TEM) analysis were performed on a Philips EM420 electron microscope at an accelerating voltage of 120 kV and JEOL 2100 electron microscope at 200 kV, respectively. TEM samples were prepared by applying a 7 μl sample solution on 300 mesh ultrathin carbon-coated Cu grids (EM Science), followed by drying overnight before observation. The thickness, as well as the size distribution of Au NTs, was measured from atomic force microscope (AFM, Veeco BioScope II) and TEM images using Image J (NIH). The morphology of Ag NPs was also characterized using ZEISS 1550VP field emission scanning electron microscopy (FESEM).

#### 7.4.4.3 Dynamic Light Scattering (DLS) measurement

The colloidal stability of Au NTs was assessed by the change of hydrodynamic diameter of NPs before and after incubation with fetal bovine serum (FBS, Life Technologies). The average particle size and size distribution of the NPs was measured using a Malvern Zetasizer Nano-ZS, with five measurements taken for each sample. Zeta potential measurements were performed in a 10mM NaBr solution. The Au NTs colloidal solution as prepared in 3.3 was centrifuged at 14,000 rpm for 20 minutes followed by resuspension of the pellets in 1 mL of 10mM NaBr. This Au NTs colloidal solution (40 μg/mL) was then incubated with 500 uL

undiluted FBS for 2 hours at 37°C under constant agitation, followed by the identical centrifugation and re-dispersion process.

## 7.5 Notes

1. For Ag NTs synthesis, the syringes, vials and pipettes should be cleaned carefully with acetone and DI to get rid of all the contaminants. Otherwise, the chemical residues and dusts in the glassware may interfere with the nucleation and the subsequent seeded growth process.

2. $NaBH_4$ (0.3 mL, 10 mM) solution should be freshly made.3. The as-prepared Ag seeds should be aged for at least 3 hours to circumvent the interference such as homogeneous nucleation arising from the residual $NaBH_4$.

4. The as-prepared Ag seeds should be kept away from light till further use. The quality of seeds is retained for 3 weeks with appropriate storage in the dark.

5. In the seeded growth step, fast seed addition and dropwise $AgNO_3$ injection into the reaction mixture enabled the rapid growth of high-quality anisotropic nanoprisms. It is noted that the twinning-crystal structure Ag seed could be disrupted when exposed to excessive amount of ascorbic acid.

6. Both CTPR3 and citrate are indispensable for the high-yield production of Ag NTs through seed-mediated process. The absence of either one will result in the poor yield of Ag NTs and Ag NPs with diverse shapes formed concomitantly.

7. The ratio of $[AA]/[Ag^+]$ (AA refers to ascorbic acid) is suggested to be within the range of 0.5 -1 for the high-yield of well-defined Ag nanoprisms. Overabundant AA has detrimental effect on the morphology of resulting Ag NTs, as evidenced by the obvious defects such as dislocations and stacking faults.

8. In additional to CTPR3, a series of CTPR proteins including CTPR3-his, CTPR6 and CTPR18 all work as potent stabilizers and shape directing agents to facilitate the growth of Ag NTs using the aforementioned protocols.

**Table 7.2** Ag seeds prepared using varied kind of proteins and the resulting Ag NPs prepared using the corresponding Ag seeds.

| Protein | Product |
|---|---|
| CTPR3,6,18 | well-defined Ag NTs, yield > 85% |
| CTPR3-cys | multiple defects, yield < 40% |
| CTPR3-his | well-defined Ag NTs, yield > 85% |
| BSA | multiple defects, yield < 30% |
| lysozyme | diverse shapes, broad size distribution |

9. A set of control experiments has been conducted to indicate that lysozyme, bovine serum albumin (BSA), and CTPR3-cys are not favorable for the anisotropic growth of Ag NTs. Thus we suggest that neither thiols nor overall positive charge are applicable in the synthetic route toward Ag NTs (***Table 7.2***).

10. The concentration of CTPR3 plays a critical role in determining the yield and quality of final products. The ideal concentration of CTPR3 was found to be approximately 1.8 μM based on morphological and UV-Vis observations.

11. Precise control over the wavelength of LSPR is attainable when less seeds (<100 μl of solution as prepared in ***section 3.1***) are used. Otherwise, bimodal absorbance profile is observed, attributed to the competitive growth between isotropic nanospheres and facet-selected NTs in the presence of a large number of nuclei.

12. The LSPR could be conveniently tuned to span a broad spectral range, from visible to NIR region (500-900nm), through the variation of the quantities of Ag seeds used during the growth step (***Figure 7.3, Table 7.3***). As the total number of seeds increased, the mean

particle size declined steadily and the resultant Ag NPs underwent a progressive shape transition from triangular nanoprisms to round disks.

**Table 7.3** The optical and morphological features of Ag nanoprisms prepared using varied amount of CTPR3-Ag seeds.

| Ag seed (µl) | LSPR $\lambda_{max}$ (nm) | Shape | Size (nm) |
|---|---|---|---|
| 10 | 849 ± 24 | NTs | 144.1 ± 25 |
| 20 | 793 ± 19 | NTs | 102.8 ± 18.9 |
| 50 | 698 ± 14 | NTs | 69 ± 7.5 |
| 100 | 572 ± 9 | NTs + disks | 38.6 ± 8.7 |
| 150 | 520 ± 11 | NTs + disks | 19.4 ± 6.1 |

13. For the purpose of long-term storage of Ag NTs, 0.3 ml of 25 mM citrate aqueous solution is typically added immediately after the synthesis. The colloidal Ag NTs are subject to the etching and deformation in the absence of sufficient capping agent, which is revealed as the dramatic blue shift of absorbance wavelength within a short while.

14. For Au NTs synthesis, all the glassware ought to be cleaned with aqua regia, followed by extensive rinsing with Milli-Q water. Preparation of aqua regia: In a glass beaker, mix hydrochloric acid (HCl) and nitric acid ($HNO_3$) in a volume ratio 3:1. The preparation should take place inside a fume hood, since the liquids and its vapors are extremely corrosive and highly oxidizing. Therefore, the use of appropriate gloves, lab coat, and chemical splash goggles is mandatory.

15. During the synthesis of Au NTs, MOPS serves as mild reducing agent while CTPR3 and NaBr were employed as the shape-directing agent. Other than MOPS, the choice of reducing agent could be further extended to other Good's buffers such as 4-(2-hydroxyethyl)-1-piperazineethanesulfonic acid (HEPES) and so forth.

16. Ag seeds are of significant importance to the production of Au NTs. In the case of Ag seeds-free synthetic process, a mixture of Au nanoprisms, five-fold penta-twinned Au NPs (decahedrons) and Au nanospheres are produced. Sizes and shapes of these structures are highly polydisperse due to the inherent drawbacks such as unavoidable self-nucleation events and poor quality of initial nuclei with diverse crystal structures.

17. The addition of Ag seeds not only accelerates the reaction but also lowers the usage of CTPR protein and NaBr without compromising the final yield. The details are listed in ***Table 7.4.***

18. The original synthetic process could be scaled up to 5ml or beyond for more efficient fabrication of Au NTs.

**Table 7.4** Comparison between one pot and seeded growth of Au NTs in terms of reaction time, yield, usage of chemicals, morphological and optical features.

| Ag seed | Reaction time | Au NTs yield | size (nm) | [CTPR] (μM) | [NaBr] (mM) | LSPR (nm) |
|---|---|---|---|---|---|---|
| **No** | 1-2 weeks | <50% | <50 | 10 | 50 | 550-580 |
| **Yes** | overnight | >75% | 50-140 | 2 | 5 | 500-900 |

19. The as-prepared Au NTs exhibited remarkable colloidal stability since no severe agglomeration was detected through DLS study during the centrifugation and incubation in FBS. The excellent colloidal stability is mainly associated with the negatively charged CTPR proteins corona with moderate binding affinity to the Au NTs surface.[36]

20. Not only CTPR3, but a series of CTPR proteins of different length (***Figure 7.1a***) can serve as alternative stabilizers and shape directing agents simply by following the identical protocols.

21. Analogous to the synthesis of Ag nanoprisms, the LSPR of Au nanoprisms can also be readily tailored from ca. 500nm to 900nm by simply adjusting the amount of Ag seeds

added in the initial growth stage (***Figure 7.4, Table 7.5***). Accordingly, the size of the Au nanoprisms could be finely tailored from 61 ± 7 nm to 137 ± 33 nm.

**Table 7.5** The optical and morphological features of Au nanoprisms prepared using varied amount of CTPR3-Ag seed solution as prepared in 3.1 (2.5-20 μl).

| Ag seed (μl) | LSPR $\lambda_{max}$ (nm) | Shape | Size (nm) |
|---|---|---|---|
| 2.5 | 922 ± 30 | NTs | 137 ± 33 |
| 5 | 762 ± 22 | NTs | 99 ± 15 |
| 10 | 675 ± 18 | NTs + disks | 79 ± 10 |
| 15 | 620 ± 13 | NTs + disks | 61 ± 7 |
| 20 | 582 ± 8 | disks + spheres | N/A |

22. In sharp contrast with the conventionally used CTAB based protocols, the depicted protocols efficiently mitigate the cytotoxicity of the Au NTs, which was ascertained by the MTT assay.[32]

## 7.6 Acknowledgements

The authors would like to thank Dr. Guoliang Liu for insightful comments, suggestions, and discussion on this research work. Authors acknowledge ICTAS Nanoscale Characterization and Fabrication Lab (NCFL) for the use of AFM, TEM, and SEM. This work was in part supported by the JFC ICTAS grant number 119106 to TZG.

## 7.7 References

(1) Beeram, S. R.; Zamborini, F. P. *ACS Nano* **2010**, *4*, 3633.
(2) Pelaz, B.; Grazu, V.; Ibarra, A.; Magen, C.; del Pino, P.; de la Fuente, J. M. *Langmuir* **2012**, *28*, 8965.
(3) Millstone, J. E.; Hurst, S. J.; Métraux, G. S.; Cutler, J. I.; Mirkin, C. A. *Small* **2009**, *5*, 646.
(4) Yu, H.; Zhang, Q.; Liu, H.; Dahl, M.; Joo, J. B.; Li, N.; Wang, L.; Yin, Y. *ACS Nano* **2014**, *8*, 10252.
(5) Xue, B.; Wang, D.; Zuo, J.; Kong, X.; Zhang, Y.; Liu, X.; Tu, L.; Chang, Y.; Li, C.; Wu, F.; Zeng, Q.; Zhao, H.; Zhao, H.; Zhang, H. *Nanoscale* **2015**, *7*, 8048.
(6) Jin, R.; Charles Cao, Y.; Hao, E.; Metraux, G. S.; Schatz, G. C.; Mirkin, C. A. *Nature* **2003**, *425*, 487.

(7) Jin, R.; Cao, Y.; Mirkin, C. A.; Kelly, K. L.; Schatz, G. C.; Zheng, J. G. *Science* **2001**, *294*, 1901.
(8) Xue, C.; Mirkin, C. A. *Angew. Chem. Int. Ed.* **2007**, *46*, 2036.
(9) Pastoriza-Santos, I.; Liz-Marzán, L. M. *Nano Lett.* **2002**, *2*, 903.
(10) Kim, M. H.; Yoon, D. K.; Im, S. H. *RSC Adv.* **2015**, *5*, 14266.
(11) Millstone, J. E.; Park, S.; Shuford, K. L.; Qin, L.; Schatz, G. C.; Mirkin, C. A. *J. Am. Chem. Soc.* **2005**, *127*, 5312.
(12) Millstone, J. E.; Métraux, G. S.; Mirkin, C. A. *Adv. Funct. Mater.* **2006**, *16*, 1209.
(13) Sau, T. K.; Murphy, C. J. *J. Am. Chem. Soc.* **2004**, *126*, 8648.
(14) Huang, Y.; Ferhan, A. R.; Gao, Y.; Dandapat, A.; Kim, D.-H. *Nanoscale* **2014**, *6*, 6496.
(15) Scarabelli, L.; Coronado-Puchau, M.; Giner-Casares, J. J.; Langer, J.; Liz-Marzán, L. M. *ACS Nano* **2014**, *8*, 5833.
(16) Chen, L.; Ji, F.; Xu, Y.; He, L.; Mi, Y.; Bao, F.; Sun, B.; Zhang, X.; Zhang, Q. *Nano Lett.* **2014**, *14*, 7201.
(17) Millstone, J. E.; Wei, W.; Jones, M. R.; Yoo, H.; Mirkin, C. A. *Nano Lett.* **2008**, *8*, 2526.
(18) Ha, T. H.; Koo, H.-J.; Chung, B. H. *J. Phys. Chem. C* **2007**, *111*, 1123.
(19) Jana, N. R.; Gearheart, L.; Murphy, C. J. *Langmuir* **2001**, *17*, 6782.
(20) Niu, W.; Zhang, L.; Xu, G. *Nanoscale* **2013**, *5*, 3172.
(21) Personick, M. L.; Mirkin, C. A. *J. Am. Chem. Soc.* **2013**, *135*, 18238.
(22) Lohse, S. E.; Burrows, N. D.; Scarabelli, L.; Liz-Marzán, L. M.; Murphy, C. J. *Chem. Mater.* **2014**, *26*, 34.
(23) Alkilany, A. M.; Nagaria, P. K.; Hexel, C. R.; Shaw, T. J.; Murphy, C. J.; Wyatt, M. D. *Small* **2009**, *5*, 701.
(24) Alkilany, A. M.; Murphy, C. J. *J. Nanopart. Res.* **2010**, *12*, 2313.
(25) Shankar, S. S.; Rai, A.; Ankamwar, B.; Singh, A.; Ahmad, A.; Sastry, M. *Nat. Mater.* **2004**, *3*, 482.
(26) Liu, B.; Xie, J.; Lee, J. Y.; Ting, Y. P.; Chen, J. P. *J. Phys. Chem. B* **2005**, *109*, 15256.
(27) Xie, J.; Lee, J. Y.; Wang, D. I. C. *J. Phys. Chem. C* **2007**, *111*, 10226.
(28) Au, L.; Lim, B.; Colletti, P.; Jun, Y.-S.; Xia, Y. *Chem. Asian J.* **2010**, *5*, 123.
(29) Li, C.; Bolisetty, S.; Mezzenga, R. *Adv. Mater.* **2013**, *25*, 3694.
(30) Xie, J.; Lee, J. Y.; Wang, D. I. C.; Ting, Y. P. *Small* **2007**, *3*, 672.
(31) Naik, R. R.; Stringer, S. J.; Agarwal, G.; Jones, S. E.; Stone, M. O. *Nat. Mater.* **2002**, *1*, 169.
(32) Geng, X.; Roth, K. L.; Freyman, M. C.; Liu, J.; Grove, T. Z. *Chem. Commun.* **2016**, *52*, 9829.
(33) Geng, X.; Leng, W.; Carter, N. A.; Vikesland, P. J.; Grove, T. Z. *J. Chem. Mater. B* **2016**, *4*, 4182.
(34) Kajander, T.; Cortajarena, A. L.; Main, E. R. G.; Mochrie, S. G. J.; Regan, L. *J. Am. Chem. Soc.* **2005**, *127*, 10188.
(35) Cortajarena, A. L.; Yi, F.; Regan, L. *ACS Chem. Biol.* **2008**, *3*, 161.
(36) Roth, K. L.; Geng, X.; Grove, T. Z. *J. Phys. Chem. C* **2016**, *120*, 10951.

# Chapter 8. Sodium lignosulfonate as a new polymeric stabilizer and shape directing agent for the rapid bioenabled synthesis of Ag nanoprisms

Xi Geng, Kristina L. Roth, Jianzhao Liu, Spencer R. Ahrenholtz, Yunhua Li, Alan R. Esker, Amanda J. Morris and Tijana Z. Grove

(Manuscript in preparation)

**Attributions:** XG synthesized and characterized the NPs with UV-Vis, TEM and HRTEM. XG also conducted colorimetric sensing of metal cations using Ag nanoprisms. KLR, JL, SRA and YL performed fluorescence, AFM, Electrochemical, SEM, respectively. Both ARE and AJM impart in-depth knowledge and expertise during the course of study. Progress on this project was made under supervision of TZG.

## 8.1 Abstract

In the present work, a sustainable biomaterial, Sodium LignoSulfonate (SLigS), has been found to serve as both a potent stabilizer and an efficient shape directing agent in the growth of well-defined Ag nanoprisms using a one-pot or seeded growth strategy. The influential effects of reactants and additives including the concentration of SLigS, $H_2O_2$ and $NaBH_4$ were studied in great detail. By scrupulous monitoring of the evolution of NPs using UV-Vis and TEM, we inferred that not only did SLigS regulate the twining crystal structure of Ag seed during the nucleation stage, but also is involved in the stabilization of the (111) facet of Ag nanoplates (NPLs) during the $H_2O_2$ induced etching process. The molecular interaction between SLigS and Ag(0)/Ag(I) were further validated via fluorescence quenching and square wave voltammetry. The as-prepared Ag nanoprisms exhibited remarkable colloidal stability and were uniformly blended with biopolymers to fabricate homogenous coatings. Since the Ag nanoprisms are

susceptible to morphological deformation in the presence of strong oxidant, they also hold great potential for the colorimetric sensing of oxidative metal cation species such as $Fe^{3+,}$ $Cr^{3+,}$ etc.

## 8.2 Introduction

Remarkable progress has been made to explore plasmonic metallic NPs, owing in large part to their tunable localized surface plasmon resonance (LSPR) band ranging from the visible to near infrared (NIR) regions.[1,2] It is well-established that LSPR, as well as the localized electromagnetic fields are closely associated with the size, shape and local dielectric environment of NPs.[1,3] As a consequence, a wide diversity of anisotropic plasmonic NPs have been synthesized and exploited for molecular sensing, bioimaging and therapeutic applications.[4,5]

An assortment of well-defined anisotropic NPs including nanowires,[6,7] nanorods,[8] nanoprisms[9,10] branched NPs,[11-13] along with the plate-like Ag nanoprisms have received tremendous attention over the last decade.[9] Intriguingly, Ag nanoprisms possess higher-ordered LSPR mode (dipole and quadrupole absorbance bands), which have been confirmed through discrete dipole approximation (DDA) simulation and UV-Vis spectroscopy.[9,14] Additionally, the in-plane dipole LSPR can be readily adjusted by manipulating the ratio of edge length to thickness, and the plasmonic hot spots located at the sharp tips entails the ultra-high colorimetric or Raman sensitivity towards analytes, such as glucose, $Hg^{+}$, and DNA, etc.[15-18]

The generic colloidal synthetic pathways of Ag nanoprisms could be categorized into either photo-induced or thermal-based approaches.[9,18-20] In the former case, selective plasmon excitation is employed to trigger the transformation of Ag nanospheres into NTs with low shape polydispersity, but at the cost of elongated time, large energy consumption and costly instrumentation. Alternatively, thermal approaches are more favourable for the rapid and scale-up synthesis of Ag nanoprisms either in aqueous or organic solutions. [21-24] At the early stage,

polymeric surfactants with terminal hydroxyl groups and polar organic solvents with high boiling temperature are typically utilized as dual functional reductant and shape directing agent to achieve the fine shape control of Ag nanoprisms. [21-24]

Inspired by the seminal work by Murphy et al, [8,25] seeded growth of Ag nanoprisms with high-yield and low polydispersity were achieved in 2008.[26] In an elegant synthesis, sodium polystyrene sulfonate (SPSS) was ingeniously introduced during the seed formation step, where the SPSS is thought to critically influence the defect structure of the initially formed seed rather than solely acted as a shape-directing adsorbate.[26] Recently, Ag nanoprisms with high aspect ratio and large NIR window have been synthesized by means of successive seed-mediated growth cycles in the presence of citrate or polyvinylpyrrolidone (PVP).[27,28] By harnessing oxidative $H_2O_2$, Ag(I) as well as a series of different shaped Ag NPs were consumed and converted to the 2D nanoprisms enclosed by the relatively stable (111) facet. [29-31] It was claimed that the adhesion of citrate ligand coupled with the borohydride anions stabilize the triangular shape of Ag NPs, while PVP or other hydroxyl-containing compound could serve as extra stabilizer.[30]

Apart from conventionally used small organic or synthetic polymeric capping agents, a host of green chemical methods have recently been developed toward noble metal nanoplates [32-34], in which biopolymers such as plant extracts[35,36] amino acids,[37] proteins[33], polyssacharides[38,39] played key roles in the kinetic control, facet-selective adsorption and reduction of precursors. Notably, attempts have also been made to successfully fabricate miscellaneous Ag nanostructures by virtue of tuning the experimental conditions such as the temperature and the concentration of polysaccharide derivatives.[39-42] Nevertheless, a series of issues and challenges still confronts us, demanding the in-depth understanding of the role of the biopolymer species as

well as the rational design of the synthetic pathway. First and foremost, the overall yield and quality of the resulting products are far from satisfactory, mainly arising from the inherent drawback of the one-pot method. Secondly, even though seed-mediated growth has been applied in some study,[39] the impact of biomass on the crystal structure of seeds is scarcely discussed. Additionally, there is an issue of the elevated temperature, which is more favorable for the homogeneous nucleation rather than the desirable epitaxial deposition. Last but not least, the oversimplified growth mechanism, particularly, the selective adsorption of biopolymers onto (111) facets, are resorted to elucidate the morphological evolution of nanoprisms.

Lignin as one of the most abundant components of renewable biomass is mainly composed of phenolic repeat units. Its derivative SLigS is a water soluble anionic polyelectrolyte possessing very compelling physicochemical properties analogous to the SPSS. In the present work, SLigS were successfully employed as stabilizer and shape directing agent for the (i) seed-mediated and (ii) $H_2O_2$ induced one-pot synthesis of 2D anisotropic Ag nanoprisms (***Scheme 8.1***). Based on our meticulous studies, it is plausible to believe appropriate physicochemical properties including the negative charge, aromatic repeating units and moderate binding affinity to Ag species are the key to the high-yield production of Ag nanoplates. The as-prepared Ag nanoprisms exhibited remarkable colloidal stability and was blended uniformly with biopolymers to fabricate homogenous SLigS-Ag coating. Since the Ag nanoprisms are susceptible to morphological deformation in the presence of a strong oxidant, they also hold great promises for the colorimetric sensing of oxidative metal cation species such as $Fe^{3+}$ and $Cr^{3+}$.

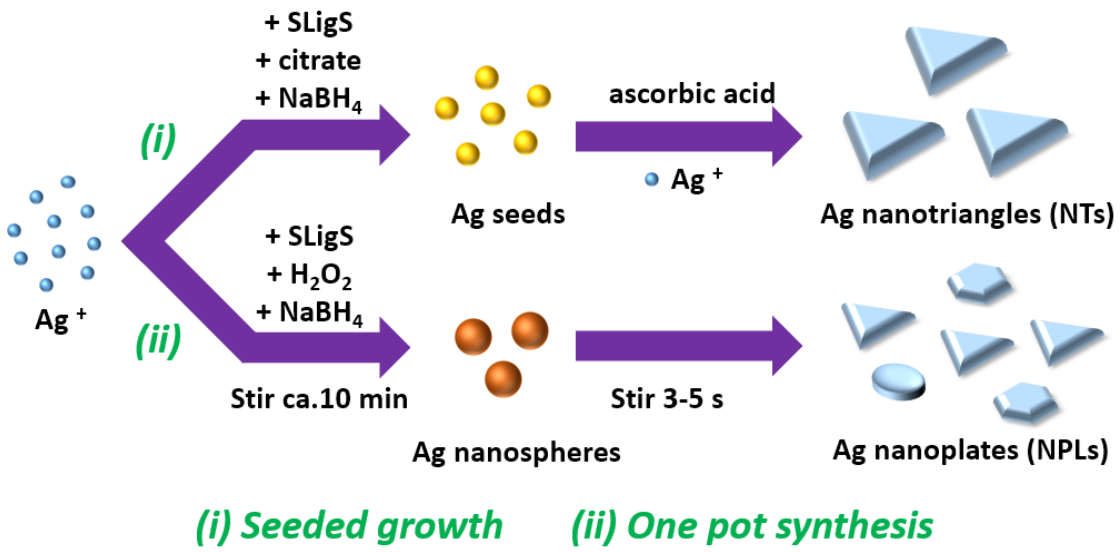


**Scheme 8.1** Schematic illustration of the synthesis of Ag nanoprisms using (i) Seed-mediated and (ii) one pot method.

## 8.3 Experimental

### 8.3.1 Chemicals and reagents

Silver nitrate (>99.5%) was purchased from Fluka. Sodium LignoSulfonate (SLigS), lignin derivatives and other chemical reagents including sodium borohydride, trisodium citrate, 30wt% $H_2O_2$, etc. were acquired from Sigma-Aldrich and Fisher Chemicals and were used as received without further purification. Deionized water (18 MΩ/cm, Millipore Milli-Q) was exclusively used for preparing all aqueous solutions and for all rinsing procedures.

### 8.3.2 Preparation of SLigS-stabilized Ag seeds and seed-mediated growth of Ag NTs

All NP synthetic procedures are performed at ambient conditions unless specified otherwise. Ag seeds and Ag NTs were prepared by a previously reported method with minor adaption.[26,43] Briefly, an aqueous solutions containing trisodium citrate (2.3 mM), $NaBH_4$ (0.55 mM) and SLigS (0.1-4 mg/ml) was first prepared in a glass vial. Then 5 ml 0.5 mM $AgNO_3$ was added dropwise at the rate of 2 mL/min into the above solution using a syringe pump (KD Scientific) under vigorous agitation. The as-prepared Ag seeds were kept in the dark and aged at

least 3 hours before use. In the subsequent step, 10-150 µl aged SLigS-stabilized Ag seeds were into the 5ml growth solution containing ascorbic acid (0.15 mM), followed by the dropwise addition of 3 ml $AgNO_3$ (0.5 mM) at the rate of 1 mL/min under stirring.

### 8.3.3 $H_2O_2$ induced one pot synthesis of Ag nanoplates (NPLs)

An aqueous solution containing 0.1mM silver nitrate and SLigS (0.5-4 mg/ml) was first made, followed by the addition of 1-60 µl hydrogen peroxide ($H_2O_2$, 30 wt%) and 0.45 ml $NaBH_4$ (20 mM). The reaction mixture was vigorously stirred for 10-20 mins until the color is no longer changed. The as-prepared Ag nanoprisms using either one pot or seed-mediated method could be easily harvested by centrifugation at 7,000 rpm for 15 mins and dispersed homogeneously in water and other organic solvents (ethanol, acetone, etc.) without forming apparent agglomeration.

### 8.3.4 Instrumentation

TEM and high resolution TEM (HR-TEM) analysis was performed on a Philips EM420 at an accelerating voltage of 120 kV and JEOL 2100 at 200 kV, respectively. TEM samples were prepared by applying a 7 µl sample solution on 300 mesh ultrathin carbon-coated Cu grids (EM Science), followed by drying overnight before observation. The morphology of Ag NPs is also characterized using ZEISS 1550VP field emission scanning electron microscopy (FESEM) and the thickness of the Ag nanoprisms were assessed using atomic force microscope (AFM, Veeco BioScope II). The UV-Vis spectra of Ag NPs were monitored using an Agilent Cary 100 Bio UV-Vis spectrophotometer. All UV-Vis measurements were conducted in 1cm path length PMMA cuvette at room temperature. Electrochemical experiments were performed on a Basi EC epsilon potentiostat using a $Ag/AgNO_3$ (0.01 M) aqueous reference electrode. The $Ag/AgNO_3$ electrode was calibrated against $Fe(CN)_6^{3-}/Fe(CN)_6^{4-}$, which all potentials are reported against.

Square-Wave Voltammetry (SWV) measurements were collected in a three-electrode arrangement using Pt mesh as a counter electrode, $Ag/AgNO_3$ reference electrode, and fluorine-doped tin oxide (FTO) working electrode. The scans were taken with a 1 mV step size, 100 mV amplitude, and 3 Hz frequency. The fluorescence quenching experiments were performed at room temperature on an Agilent Cary Eclipse fluorimeter using the 1cm path length quartz cuvette. Briefly, aqueous SLigS solution was titrated every 10 min with $AgNO_3$ or Ag NPs colloidal solutions.

### 8.3.5 Colorimetric detection of oxidative metal cations: $Fe^{3+}$, $Cr^{3+}$

10 μL of metal cations ($M^{n+}$,10 mg/mL) aqueous solution was added to 1 mL of diluted colloidal Ag NT solution ( $[M^{n+}]$ = 10 ppm, $[Ag^0]$ = 38 μM, $Abs_{AgNTs} \approx 0.4$), and the corresponding UV−vis spectra were recorded accordingly. The selectivity for $Fe^{3+}$, $Cr^{3+}$ was confirmed by adding other metal ions to the final concentration of 20 ppm instead of $Fe^{3+}$, $Cr^{3+}$.

## 8.4 Results and discussion

### 8.4.1 Morphological features of Ag NTs and Ag NPLs

As shown in the ***Figure S1***, well dispersed Ag nanospheres (4.3 ± 1.2 nm) along with considerable amount of tiny Ag nanoclusters (< 2 nm) were produced at the initial stage through rapid reduction of $AgNO_3$ by $NaBH_4$. The as-prepared Ag seeds with characteristic extinction peak at 408 nm were aged for at least 3 h in the dark until further usage. Triangular Ag nanoprisms were subsequently prepared as depicted in the ***scheme 8.1a***, and the planar fcc structure of Ag NPs is ascertained by HR-TEM, selected area electron diffraction (SAED) pattern and AFM characterization (***Figure 8.1a-c***).[9] The average edge length and thickness of Ag NTs is estimated to be 97 ± 19 nm and 10 ± 2 nm, respectively, as shown in ***Figure 8.1c-d***. Aside from the seeded growth route, high yield production of Ag nanoplates (NPLs) were also

attained in the presence of appropriate amount of $H_2O_2$, $NaBH_4$ and SLigS, evidenced by the observation of overwhelming existence of triangular and disk-like NPLs in ***Figure 8.1e***. It is noteworthy that the absence of SLigS results in the poor yield as well as broad morphological

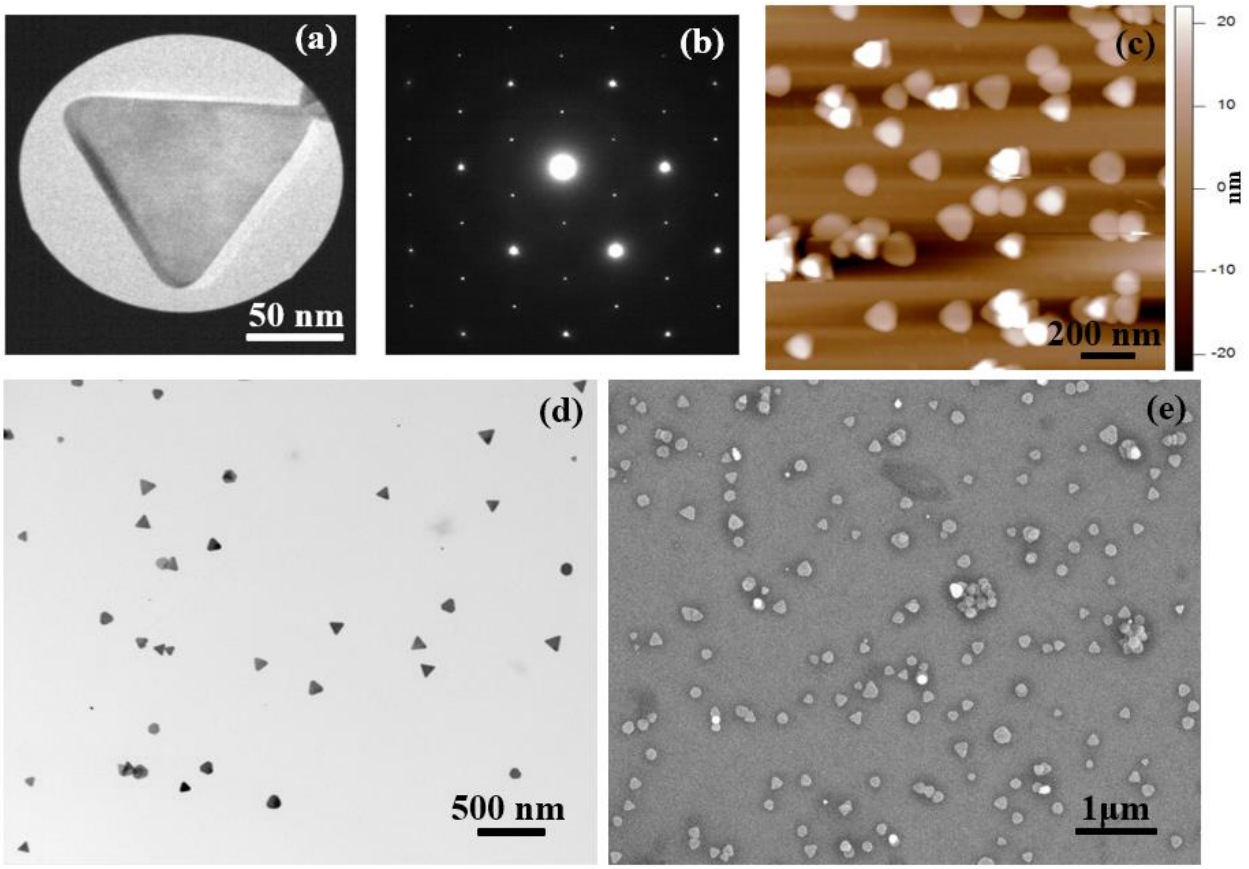


**Figure 8.1** (a) HRTEM image and (b) SAED pattern of individual Ag nanoprism (c) AFM and (d) TEM image of Ag NTs prepared through seed mediated method using 30 µl SLigS-Ag seed. (e) SEM image of Ag NPLs prepared through $H_2O_2$ induced one-pot synthesis in the presence of 0.1 mM $AgNO_3$, 4.9 mM $H_2O_2$, 0.5 mg/ml SLigS and 1.1 mM $NaBH_4$.

distribution of Ag NPs under similar experimental conditions (***Figure S2***). It is plausible to surmise SLigS might play a significant role in the controlled synthesis of anisotropic 2D Ag nanoplates. In view of the fact that the growth mechanism for these two synthetic approaches differs substantially from one another, further elaboration on the role of SLigS will be divided into two sections.

### 8.4.2 Influential factors associated with seeded growth approach toward Ag NTs

### 8.4.2.1 Effect of concentration of SLigS

Great advancement has been recently made to extend seeded growth strategy toward silver nanoprisms in a reproducible manner.[26,44,45] The presence of seed nanocrystals with planar-twinning allows for the preferential epitaxial deposition of metal atoms thereby realizing the precise size and shape control.[46,47] Our group has demonstrated that PVP, SPSS could be replaced by biomacromolecules such as peat protein without impairing the yield and quality of the Ag nanoprisms during the seeded-growth.[43] In quest of a generic synthetic approach and expanded library of shape directing agent, sustainable lignin derivatives were exploited to regulate the Ag seed formation. Interestingly, only a tiny amount of SLigS (2.3 μg/ml) additive could exert significant impact on the quality of Ag seeds as well as the final Ag NPs, as compared with the original synthetic protocol.[26] As listed in the ***Table 8.1***, the LSPR band of Ag seeds keeps invariable regardless of the concentration of SLigS. By taking a close inspection of the LSPR profile (***Figure S3***), it is revealed that both the intensity and the full width at the half maximum (FWHM) of the Ag seeds are similar for the first four entries of ***Table 8.1***. And the as-prepared Ag NTs featured sharp NIR peaks around 800 nm and well-defined triangular contours (***Table 8.1***, ***Figure 8.2 and S3b***). Since a negligible amount of citrate or SLigS are present during the second step, the face-selective growth of Ag NTs is primarily driven by the innate planar twinning defects of Ag seeds rather than the adsorbate-induced the suppression of (111). When excess amount of the SLigS was added (69.1 μg/ml), the LSPR intensity is accentuated (***Table 8.1***) indicating that less Ag seeds were produced due to the incomplete reduction. Notably, an apparent trend of $\lambda_{NP}$ blue shift was observed implying that the overdose SLigS (>50 μg/ml) is not favourable for the growth of Ag NTs.

**Table 8.1** LSPR wavelength and intensity of Ag seeds prepared in the presnece of various amounts of SLigS (column 2, 3) and Ag NTs prepared using 10 µl corresponding Ag seed (column 4, 5).

| [SLigS] (µg/ml) | $\lambda_{seed}$ (nm) | Intensity | $\lambda_{NP}$ (nm) | Intensity |
|---|---|---|---|---|
| 2.3 | 400 | 2.23 | 839 | 2.37 |
| 7.7 | 401 | 2.44 | 826 | 2.52 |
| 23.0 | 400 | 2.34 | 776 | 2.75 |
| 46.1 | 401 | 2.26 | 762 | 2.61 |
| 69.1 | 401 | 1.87 | 707 | 2.58 |
| 92.2 | 401 | 1.76 | 682 | 2.34 |

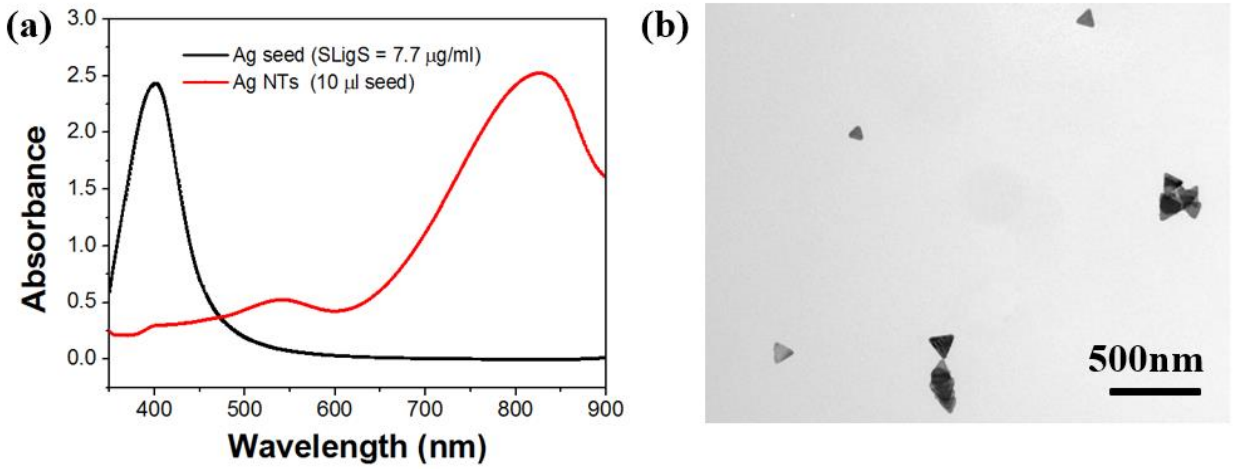


**Figure 8.2** (a) UV-Vis spectra of Ag seed prepared in the presence of 7.7 µg/ml SLigS and Ag NTs prepared using 10 µl Ag seeds; (b) TEM images of Ag NTs corresponding to **Figure 8.2a.**

### 8.4.2.2 Morphology evolution and growth mechanism

The morphological evolution of Ag NTs was monitored by UV-Vis and TEM during the course of the reaction. A set of experiments was performed under the condition of fixed volume of SLigS-Ag seeds and various amounts of $Ag^+$ precursors. The obtained NPs were subsequently capped by 2 mM citrate to prevent further morphological change. As we ratcheted up [$Ag^+$], a mounting intensity and gradual red shift of LSPR band were identified (***Figure 8.3a***). This dramatic color change (bright yellow → purple) is consonant with morphological evolution from

spherical Ag seeds to nanodisks and eventually shape into triangular nanoprisms. Initially, the size of Ag seed is enlarged due to the lateral growth of the NPs on the high surface energy

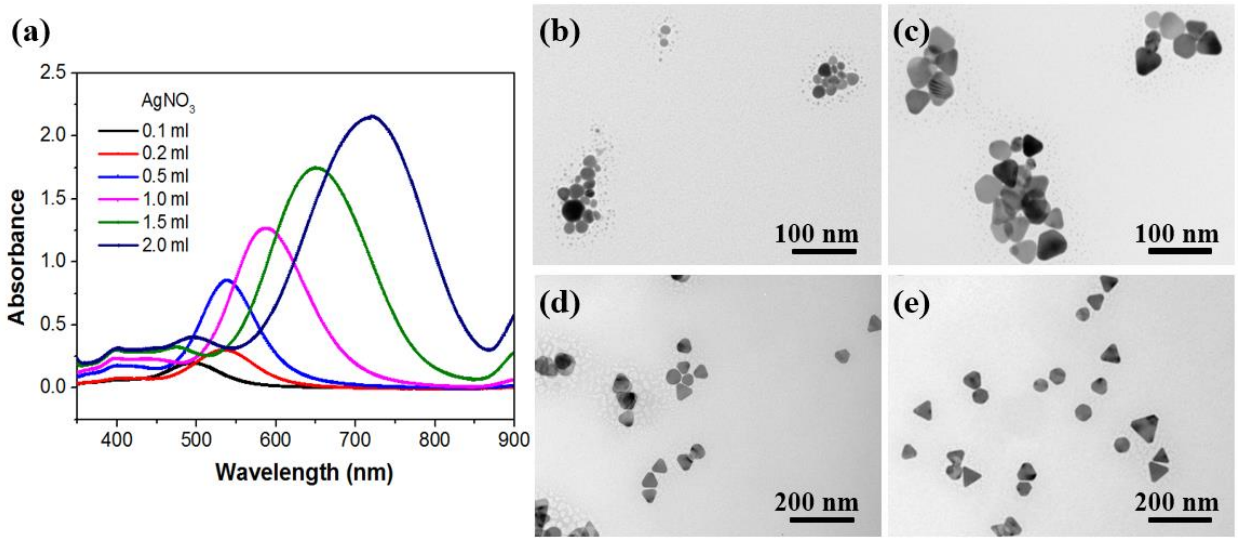


**Figure 8.3** (a) UV-Vis spectra of Ag NPs corresponding to different injection volume of 0.5mM $AgNO_3$. (b) TEM images of Ag NPs corresponding to the samples in **Figure 8.3a**-red (c) **Figure 8.3a**-light blue (d) **Figure 8.3a**-green (e) **Figure 8.3a**-dark blue.

facets, (110) and (100). (***Figure 8.3b***). Consecutive epitaxial growth into small nanoplates was confirmed by continuous injection of Ag precursors. (***Figure 8.3c-e***) No further shape transformation takes place once the intact triangular contour is formed (***Figure 8.1c***). Additionally, we observe a large number of tiny Ag nanoclusters at the beginning stage (***Figure 8.3b-d***), which vanished in the later stage (***Figure 8.3e***). Identical experimental observations have been obtained in the case of protein-aided seeded growth.[43] Therefore, the epitaxial deposition of Ag atom in concert with Ostwald ripening can be used to account for the growth mechanism[48]

**8.4.2.3 Effect of SLigS-Ag seed.**

The morphology of Ag NPs is strongly dictated by the total number of seeds added during the growth step. When 10 µl SLigS-stabilized Ag seed was applied, the majority of

products fall into the category of triangular shape and the mean edge length L was measured to be 110 ± 23 nm (***Figure 8.4b***). As the volume of Ag seed increases (30 µl → 50 µl), the resultant Ag NPs undergoes a progressive shape transition from smaller NTs to the mixture of small round disks and NTs (***Figure 8.4c-d***). Since the LSPR band is determined by the aspect ratio as well as the sharpness of the vertexes,[49] it could be conveniently tuned to span a broad spectral range from visible to NIR region (550-820 nm) (***Figure 8.4a***).[26]

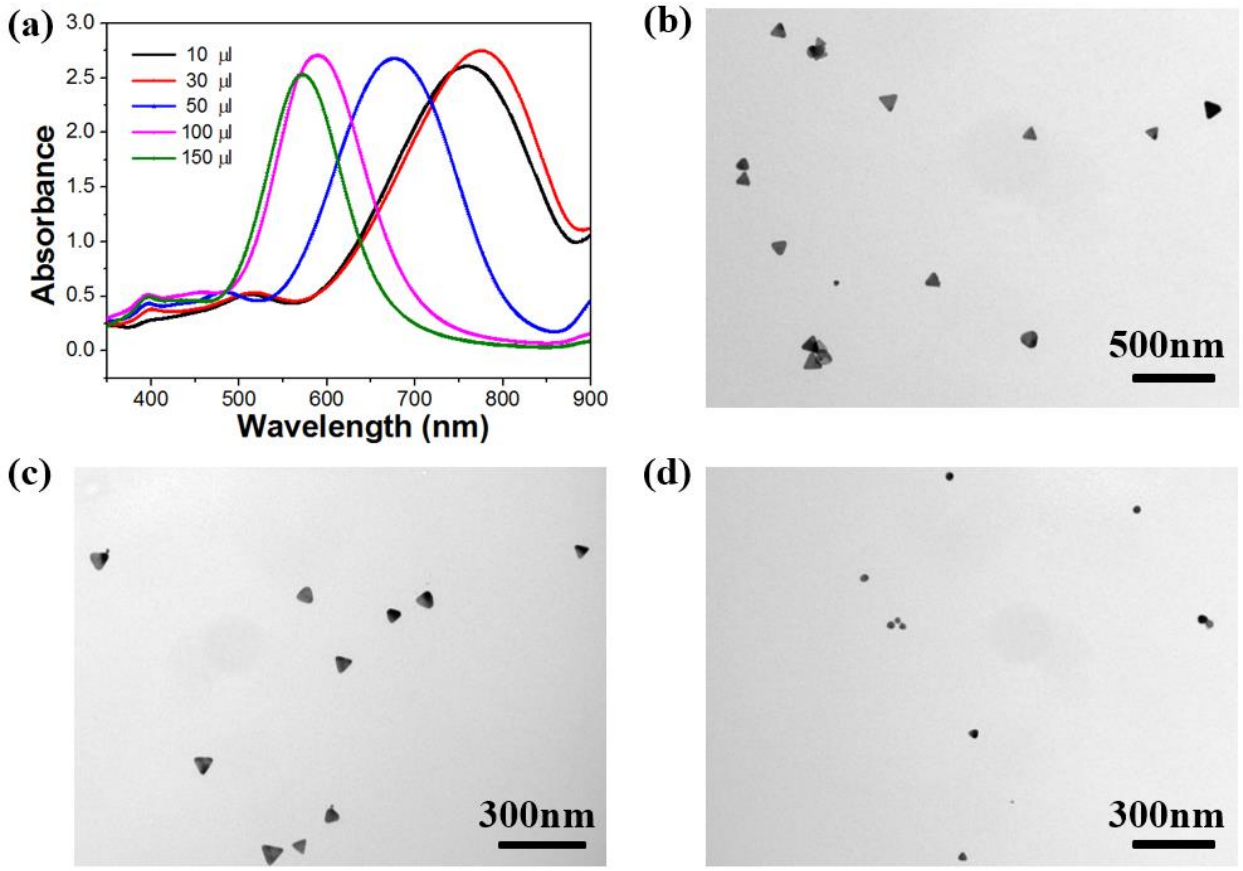


**Figure 8.4** (a) UV-Vis spectra of the collodial Ag NTs obtained using different volume of Ag seed_3 in **Figure S3(a).** TEM images of selected samples prepared using (b) 10 µl (c) 30 µl and (d) 50 µl Ag seed_3.

### 8.4.3 Mechanistic investigation on the one-pot synthesis of Ag NPLs

$H_2O_2$ has a standard redox potential of 1.763 V and 0.867 V in acidic and alkaline solution, respectively, therefore has been widely utilized as a powerful oxidant. [30] In 2005,

Mirkin's group proposed the new paradigm for Ag nanoprisms synthesis, in which an aqueous growth solution containing a mixture of $AgNO_3/H_2O_2$/citrate/PVP were prepared, followed by the addition of $NaBH_4$ to launch the formation of Ag NTs.[29] Follow up research has unravelled that $H_2O_2$ and citrate are the key reagents in favour of Ag nanoprisms formation, whereas PVP were found to serve as extra stabilizers to impart the colloidal and morphological stability.[31]

**8.4.3.1 Effect of concentration of SLigS.**

Yin and colleagues recently identified a set of di- and tri-carboxylate compounds that is able to direct the lateral growth of Ag nanoprisms.[30] Inspired by their findings, we are interested to explore a broad spectrum of renewable compounds as well as more generic green chemical approaches to this end. As we know the controlled synthesis of anisotropic Ag NPs requires the fine adjustment of the ratio of metal precursors to stabilizer. Thus various amounts of SLigS was introduced into the reaction system while keeping the concentration of the other reagents constant. Unlike in the case of the seeded growth pathway, moderate concentration of SLigS (0.5 mg/ml) is indispensable to reach high yield (***Table 8.2***, ***Figure 8.5c-d***). The observed trend can be explained by taking into account of dual roles of SLigS. On the one hand, the complexation between SLigS and $AgNO_3$ slow down the reduction kinetics to avert the undesirable homogeneous nucleation. On the other hand, SLigS also acted as a ligand to govern the face-selective growth. Insufficient amount of SLigS (0.1 - 0.2 mg/ml) can not effectively halt the rapid reduction, evidenced by the small Ag NPs with random shapes are produced (***Table 8.2, Figure 8.5b***). Moderate amount of [SLigS] allows for the fine adjustment of reduction kinetics so that $H_2O_2$ could wield its oxidizing power onto the newly formed nanocrystal. As a consequence, facets with high surface energy faded away while the stable (111) facet survived during the process. This will in turn direct the preferential atom by atom deposition of elemental

Ag onto the edge of the Ag nanocrystal seed (***Table 8.2, Figure 8.5c-d***). Nevertheless, overabundance of SLigS will dramatically reduce the available Ag atom feedstock and etchant $H_2O_2$ is no longer accessible to the passivated Ag surface due to the dense surface functionalization. As shown in the ***Table 8.2***, a flattened line with a small hump at 850 nm was observed, which can be assigned to the LSPR of a mixture of large Ag NPLs coupled with tiny Ag nanoclusters.

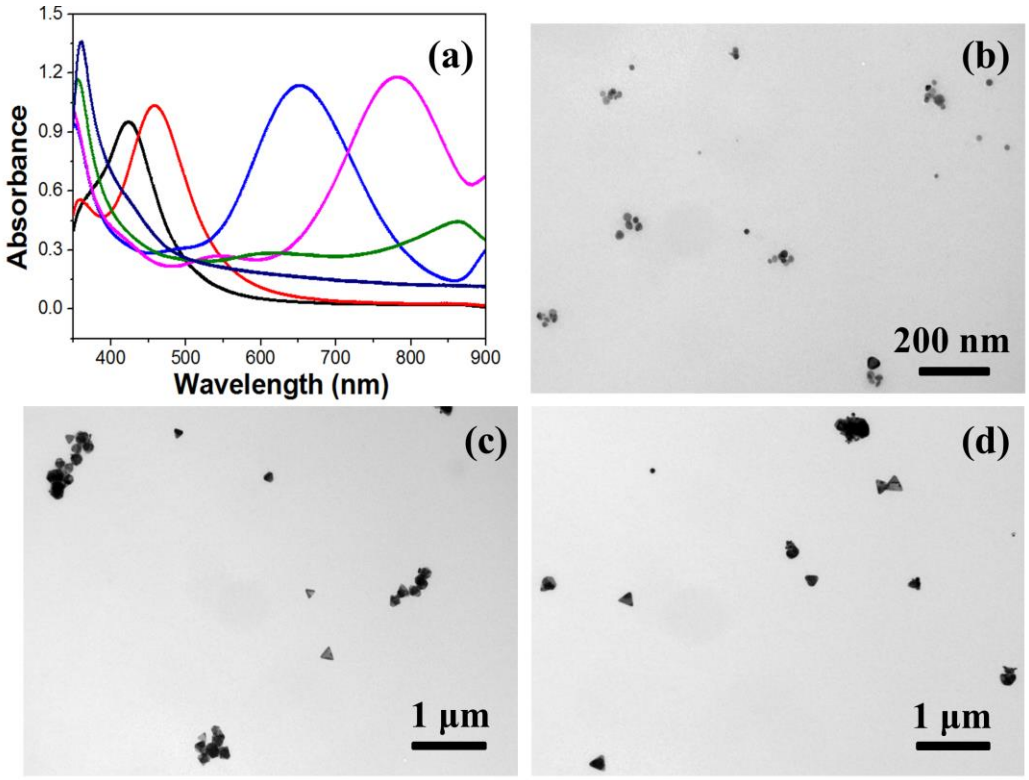


**Figure 8.5** (a) UV-Vis spectra of Ag NPs prepared using varied concentration of SLigS: 0.1 mg/ml (black), 0.2 mg/ml (red), 0.35 mg/ml (light blue), 0.5 mg/ml (magenta), 0.75 mg/ml (dark blue) and 1 mg/ml (green), respectively. TEM images of Ag NPs corresponding to samples containing (b) 0.2 mg/ml (c) 0.5 mg/ml (d) 0.75 mg/ml SLigS.

A time course UV-Vis study was carried out to probe the growth mechanism of Ag NPLs. An induction period of 12 min was revealed in ***Figure S4*** without the appearance of conspicuous LSPR peak in the NIR region. After a close inspection on the extinction profile, a small hump in the 450 nm - 550 nm region gradually grew, signifying the formation of tiny amount of Ag

nanospheres and miscellaneous shaped Ag NPs (***Figure S4 inset***). Then it was followed by a sharp transition during the period of 13-14 min, intense LSPR peak emerged instantly and remained unchanged afterwards. Hence, the role of SLigS during the shape evolution can be elaborated as follows: (i) At the initial stage, the coordination of SLigS with $Ag^+$ hinder the rapid production of isotropic Ag NPs. (ii) During the induction period, Ag NPs enclosed by (111) facets are produced after a concert etching and reducing process with the aid of SLigS/$H_2O_2$/$NaBH_4$. It resembles the conventionally studied PVP/Citrate/$H_2O_2$/$NaBH_4$ quaternary system,[31] in which the SLigS substitute citrate and PVP and play a dual role as a stabilizer and surface capping agent. (iii) SLigS might also serve as efficient capping agent to passivate (111) facets thereby facilitating the overgrowth of Ag NPLS. Eventually, SLigS-stabilized Ag NPLs with high endurance toward $H_2O_2$ etching exclusively survive and all the rest of Ag stock were depleted.

**Table 8.2** LSPR wavelength and intensity of Ag NTs prepared in the presnece of various amounts of SLigS.

| [SLigS] (mg/ml) | $\lambda_{NP}$ (nm) | Intensity |
|---|---|---|
| 0.1 | 422 | 0.95 |
| 0.2 | 458 | 1.04 |
| 0.35 | 652 | 1.37 |
| 0.5 | 781 | 1.18 |
| 0.75 | 860 | 0.45 |
| 1 | N/A | N/A |

### 8.4.3.2 Effect of concentration of $H_2O_2$ and $NaBH_4$

The concentration of $H_2O_2$ is of considerable significance to the morphological and optical properties of resulting Ag NPs. Intermediate concentrations of $H_2O_2$ (3.7 mM – 8.6 mM) facilitate the Ag NPLs growth by scavenging diverse shaped Ag NPs other than Ag NPLs (***Table 8.3, Figure S5***). Yet excessive $H_2O_2$ caused detrimental issues by consuming the well-defined

Ag NPLs. For instance, the freshly made sample in the presence of 12.3 mM $H_2O_2$ exhibited a peak located at around 730 nm, which experienced a massive peak shift to 586 nm in less than one minute (***Table 8.3***). As shown in ***Figure S5d,*** smaller Ag NPLs are surrounded by a large number of small Ag nanoclusters (NCs). The continuous etching process in line with the concomitant redeposition of Ag(I) and Ag NCs lead to emergence of irregular Ag NPLs with broad size distribution ***Figure S5f***. Although moderate up-drift of the aspect ratio was reported as the [$NaBH_4$] increased,[29,30,38] our experimental results suggested that $NaBH_4$ exerted minor effects on the LSPR of Ag NPLs once the concentration is controlled within the range of 1 mM - 2.5 mM. $AgNO_3$ can not be fully reduced under the condition of low [$NaBH_4$] (<0.6 mM). When [$NaBH_4$] is above 5 mM, there is a strong propensity toward homogenous nucleation of nanospheres, shown as the broad hump in the NIR region and large shoulder (400 nm - 500 nm) (***Figure S6***).

**Table 8.3** LSPR wavelength and intensity of Ag NTs prepared in the presnece of varopis amounts of [$H_2O_2$].

| [$H_2O_2$] (mM) | $\lambda_{NP}$ (nm) | Intensity |
|---|---|---|
| 2.5 | N/A | N/A |
| 3.7 | 788 | 0.99 |
| 4.9 | 781 | 1.18 |
| 8.6 | 652 | 1.14 |
| 12.3 | 586 | 1.07 |
| 24.6 | 546 | 1.05 |

### 8.4.3.3 Effect of different types of Lignin derivatives

Further synthesis attempts have been made to replace SLigS with crude lignin, ligno propionate, and ligno 2-hydroxyl ether (magenta). Despite the low solubility, a trace amount of soluble lignin derivatives is adequate to assist the formation of high-quality Ag seeds, followed by the seeded-growth of well-defined Ag NTs (***Figure S7a-b***). As aforementioned, a modest

amount of SLigS is required for kinetic control, selective etching and stabilization of (111) facet during the one-pot synthesis. All three compounds fail to govern the growth of Ag NPLs due to the limited solubility at neutral pH (***Figure S7c, e***). Our results demonstrated that the strong binding affinity to metal NPs is not the sole criterion for the eligible biopolymer stabilizer/shape directing agent. We postulate that appropriate physicochemical properties including the number of polar functional groups, surface charge and water solubility are crucial to the controlled synthesis of Ag nanoprisms. Therefore, a broad library of biomaterials including proteins, lignin and cellulose derivatives can be harnessed for the bioenabled synthesis of Ag nanoprisms and other anisotropic noble metal NPs.

**8.4.4 Morphological and colloidal stability**

It is well recognized that the unprotected Ag NTs are subject to oxidation under ambient condition. The degradation results in a conspicuous morphological transformation from triangular to round disk which is concomitant with a blue shift of LSPR band.[50,51] Enhanced morphological and colloidal stability can be realized by post-addition of extra amount of capping agents. As shown in the ***Figure 8.6a and c***, only a marginal peak shift and decline in intensity was observed for citrate protected-Ag NTs after storage for one month. For Ag NTs prepared using aged Ag seeds, their LSPR band seems to shift slightly toward lower wavelength (776 → 730 nm), while the intensity remained almost unchanged as compared with their counterparts using fresh Ag seeds. To our surprise, the intensity increase by 25 % in the case of Ag NPLs after storage for one month, implying that the presence of SLigS not only stabilize the Ag NPLs but also facilitate the complete conversion of Ag species during the process (***Figure 8.6b, e)***.

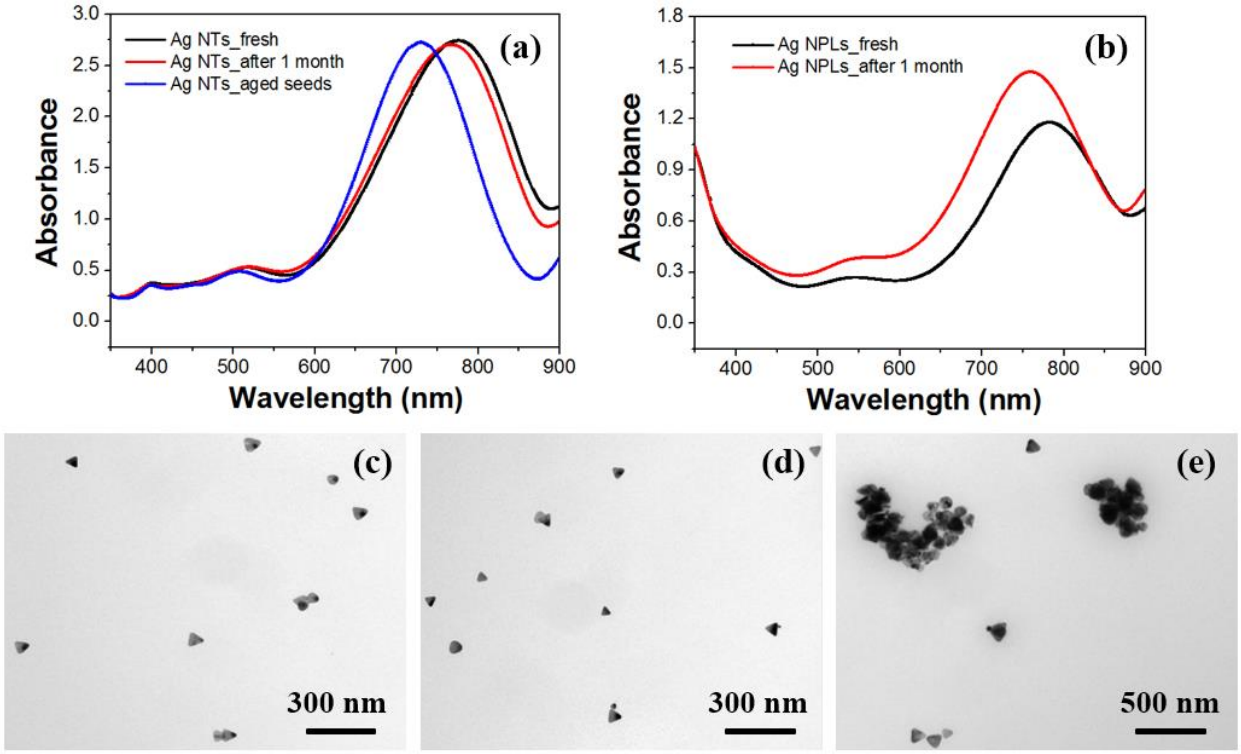


**Figure 8.6** (a) UV-Vis spectra of Ag NTs prepared using 30 µl Ag seed freshly made (black), stored at r.t in the dark for one month (red) and Ag NTs prepared using 30 µl Ag seed stored for one month (blue). (b) UV-Vis spectra of Ag NPLs prepared using one pot method (black), stored at r.t in the dark for one month (red). (c) TEM images of Ag NTs corresponding to **Figure 8.6(a)**_red (d) Ag NTs corresponding to **Figure 8.6(a)**_blue (e) Ag NPLs corresponding to **Figure 8.6(b)**_red.

Overall, the SLigS/Citrate protected Ag seeds and Ag NTs and Ag NPLs exhibit excellent colloidal stability and structural integrity after long-term storage. Additionally, the homogenous SLigS-Ag NTs solutions could be drop-casted onto either glass slide or aluminum foil substrate to form relatively uniform thin film without the occurrence of severe phase separation (***Figure S8b, e)***. This hybrid material may potentially be tapped for antibacterial coating, detection and removal of hazardous dyes and heavy metal ions. [52,53]

### 8.4.5 Molecular interactions between SLigS and Ag(0)/Ag(I) species

Lignosulfonate exhibits intrinsic fluorescence due to the conjugation of carbonyl, biphenyl, and stilbene groups.[54] The SLigS solution was thus titrated by $AgNO_3$ and Ag

nanospheres to further illustrate the molecular interaction between biopolymer and inorganic species. Once the Ag(I)/Ag(0) was added, the fluorescence signal of SLigS solution experienced a gradual drop. This drop could be attributed to the binding between Ag species and functional groups or the disruption of the conjugated structures by the neighboring Ag ions, both of which produce a change in the chemical environment of the SLigS. To analyze the quenching of the fluorescence signal the data was fit using the Stern-Volmer equation.

$$(\frac{F_0}{F}) = 1 + K_{SV}[Q] \quad (1)$$

**Table 8.4** Binding constant derived from Hill equation

| | $AgNO_3$ | Ag nanospheres |
|---|---|---|
| $K_a$ ($M^{-1}$) | 241 | 4.04 x $10^6$ |
| n | 0.84 | 2.03 |

Where $F_0$ and F are the fluorescence intensities in the absence and presence of the quencher, $K_{sv}$ is the Stern-Volmer quenching constant, and [Q] is the concentration of the Ag species. As shown in ***Figure S9***, the shape of the Stern-Volmer plot is linear for the titration with Ag(I) and exhibits upward curvature with Ag(0). The upward curvature suggests that the decrease in the fluorescence signal is not solely due to random collisional interactions or specific binding events at the multiple accessible sites on SLigS, but a combination, and therefore the Stern-Volmer relationship is not valid. To further evaluate the equilibrium binding constant and degree of cooperativity of the complex formation we can use the Hill equation:

$$\log(\frac{F_0 - F}{F}) = \log K_a + n \log[Q] \quad (1)$$

where $F_0$ and F are the same as in Equation 1, $K_a$ is the binding constant, and the Hill coefficient, n, indicates the degree of cooperativity in binding. From ***Figure 8.7a*** the $K_a$ for Ag(0) is much larger than Ag(I) indicating a stronger binding interaction between the SLigS and the Ag NPs. A

value of n > 1 for the interaction with Ag NPs, indicates positive cooperativity, whereas n <1 in the case of quenching by Ag ions implies the complexation between Ag(I)-SLigS may prevent further binding events due to the steric-hindrance or electrostatic repulsion.[55]

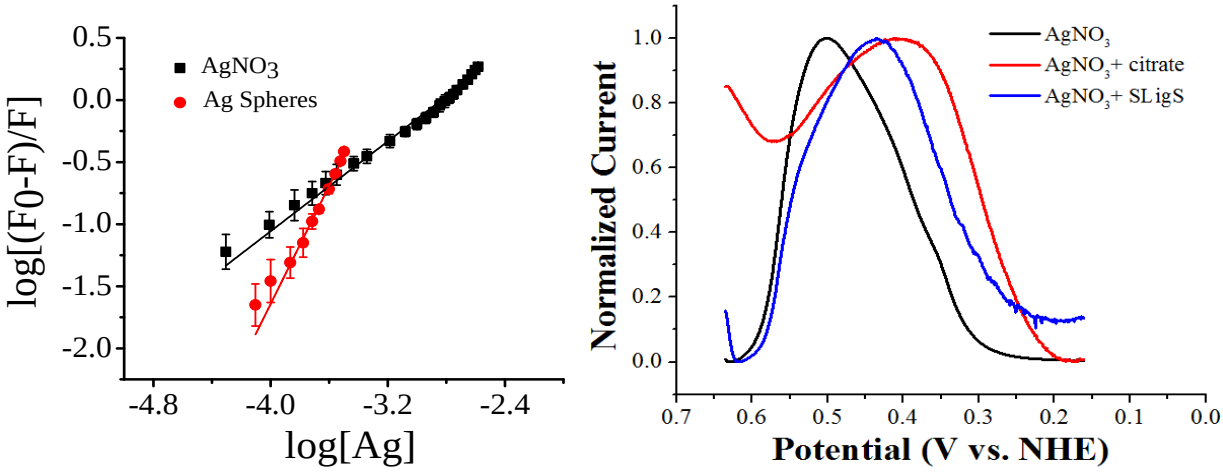


**Figure 8.7** (a) Double logarithmic plot of fluorescence data from adsorption of Ag(0) or Ag(I) to SLigS. (Ag stands for the concentration of Ag element) (b) Square wave voltammetry profiles of aqueous solutions containing (i) 5 mM $AgNO_3$(black), (ii) 5 mM $AgNO_3$ and citrate 1 mg/ml (red) (iii) 5 mM AgNO3 and SLigS 1 mg/ml (blue).

By taking advantage of the complexation between phenolic/ether moieties with Ag ions, the reduction kinetics of Ag(I) could be readily tuned by adding SLigS. As shown in the ***Figure 8.7b***, the $E_{1/2}$ for the $Ag^{+/0}$ redox process was found to be 502 mV vs. NHE initially. In the presence of either SLigS or citrate, the reduction of $Ag^+$ became more difficult, as indicated by the potential shift to more negative value of 0.435 mV and 0.412 mV, respectively. Note that SLigS bears fewer hydroxyl groups than citrate when the total mass is fixed, and the sulfonate group is a weaker ligand compared with the carboxylate groups of citrate in terms of binding to $Ag^+$. Accordingly, the order of $E_{1/2}$ is observed as follows: citrate < SLigS < no ligands. Additionally, slow reduction kinetics were consistent with the longer induction time during the course of the one-pot synthesis. Computational along with Mass spectrometry studies have previously demonstrated the relatively strong complexation between citrate with Ag ions and the

(111) facet of Ag NPs.[28,56] Similarly, coordination of SLigS and Ag(0)/Ag(I) will exert significant impact on the facet-selective growth of 2D Ag nanostructures.

### 8.4.6 Colorimetric sensing of oxidative metal cations

Owing to the high extinction coefficient in the visible-light region, functionalized Ag NPs have been widely used as colorimetric sensing of metal ions based on the aggregation induced LSPR change.[57-59] Even though this method offers excellent sensitivity and selectivity, it still suffers several disadvantages such as the poor reproducibility and undesirable interference. For instance, the drastic LSPR shift is also correlated to the other influential factors such as the processing of NPs, the pH and the ionic strength of the sample solution. Additionally, the spectra of aggregated NPs features an ill-defined broad hump restraining their potential applications for visual assays. Anisotropic Ag NTs possess sharp vertices and intense NIR absorbance located at approximately 800 nm, and the in-plane dipole LSPR peak of Ag NTs is apt to undergo a dramatic blue shift as the corner tips are rounded.[16] As depicted in the ***Figure 8.8a***, injection of oxidative metal cations, $Fe^{3+}$, caused a significant LSPR shift which is ascribed to the preferential etching of the highly reactive sharp tips. A further increase of the [$Fe^{3+}$] (10 - 11 ppm) etched the less stable edges rather than the top (111) facets, thereby changing the aspect ratio. The plate-like structure was severely damaged when a large number of surface Ag atoms are dissolved in the presence of 14 ppm $Fe^{3+}$. Although no linear relation between LSPR wavelength and [Ag NTs] has been revealed, a calibration curve could be plotted for the quantitatively detection of $Fe^{3+}$ in the range of 0-13 ppm (***Figure S10***). To test the colorimetric selectivity of Ag NTs toward $Fe^{3+}$, a series of metal cations (20 ppm) were likewise examined. No significant peak shift was observed except for $Al^{3+}$, which probably induced an unexpected

agglomeration, (***Figure 8.8b***). Thus, the colorimetric response mainly arises from the degradation of Ag NTs, which is also validated by adding $Cr^{3+}$.

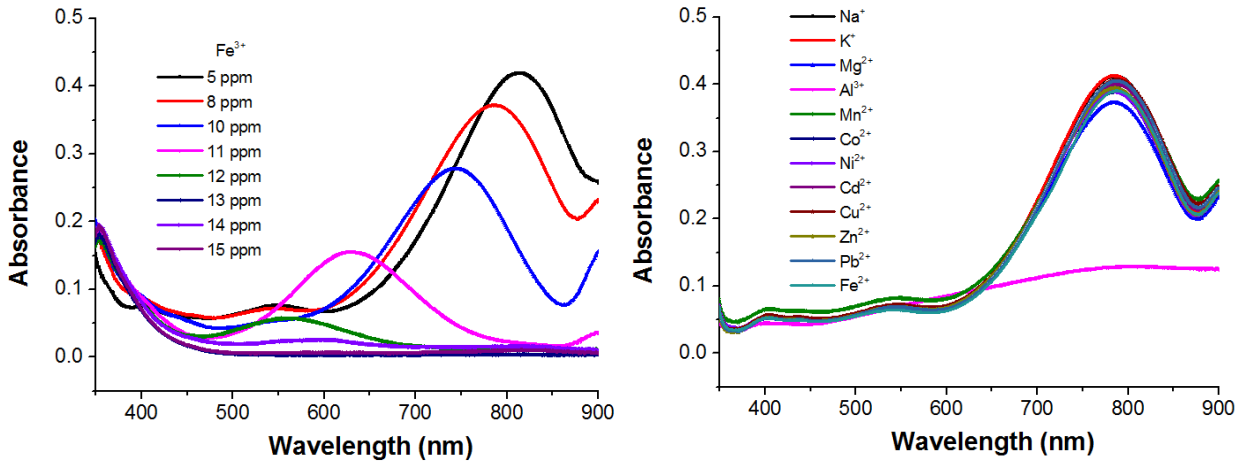


**Figure 8.8** UV-Vis spectra of Ag NTs solution after addition of (a) varied concentration of $Fe^{3+}$ (b) different kinds of metal cations.

## 8.5. Conclusions

A new bioenabled synthetic paradigm is provided to synthesize well-defined Ag nanoprisms in either a one-pot or seeded growth manner. Sodium LignoSulfonate as well as a series of lignin derivatives were tested as potential stabilizers and shape directing agents. A variety of influential factors including the SLigS, Ag seeds, $H_2O_2$ and $NaBH_4$ were systematically investigated through integrated spectral and morphological characterization. The molecular interactions between SLigS and Ag(0)/Ag(I) were confirmed to dictate the reduction kinetics, the quality of Ag seed, as well as surface passivation of (111) facet. The as-prepared Ag nanoprisms exhibited excellent colloidal stability and sensitive colorimetric response to the strong oxidative metal cations such as $Fe^{3+}$ and $Cr^{3+}$.

## 8.6 Acknowledgements

The authors would like to acknowledge Dr. Chao Wang and Dr. Richard A. Venditti for providing the lignin derivatives and we are thankful to ICTAS Nanoscale Characterization and

Fabrication Lab (NCFL) for the use of AFM, TEM, and SEM. This work was in part supported by the JFC ICTAS grant number 119106 to TZG.

## 8.7 References

(1) Pastoriza-Santos, I.; Liz-Marzan, L. M. *J. Mater. Chem.* **2008**, *18*, 1724.
(2) Zhang, Q.; Tan, Y. N.; Xie, J.; Lee, J. Y. *Plasmonics* **2008**, *4*, 9.
(3) Lohse, S. E.; Burrows, N. D.; Scarabelli, L.; Liz-Marzán, L. M.; Murphy, C. J. *Chem. Mater.* **2014**, *26*, 34.
(4) Dreaden, E. C.; Alkilany, A. M.; Huang, X.; Murphy, C. J.; El-Sayed, M. A. *Chem. Soc. Rev.* **2012**, *41*, 2740.
(5) Tokel, O.; Inci, F.; Demirci, U. *Chem. Rev.* **2014**, *114*, 5728.
(6) Sun, Y.; Mayers, B.; Herricks, T.; Xia, Y. *Nano Lett.* **2003**, *3*, 955.
(7) Qian, Z.; Park, S.-J. *Chem. Mater.* **2014**, *26*, 6172.
(8) Gole, A.; Murphy, C. J. *Chem. Mater.* **2004**, *16*, 3633.
(9) Jin, R.; Cao, Y.; Mirkin, C. A.; Kelly, K. L.; Schatz, G. C.; Zheng, J. G. *Science* **2001**, *294*, 1901.
(10) Scarabelli, L.; Coronado-Puchau, M.; Giner-Casares, J. J.; Langer, J.; Liz-Marzán, L. M. *ACS Nano* **2014**, *8*, 5833.
(11) Xie, J.; Lee, J. Y.; Wang, D. I. C. *Chem. Mater.* **2007**, *19*, 2823.
(12) Kuo, C.-H.; Huang, M. H. *Langmuir* **2005**, *21*, 2012.
(13) Saverot, S.; Geng, X.; Leng, W.; Vikesland, P. J.; Grove, T. Z.; Bickford, L. R. *RSC Adv.* **2016**, *6*, 29669.
(14) Millstone, J. E.; Park, S.; Shuford, K. L.; Qin, L.; Schatz, G. C.; Mirkin, C. A. *J. Am. Chem. Soc.* **2005**, *127*, 5312.
(15) Xia, Y.; Ye, J.; Tan, K.; Wang, J.; Yang, G. *Anal. Chem.* **2013**, *85*, 6241.
(16) Chen, L.; Fu, X.; Lu, W.; Chen, L. *ACS Appl. Mater. Interfaces* **2013**, *5*, 284.
(17) Yang, X.; Yu, Y.; Gao, Z. *ACS Nano* **2014**, *8*, 4902.
(18) Xue, B.; Wang, D.; Zuo, J.; Kong, X.; Zhang, Y.; Liu, X.; Tu, L.; Chang, Y.; Li, C.; Wu, F.; Zeng, Q.; Zhao, H.; Zhao, H.; Zhang, H. *Nanoscale* **2015**, *7*, 8048.
(19) Jin, R.; Charles Cao, Y.; Hao, E.; Metraux, G. S.; Schatz, G. C.; Mirkin, C. A. *Nature* **2003**, *425*, 487.
(20) Xue, C.; Mirkin, C. A. *Angew. Chem. Int. Ed.* **2007**, *46*, 2036.
(21) Xiong, Y.; Siekkinen, A. R.; Wang, J.; Yin, Y.; Kim, M. J.; Xia, Y. *J. Mater. Chem.* **2007**, *17*, 2600.
(22) Xiong, Y.; Washio, I.; Chen, J.; Cai, H.; Li, Z.-Y.; Xia, Y. *Langmuir* **2006**, *22*, 8563.
(23) Pastoriza-Santos, I.; Liz-Marzán, L. M. *Nano Lett.* **2002**, *2*, 903.
(24) Kim, M. H.; Yoon, D. K.; Im, S. H. *RSC Adv.* **2015**, *5*, 14266.
(25) Jana, N. R.; Gearheart, L.; Murphy, C. J. *Langmuir* **2001**, *17*, 6782.
(26) Aherne, D.; Ledwith, D. M.; Gara, M.; Kelly, J. M. *Adv. Funct. Mater.* **2008**, *18*, 2005.
(27) Zhang, Q.; Hu, Y.; Guo, S.; Goebl, J.; Yin, Y. *Nano Lett.* **2010**, *10*, 5037.
(28) Zeng, J.; Xia, X.; Rycenga, M.; Henneghan, P.; Li, Q.; Xia, Y. *Angew. Chem. Int. Ed.* **2011**, *50*, 244.
(29) Metraux, G. S. M., Chad A. *Adv. Mater.* **2005**, *27*, 2685.
(30) Zhang, Q.; Li, N.; Goebl, J.; Lu, Z.; Yin, Y. *J. Am. Chem. Soc.* **2011**, *133*, 18931.

(31) Tsuji, M.; Gomi, S.; Maeda, Y.; Matsunaga, M.; Hikino, S.; Uto, K.; Tsuji, T.; Kawazumi, H. *Langmuir* **2012**, *28*, 8845.
(32) Yu, L.; Banerjee, I. A.; Matsui, H. *J. Am. Chem. Soc.* **2003**, *125*, 14837.
(33) Xie, J.; Lee, J. Y.; Wang, D. I. C.; Ting, Y. P. *Small* **2007**, *3*, 672.
(34) Naik, R. R.; Stringer, S. J.; Agarwal, G.; Jones, S. E.; Stone, M. O. *Nat. Mater.* **2002**, *1*, 169.
(35) Shankar, S. S.; Rai, A.; Ankamwar, B.; Singh, A.; Ahmad, A.; Sastry, M. *Nat. Mater.* **2004**, *3*, 482.
(36) Liu, B.; Xie, J.; Lee, J. Y.; Ting, Y. P.; Chen, J. P. *J. Phys. Chem. B* **2005**, *109*, 15256.
(37) Shao, Y.; Jin, Y.; Dong, S. *Chem. Commun.* **2004**, 1104.
(38) Jiang, F.; Hsieh, Y.-L. *Biomacromolecules* **2014**, *15*, 3608.
(39) Singh, V.; Khullar, P.; Dave, P. N.; Kaur, G.; Bakshi, M. S. *ACS Sustain. Chem. Eng.* **2013**, *1*, 1417.
(40) Byeon, J. H.; Kim, Y.-W. *ACS Macro Lett.* **2014**, *3*, 205.
(41) Ferraria, A. M.; Boufi, S.; Battaglini, N.; Botelho do Rego, A. M.; ReiVilar, M. *Langmuir* **2010**, *26*, 1996.
(42) Nabeela, K.; Thomas, R. T.; Nair, J. B.; Maiti, K. K.; Warrier, K. G. K.; Pillai, S. *ACS Appl. Mater. Interfaces* **2016**, *8*, 29242.
(43) Geng, X.; Leng, W.; Carter, N. A.; Vikesland, P. J.; Grove, T. Z. *J. Chem. Mater. B* **2016**, *4*, 4182.
(44) Li, N.; Zhang, Q.; Quinlivan, S.; Goebl, J.; Gan, Y.; Yin, Y. *ChemPhysChem* **2012**, *13*, 2526.
(45) Liu, X.; Li, L.; Yang, Y.; Yin, Y.; Gao, C. *Nanoscale* **2014**, *6*, 4513.
(46) Niu, W.; Zhang, L.; Xu, G. *Nanoscale* **2013**, *5*, 3172.
(47) Xia, Y.; Xia, X.; Peng, H.-C. *J. Am. Chem. Soc.* **2015**, *137*, 7947.
(48) Radha, B.; Kulkarni, G. U. *Cryst. Growth Des.* **2011**, *11*, 320.
(49) Millstone, J. E.; Hurst, S. J.; Métraux, G. S.; Cutler, J. I.; Mirkin, C. A. *Small* **2009**, *5*, 646.
(50) Gao , C.; Lu , Z.; Liu , Y.; Zhang, Q.; Chi, M.; Cheng, Q.; Yin, Y. *Angew. Chem. Int. Ed.* **2012**, *51*, 5629.
(51) Martinsson, E.; Shahjamali, M. M.; Enander, K.; Boey, F.; Xue, C.; Aili, D.; Liedberg, B. *J. Phys. Chem. C* **2013**, *117*, 23148.
(52) Lü, Q.-F.; Luo, J.-J.; Lin, T.-T.; Zhang, Y.-Z. *ACS Sustain. Chem. Eng.* **2014**, *2*, 465.
(53) Ramalingam, B.; Khan, M. M. R.; Mondal, B.; Mandal, A. B.; Das, S. K. *ACS Sustain. Chem. Eng.* **2015**, *3*, 2291.
(54) Nugroho Prasetyo, E.; Kudanga, T.; Østergaard, L.; Rencoret, J.; Gutiérrez, A.; del Río, J. C.; Ignacio Santos, J.; Nieto, L.; Jiménez-Barbero, J.; Martínez, A. T.; Li, J.; Gellerstedt, G.; Lepifre, S.; Silva, C.; Kim, S. Y.; Cavaco-Paulo, A.; Seljebakken Klausen, B.; Lutnaes, B. F.; Nyanhongo, G. S.; Guebitz, G. M. *Bioresour. Technol.* **2010**, *101*, 5054.
(55) Roth, K. L.; Geng, X.; Grove, T. Z. *J. Phys. Chem. C* **2016**, *120*, 10951.
(56) Zeng, J.; Tao, J.; Li, W.; Grant, J.; Wang, P.; Zhu, Y.; Xia, Y. *Chem. Asian. J* **2011**, *6*, 376.
(57) Bhattacharjee, Y.; Chakraborty, A. *ACS Sustain. Chem. Eng.* **2014**, *2*, 2149.
(58) Sung, H. K.; Oh, S. Y.; Park, C.; Kim, Y. *Langmuir* **2013**, *29*, 8978.
(59) Annadhasan, M.; Muthukumarasamyvel, T.; Sankar Babu, V. R.; Rajendiran, N. *ACS Sustain. Chem. Eng.* **2014**, *2*, 887.

## 8.8 Supplemental Information

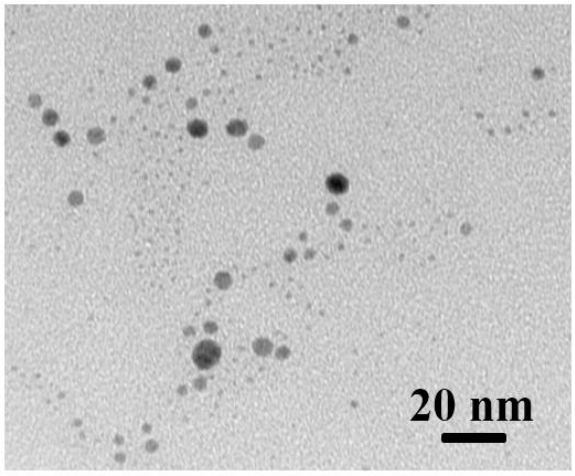


**Figure S1.** TEM image of Ag seeds prepared in the presence of 23 µg/ml SLigS

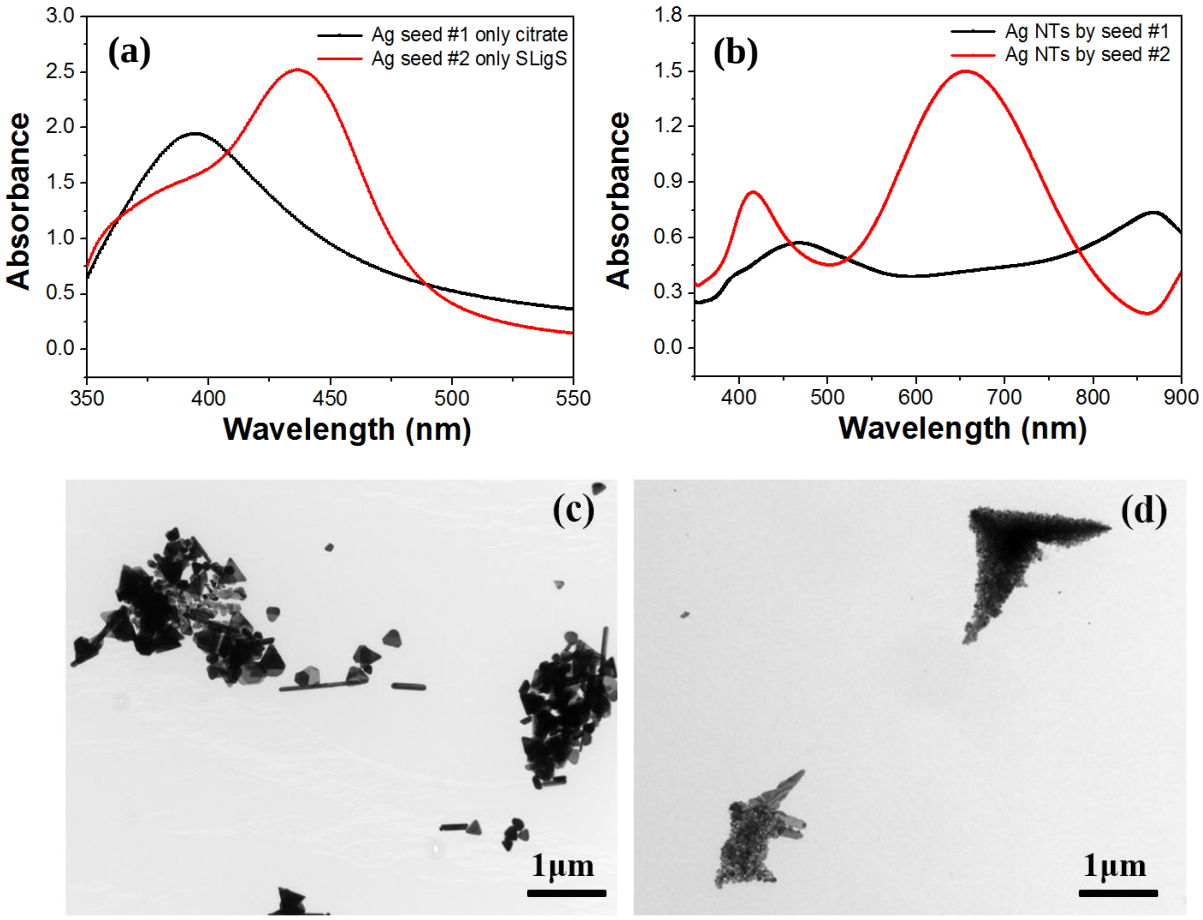

**Figure S2**. (a) UV-Vis spectra of Ag seed prepared in the absence of citrate (seed_1) or in the absence of SLigS (seed_2). (b) UV-Vis of Ag NPs prepared using corresponding seed. (c,d) TEM images of Ag NPs prepared using seed_1 and seed_2, respectively.

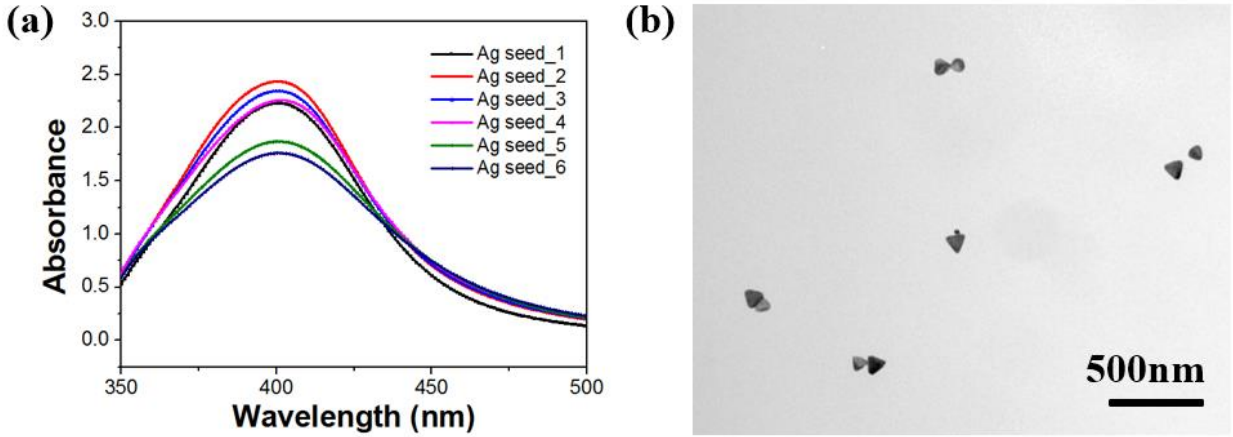


**Figure S3**. (a) UV-Vis spectra of Ag seeds prepared in the presence of 2.3 μg/ml (black), 7.7 μg/ml (red), 23.0 μg/ml (light blue), 46.1 μg/ml (magenta), 69.1 μg/ml (green), 92.2 μg/ml SLigS (b) TEM images of Ag NTs prepared using **Figure S3a** seed_4.

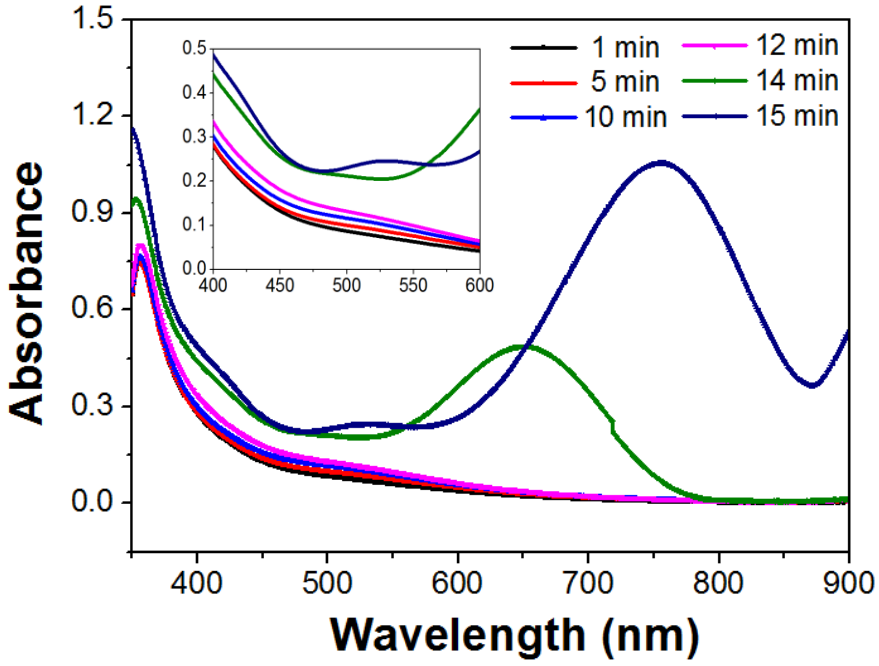


**Figure S4.** Time-course UV-Vis spectra for one pot synthesis of Ag NPLs.

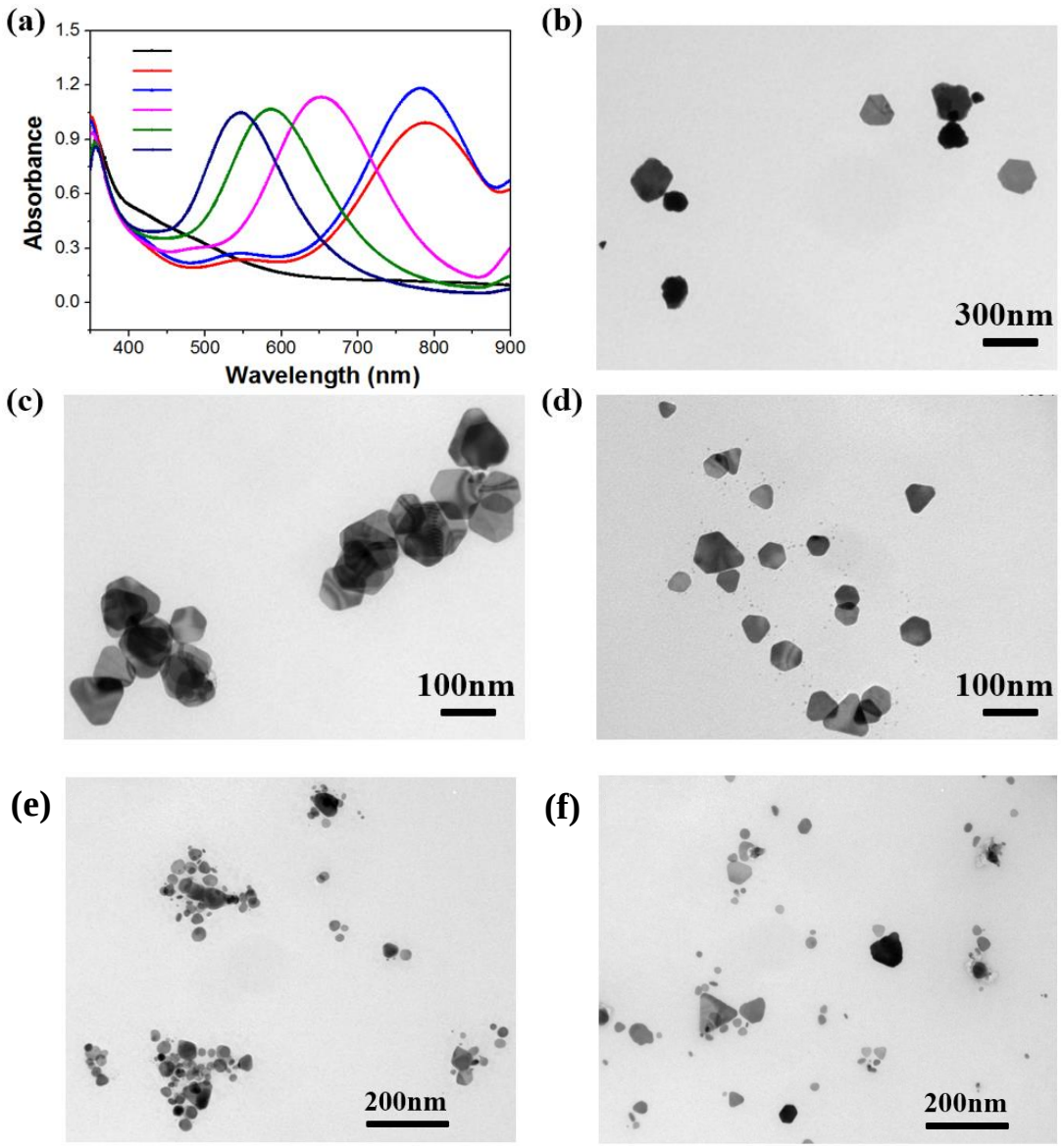


**Figure S5.** (a) UV-Vis spectra of Ag NPs prepared using varied concentration of $H_2O_2$: 2.5 mM (black), 3.7 mM (red), 4.9 mM (light blue), 8.6 mM (magenta), 12.3 mM (green) and 24.6 mM (dark blue), respectively. TEM image of Ag NPs corresponding to (b)**Figure S5a**-black (c)**Figure S5a**-red (d)**Figure S5a**-magenta (e)**Figure S5a**-green and (f) **Figure S5a**-dark blue.

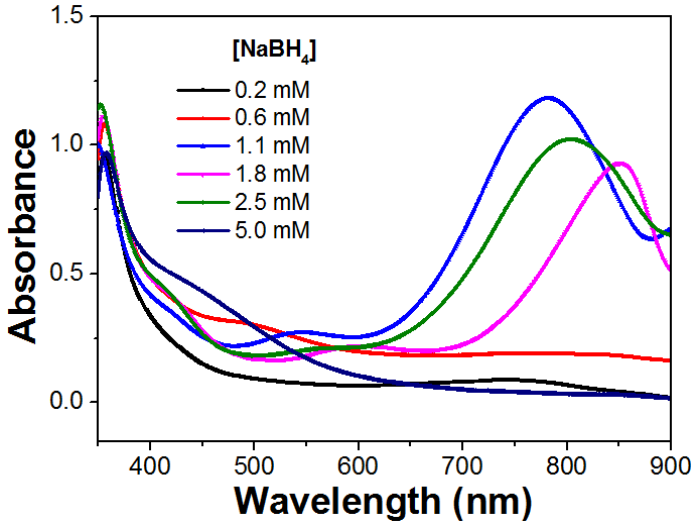


**Figure S6.** UV-Vis spectra of Ag NPs prepared using various amounts of $NaBH_4$

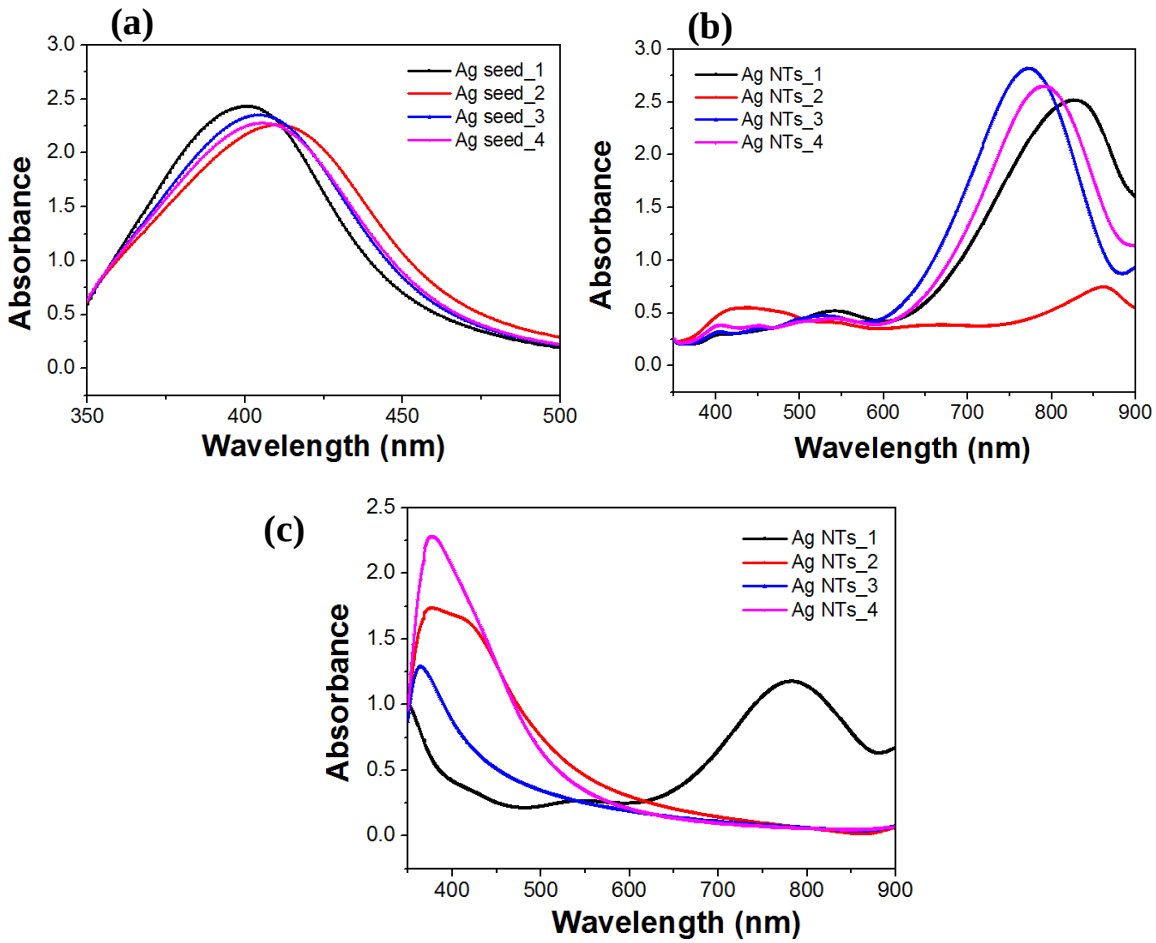

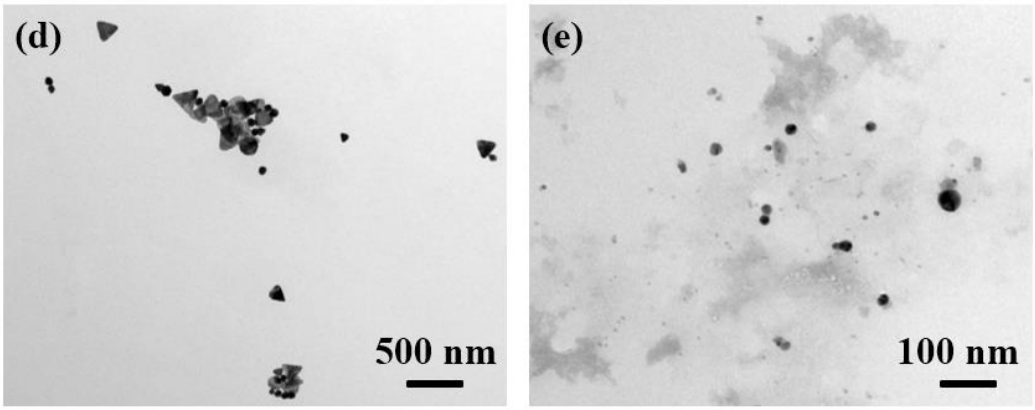


**Figure S7.** (a) UV-Vis spectra of Ag seed prepared using 4 different lignin derivatives: SLigS (black), Lignin (red), Ligno propionate (blue) and Ligno 2-hydroxyl ether (magenta) (b) UV-Vis spectra of Ag NTs prepared using 30 µl corresponding Ag seeds. (c) UV-Vis spectra of Ag NTs prepared usign one-pot method in the presence of varied kinds of lignin derivatives (0.5 mg/ml): SLigS (black), Lignin (red), Ligno propionate (blue) and Ligno 2-hydroxyl ether (magenta). (d,e) TEM images of Ag NPs corresponding to **Figure S7**b_red line and **Figure 7c**_red line, respectively.

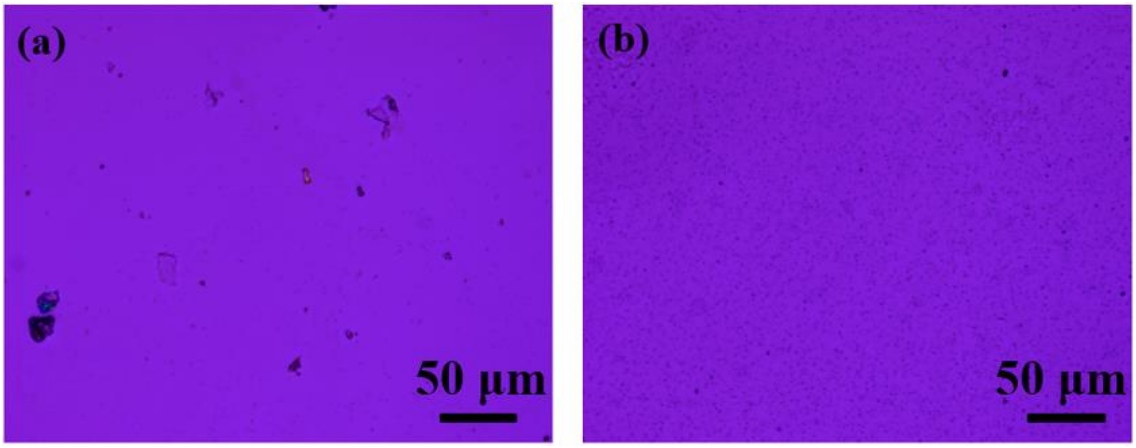


**Figure S8**. Opitcal microscopic image of Ag NTs/SLigS nanocomposite film prepared by drop casting of 50 µl aqueous solutions cotaining (a) 2 mg/ml SLigS (b) 2 mg/ml SLigS and 2 mg/ml Ag NTs on glass microscope slide.

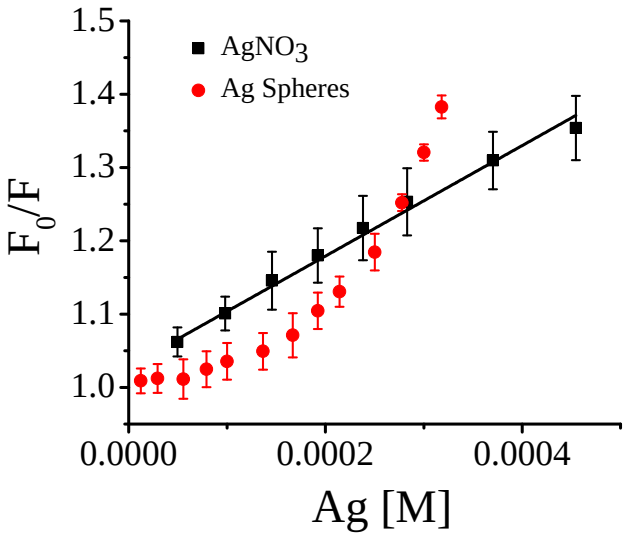


**Figure S9**. Stern-Volmer plot of fluorescence data resulting from adsorption of Ag(0) or Ag(I) to SLigS. (Ag stands for the concentration of Ag element.)

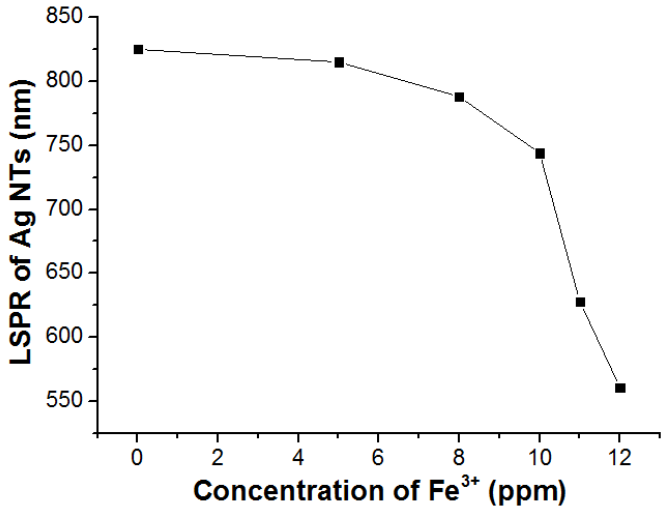


**Figure S10**. LSPR shift of Ag NTs vs. concentration of $Fe^{3+}$

# Chapter 9. Overall Conclusions

Utilization of anisotropic plasmonic noble metallic nanoparticles (APMNs) in biomedical applications relies on the development of green synthetic methods to produce stable NPs with high morphological control. We demonstrate that biological Good's buffers, such as MOPS and HEPES, can be utilized as mild reducing agents for the controlled synthesis of gold nanostars (Au NSTs) and gold nanoprisms. In a biomineralization-mimicry system containing $HAuCl_4$, MOPS and CTPR protein, the morphology and optical properties of as-synthesized Au NPs are determined by both the $[HAuCl_4]$/[CTPR] ratio and the CTPR shape. Further fluorescence quenching and heteronuclear 2D NMR studies reveal that the complexation between CTPR3 and Au(III) are dependent upon multiple factors including ionic strength and the residue identities. Whereas, the Au NPs were found to preferentially bind to the negatively charged face of the protein. The better understanding of protein-ion and protein-NP interactions enable rational deign of proteins for biomimetic synthesis of metallic NPs.

In the search for green chemical routes toward the synthesis of APMNs, attempts have been made to incorporate biomimetic synthesis into the seeded-growth process. In an elegant example shown in Chapter 5, CTPR proteins are utilized as potent stabilizers to facilitate the formation of planar-twinned Ag seeds, which is followed by the high-yield production of nanoprisms Ag nanoprisms in a subsequent step. Since only a negligible amount of CTPR is involved in the growth step, the triangular shape of the final products is predominantly dictated by the unique crystal structure of the seeds. Time-course TEM and UV-Vis observations imply that the growth mechanism can be interpreted by the combination of facet selective lateral growth and thermodynamically driven Ostwald ripening. Additionally, an expanded library

encompassing sustainable biomaterials like lignin- and cellulose- derivatives has also been identified to facilitate the controlled growth of Ag nanoprisms.

Furthermore, a novel seed-mediated biomineralization method has been developed to prepare gold nanotriangles (Au NTs) with tunable edge length at ambient conditions. Over 80% of the total number of NPs falls into the category of planar Au NTs after purification by salt-triggered selective sedimentation. In sharp contrast to the conventional CTAB/CTAC-assisted protocols, the seed-mediated biomineralization has the potential to provide unprecedented control over NP size and shape while maintaining biocompatibility requirements. It is noted that CTPR and NaBr cooperatively engaged in the kinetics control as well as the selective suppression of the low-index (111) facet. The well-defined morphologies, tailored plasmonic absorbance from visible-light to the near infrared (NIR) region, colloidal stability and biocompatibility are attributed to the synergistic action of CTPR, halide ions ($Br^-$), and CTPR-stabilized Ag seeds.

Admittedly, remarkable progress has been witnessed in the areas of biomimetic synthesis and biomineralization of APMNs. The current trend of studies in this area are still focusing on the specific case study, which lacks the universal principles that can be applied to different circumstances. In additional to that, only very limited types of nanostructures including the nanoplates, nanowires, branched and dendritic NPs are produced in high yield through bioenabled approaches. The further advancement of this field hinges on the collaborative contributions from multidisciplinary studies. As shown previously, the quantitative analysis of NP populations relies mainly upon the electron microscopic characterization, which lacks of potent data processing tools to distinguish different shapes. Recently, a computational method has been reported to algorithmically analyze the microscopic images which enables the structural

quantification of heterogeneous nanostructure populations. By introducing a shape-specific parameter, d(θ) (the distance from the edge of the particle to its center as a function of angle), a mixture of NPs containing multiple unique shapes could be readily differentiated.[1] Our research group is attempting to employ similar data processing software to characterize the morphology of NP populations in a more precise manner. Although we have demonstrated that biosustainable materials with specific physicochemical properties can serve as efficient stabilizers and crystal growth modifiers, the profound understanding of the roles of biomolecules and the rational design of biomimetic systems are still highly demanded to bridge the broad gap between bioenabled synthesis and traditional colloidal synthesis. Collaborative research project has been initiated to pinpoint the fundamental interactions between APMNs and self-assembled monolayers (SAMs) under the conditions analogous to the biomineralization environment. And preliminary results have shown the binding affinity between Au NPs and SAMs are closely correlated to the morphology of NPs, the concentration of biological buffers, the end groups of SAMs as well as the smoothness of the substrate. Further exploration is underway with the aid of integrated quartz crystal microbalance (QCM) and microscopic studies.

**Reference**

(1) Laramy, C. R.; Brown, K. A.; O'Brien, M. N.; Mirkin, C. A. *ACS Nano* **2015**, *9*, 12488.